

Petrogenesis of the Boothia Ferroan Granite Complex, Boothia Peninsula, Nunavut

by

Alix M. Osinchuk

A thesis submitted in partial fulfillment of the requirements for the degree of

Master of Science

Department of Earth and Atmospheric Sciences
University of Alberta

© Alix M. Osinchuk, 2021

Abstract

Reconnaissance regional mapping as part of the Geological Survey of Canada's Geomapping for Energy and Minerals (GEM-2) project documented three voluminous, massive to weakly foliated felsic plutons in Boothia Peninsula, Nunavut. Uranium-lead zircon and monazite geochronology reveals this magmatism, herein called the Boothia Ferroan Granite Complex (BFGC), occurred between 1841 and 1823 Ma, an age range scarcely reported within this region. The emplacement of the BFGC is contemporaneous with widespread Paleoproterozoic granite 'blooms' in the Churchill Province associated with the late-accretion to post-collisional stages of the Trans-Hudson orogeny (Peterson *et al.*, 2002; 2015b), and extends the northern limit of tectonothermal effects linked to the orogen to > 1400 km from the orogenic front. A comprehensive study of the granitoids involving U-Pb geochronology, whole-rock and mineral geochemistry, samarium-neodymium and lutetium-hafnium isotope geochemistry, and geothermobarometry was conducted to determine the petrogenesis of the BFGC. This research allows us to investigate potential tectonic mechanisms responsible for this widespread granitic within the Churchill Province, and in turn provides important insights into the nature of late- to post-tectonic magmatism associated with continental collisions.

The BFGC comprises four suites of granitoids: the fayalite, charnockite, hornblende-biotite and garnet-biotite suites. These granitoids are dominantly ferroan (high Fe/Mg) and potassic, include both metaluminous and peraluminous varieties, and are relatively enriched in incompatible elements. This study reveals: 1) the BFGC represents high-temperature (> 800°C to up to 950°C), reduced, and relatively H₂O-poor magmatic rocks, as evidenced by amphibole-plagioclase, titanium-in-zircon and zircon saturation geothermometric constraints and the presence of high-temperature anhydrous minerals (fayalite, orthopyroxene, inverted pigeonite);

2) the BFGC was emplaced at mid-crustal pressures between 5.1-6.3 kbar (~18-22 km depth) in an overthickened (50-60 km) crust, partially assimilating semi-pelitic country rock during emplacement; 3) BFGC magmatism is spatially associated with shearing associated with far-field stresses of the Trans-Hudson orogen; and 4) strongly negative initial $\varepsilon\text{Nd}_{1.83\text{Ga}}$ (-7.1 to -8.3) and zircon-derived $\varepsilon\text{Hf}_{1.83\text{Ga}}$ (-8.4 to -10.8) values, which overlap those of basement rocks in the Boothia Peninsula. However, geochemical and isotopic variations within the BFGC granitoid suites suggest their derivation from two main source rocks, a mixed Boothia basement source, comprising 2.56-2.52 Ga Boothia porphyroclastic granites and 2.48 Ga Boothia basement mafic rocks, and a light rare earth element-enriched mafic source rock, not exposed at the surface in Boothia Peninsula but hypothesized to be present at lower crustal depths.

I propose that BFGC magmatism was triggered by a partial lithospheric delamination event that occurred across the Churchill Province hinterland during the late stages of the Trans-Hudson orogen. Mantle upwelling associated with this event, along with radiogenic heating associated with crustal thickening in the hinterland, provided the heat required to generate high-temperature magmas within the lower crust and a previously metasomatized sub-continental lithospheric mantle. The generation of LREE-enriched mantle melts and coeval granitic magmatism through lithosphere delamination is also the proposed petrogenesis of ~1.83 Ga ultrapotassic magmas that intruded synchronously with widespread Hudson granite magmatism in the Churchill Province (Peterson *et al.*, 2002; Cousens *et al.*, 2001; Sandeman and Hadlari, 2010). The data obtained in the present study in conjunction with data collected from widespread ca. 1.83 Ga magmatism elsewhere in the Churchill Province implies lithospheric delamination within a collisional orogen has the capacity to produce a 1) ~1400 km extent of synchronous magmatism

in the hinterland orogenic plateau, and 2) high-temperature partial melts distal from the orogenic front.

Preface

This research was conducted in collaboration with the Geological Survey of Canada's (GSC) Geomapping for Energy and Minerals (GEM-2) as part of the 2017-2018 Boothia Peninsula-Somerset Island Project, directed by Dr. Mary Sanborn-Barrie. Fieldwork and sample collection would not have been possible without the expertise of Mary Sanborn-Barrie, Dr. Daniele Regis, and Angela Ford of the GSC. Fieldwork observations and sample collection was also assisted by the following geoscience students: Derek Drayson, Jacob Ballinger, Joanne Angai, Jefferson Fraser, Jacob VanderWal, Talia Moum, Lora Blondin, Carson Kinney, Sean Hicks, Zina Boileau, Madison Ritchie, Pascal Voegeli, and Emily Creaser.

Sample processing and powdering for whole-rock and Sm-Nd geochemistry was conducted by Actlabs. Sm-Nd isotopic analysis was overseen by Isotope Geochemistry and Geochronology Research Centre (IGGRC) at Carleton University, directed by Dr. Daniele Regis. Dr. Regis also conducted U-Pb geochronology via SHRIMP on select samples documented within this thesis, as well as zircon separation of sample 17SRB-O009. I oversaw and collected the remaining sample crushing, processing, mineral separation, and data collection related to this work.

All ideas that are presented in this thesis are my own, though they have been developed and refined by my supervisors and collaborators including Drs Tom Chacko, Larry Heaman, Mary Sanborn-Barrie, Daniele Regis, and Ph. D. candidate Derek Drayson.

Acknowledgements

First and foremost, I wish to acknowledge and thank my supervisors Tom Chacko and Larry Heaman for their unwavering support and boundless patience. They have both dedicated their knowledge, time, and research rigor into this project, which undoubtedly improved the quality of this thesis immensely. I would like to thank Tom for always being available and willing to guide me through a wide scope of ideas with clear and concise explanations. I always look forward the enthusiastic discussions of research projects, new techniques, and best methods to improve and build upon my research. He has inspired what it means to be a dedicated mentor and scientist, and will always be grateful for his unjudgmental advice, whether it be research or life related. I would like to thank Larry teaching me to always strive to produce high-quality research within my work, instilling the value of precision and transparency, and thank him for the reminders to be assertive and confident in my research. He has been instrumental in my growth as a researcher, both in this project and my undergraduate thesis. I truly could not think of a better supervisory committee to guide my studies and research, and I am honored that I had this opportunity to do so. I am truly indebted to both will always be very grateful with the time I spent under their tutelage.

I could not have had this incredible research opportunity without the support and direction of Mary Sanborn-Barrie. I thank her for her research expertise, inspiring work ethic, and unequivocal advice and discussions both on and off the field. I would also like to thank Daniele Regis, who provided invaluable research data, insight, and suggestions to further my research career, as well as Angela Ford, who was the technical and sassy backbone to the Boothia-Somerset project. I would also like to thank every member of the ‘Nuna Fam’ and ‘Creswell Crew’ (Derek, Jo, Jeff, Jacob V, Jacob B, Talia, Lora, Carson, Sean, Zina, Madisen, Pascal, and Emily) for creating unforgettable memories during fieldwork.

I would like to thank several individuals at the University of Alberta who provided support and expertise for this project: Dr. Andy DuFrane for data collection for U-Pb and zircon trace elements, Dr. Chiranjeeb Sarkar for his assistance with LASS-ICPMS acquisition and correction, Dr. Andrew Locock for assistance in EMPA standard analysis and identifying obscure trace minerals. I would also like to thank James LeBlanc for an eventful introduction to TIMS sample

preparation at the latter stages of my degree. My scientific education and teaching development greatly benefitted from Dr. Bob Luth and Marilyn Huff, who would always provide and discuss feedback for the benefit of their TAs and students. Robert Creaser is thanked for taking part of this thesis as my third examiner.

There are a variety of colleagues and friends that I would like to thank that contributed both to my research and personal development over the course of my studies. Derek Drayson, who is always there to sound board discussion for Boothia Peninsula, future research, and general graduate student life. Mike Belosevic, who provided both valuable scientific insight, teaching guidance, and entertaining discussions – especially on Wednesdays. Madisen Sagan, who provided great sample preparation training and expertise in zircon systematics. To Matt Hardman, Elaine Lord, Nicole Meyer, and Denny Smyth, who provided friendship and support that made the office a welcoming space as well encouraged my attempts at community writing.

Last but very much not least, I would like to thank my partner Saturday who provided constant support during long-road of pursuing of my career and aspirations. Thank you for being assuring voice during the long field seasons, and always providing a fresh voice of reason for me to rely on when I got in my head or stuck in a loop. I would also like to thank my family, whose enthusiasm has always encouraged me and driven me forward.

Table of Contents

Abstract.....	ii
Preface.....	v
Acknowledgements.....	vi
Table of Contents	viii
List of Tables	x
List of Figures.....	xii
Introduction	1
Regional Geology	4
Lithological Units of the Boothia Ferroan Granitoid Complex.....	9
Fayalite Granite	9
Charnockite	11
Hornblende-Biotite Granite.....	11
Garnet-Biotite Suite	16
Methodology	16
Zircon and Monazite Sample Preparation.....	16
U-Pb geochronology	18
Sm-Nd and Lu-Hf isotope determinations.....	18
Major- and Trace-element Geochemistry	20
Mineral Chemistry and Geothermobarometry.....	20
Zircon Minor- and Trace-Element Geochemistry.....	21
Results.....	22
Whole-Rock Geochemistry.....	22
Fayalite Granite.....	24
Charnockite.....	25
Hornblende-Biotite Granite.....	25
Garnet-Biotite Suite	28
Mineral Chemistry.....	28
U-Pb Geochronology.....	31
Fayalite Granite.....	32
Charnockite.....	34

Hornblende-Biotite Granite	34
Garnet-Biotite Suite	37
Zircon Trace Elements.....	39
Nd and Hf Isotope Compositions.....	44
Discussion	48
Emplacement Ages of the Boothia Ferroan Granite Complex.....	48
Intensive Parameters.....	50
Temperature of emplacement.....	50
Pressure of emplacement.....	56
Oxygen Fugacity	59
Petrogenesis of the Boothia Ferroan Granite Complex	61
Source rock characteristics.....	61
Petrogenesis of the Fayalite, Charnockite and Hornblende-Biotite Suites.....	63
Petrogenesis of the Garnet-Biotite Suite	64
Heat Trigger and Mantle Input	66
Location of magmatism	68
Tectonic Models.....	69
Slab Failure	70
Partial Lithospheric Delamination	73
Conclusions.....	75
References	78
Appendix 1: LA/LASS-ICPMS Operation Parameters and Standard Verification	93
Appendix 2: Compiled U-Pb Geochronology	100
Appendix 3: Compiled U-Pb Geochronology standards.....	126
Appendix 4: Compiled Lu-Hf and Sm-Nd Isotopic Analyses	135
Appendix 5: Zircon Trace-Element analyses and Standards.....	141
Appendix 6: Sample Locations.....	147
Appendix 7: Extended Comparison to Churchill late- to post-tectonic magmatism.....	148
Hudson Granites and Coeval Minettes	148
Kivalliq Igneous Suite / Nueltin granites	150
Cumberland batholith	151

List of Tables

Table 1: Major- and Trace-element geochemistry	23
Table 2: Anhydrous mineral composition	29
Table 3: Hydrous mineral composition.....	30
Table 4: Oxide mineral composition	31
Table 5: Summary of U-Pb geochronology	32
Table 6: Zircon minor- and trace-element composition.....	41
Table 7: Summary of whole-rock Sm-Nd and zircon Lu-Hf isotopic composition.....	44
Appendix 1, Table 1: LA-ICMPS Operation Parameters and Standards (Zircon)	92
Appendix 1, Table 2: LA-ICMPS Operation Parameters and Standards (Monazite).....	94
Appendix 1, Table 3: LASS-ICMPS Operation Parameters and Standards	96
Appendix 2, Table 1: Compiled U-Pb Geochronology.....	98
Appendix 3, Table 1: Compiled LA-ICPMS Standard Analyses (Zircon)	124
Appendix 3, Table 2: Compiled LA-ICPMS Standard Analyses (Monazite)	127
Appendix 3, Table 3: Compiled LASS-ICPMS Standard Analyses.....	128
Appendix 4, Table 1: Compiled Zircon Lu-Hf isotopic analyses.....	133
Appendix 4, Table 2: Compiled whole rock Sm-Nd isotopic analyses	138
Appendix 5, Table 1: Zircon Trace-Element Compilation.....	139
Appendix 5, Table 2: Standard Analysis for Zircon Trace-Elements	140
Appendix 6, Table 1: Sample Locations	145

List of Figures

Figure 1: Simplified Regional Geology Map	2
Figure 2: Geological Map of Boothia Peninsula	6
Figure 3: Sample Location Map	8
Figure 4: Q-ANOR	10
Figure 5: Field photos of the BFGC	12-13
Figure 6: Petrographic photos of the BFGC	15
Figure 7: BSE of trace minerals in Hornblende-Biotite Granite	17
Figure 8: Major-element geochemistry	24
Figure 9: REE and Incompatible element spider diagrams	26
Figure 10: Trace-element discrimination diagrams	27
Figure 11: U-Pb geochronology	35-36
Figure 12: CL and BSE images of monazite and zircon	38
Figure 13: REE composition of zircons within representative samples	40
Figure 14: Zircon trace element discrimination diagrams	43
Figure 15: Whole Rock Nd isotopic evolution	45
Figure 16: Zircon Hf isotopic evolution	46
Figure 17: Summary and Comparison of U-Pb ages of the BFGC	49
Figure 18: $T_{\text{Ti-zircon}}$ and T_{ZircSat} constraints	52
Figure 19: Pressure and Temperature estimates of emplacement	56
Figure 20: Oxygen fugacity	60
Figure 21: Slab-failure trace-element discrimination diagrams	71
Appendix 1, Figure 1: Secondary standards for LA-ICPMS (zircon)	93
Appendix 1, Figure 2: Secondary standards for LA-ICPMS (monazite)	95
Appendix 1, Figure 3: U-Pb Concordia of secondary standards for LASS-ICPMS	97
Appendix 1, Figure 4: $^{176}\text{Hf}/^{177}\text{Hf}$ of secondary standards for LASS-ICPMS	98

INTRODUCTION

The Paleoproterozoic is a crucial period of global crust formation and amalgamation associated with the assembly of supercontinent *Nuna* (Hawkesworth *et al.*, 2009). Many Paleoproterozoic orogenic belts are characterized by voluminous syn- to post-collisional felsic magmatism (Eklund *et al.*, 1998; Griffin *et al.*, 2000; Peterson *et al.*, 2002; Barros *et al.*, 2009). Although these granite “blooms” are common, their petrogenesis is not always clearly defined (Brown, 2013). Many post-collisional granites share similar characteristics; they are typically emplaced 10 to 30 million years after collision (Whalen and Hildebrand, 2019), and generally have higher silica and incompatible element contents than continental-arc granites (Pearce *et al.*, 1984; Bonin, 2004). However, there are also differences in their character that can reflect features unique to the tectonic environment in which they were derived. For example, some granite blooms are spatially and temporally associated with mafic and/or potassic (syenitic) magmatism (Eklund *et al.*, 1998; Cousens *et al.*, 2001) whereas this mafic/alkaline association can be completely absent in other post-collisional granites (Whalen *et al.*, 2010). To fully resolve the nature of Paleoproterozoic orogens, it is important for us to better understand the mechanisms by which these different types of post-tectonic granite blooms form.

Several 2.0 – 1.8 Ga orogenies and their associated plutons have stitched together the core of Laurentia, providing insight on Paleoproterozoic tectonics and the assembly of *Nuna*. There are, however, key regions in Laurentia, particularly in the Canadian Arctic, that have long been understudied due to the difficulty and expense of accessing these remote regions. One such region is Boothia Peninsula and Somerset Island in western Nunavut. The basement rocks of this area were exhumed during the Devonian-age Caledonian orogeny (Kerr and Christie, 1965) and affords an opportunity to study the Precambrian history of the northern portion of the Churchill Province. The rocks in this corridor are inferred to be part of either the Rae craton or one of several other terranes that have been proposed to make up the western boundary of this craton (Fig. 1; (Frisch and Hunt, 1993; Schultz *et al.*, 2007; Berman *et al.*, 2013; Pehrsson *et al.*, 2013a). This region is therefore critical for evaluating the Neoarchean and Paleoproterozoic history of the western Canadian Shield.

The last lithological study that was done on the basement rocks of Boothia Peninsula was reconnaissance mapping in the 1960s (Blackadar, 1967). This work separated the basement into

mafic and felsic gneisses, with limited insights into the protoliths of these high-grade metamorphic rocks. More recently, reconnaissance mapping of basement rocks of Somerset Island and portions of northern Boothia Peninsula along with supporting U-Pb and K-Ar geochronology was undertaken by Frisch and Hunt (1993). Significant advancements in geochronological techniques since the study of Frisch and Hunt (1993), in addition to availability of much more information on the Rae craton, suggest that further geological investigation of Boothia Peninsula is warranted. In 2017 and 2018, regional mapping in Boothia Peninsula and Somerset Island was conducted by the Geological Survey of Canada as part of the Geo-mapping

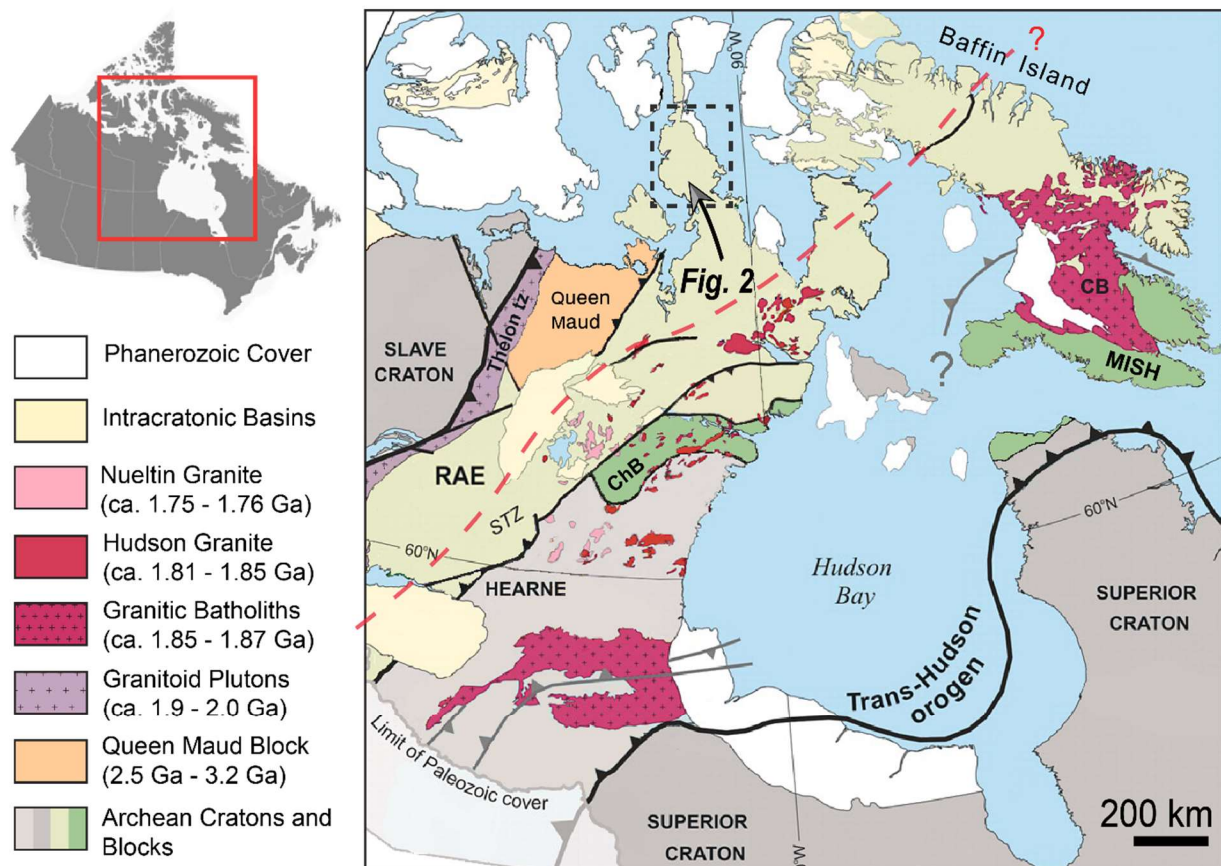


Figure 1: Simplified Geology Map of the Western Churchill Province, after Pehrsson *et al.* (2013a), highlighting Paleoproterozoic felsic plutonism. Red line indicates previous known extent of crust affected by the Trans-Hudson orogeny (from Corrigan *et al.*, 2009) Black dashed box indicates region of study and location of Boothia Peninsula. Abbreviations are as follows: CB = Cumberland Batholith, STZ = Snowbird Tectonic Zone, ChB = Chesterfield Block, MISH = Amalgamation of the Meta-Incognita, Sugluk Block, and Hall Peninsula Block

for Energy and Minerals (GEM-2) program. The overall objective of this mapping project is to develop a complete tectonic framework for the northern borders of the Rae craton.

In previous mapping studies (Frisch and Hunt, 1993), Boothia Peninsula was inferred to have a late Neoarchean or early Paleoproterozoic history with little evidence of post-ca. 1.9 Ga granitic plutons. Widespread Paleoproterozoic (ca. 1.85-1.80 Ga) granitic magmatism documented throughout the Churchill Province is typically considered a far-field response to Trans-Hudson orogen (THO) tectonism, which was associated with closure of the Manikewan Ocean and subsequent collision of the Churchill Province with the Superior craton (Corrigan *et al.*, 2001; Weller and St-Onge, 2017). Minor pegmatite dykes associated with 1.81 Ga deformation occurs in the Boothia mainland area south of Boothia Peninsula (Hinchey *et al.*, 2011). This igneous and metamorphic activity was previously thought to be the northwestern-most expression of the THO. Paleoproterozoic granitoid magmatism is widespread in the Churchill Province (Fig. 1), and whereas petrogenetic models have been proposed for these suites (Peterson *et al.*, 2002), it is not yet clear why this contemporaneous magmatism spans across much of the Rae and Hearne cratons or whether the characteristics of this magmatism are consistent throughout these cratons.

In the southeast portion of Boothia Peninsula, three regionally extensive, late- to post-tectonic ca. 1.83 Ga plutons were documented during the 2017 field season (Fig. 2 and 3). These relatively undeformed plutons contrast with the poly-deformed plutonic and metasedimentary basement rocks within Boothia Peninsula, and differ mineralogically and geochemically from other ca. 1.9-1.8 Ga post-collisional granites, such as the Cumberland Batholith (Whalen *et al.*, 2010) and Hudson Granites (Peterson *et al.*, 2002), found elsewhere within the Churchill Province. In this study, the timing of emplacement, petrogenesis and origin of these plutons, herein named the Boothia Ferroan Granitoid Complex (BFGC), is investigated using a combination of U-Pb geochronology, major-, trace-element and isotope (Nd, Hf) geochemistry and thermobarometric calculations. To further trace and quantify the extent to which these plutons interacted with their host Archean continental crust, the geochemical and isotopic (Nd, Hf) characteristics of the dominant basement material of Boothia Peninsula are also investigated. In doing so, this study of Precambrian rocks in the Boothia Peninsula aims to characterize the nature of the continental crust and lithosphere in the region and provide insights into the tectonic processes operating in the northern Churchill Province during the Trans-Hudson orogeny.

REGIONAL GEOLOGY

This study mainly focuses on the plutonism of the Churchill Province during the middle to late Paleoproterozoic; the broader tectonic history of the Churchill Province is reviewed to provide insight on the nature of the crust and underlying mantle lithosphere into which the Paleoproterozoic plutons were emplaced. The Churchill Province is an amalgamation of two larger Archean cratons, the Rae and Hearne cratons, and several smaller continental blocks that make up the continental core of Laurentia (Hoffman, 1988; Berman *et al.*, 2007; Pehrsson *et al.*, 2013a; LaFlamme *et al.*, 2014; Sanborn-Barrie *et al.*, 2014; Liu *et al.*, 2016). The Churchill Province extends >1500 km from northern Saskatchewan (Fig. 1) into the Canadian Arctic Archipelago to Baffin Island. The Rae craton, which makes up the northwestern half of the Churchill Province in which Boothia Peninsula is situated, comprises Mesoarchean (ca. 3.2 – 3.0 Ga) to Neoarchean (ca. 2.9 – 2.75 Ga) tonalitic gneisses (Ryan *et al.*, 2009; LaFlamme *et al.*, 2014; Sanborn-Barrie *et al.*, 2014), and Neoarchean greenstone belts ranging in age from ca. 2.73 to 2.71 Ga (Sanborn-Barrie *et al.*, 2014). Neodymium model ages of felsic plutonic rocks and Os isotope model ages of peridotite xenoliths indicate conjoined lithospheric mantle and initial amalgamation of the Rae craton at ca. 2.7-2.6 Ga (Hinchey *et al.*, 2011; Sanborn-Barrie *et al.*, 2014; Liu *et al.*, 2016). The Meso- and Neoarchean basement rocks were then intruded by felsic plutons at ca. 2.66 Ga and ca. 2.63-2.58 Ga, which are proposed to be the product of syn-to post-collisional crustal thickening across the northern Rae craton (Hinchey *et al.*, 2011; Peterson *et al.*, 2015a).

The western boundary of the northern Rae is flanked by the Queen Maud Block (QMB), and is delineated by an aeromagnetic high between ca. 2.6-2.7 Ga, orthopyroxene-absent granitoids of the Rae and commonly orthopyroxene-bearing, ca. 2.50 – 2.46 Ga QMB granitoids (Schultz *et al.*, 2007). One model proposes that the QMB granitoids, along with minor ca. 2.48 Ga mafic magmatism and the ca. 2.44 - 2.39 Ga Sherman Group sedimentary basin is the product of a continental rifting event (Schultz, 2007; Schultz *et al.*, 2007; Tersmette, 2012). Alternatively, concurrent deformation further inland to the Rae craton led Berman *et al.* (2013) to suspect that QMB magmatism occurred in a higher temperature back-arc basin or ridge subduction in a convergent setting, as part of the Arrowsmith orogeny. Farther west, the Queen Maud Block comprises mixed Mesoarchean to Neoarchean gneisses (ca. 3.2 – 3.1 Ga, ca. 2.7 Ga) which is then bounded by the Thelon tectonic zone (Ttz) to the west (Tersmette, 2012) . As Boothia

Peninsula appears to be an along strike extension to the aeromagnetic signatures recorded in the Queen Maud Block and western Rae (Thomas, 2018), understanding the relationship and genesis of the QMB will become crucial for understanding the nature of Neoarchean plutonism of Boothia Peninsula.

Much of the western Rae craton and QMB were subsequently deformed, reworked and metamorphosed to upper amphibole or granulite grade at ca. 2.35-2.38 Ga during the Arrowsmith orogeny (Berman *et al.*, 2005; Hartlaub *et al.*, 2007; Schultz *et al.*, 2007). Ca. 2.35 – 2.30 Ga syn- to post-collisional magmatism and coeval sedimentary basin development occurred in the southwestern Rae craton (Hartlaub *et al.*, 2007; Ashton *et al.*, 2013). Further north, the Arrowsmith orogeny manifests as deformation and high-grade metamorphism with associated monazite and zircon growth (Berman *et al.*, 2013) rather than distinct magmatic events. The Arrowsmith orogeny is described as either a classic Andean-arc convergent margin (Berman *et al.*, 2013) or continental collision along the east margin of the Rae Craton, and is one of the proposed mechanisms of collision between the Slave Craton and the Churchill Province (Hartlaub *et al.*, 2007; Schultz, 2007).

The ca. 2.0-1.9 Ga Thelon tectonic zone (TTZ) (Thompson, 1989), which borders the west of the QMB, is described as a proposed mechanism of Slave-Churchill collision (Hoffman, 1988; Berman *et al.*, 2018), or as an intracontinental collisional belt (Thompson, 1989; Chacko *et al.*, 2000; Tersmette, 2012). Reconnaissance U-Pb zircon and monazite geochronology indicates ca. 1.94-1.90 metamorphic rocks outcrop along the western coast of Somerset Island (Frisch and Hunt, 1993), suggesting the TTZ extends from the west of the QMB to Somerset Island (Fig. 1) and, potentially, into western Boothia Peninsula. TTZ metamorphism and deformation is limited in the QMB (Tersmette, 2012), however ca. 2.01 – 1.92 Ga metamorphism, deformation, and sedimentation discovered in the 2017 field season (Fig. 2) (Regis *et al.*, in preparation) indicates the Thelon crustal reworking was significant in western Boothia Peninsula.

The Thelon tectonic zone, along with the Trans-Hudson Orogen, are part of many ca. 2.0 – 1.8 Ga orogenic belts worldwide that formed during the amalgamation of *Nuna* (Zhao *et al.*, 2004; Evans and Mitchell, 2011; Pehrsson *et al.*, 2013b), catalyzed by widespread rifting that occurred between ca. 2.2 – 2.0 Ga (Aspler *et al.*, 2001). The Churchill Province experienced partial rifting and crustal thinning at this time, evidenced by mafic dyke swarms and intracratonic basin

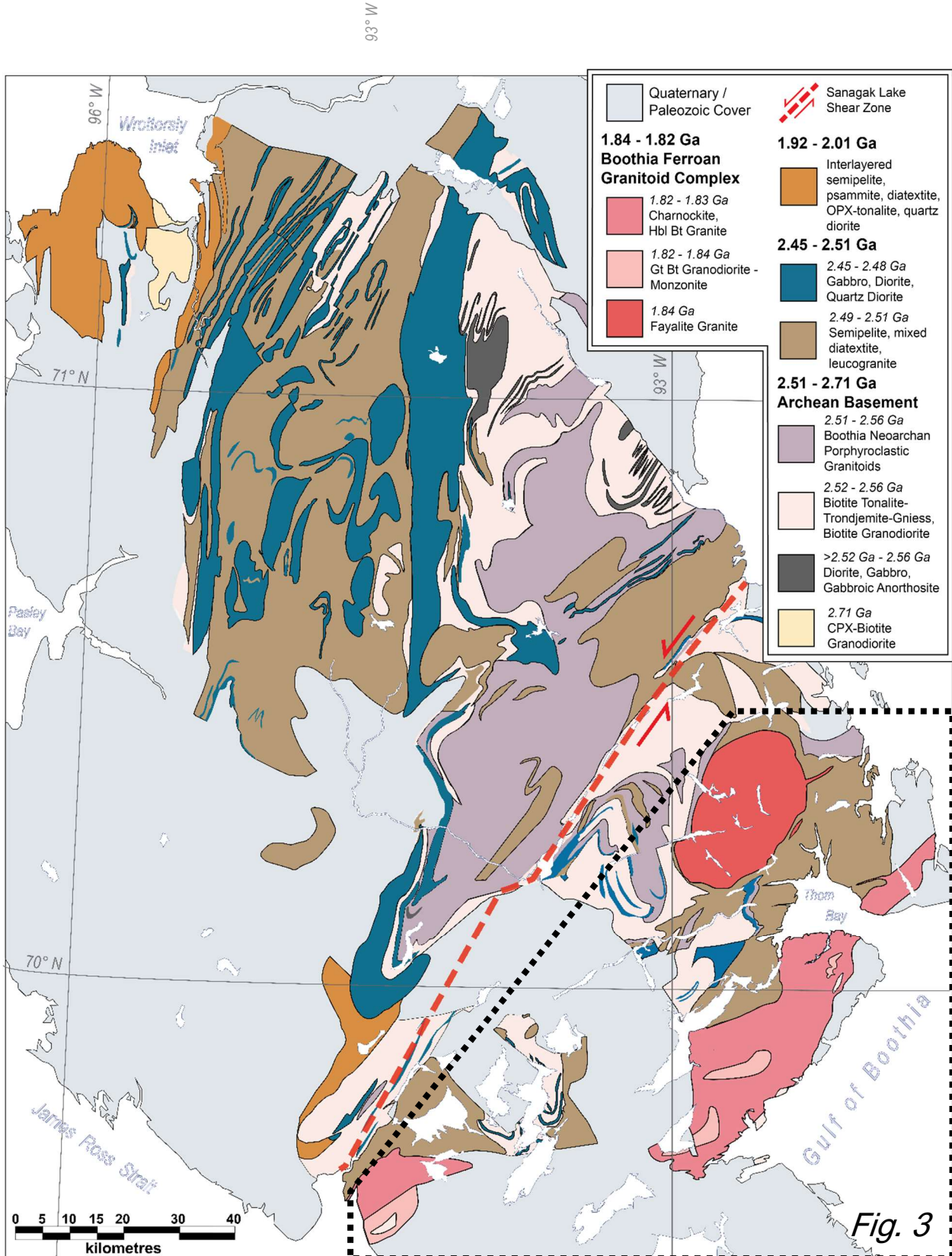


Figure 2: Simplified geological map of Boothia Peninsula from Sanborn Barrie et al. (in prep). Black dotted line indicates inset of Figure 3 and extent of sample map highlighting the Boothia Ferroan Granitoid Complex.

development across in the Churchill Province (Patterson and Heaman, 1991; Heaman and LeCheminant, 1993; Aspler *et al.*, 2002; Maurice *et al.*, 2009; Rainbird *et al.*, 2010). The THO and its associated magmatism was the last regional-scale event to affect the crustal structure of the Churchill Province. The initiation of the THO magmatism occurred in several orogenic phases as early as 1.92 Ga (Corrigan *et al.*, 2001; Berman *et al.*, 2007), with terminal collision occurring ca. 1.83-1.80 Ga (Corrigan *et al.*, 2009), and post-collisional extension continuing until ca. 1.75 Ga (Scott *et al.*, 2015). Much of the magmatism is proximal to several NE-trending crustal-scale shear zones that formed contemporaneously to the early stages of the THO within the Churchill Province. The most prominent shear zone is the 1.91 Ga Snowbird Tectonic Zone (STZ), and it is recognized as the boundary between the Rae and Hearne cratons. The STZs tectonic significance as either a Neoarchean arc, an intracontinental fault, or a Paleoproterozoic suture has been debated in recent study and remains enigmatic (Mahan and Williams, 2005; Regan *et al.*, 2017; Sanborn-Barrie *et al.*, 2019). The perpetual reworking and complicated tectonism prior to and during the early stages of the THO provided several Paleoproterozoic structures that could prove to be important conduits for magmas, and is suggested to have left a relatively weak lithospheric mantle underneath the Churchill craton (Liu *et al.*, 2016).

Figure 1 highlights areas of widespread THO-associated magmatism within the Churchill Province and the previous estimate of the northernmost extent of THO deformation and magmatism (Corrigan *et al.*, 2009), including the ca. 1.85 – 1.81 Ga Hudson Granites and concurrent ultrapotassic magmatism (Christopher Island Formation, Cousens *et al.*, (2001); Hearne lamprophyres, (Sandeman and Hadlari, 2010)) and the anorogenic ca. 1.77 - 1.73 Ga Kivalliq Igneous Suite and Nueltin granites. The Hudson Granite plutons are syn- to post-tectonic granitoids (mostly monzo- and syenogranites), spatially associated with THO shear zones and faults, that were emplaced during terminal collision of the Superior and Churchill Provinces (Peterson *et al.*, 2002; van Breemen *et al.*, 2005; Scott *et al.*, 2015). The Nd isotopic compositions of the Hudson Granite suite is consistent with these magmas being derived by partial melting of the middle and lower crust (Peterson *et al.*, 2002). Though crustal thickening would have contributed to melting of the Hudson Granites due to radiogenic derived heat, the co-eval minette magmatism suggests melts of enriched sub-continental lithospheric mantle interacted with the crust, and the contributed mantle input would provide significant heat input to

trigger further crustal melting (Cousens *et al.*, 2001; Peterson *et al.*, 2002; van Breemen *et al.*, 2005). The mantle-crust interaction required to generate both the minettes and Hudson Granites is suggested to be triggered by some type of disruption of the structure of the lithosphere, while contemporaneous shear zones and strike-slip faulting promoted pluton emplacement (Peterson *et al.*, 2002). Following the emplacement of the Hudson Granite, upwelling mantle interpreted to be resulting from partial lithospheric mantle delamination gave rise to the 1.77-1.73 Ga bimodal Kivalliq Igneous Suite, which includes the rapakivi Nueltin granites, rhyolitic volcanism, and mafic intrusions (Peterson *et al.*, 2015b; Scott *et al.*, 2015). The implication of widespread felsic

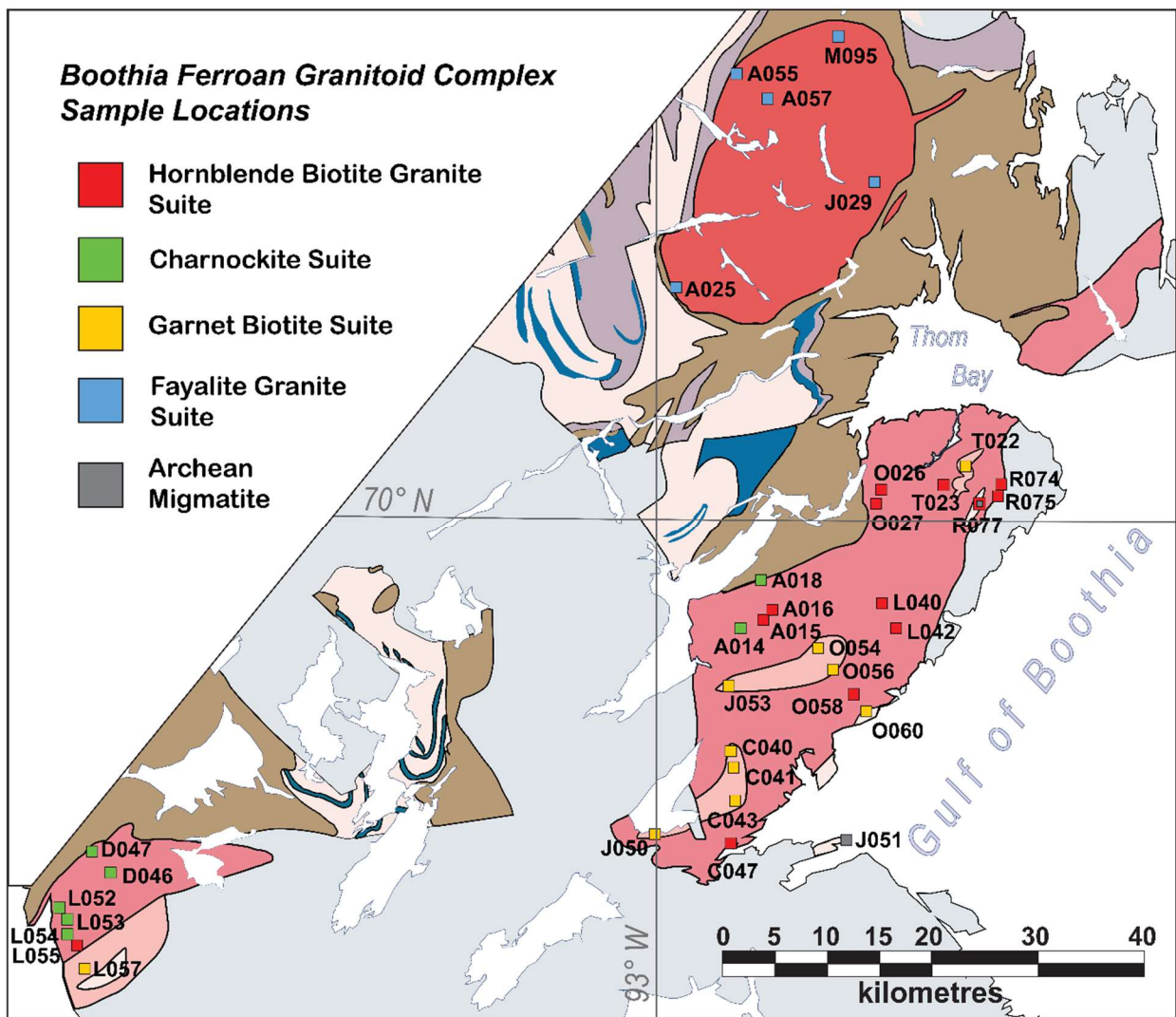


Figure 3: Inset map of the Boothia Ferroan Granitoid Complex, showing sample localities of each of the four suites of the Boothia Ferroan Granitoid Complex as well as Neoarchean migmatite xenoliths. Samples names are all prefixed by “17SRB”.

magmatism of both the Hudson Granites and Kivilliq-Nueltin suites is that lithospheric mantle instability of the Churchill craton during and following the THO resulted in significant mantle heat input, and therefore, voluminous magmatism within the Southern Rae and Northern Hearne. In addition, the 1.87 – 1.84 Ga Cumberland Batholith (CB), which occurs at the border between the Rae and Meta Incognita-Sugluk-Hall Peninsula block (MISH, Fig. 1), is an extensive batholith also attributed to slab-break off or large-scale lithospheric delamination (Whalen et al., 2010; Whalen and Hildebrand, 2019). Unlike the Hudson Granites, which occur in the hinterland distant Superior-Churchill plate boundary, the Cumberland Batholith is located near the plate boundaries associated with the amalgamation of the MISH, Rae Craton, and Hall Peninsula. Though these igneous suites differ from each other, their petrogenetic commonality is that they all required a period of crustal thickening followed by interaction with mantle in varying degrees, whether that be as a heat source or the incorporation of mantle-derived magmas (Peterson et al., 2002; Whalen et al., 2010).

LITHOLOGICAL UNITS OF THE BOOTHIA FERROAN GRANITOID COMPLEX

The Boothia Ferroan Granitoid Complex, or BFGC, comprises three plutonic bodies located between the southeast coast and central region of Boothia Peninsula. These three plutons (designated the northeast, southeast, and southwest plutons by their relative positions on Boothia Peninsula, Fig. 3) collectively comprise four suites of felsic plutonic rocks with relatively high Fe/Mg: the fayalite, charnockite, hornblende-biotite, and garnet-biotite granite suites. These four suites can be distinguished on the basis of their mineralogy, texture, and field relationships; the distinction between suites is further supported by differences in their respective major- and/or trace-element compositions (Fig 4).

Fayalite Granite

The fayalite granite suite occurs exclusively in the northeast pluton, separate from the other suites in the BFGC (Fig. 3). This suite is remarkably homogeneous, consisting of coarse grained, inequigranular, fayalite, biotite ± amphibole syenogranite to monzogranite (Fig. 4), with abundant accessory apatite and variable amounts of magnetite and ilmenite. The pluton is variably weathered, with the most extensively weathered outcrops disaggregating into dark-brown grus. The contacts of the pluton, where observed, are gradational and obscured by

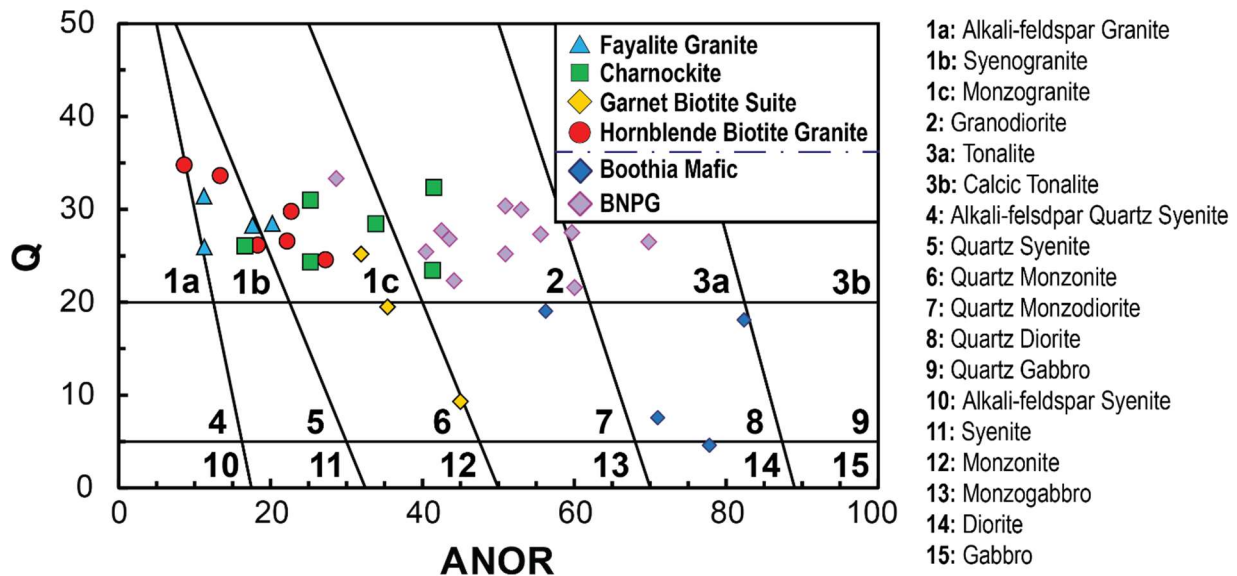


Figure 4: Normative Quartz-Anorthite (Q-ANOR) classification diagram for the Boothia Ferroan Granitoid Complex and their source rocks; see text for discussion. BNPG = Boothia Neoarchean porphyroclastic granitoids. Q = Quartz / (Quartz + Albite + Anorthite + Orthoclase) * 100; ANOR = Anorthite / (Anorthite + Orthoclase) *100

extensive melting of the surrounding metasedimentary country rocks. The margins show extensive sericite alteration of plagioclase, and fayalite is less common; this is likely a consequence of super- and sub-solidus interaction of the granite magma with the melted country rock during the pluton's emplacement. The pluton exhibits a very weak SW-striking fabric coincident with the regional fabric, although this fabric is not visible in smaller hand samples. Some degree of post-emplacement deformation has occurred in the fayalite granite as evidenced by common bent polysynthetic twins in plagioclase and the development of sub-grain boundaries in quartz.

Much of the biotite, and to a lesser extent amphibole, within the fayalite granite suite appears to be a breakdown reaction of fayalite. The biotite associated with the fayalite shows symplectite texture with quartz and feldspar (Fig 6a), demonstrating the breakdown reaction occurring during quartz and feldspar crystallization. In other portions of the sample, fayalite is commonly altered to iddingsite and other iron oxides. Myrmekite exsolution is also prevalent throughout the samples. Ilmenite is the dominant oxide within the suite, with subordinate magnetite showing typical oxyexsolution of ilmenite. Despite many fayalitic granites showing rapakivi textures in

other localities (Frost and Frost, 1997; Huang *et al.*, 2011), rapakivi was absent from the fayalite granite suite of the BFGC.

Charnockite

The charnockite suite is most abundant in the southwestern pluton, although minor occurrences of the suite also occur in the northern border of the southeast pluton (Fig 3). The field relationships for the former pluton are more apparent and are therefore described here. As the name implies, the suite encompasses orthopyroxene-biotite ± Fe-amphibole ± clinopyroxene syenogranite and monzogranite, with two samples plotting in the granodiorite field on the Q-AnOR diagram (Fig 4). The charnockite suite has a higher plagioclase to alkali feldspar ratio than the fayalite granite suite, but the uniform, coarse grained, inequigranular, textures are comparable in the two suites (Fig. 5a-d). Both dominant ilmenite and subordinate magnetite are present, however, magnetite is much more abundant than in the fayalite granite. Though ilmenite oxyexsolution is present in the magnetite of one charnockite sample (17SRB-D046), it is absent in similar charnockite samples.—Three samples (17SRB-D46A, 17SRB-D48A, 17SRB-L52A) contain discrete grains of both ortho- and clinopyroxene with the latter encompassing rounded mm-scale exsolution lamellae of orthopyroxene. Apatite is an abundant accessory mineral within the charnockite suite, as are very large euhedral and blocky zircons.

The gradational contact of the northern margin of the southwest pluton transitions into a strongly deformed metasedimentary and leucogranite country rock. Approximately 5 km south of the northern margin of the pluton, the pyroxenes become less abundant and the rocks become finer grained until eventually, pyroxene is present in only trace amounts or completely altered to epidote and chlorite. Like the fayalite granite suite, a weak fabric coincident with the SW regional foliation was noted in outcrop, and deformation textures within most thin sections are common.

Hornblende-Biotite Granite

The hornblende-biotite granite suite is the most voluminous magmatic suite in the BFGC, dominating much of the southeastern pluton and including one sample occurrence within the southwest pluton. The suite consists of amphibole-biotite syenogranite, monzogranite, and minor quartz syenite with accessory apatite, allanite, and abundant zircon. The hornblende-biotite granites proximal to the charnockite samples of the southeast pluton (17SRB-A015, 17SRB-

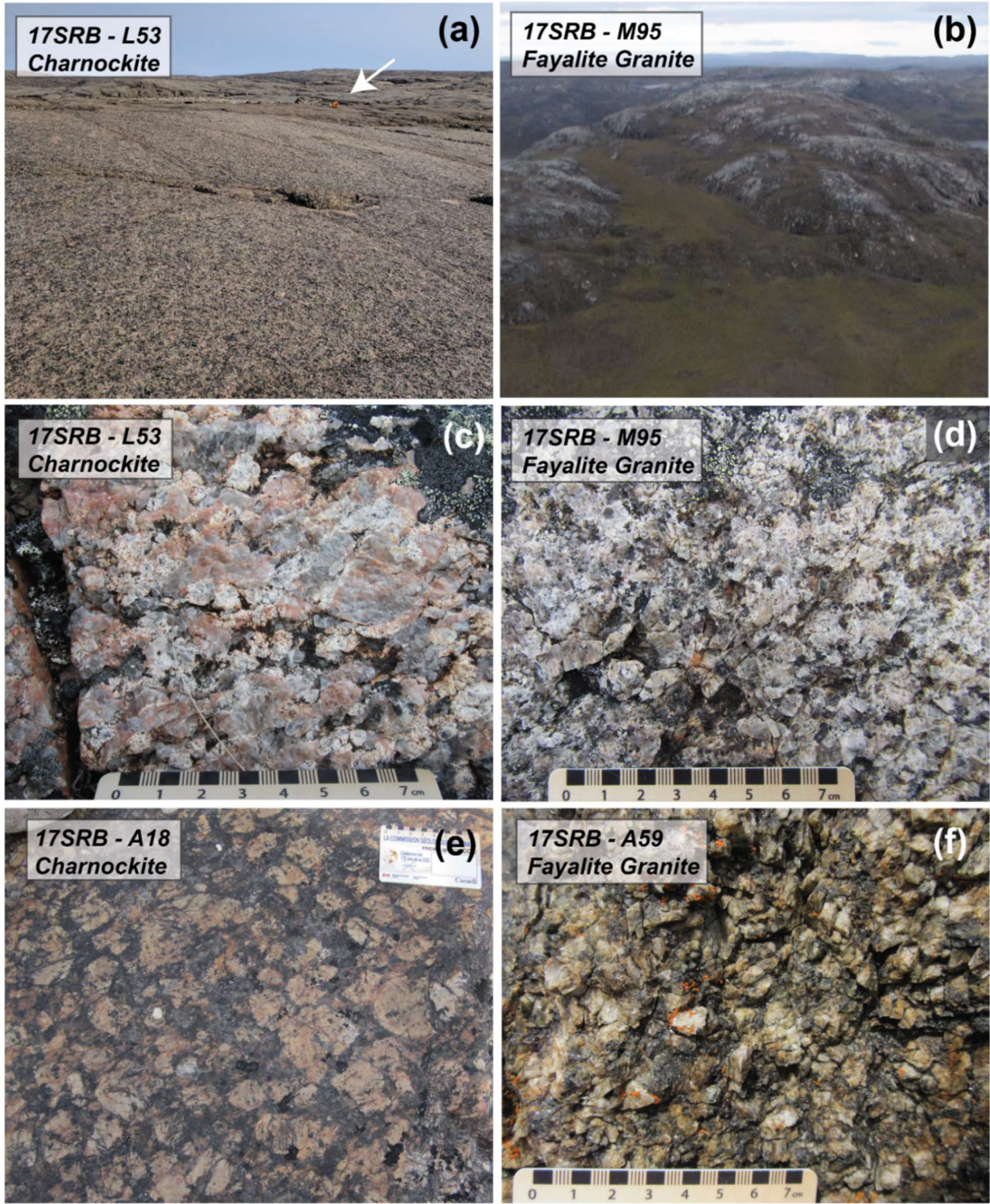


Figure 5: Caption on p. 14

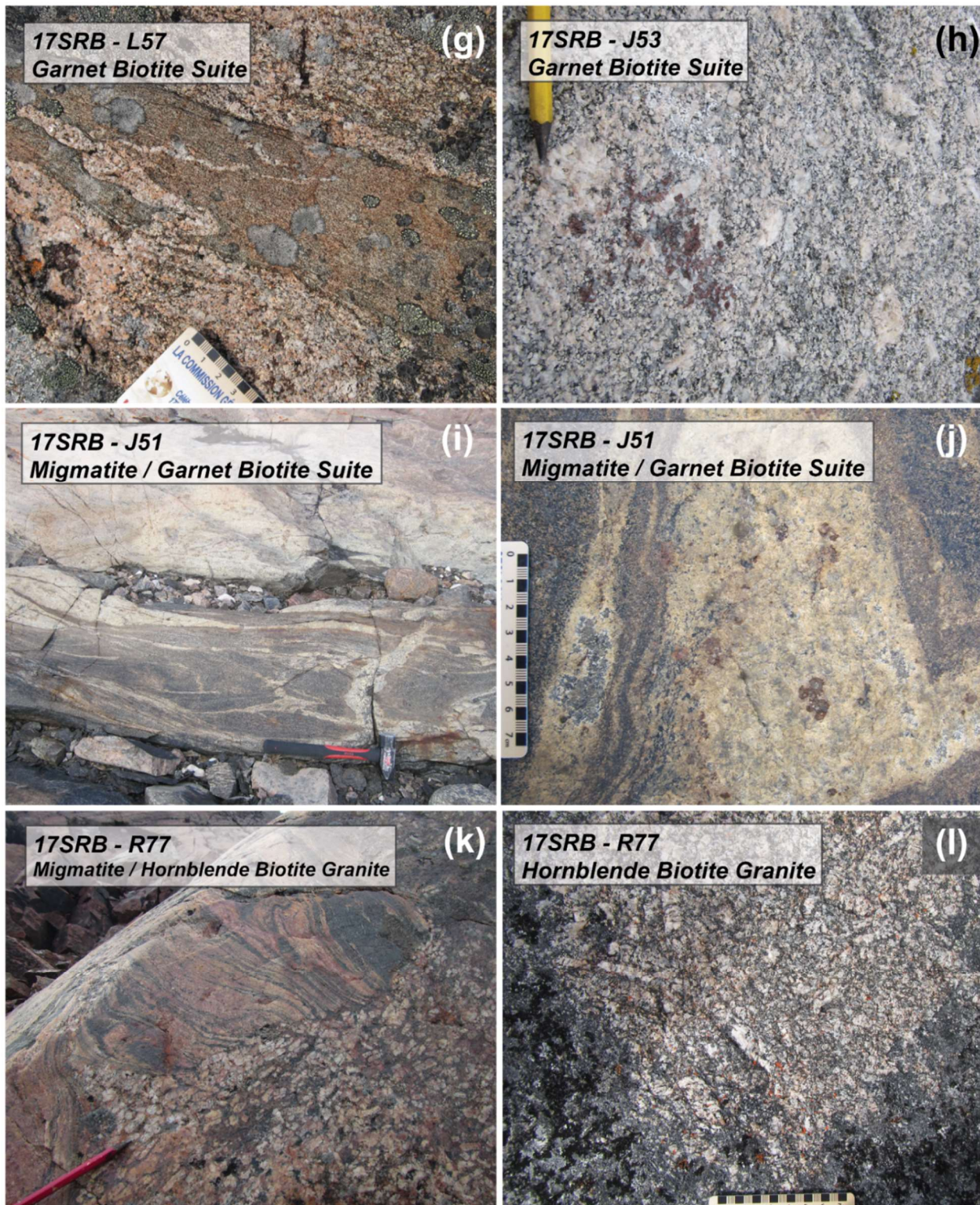


Figure 5: Caption on p. 14

Figure 5: Field photographs of the Boothia Ferroan Granitoid Complex. a) Homogenous outcrop of the charnockite suite in the southeast pluton. Arrow denotes geologist for scale. b) Helicopter photograph of a rounded outcrop of the fayalite granite. c) Coarse-grained charnockite, with orthopyroxene is less abundant. d) Less weathered fayalite granite. e) Charnockite with high abundance of orthopyroxene. f) Crumbled brown weathering of the fayalite granite. g) Garnet biotite monzogranite with hornblende biotite quartz diorite mafic xenolith. h) Garnet biotite quartz monzonite, with minor red garnet clusters. i) Biotite rich melanosome of the migmatite xenolith within the garnet biotite suite. j) Small garnet clusters within garnet biotite granodiorite, bordering migmatite melanosome. k) Large migmatite xenolith within the hornblende biotite granite, showing rare alkali feldspar megacrysts. Alkali-feldspar laths and phenocrysts within the hornblende biotite granite show trachytic texture around the margin of the xenolith. l) Weathered surface of hornblende biotite granite, showing simple twinned feldspar laths.

A016), consists of inequigranular and medium-grained granitoids similar in texture to the charnockite suite but devoid of orthopyroxene and with a considerably higher alkali feldspar content. The texture gradually shifts to a distinct porphyritic texture with alkali feldspar laths ranging from 5 to 30 mm in length at the interior of the pluton. The amphibole content is highly variable, from trace amounts to ~10 volume %. Alteration is moderate to extensive, with chloritization of biotite and amphibole, sericitization of plagioclase, and iron staining of alkali feldspars. The hornblende-biotite granite suite hosts secondary mineral growth unique to this suite within the the BFGC. Secondary fluorite, which lacks typical cubic crystal habit, is associated with acicular anatase (TiO_2 polymorph) and parisite (REE-fluorocarbonate). Anatase is spatially associated with fluorite, although their precise genetic relationship is unclear. Parisite is associated with Ti-rich phases, such as anatase and primary ilmenite. Backscatter electron images show that tparisite has a colloform growth texture interlayered with Ti-rich material (Fig 6).

Near the southern margin of the southeastern pluton, large migmatite xenoliths occur within the hornblende-biotite granite. The xenoliths range from to ~20 cm to spanning entire large (>50 m) outcrops. The migmatites are monzogranite dominated by heavily chloritized biotite, minor amphibole, and have rare alkali feldspar megacrysts (Fig 1k). In a few sample localities (17SRB-J050, 17SRB-J051, 17SRB-L057), migmatite xenoliths and schlieren occur in proximity to garnet-biotite suite rocks, which are described below.

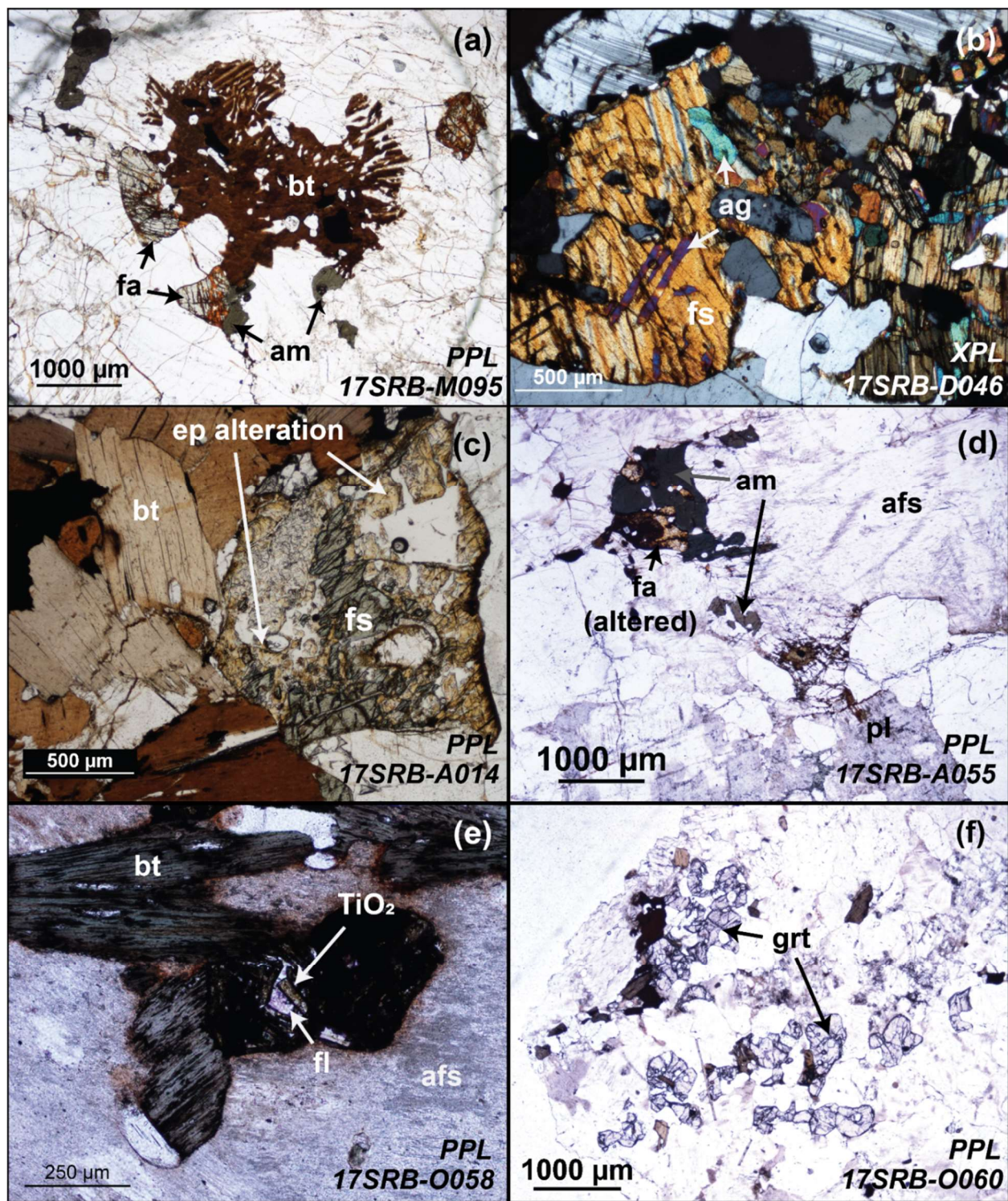


Figure 6: Caption on pg. 15

Figure 6: Photomicrographs of the Boothia Ferroan Granitoid Complex. a) Fayalite (fa) breakdown reaction to biotite (bt) and amphibole (am), along with biotite-feldspar symplectite of the fayalite biotite suite. Fayalite granite also shows iddingsite alteration along large fractures. b) Coarse exsolution of augite (aug) within ferrosilite (fs) within the charnockite suite. c) Extensive epidote group alteration of ferrosilite within the charnockite suite. d) Sericitization of plagioclase (pl) and perthite exsolution in alkali feldspar (afs) alongside Fe-rich amphibole and extensive altered fayalite within a sample near the margin of the fayalite granite suite. e) Heavily chloritized biotite and sericitized alkali feldspar occurring with acicular secondary TiO_2 phase occurring with purple fluorite (fl) within the hornblende biotite granite suite. f) Accessory mottled garnet, indicating partial breakdown of garnet (grt) within the garnet biotite suite.

Garnet-Biotite Suite

The garnet-biotite suite is distinct from the other suites of the BFGC as it has less quartz and a higher plagioclase to alkali feldspar ratio. The suite consists of fine grained biotite ± garnet granodiorite, quartz monzonite, and monzogranite, with abundant and large grains of accessory monazite. Alkali feldspar does not occur as distinct laths and amphibole is completely absent, distinguishing this suite from the hornblende-biotite granite. The garnet-biotite suite exclusively occurs on the southernmost parts of the southeast and southwest plutons, only in vicinity of the hornblende-biotite granite suite. While a direct contact was not observed due to bedrock cover, the transition between the two suites occurs within a ~100 m interval. In two sample locations, the garnet-biotite suite hosts elongate hornblende- and biotite-rich quartz diorite to gabbroic xenoliths. These rare xenoliths range from a few cm to 20 cm in size (Fig. 5g-j) and are the only mafic- to intermediate-composition rocks observed in the BFGC.

METHODOLOGY

Zircon and Monazite Sample Preparation

Zircon grains were analyzed for their isotopic (U-Pb and Lu-Hf) and trace-element compositions, both in-situ in polished ~30 μm -thick thin section and in grain separates mounted on a 1-inch epoxy disk. Monazite was also analysed in a few samples for its U-Pb isotope composition but only in thin section. To separate zircon, a mix of traditional and new separation techniques were used to achieve the same separation results. In the traditional separation, the samples were first crushed by a jaw crusher and then milled using a disk mill. Powdered samples were separated by light and heavy fractions with a Wilfley shaker table. The heavy fraction was further separated using Frantz isodynamic separation and methyl iodide (MI) heavy liquid

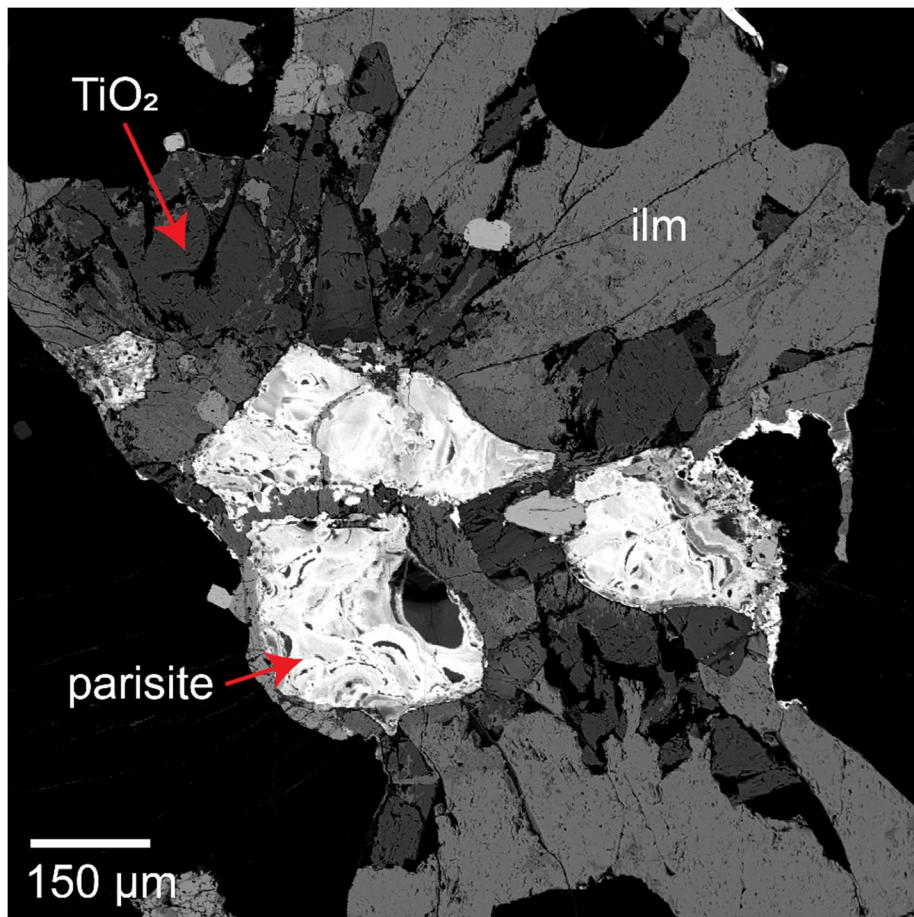


Figure 7: Back-scatter electron (BSE) image of trace minerals parisite-(Ce), secondary TiO_2 and primary ilmenite within the hornblende biotite granite suite (sample 17SRB-R075). Colloidal habit of the parisite indicates relatively low temperature growth.

separation. A modified separation technique, which uses a smaller sample volume, was also used (Söderlund and Johansson, 2002). In this technique, crushed samples were powdered to a heterogeneous grain size using a tungsten-carbide shatterbox and separated with a Wilfley shaker table similar to traditional separation. The heavy fraction was decanted into a petri-dish where the magnetic minerals were removed with a pen magnet. The separated zircons were individually selected for analysis using a binocular microscope. If possible, the selected grains exhibited the fewest fractures and visible lattice damage; however, a variety based on size and morphology of zircons were picked to avoid sampling bias. The selected zircons were then mounted on 1-inch epoxy rounds and polished using $1.0\ \mu\text{m}$ and $0.1\ \mu\text{m}$ alumina powder. All zircons and monazites, both in-situ and separated, were imaged with cathodoluminescence (CL) and high-contrast backscatter electron (BSE) techniques using the Zeiss EVO scanning electron microscope (SEM)

at the University of Alberta prior to analyses in order to identify zonation within the grains as well as prominent fractures and radiation damage.

U-Pb geochronology

Uranium-lead isotope ratios were acquired using both laser ablation inductively coupled plasma mass spectrometry (LA-ICPMS) and laser ablation split-stream inductively coupled plasma mass spectrometry (LASS-ICPMS). The latter technique is detailed in the Lu-Hf section below. LA-ICPMS analyses were conducted with the New Wave Research UP213 Nd-YAG Laser ablation system and Nu-Plasma I Multi-Collector ICPMS at the Canadian Centre for Isotopic Microanalysis. The analytical techniques used are outlined in Simonetti et al. (2006) and further details of operating conditions and instrumentation parameters for the laser ablation system and Nu-Plasma I Multi-Collector are detailed in Table 1 and Table 2 in Appendix 1, after the standard template recommended by Horstwood et al. (2016). The zircon LH94-15 (Ashton et al., 1999) was used as the primary standard for mass bias correction in U-Pb isotope analyses of zircon, and zircons GJ1 (Jackson et al., 2004), FC1 (Paces and Miller, 1993), and OG1 (Stern et al., 2009) as secondary standards. Monazite analysis used a monazite from Western Australia (WA, Simonetti et al., 2006; Heaman, unpublished data) as a primary standard, with Madagascar (MAD, Simonetti et al., 2006; Heaman, unpublished data) and 44069 (Aleinikoff et al. 2006) as secondary standards. All unknown and reference materials were analysed at the same instrument conditions. A detailed compilation of results for LA-ICPMS and LASS-ICPMS can be found in Appendix 2, with a compilation of primary and secondary standards in Appendix 3. Additional zircon U-Pb geochronology was conducted on the Sensitive High Resolution Ion Microprobe (SHRIMP) at the Geological Survey of Canada (Sanborn-Barrie et al., 2018; Regis, unpublished data) as part of the larger Boothia Peninsula-Somerset Island project.

Sm-Nd and Lu-Hf isotope determinations

Sample powders remaining after whole-rock major- and trace-element analysis were sent to researchers at the Isotope Geochemistry and Geochronology Research Centre (IGGRC) at Carleton University for whole-rock Sm-Nd isotopic analysis, using a ThermoFinnigan Triton TI thermal ionization mass spectrometer (TIMS). The full experimental procedures used are detailed in the appendix of Richard et al. (1976). Uncertainties in measured $^{147}\text{Sm}/^{144}\text{Nd}$ and

$^{143}\text{Nd}/^{144}\text{Nd}$ ratios were estimated to be 1% and ± 0.00001 , respectively. The latter uncertainty is the reproducibility of measured $^{143}\text{Nd}/^{144}\text{Nd}$ ratios in BCR-2 standard.

Lu-Hf and U-Pb isotope analyses of zircon were obtained concurrently using the LASS-ICPMS method, which involves splitting the ablated material from a static spot on a zircon grain into two separate mass spectrometers. The analyses were done at the Arctic Resources Laboratory at the University of Alberta following the procedures of Fisher et al. (2014). The Lu-Hf isotope measurements were made using a multiple faraday cup detector array on a Thermo Scientific Neptune Plus Multi Collector ICPMS; the U-Pb measurements were obtained using a single secondary electron multiplier (SEM) ion counter via peak hopping on a Thermo Scientific Element XR ICPMS. Further operation parameters on both instruments are detailed in Table 3 of Appendix 1.

Five natural and synthetic zircons (LH94-15: Ashton et al. (1999), GJ1: Jackson et al. (2004), Plesovice: Sláma et al. (2008), MUN-1 and MUN-3: Fisher et al. (2011)) served as standards for one or both of U-Pb and Lu-Hf isotope analyses. These standards were analysed after initial system start up and prior to the analysis of the samples. Additionally, each standard was analysed once after every 10 sample analyses. After acquisition, the Lu-Hf and U-Pb isotope data of the unknowns and standards were processed using the Iolite software (Paton et al., 2011). Individual integrations were trimmed where necessary to avoid irregular signal or complex zones of Lu-Hf or U-Pb isotopic ratios. Zircon LH94-15 was used as the primary reference material for mass bias correction of the U-Pb data while Plesovice was used as a primary standard for the Lu-Hf data. The measured $^{173}\text{Yb}/^{176}\text{Yb}$ ratio of Yb-doped synthetic zircons MUN-1 and MUN-3 was calibrated to best fit the results reported by Fisher *et al.*, 2011. This calibrated ratio was applied to ^{176}Hf for all samples to correct for the large ^{176}Yb isobaric interference found in zircon (Fisher *et al.*, 2014). Zircon GJ1 served as a secondary standard for both Lu-Hf and U-Pb ratios, while Plesovice served as an additional secondary standard for U-Pb data. Downhole fractionation corrections were applied separately for each session. However, even with an appropriately chosen primary reference material, there can still be under- or over-correction for downhole fractionation during ablation on sample zircons (Ver Hoeve *et al.*, 2018). Though the data acquired on the GJ1 secondary standard over all analytical sessions are concordant and the cumulative $^{207}\text{Pb}/^{206}\text{Pb}$ weighted average age within error of the accepted value (Appendix 1,

Figure 3 and 4), the results for GJ1 in individual sessions 1, 2, and 3 (Appendix 1, Figure 4) deviate from the accepted value. The recorded concordant ages in these sessions are slightly younger (ca. 10 Ma out of error) of the reported TIMS age of the GJ1 secondary standard. Appendix 2 indicates which samples were analysed in these sessions, and the results disclose sample ages that may be also report younger U-Pb ages.

Propagated present-day $^{176}\text{Lu}/^{177}\text{Hf}$ and $^{176}\text{Hf}/^{177}\text{Hf}$ errors were derived in Iolite (Paton *et al.*, 2011) after ^{176}Yb correction. The uncertainty of ϵ_{Nd} and ϵ_{Hf} were fully propagated from calculated initial $^{143}\text{Nd}/^{144}\text{Nd}$ and $^{176}\text{Hf}/^{177}\text{Hf}$ using the model 1 calculation from Ickert, 2013. Weighted averages and 2σ errors were calculated of initial $^{176}\text{Hf}/^{177}\text{Hf}$ and ϵ_{Hf} results from 5 to 51 zircons per sample. The whole rock Sm-Nd and weighted average Lu-Hf results of zircon are summarized in Table 7.

Major- and Trace-element Geochemistry

Major- and trace-element analyses of whole-rock samples were obtained at Activation Labs Ltd. (Actlabs) in Ancaster, Ontario. Samples were first trimmed of visible veins and alteration and then powdered using an agate mill. An additional four samples (17SRB-L52A, 17SRB-A59A, 17SRB-C47A, 17SRB-D46A) from the Boothia Ferroan Granitoid Complex were powdered at the rock crushing facility at the University of Alberta using a tungsten carbide shatterbox and also analysed at Actlabs. Major elements were determined by inductively coupled plasma optical emission spectrometry (ICP-OES) on powders that had undergone tetraborate fusion; trace elements were determined on solutions made from the fused powders using ICP-MS. The major- and trace-element analyses are reported in Table 1.

Mineral Chemistry and Geothermobarometry

Mineral compositions were determined in selected samples using the electron probe microanalyzer (EPMA) in the Electron Microprobe Laboratory at the University of Alberta. The mineral analyses were done on carbon-coated polished thin sections using natural and synthetic mineral standards to convert the measured X-ray counts in the unknown minerals to elemental concentrations. Two different EPMA instruments, the JEOL 8900R and the CAMECA SX100, were used for the analyses. *Probe for EPMA* software (Donovan *et al.*, 2007) was used for data processing. Analyses with excessive or deficient oxide weight percent totals (within ± 1.5 wt, %

of 100% for anhydrous silicates, between 94-99 % for hydrous silicates) resulting from either mixed phases or poor beam focus were screened from the data.

Mineral compositions of five representative samples from the Boothia ferroan granite complex were analysed to assess the magmatic conditions of these rocks as well as to confirm the identification of major and accessory minerals within the complex. Fayalite-titanomagnetite-quartz in the fayalite granite and ferrosilite-magnetite-quartz in the charnockite suite was used to calculate the oxygen fugacity and the amphibole-plagioclase equilibrium was used as to estimate the temperature of magma emplacement. Several geobarometers were implemented to determine the emplacement pressures of the BFGC plutons including the Al-in-hornblende barometer (Mutch *et al.*, 2016), fayalite-quartz-ferrosilite equilibrium, and the garnet-aluminosilicate-silica-plagioclase (GASP) barometer.

Zircon Minor- and Trace-Element Geochemistry

Zircon trace-element compositions were determined using the New Wave Research UP213 Nd-YAG Laser ablation system coupled with a Thermo Scientific iCAP-Q Quadrupole ICPMS at the Canadian Centre for Isotopic Microanalysis at the Department of Earth and Atmospheric Science of University of Alberta. Ninety eight zircons from 6 samples were analysed for their Si, P, Sc, Ti, Th, U, and rare-earth-element (REE) contents. NIST612 glass was used as the primary calibration standard, using Si as the internal standard element for converting counts per second to concentration of elements of interest. The Si concentration of the zircon is assumed to be the formula Si wt. % of zircon for these calculations. Well known trace-element concentrations of synthetic zircon 91500 (Wiedenbeck *et al.*, 1995, 2004; Fu *et al.*, 2008; see Appendix 5) was used as a secondary standard. The laser spot size was 40 μm and the fluence rate was 4 J/cm². The analyses consisted of a 15 seconds of baseline measurement and 45 second ablation time, resulting in a 20-35 second total peak integration time after baseline correction is applied using Iolite. Apart from the fluence, spot size, and ablation time, the sample introduction using the laser ablation system, such as gas flow and carrier gas, is similar to what is outlined for LA-ICPMS in Appendix 1. The titanium isotope ⁴⁹Ti was analysed and converted to a total Ti concentration for the purposes of Ti-in-zircon thermometry (Watson and Harrison, 2005). Within the sessions the samples were analysed, the converted total Ti concentration of the secondary standard conformed to accepted values (Fu *et al.*, 2008; Session 1 and 2, Appendix 5).

Spots with excess P (>1000 ppm) were discarded to avoid data affected by contamination from inclusions or defects in the zircon not apparent in BSE or CL imagery. A compilation of zircon trace-element and standard analyses can be found in Appendix 5.

RESULTS

Whole-Rock Geochemistry

Major- and trace-element geochemical data were acquired for 19 samples from the BFGC. Individual analyses are reported in Table 2. Major-element discrimination diagrams for granitoids from Frost et al. (2001) and LeMaitre (1989) were used to further classify the rocks of the BFGC (Fig. 8), with each diagram plotted against wt. % SiO₂. The distinguishing characteristic of the complex, as its ferroan name implies, is the high Fe/Mg of the rocks as represented by their high Fe* values, where $\text{Fe}^* = \text{FeO}_T / (\text{FeO}_T + \text{MgO})$ (wt. %). All samples from the complex are either within the ferroan granite field or just below the ferroan – magnesian field boundary (Fig. 8a). Notably, the fayalite suite reaches Fe* values as high as 0.97. The aluminium saturation index (ASI) values of the complex indicate that the rocks are mostly metaluminous to moderately peraluminous (Fig. 8c), except for two samples from pluton margins with pervasive sericitic alteration (unfilled symbols), which are strongly peraluminous (ASI > 1.1). Most of the BFGC suites include both metaluminous and peraluminous varieties except for the garnet-biotite suite, which is exclusively peraluminous. On the MALI (Na₂O + K₂O – CaO) diagram (Fig. 8b), the fayalite, hornblende-biotite and garnet-biotite suite rocks plot largely in the alkali-calcic field whereas the charnockite suite includes samples plot in all three of the calcic, calc-alkalic and alkali-calcic fields.

In terms of its trace-element compositions, the BFGC in general and the hornblende-biotite suite in particular is enriched in light rare earth elements (LREE) and other incompatible elements relative to primitive mantle (McDonough and Sun, 1995) (Fig. 9). Cerium exceeds 250 ppm for most samples, reaching up to 2200 ppm. The degree of rare earth-element fractionation is highly variable, with $(\text{La/Yb})_N$ ranging from 15.6 to 184.1. All suites show pronounced negative Nb, Ta, and Ti anomalies when normalized to primitive mantle compositions (average $\text{Nb/Nb}^* = 0.08 - 0.28$, $\text{Ta/Ta}^* = 0.06 - 0.31$, and $\text{Ti/Ti}^* = 0.09 - 0.16$) indicating that each suite had Ti-rich phase such as rutile in the melt residue or had been removed from the melt via fractional crystallization (Peters and Day, 2014). In trace-element discrimination diagrams (Fig. 10), the BFGC plots

Table 1: Major- and trace-element geochemical compositions for Boothia Ferroan Granite Complex

Suite	Hbl-Bt Granite						Grt-Bt Suite			Fayalite Granite				Charnockite					
	17SRB-A015A3	17SRB-C047A	17SRB-O056A	17SRB-R075A1	17SRB-R077B2	17SRB-R074B2	17SRB-J053A2	17SRB-O054A	17SRB-T024A	17SRB-A025A4	17SRB-A059A	17SRB-J029A3	17SRB-M095A2	17SRB-L053A	17SRB-L054A	17SRB-A014A	17SRB-A018A	17SRB-D046A	17SRB-L052A
wt%																			
SiO ₂	73.11	66.25	68.60	64.26	65.63	72.24	55.51	63.02	59.49	69.54	68.85	68.30	68.09	66.82	68.17	69.17	65.88	68.06	61.34
TiO ₃	0.24	1.26	0.65	0.98	1.12	0.38	2.18	1.83	2.03	0.43	0.45	0.58	0.56	0.58	0.53	0.82	1.38	0.64	1.81
Al ₂ O ₃	12.15	13.85	14.47	14.14	13.89	12.41	16.96	14.01	15.13	13.35	14.37	13.02	13.32	15.54	14.72	13.77	13.34	14.43	14.57
FeO _T	1.80	4.93	2.82	6.41	4.90	2.82	7.71	5.86	6.14	3.13	4.21	3.64	5.36	5.08	3.13	3.60	6.08	3.28	7.46
MnO	0.01	0.05	0.04	0.06	0.08	0.02	0.06	0.03	0.06	0.05	0.06	0.07	0.07	0.03	0.03	0.04	0.09	0.08	0.12
MgO	0.45	1.44	0.69	1.18	1.36	0.37	2.01	1.43	1.92	0.59	0.34	0.24	0.16	0.80	0.65	0.74	1.55	0.36	1.30
CaO	1.17	2.45	2.09	3.25	2.38	1.57	4.86	3.69	4.14	1.13	1.29	2.11	2.38	2.91	1.94	2.60	4.10	3.53	4.97
Na ₂ O	1.56	2.09	2.19	2.05	2.26	2.00	3.36	2.65	2.61	2.23	2.44	2.19	2.24	2.23	2.02	2.16	2.31	2.71	2.28
K ₂ O	7.38	5.20	6.71	5.55	5.72	6.36	3.54	4.41	4.47	6.17	6.81	5.97	5.77	6.11	6.90	5.46	3.51	4.53	4.13
P ₂ O ₅	0.02	0.44	0.19	0.27	0.30	0.06	1.00	0.88	0.85	0.13	0.18	0.20	0.20	0.28	0.19	0.24	0.44	0.17	0.94
LOI	0.79	1.44	0.80	0.89	1.06	0.90	1.40	0.79	1.19	0.95	1.04	0.31	0.18	0.78	0.71	0.82	0.20	0.44	0.55
Total	98.83	99.96	99.91	99.76	99.25	99.45	99.47	99.25	98.71	98.62	100.50	98.93	98.63	99.56	99.50	99.81	99.57	99.75	100.30
Na ₂ O + K ₂ O - CaO	7.77	4.84	6.81	4.35	5.60	6.79	2.04	3.37	2.94	7.27	7.96	6.05	5.63	5.43	6.98	5.02	1.72	3.71	1.44
FeO ^T / (FeO ^T + MgO ^T) ¹	0.80	0.77	0.80	0.84	0.78	0.88	0.79	0.80	0.76	0.84	0.93	0.94	0.97	0.86	0.83	0.83	0.80	0.90	0.85
A/CNK - P ¹	0.96	1.11	1.02	0.97	1.03	0.96	1.07	1.02	1.03	1.10	1.08	0.97	0.97	1.04	1.06	1.01	0.95	0.94	0.97
M value ²	1.48	1.59	1.55	1.74	1.62	1.51	2.01	1.86	1.90	1.38	1.51	1.61	1.62	1.57	1.49	1.55	1.78	1.74	2.13
ppm																			
Sc	3	17	10	24	24	7	15	8	11	10	15	15	14	10	13	10	16	22	29
V	7	59	37	41	58	12	101	82	95	7	5	7	6	23	19	44	89	11	90
Cr	60	BDL	120	110	110	130	80	80	90	100	BDL	90	70	100	110	70	120	BDL	BDL
Co	2	34	4	7	7	2	13	9	11	2	45	4	3	3	3	5	11	48	29
Zn	BDL	100	80	150	70	40	240	150	220	260	90	120	90	90	60	80	110	130	180
Ga	21	26	23	35	29	25	48	31	36	23	24	24	23	31	27	22	21	28	30
Ge	1.9	1.8	1.5	2.4	2.7	2.1	3.1	1.7	1.9	1.8	1.8	1.7	1.9	1.8	1.5	1.6	1.5	1.6	1.7
Rb	320	168	277	230	161	329	224	238	194	238	223	201	178	180	208	237	94	100	108
Sr	104	290	354	274	313	139	310	272	413	135	173	145	158	452	365	337	413	546	535
Y	43.7	60.5	27.3	97.1	99	55.2	68.9	48.7	34.2	31.8	25.7	36.4	31.2	32.3	33.4	32.9	39.3	37.1	60.4
Zr	352	748	422	1251	1191	492	1122	907	1275	250	291	393	377	527	559	483	585	777	851
Nb	7.3	29.7	16.7	39.3	39.4	17.2	55.7	66.2	46.5	28.4	14.7	22.7	16.2	16.8	17.5	18.8	25.4	18.5	35.1
Ba	451	1888	2520	1660	1743	711	1337	1645	2354	1563	1779	1424	1601	3045	2931	2156	1719	4305	2454
La	258	179	145	634	764	329	1100	339	374	60	50.6	80.4	66.6	208	117	129	130	120	220
Ce	468	390	292	1290	1460	617	2200	716	829	128	106	168	140	400	241	266	274	246	468
Pr	46.7	46.2	32.6	142	152	62.3	239	83.9	99.5	15	12.9	20	16.9	44	29.3	30.5	31.8	30.2	55.4
Nd	142	177	113	479	493	191	802	314	364	55.8	50.9	76	65.4	152	113	109	116	121	210
Sm	18.8	29.9	17.1	66.3	62	25.4	95.6	52	46.3	10.7	9.46	13.8	11.5	20.1	19.2	17.8	18.8	19.2	32.1
Eu	1.3	3.2	3.0	4.9	3.4	1.8	4.2	3.1	4.6	2.0	2.2	2.0	2.2	4.6	4.0	3.0	3.1	6.1	5.5
Gd	9.99	19.2	9.69	34.9	33.3	13.3	39.3	29.5	19.9	7.57	7.1	9.62	8.3	11	11.6	10.4	11.8	12.8	20
Tb	1.12	2.58	1.21	4.36	4.04	1.66	3.94	3.63	1.93	1.16	1	1.35	1.16	1.32	1.47	1.39	1.52	1.59	2.43
Dy	5.43	12.9	6.04	21.5	20.9	8.26	17	15.5	8.43	6.31	5.02	7.47	6.42	6.94	7.67	7.12	7.92	8.26	12.5
Ho	0.94	2.24	1.01	3.62	3.69	1.49	2.61	1.96	1.27	1.15	0.95	1.34	1.21	1.16	1.29	1.26	1.43	1.45	2.18
Er	2.4	6.1	2.62	9.76	10.2	3.95	6.35	3.88	2.97	3.21	2.55	3.7	3.39	3.25	3.36	3.34	4.03	3.94	5.91
Tm	0.3	0.8	0.3	1.3	1.4	0.5	0.7	0.5	0.3	0.4	0.3	0.5	0.5	0.4	0.4	0.4	0.6	0.5	0.7
Yb	1.6	4.5	1.8	7.2	8.1	2.7	4.1	2.7	1.8	2.6	2.2	3.3	2.8	2.5	2.4	2.6	3.5	3.0	4.6
Lu	0.2	0.6	0.3	1.1	1.2	0.4	0.6	0.4	0.2	0.4	0.3	0.5	0.4	0.4	0.4	0.4	0.5	0.5	0.7
Hf	9.5	18.3	10.6	27.6	27.3	14.5	30.2	20.8	28.2	5.5	6.7	9.1	8.2	12.2	12.8	11.7	12.9	16.3	18.3
Ta	0.2	1.9	0.9	1.2	2.2	0.5	2.4	1.8	2.0	1.3	1.1	1.4	1.2	0.7	0.5	1.1	1.5	0.8	1.6
Tl	1.8	0.8	1.5	1.2	0.8	1.7	1.2	1.0	0.9	1.5	1.0	1.1	0.8	0.8	1.0	1.2	0.6	0.4	0.6
Pb	66	26	53	39	26	63	42	40	33	49	31	43	31	40	38	33	27	23	26
Th	200	11.1	15.3	106	116	159	518	102	41.3	13.9	5.07	14.2	8.44	32.2	8.21	10.8	9.16	3.84	15.3
U	13.9	0.83	1.48	2.98	3.64	5.35	12.2	2.97	1.5	1.96	1.05	2.85	1.62	0.7	0.61	1.56	1.03	0.42	1.34
(Th/Nb) ³	226.76	3.09	7.58	22.32	24.37	76.51	76.97	12.75	31.67	4.05	2.85	5.18	4.31	15.86	3.88	4.75	2.98	1.72	3.61
(La/Yb) ³	108.38	26.95	53.63	59.60	64.51	82.02	184.39	85.13	138.33	15.71	15.58	16.58	16.42	56.62	33.46	34.16	25.64	27.13	32.62
(La/Sm) ⁴	8.6	3.7	5.3	6.0	7.7	8.1	7.2	4.1	5.0	3.5	3.3	3.6	3.6	6.5	3.8	4.5	4.3	3.9	4.3
(Gd/Yb) ⁴	5.0	3.4	4.3	3.9	3.3	3.9	7.8	8.8	8.8	2.4	2.6	2.4	2.4	3.6	3.9	3.3	2.8	3.4	3.5
Eu/Eu ⁵	0.28	0.41	0.71	0.31	0.23	0.30	0.21	0.24	0.46	0.67	0.81	0.53	0.68	0.95	0.81	0.67	0.64	1.19	0.66

¹Calculated on a molar basis; ²Cation ratio (Na + K + 2*Ca) / (Al*Si); ³Normalized to primitive mantle values from McDonough and Sun (1995); ⁴Normalized to chondritic values from McDonough and Sun (1995); ⁵Eu/Eu* = EuN / V(LaN * GdN)

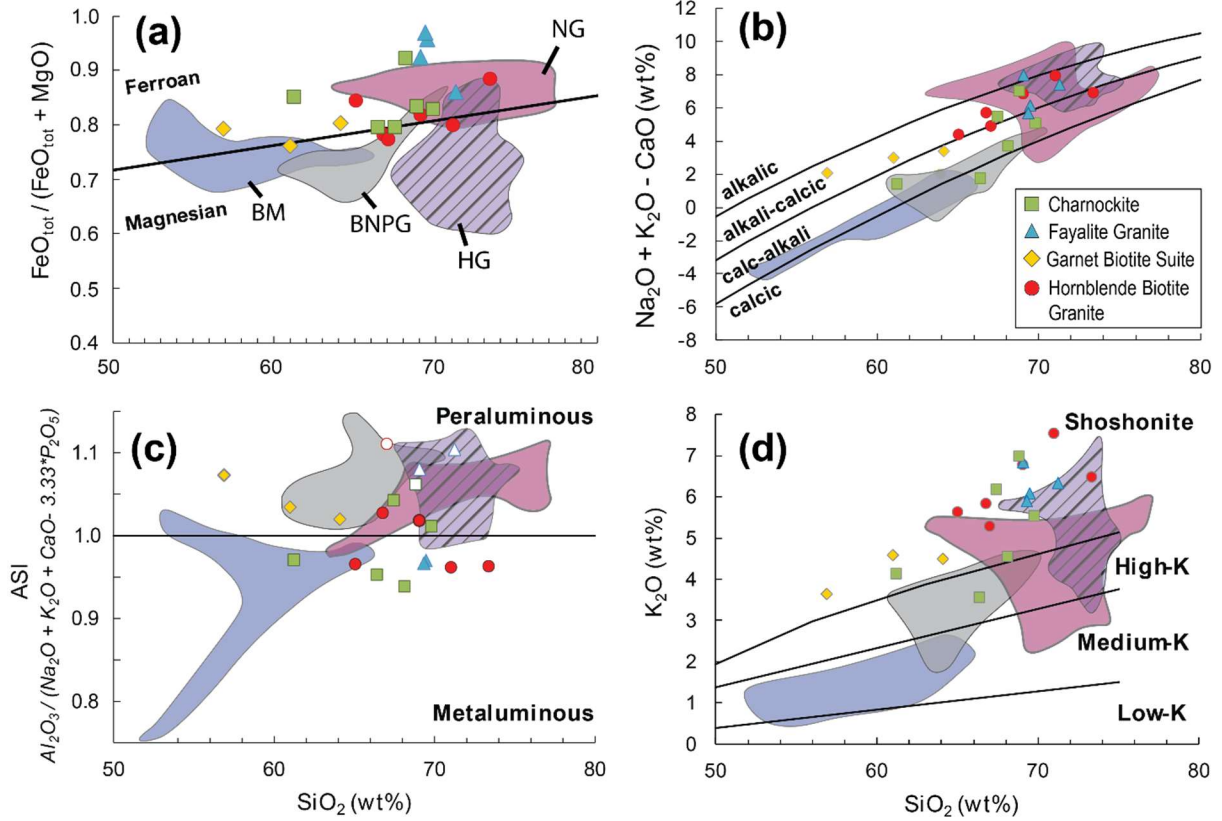


Figure 8: Granitoid major element discrimination diagrams of the Boothia ferroan granitoid complex. Diagrams 3a-c based on Frost et al. (2001) and diagram 3d from LeMaitre (1989). The shaded regions represent analyses from the Nueltin granites (NG, Peterson et al., 2002; Peterson et al., 2015) and the Hudson Granites (HG, Peterson et al., 2002) for comparison (see Appendix 7 for discussion), and Boothia Neoarchean porphyroclastic granitoids and Boothia mafics (BNPG and BM, this study) as a potential source rock. a) Fe-number ($\text{Fe}^* = \text{FeO}_{\text{tot}} / (\text{FeO}_{\text{tot}} + \text{MgO})$ in wt. %) vs wt.% SiO₂. Fe* is calculated on a wt. % from total Fe converted to FeO. b) Modified Alkali-Lime Index (MALI = Na₂O + K₂O - CaO in wt. %) vs. wt. % SiO₂ diagram discriminating alkali, alkali-calcic, calc-alkali and calcic fields. c) Aluminium Saturation Index (ASI) calculated on a molar basis, corrected for the CaO in apatite. Symbols that are unfilled are from sericitized samples, which may affect ASI values. d) K₂O vs SiO₂ in wt. % showing high-K, medium-K, low-K fields are from LeMaitre (1989), shoshonite field from Rickwood (1989).

along the borders of the within-plate granites (WPG), volcanic-arc granites (VAG), and syn-collisional granites (syn-COLG), which is consistent with observed post-collisional granites (Pearce, 1996).

Fayalite Granite

The fayalite granite suite has the highest Fe* and the highest average silica content in the BFGC (68.1 – 69.5 wt. %, average 68.7 wt. %, SiO₂); the compositions for the fayalite granite suite are

also the most uniform between samples ($n = 4$). It also has high alkali contents , plotting in alkali to alkali-calcic fields on the MALI diagram. Despite its higher concentration of K_2O and Na_2O , on average the fayalite granite suite has the lowest abundance of incompatible trace elements and REE within the BFGC; this contrasting relationship between major- and trace-element compositions is also explored with the garnet-biotite suite. Fractionation between LREE and HREE is moderate (average $(La/Yb)_N = 16.0$), which is the lowest in the BFGC. The fayalite granites have relatively small negative Eu anomalies ($Eu/Eu^* = 0.66$) and flat HREE slopes ($(Gd/Yb)_N = 2.4$). This suite also has a relatively low Th content, resulting in a flatter $(Th/U)_{PM}$ slope (= 1.4) when compared to the other suites of BFGC.

Charnockite

The charnockite suite is the most variable in its major-element composition, with SiO_2 varying between 61– 69 wt. % and Fe^* values ranging from 0.92 – 0.80. Samples with greater proportion of clinopyroxene are higher in CaO , which leads to a more metaluminous composition and individual analyses that plot in the calc-alkaline or calcic rather than alkali-calcic fields on the MALI diagram (Fig. 3b). In clinopyroxene-absent samples, particularly those in which orthopyroxene is significantly altered, the charnockites are moderately peraluminous ($ASI = 1.10 – 1.05$). The charnockite suite shares some of the trace-element characteristics seen in the fayalite granite suite, such as a relatively flat HREE pattern, although the charnockite suite is more LREE enriched (average $(La/Yb)_N = 34.9$) (Fig. 9). The Eu anomaly varies between samples from slightly positive and slightly negative, but on average is very slightly negative ($Eu/Eu^*= 0.81$), which indicates limited plagioclase involvement in magma generation and fractionation.

Hornblende-Biotite Granite

Like the charnockite suite, there is significant variability in silica (64 – 73 wt. %), ASI and Fe^* in the hornblende-biotite granite suite. The hornblende-biotite suite has the most samples in the BFGC straddling the boundary between ferroan and magnesian granitoids ($Fe^* = 0.77 – 0.88$). Most samples are metaluminous, however, samples with only minor amounts of hornblende have a weakly peraluminous composition. The hornblende-biotite granite suite has the highest alkali content, notably with K_2O contents up to 7.5 wt. %. The fractionation in the HREE remains similar ($(Gd/Yb)_N = 3.9$) between the charnockite suite, fayalite granite suite, and hornblende-

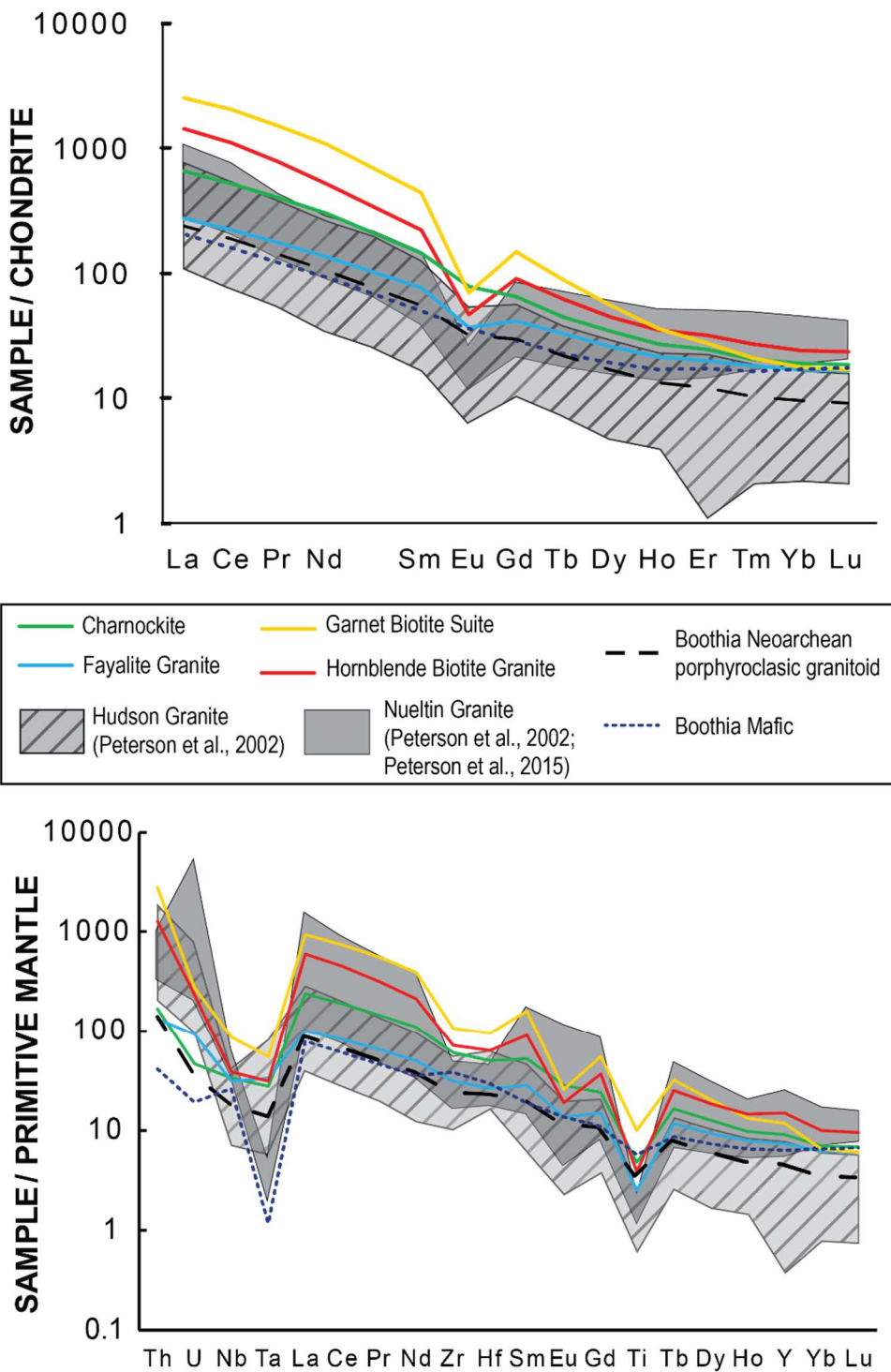


Figure 9: Chondrite normalized rare-earth element and primitive mantle normalized incompatible element plots of the averaged values of each suite of the Boothia ferroan granitoid complex. Normalization values are from McDonough and Sun (1995). A range for the Hudson Granite and Nueltin granite is shown for comparison, as well as an average value for the Boothia Neoarchean porphyroclastic granitoids and 2.48 Ga Boothia mafic-

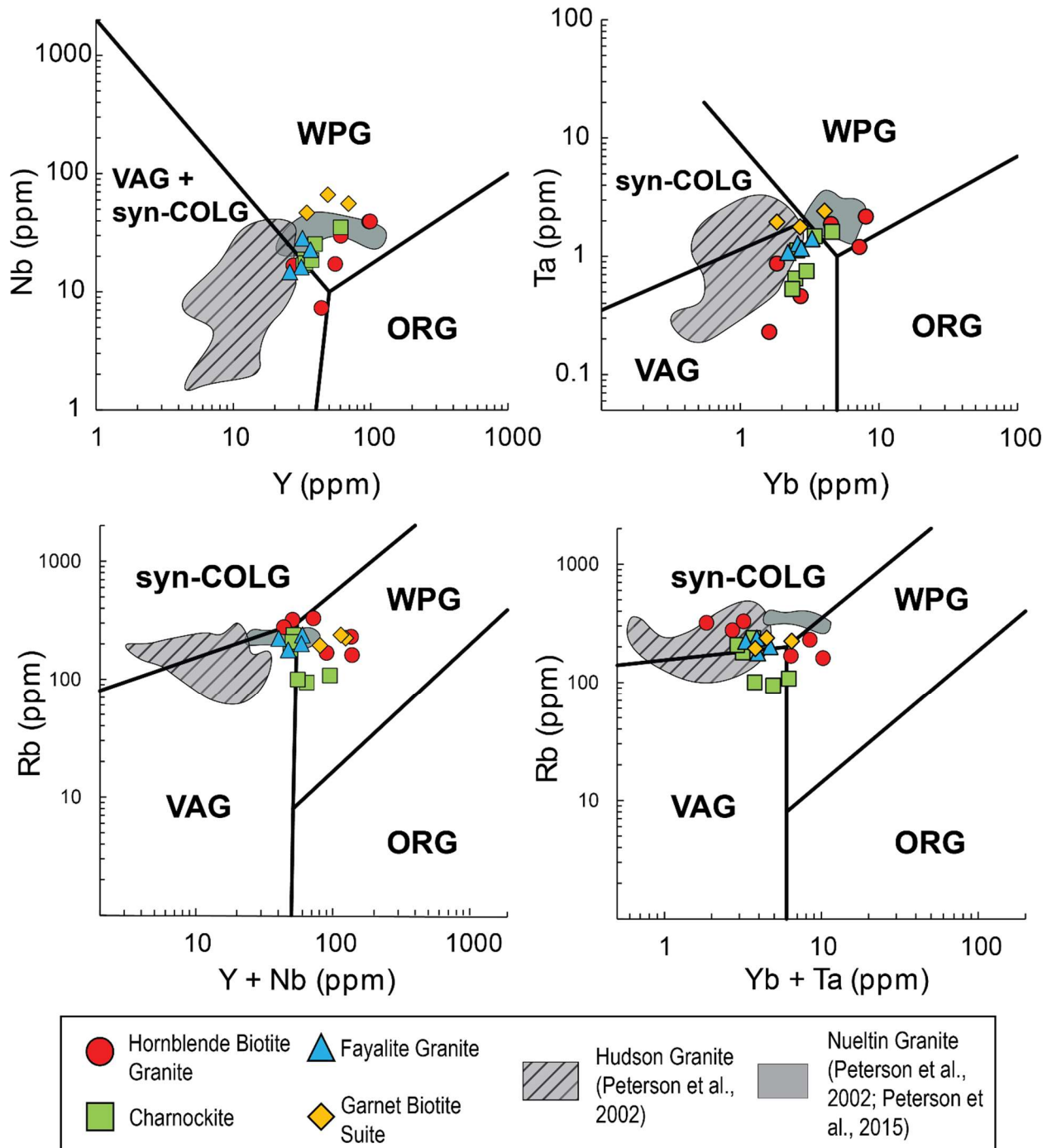


Figure 10: Trace element discrimination diagrams of the Boothia ferroan granite complex after Pearce *et al.* (1984). Shaded regions represent Hudson granite (Peterson et al., 2002) and Nueltin granites as a part of the Kivalliq suite (see Appendix 7 for comparison discussion). VAG = Volcanic Arc Granite, syn-COLG = syn-collisional granite, WPG = within plate granite, ORG = oceanic ridge granite.

biotite suite. The LREEs, however, are much more enriched in the hornblende-biotite suite with average $(\text{La/Yb})_N = 64.9$, quadruple that of the fayalite suite. The negative Eu anomaly is also substantially larger in the hornblende-biotite suite ($\text{Eu/Eu}^* = 0.33$), indicating higher degrees of plagioclase fractionation. Though all suites show negative Nb, Ta, and Ti anomalies, the hornblende-biotite granite suite shows the strongest anomalies among the BFGC.

Garnet-Biotite Suite

The garnet-biotite suite exhibits some unique geochemical traits compared to the other three suites in the BFGC. As previously mentioned, the garnet-biotite suite is exclusively peraluminous, and the ASI increases with decreasing SiO_2 contents (55.5 – 63.0 wt. %). Fe^* values are similar to the hornblende-biotite granite suite, bordering between ferroan and magnesian fields. Despite having the lowest SiO_2 , which typically is characteristic of less evolved granitoids, the garnet-biotite suite has the highest incompatible elements and LREE concentrations. The extreme enrichment of the LREE (average $(\text{La/Yb})_N = 135.7$) and strong negative Eu anomaly ($\text{Eu/Eu}^* = 0.28$) suggests that the garnet-biotite suite is highly evolved. The fractionation between HREE is more pronounced, with an average $(\text{Gd/Yb})_N$ value of 8.46, more than double that of the other suites. Incompatible element trends are similar to that of the hornblende-biotite granite suite, though the garnet-biotite suite has a higher abundance of incompatible elements overall.

Mineral Chemistry

Tables 2 - 4 show the average major- and minor-element compositions of anhydrous silicates, hydrous ferromagnesian silicates, and oxides, respectively, from 5 representative samples (17SRB-R075A, 17SRB-J053A1, 17SRB-L052A, 17SRB-M095, 17SRB-D046) of each of the suites. Averages are compiled from analyses of 3 grains per mineral, each with five analyses per grain.

All anhydrous ferromagnesian minerals have high X_{Fe} (molar $\text{Fe}/(\text{Fe} + \text{Mg})$), with the fayalite and garnet notably near end-member composition ($X_{\text{Fe}} = 0.970$ and 0.921 respectively) whereas pyroxenes in the charnockite suite have somewhat lower X_{Fe} (0.863 to 0.760). The CaO content of the garnet in 17SRB-J053A1 is relatively low, averaging 3.0 wt. %, which suggests the garnet crystallized from relatively Ca-poor melts. Orthopyroxene in 17SRB-D046 occurs with rounded mm-scale exsolution lamellae of augite. The composition of the pre-exsolved primary pyroxene

(pigeonite) in this sample was reconstructed using BSE image analysis to calculate the relative proportions of host orthopyroxene and augite lamellae. The hydrous silicates have lower X_{Fe} than the co-existing anhydrous silicates, likely due to equilibrium partitioning of Fe and Mg between these minerals. High TiO_2 characterizes both biotite (4.6 – 5.6 wt. %) and amphibole (1.5 – 2.1 wt. %) in these samples. The hydrous minerals are also high in F (biotite: 2.0 – 3.5 wt. %;

Table 2: Representative anhydrous ferromagnesian silicate analyses from Boothia Ferroan Granitoid Complex

	Fayalite 17SRB-M95	Garnet 17SRB-J53-A1	Ferrosilite 17SRB-L52	Ferrosilite 17SRB-D46	Augite 17SRB-D46	Pigeonite* 17SRB-D46
	Fayalite Granite	Bt-Grt Granodiorite	Charnockite	Charnockite	Charnockite	Charnockite
SiO_2	29.42	36.95	47.18	46.26	48.37	46.71
TiO_2	0.00	0.03	0.09	0.10	0.15	0.11
Al_2O_3	0.00	20.65	0.63	0.34	0.94	0.47
ZnO	0.13	0.00	0.15	0.18	0.07	0.16
FeO	67.76	36.28	41.60	46.26	25.47	41.80
MnO	1.29	1.75	1.28	1.40	0.68	1.25
MgO	1.16	1.74	7.38	4.12	3.73	4.03
CaO	0.02	3.04	0.87	0.86	19.73	4.91
Na_2O	0.00	0.00	0.00	0.00	0.22	0.05
Total	99.77	100.43	99.19	99.52	99.33	99.48
<i>Cation proportions calculated on the basis of 4 oxygen for olivine, 6 oxygen for pyroxene, and 12 oxygen for garnet</i>						
Si	0.993	2.993	1.972	1.978	1.968	1.976
Ti	0.000	0.002	0.003	0.003	0.005	0.004
Al	0.000	1.972	0.031	0.017	0.045	0.012
Zn	0.003	0.000	0.005	0.006	0.002	0.005
Fe	1.913	2.458	1.454	1.654	0.867	1.479
Mn	0.037	0.120	0.045	0.051	0.023	0.045
Mg	0.058	0.211	0.460	0.262	0.226	0.254
Ca	0.001	0.264	0.039	0.039	0.860	0.223
Na	0.000	0.000	0.000	0.000	0.017	0.002
X_{Fe}	0.970	0.921	0.760	0.863	0.793	0.853

*Reconstructed using image analysis

Table 3 : Representative hydrous silicate analyses from Boothia Ferroan Granitoid Complex

	Biotite 17SRB-J53-A1	Biotite 17SRB-L52	Biotite 17SRB-M95	Biotite 17SRB-R75-A	Pargasite 17SRB-L52	Pargasite 17SRB-D46	Hastingsite 17SRB-M95	Hastingsite 17SRB-R75-A
	Garnet Biotite Suite	Charnockite	Fayalite Granite	Hbl-Bt Granite	Charnockite	Charnockite	Fayalite Granite	Hbl-Bt Granite
SiO ₂	36.00	36.00	33.89	35.37	39.95	39.19	38.43	38.13
TiO ₂	4.98	4.81	4.55	5.07	1.81	2.14	1.64	1.48
Al ₂ O ₃	13.47	13.15	13.88	13.08	11.27	10.91	11.65	11.84
ZnO	0.09	0.09	0.09	0.09	0.07	0.08	0.08	0.08
FeO	23.00	23.79	31.73	26.84	24.37	27.58	29.86	27.88
MnO	0.06	0.12	0.09	0.20	0.31	0.35	0.26	0.47
MgO	9.45	8.89	3.01	6.02	5.73	3.55	2.04	3.17
CaO	0.01	0.01	0.01	0.00	10.91	10.76	10.54	10.43
Na ₂ O	0.10	0.07	0.03	0.08	1.54	1.66	1.60	1.57
K ₂ O	9.42	9.37	9.10	9.38	2.06	2.00	1.77	2.27
F	2.53	2.00	0.48	3.47	1.26	1.32	0.56	1.91
Cl	0.27	0.20	0.09	0.30	0.26	0.18	0.14	0.47
O = F, Cl	-1.12	-0.89	-0.23	-1.54	-0.59	-0.60	-0.27	-0.91
Total	98.22	97.60	96.74	98.38	98.95	99.12	98.28	98.78

Cation proportions calculated on the basis 11 oxygens for biotite and 23 oxygens for amphibole							
Si	2.772	2.792	2.738	2.795	6.281	6.258	6.217
Ti	0.288	0.280	0.276	0.301	0.214	0.257	0.199
Al	1.223	1.202	1.322	1.218	2.090	2.053	2.220
Zn	0.005	0.005	0.005	0.005	0.008	0.010	0.009
Fe	1.481	1.543	2.143	1.774	3.204	3.684	4.040
Mn	0.004	0.008	0.006	0.013	0.042	0.048	0.035
Mg	1.085	1.027	0.362	0.709	1.342	0.846	0.492
Ca	0.000	0.001	0.001	0.000	1.838	1.842	1.827
Na	0.014	0.010	0.004	0.012	0.470	0.515	0.503
K	0.925	0.927	0.938	0.946	0.414	0.407	0.364
F	0.616	0.491	0.124	0.868	0.627	0.666	0.285
Cl	0.035	0.026	0.013	0.040	0.070	0.048	0.037
X _{Fe}	0.577	0.600	0.855	0.714	0.705	0.813	0.891

amphibole: 1.3 – 1.9 wt. %), except in fayalite granite sample 17SRB-M095, where both biotite and amphibole have markedly lower F contents (~ 0.5 wt. %). Experimental studies have shown that Ti and F greatly increase the thermal stability of biotite (Peterson et al., 1991; Dooley and Patino-Douce, 1996) and may do the same for amphibole. Ilmenite and magnetite are the dominant Fe-Ti oxides in the BFGC samples, with the exception of sample 17SRB-J053A1 (garnet-biotite suite), which has rare occurrences of ilmenite and completely lacks primary

Table 4 : Representative oxide analyses from Boothia Ferroan Granitoid Complex

	Ilmenite	Ilmenite	Ilmenite	Ilmenite	Magnetite	Magnetite	Magnetite	Magnetite	TiO ₂ *
	17SRB-D46	17SRB-L52	17SRB-M95	17SRB-R75-A	17SRB-D46	17SRB-L52	17SRB-M95	17SRB-R75-A	17SRB-J53-A1
	Charnockite	Charnockite	Fayalite Granite	Hbl-Bt Granite	Charnockite	Charnockite	Fayalite Granite	Hbl-Bt Granite	Garnet Biotite Suite
SiO ₂	0.01	0.00	0.00	0.00	0.09	0.07	0.10	0.11	0.10
TiO ₂	49.61	50.09	49.60	50.23	0.11	0.72	0.56	0.40	97.23
Al ₂ O ₃	0.02	0.05	0.03	0.02	0.23	0.53	0.36	0.22	0.04
V ₂ O ₃	0.00	0.00	0.00	0.00	0.17	0.65	0.09	0.28	0.10
Cr ₂ O ₃	0.00	0.00	0.00	0.00	0.04	0.02	0.00	0.02	0.04
ZnO	0.00	0.00	0.00	0.01	0.00	0.03	0.04	0.02	0.00
FeO	47.76	47.37	48.18	47.34	92.58	91.11	91.87	92.34	0.37
MnO	0.86	1.11	0.76	1.01	0.00	0.02	0.00	0.00	0.00
MgO	0.04	0.03	0.01	0.00	0.00	0.00	0.00	0.00	0.00
Total	98.32	98.64	98.58	98.60	93.22	93.15	93.02	93.40	97.87
<i>Cation proportions normalized to a total of 2, 3, and 1 cations for ilmenite, magnetite, and TiO₂ respectively</i>									
Si	0.000	0.000	0.000	0.000	0.003	0.003	0.004	0.004	0.001
Ti	0.956	0.962	0.953	0.966	0.003	0.021	0.016	0.012	0.992
Al	0.001	0.001	0.001	0.001	0.010	0.024	0.017	0.010	0.001
V	0.000	0.000	0.000	0.000	0.005	0.020	0.003	0.009	0.001
Cr	0.000	0.000	0.000	0.000	0.001	0.001	0.000	0.001	0.000
Zn	0.000	0.000	0.000	0.000	0.000	0.001	0.001	0.001	0.000
Fe ³⁺	0.087	0.075	0.093	0.068	1.970	1.908	1.941	1.949	0.000
Fe ²⁺	0.936	0.937	0.936	0.944	1.007	1.022	1.019	1.015	0.004
Mn	0.019	0.024	0.016	0.022	0.000	0.001	0.000	0.000	0.000
Mg	0.002	0.001	0.000	0.000	0.000	0.000	0.000	0.000	0.000

magnetite. Rather, the oxides in 17SRB-J053A1 are secondary rutile and TiO₂ polymorphs such as anatase. Some magnetite grains in 17SRB-M095 and 17SRB-D046 contain coarse ilmenite oxyexsolution lamellae. Using the average ilmenite and magnetite compositions and the relative proportion of ilmenite lamellae within magnetite determined from BSE images, the compositions of the primary pre-exsolved titanomagnetite was calculated to be **Mt₃₇Usp₆₃** in 17SRB-M95 (fayalite granite) and **Mt₄₂Usp₅₈** in 17SRB-D046 (cpx-bearing charnockite).

U-Pb Geochronology

BFGC zircons show remarkable U-Pb age homogeneity, with consistent ²⁰⁷Pb/²⁰⁶Pb ages between ~1800 and 1850 Ma on individual spots. Minimal zircon inheritance was noted among nearly >300 individual spots analysed. The errors in weighted average and concordia ages,

unless otherwise stated, are reported at the 2σ or 95% confidence level. A summary of results for each sample can be found in Table 5. The full U-Pb dataset is reported in Appendix 2.

Fayalite Granite

Four samples (17SRB-A025A4, 17SRB-J029A3, 17SRB-M095A, and 17SRB-A055A3) were selected for U-Pb zircon isotopic analysis from the fayalite granite suite. The zircons are blocky,

Table 5: Summary of U-Pb geochronology of the Boothia Ferroan Granitoid Complex

Sample Name	Method	Age (Ma) $\pm 2\sigma$	Age Calculation	n	MSWD
<i>Charnockite</i>					
17SRB-A018A	LA-ICPMS	1834.5 \pm 4.4	$^{207}\text{Pb}/^{206}\text{Pb}$ Weighted Average	18	1.30
17SRB-D046A	LASS-ICPMS	1831.6 \pm 4.3	$^{207}\text{Pb}/^{206}\text{Pb}$ Weighted Average	18	1.20
17SRB-D048A	LASS-ICPMS	1826.2 \pm 6.4	$^{207}\text{Pb}/^{206}\text{Pb}$ Weighted Average	20	0.99
17SRB-L053A	LASS-ICPMS	1826.9 \pm 4.8	$^{207}\text{Pb}/^{206}\text{Pb}$ Weighted Average	15	0.47
17SRB-L054A	LA-ICPMS	1823.1 \pm 4.7	$^{207}\text{Pb}/^{206}\text{Pb}$ Weighted Average	25	1.02
<i>Hbl-Bt Granite</i>					
17SRB-A015A3	LASS-ICPMS	1825.9 \pm 3.3	$^{207}\text{Pb}/^{206}\text{Pb}$ Weighted Average	51	0.47
17SRB-R077B2	SHRIMP	1826.4 \pm 2.3	$^{207}\text{Pb}/^{206}\text{Pb}$ Weighted Average	32	1.19
17SRB-C047A	LASS-ICPMS	1829.9 \pm 6.6	$^{207}\text{Pb}/^{206}\text{Pb}$ Weighted Average	13	0.87
17SRB-R75A1	LASS-ICPMS	1827.7 \pm 3.6	$^{207}\text{Pb}/^{206}\text{Pb}$ Weighted Average	19	2.10
<i>Fayalite Granite</i>					
17SRB-A025A4*	LASS-ICPMS	1827.7 \pm 2.6	$^{207}\text{Pb}/^{206}\text{Pb}$ Weighted Average	35	1.10
17SRB-J029A3	SHRIMP	1841.1 \pm 4.5	$^{207}\text{Pb}/^{206}\text{Pb}$ Weighted Average	25	1.40
17SRB-M095A	LA-ICPMS	1841.0 \pm 4.5	$^{207}\text{Pb}/^{206}\text{Pb}$ Weighted Average	18	0.34
17SRB-A055A3	LA-ICPMS	1835.6 \pm 5.8	$^{207}\text{Pb}/^{206}\text{Pb}$ Weighted Average	11	0.45
<i>Grt-Bt Suite</i>					
17SRB-O054A	LASS-ICPMS	1836 \pm 26	$^{207}\text{Pb}/^{206}\text{Pb}$ Weighted Average	8	7.10
17SRB-J053A (zircon cores)	LASS-ICPMS	1846 \pm 22	$^{207}\text{Pb}/^{206}\text{Pb}$ Weighted Average	5	2.60
17SRB-J053A (monazite cores)	LA-ICPMS	1826.1 \pm 5.1	$^{207}\text{Pb}/^{206}\text{Pb}$ Weighted Average	16	0.59
17SRB-J053A (zircon and monazite rims)	LASS-ICPMS, LA-ICPMS	1803.2 \pm 7.7	$^{207}\text{Pb}/^{206}\text{Pb}$ Weighted Average	15	2.60
<i>Migmatite Xenolith</i>					
17SRB-J051A1	LA-ICPMS	2596 \pm 47	Upper Intercept Age	12	1.80

* Secondary Standard ~10 Myr younger

euhedral grains with coarse oscillatory zoning or homogeneous coarse fragments with no clear zonation and lack evidence of metamorphic rims or regrowth. (Fig. 12a). Zircons are variable in size, from ~20 to ~400 μm in length. Larger zircon crystals contain abundant apatite inclusions and are commonly fractured. Despite the occurrence of some large zircons, in comparison to the other suites in the BFGC the fayalite granite is the most zircon-poor.

Samples 17SRB-J029A3 and 17SRB-M095A are fayalite syenogranites that also contain magnetite and ilmenite and a variable amount of Fe-amphibole. These two samples display different degrees of deformation; 17SRB-J029A3 is mostly massive whereas 17SRB-M095A exhibits a weak fabric coincident with the regional fabric. 17SRB-J029A3 was dated via SHRIMP and yielded a U-Pb zircon age of 1841.1 ± 4.5 Ma ($n = 25$, MSWD = 1.4) (Regis, unpublished data), while 17SRB-M095A was dated via LA-ICPMS and yielded an identical age of 1841.0 ± 4.5 Ma ($n = 18$, MSWD = 0.35). The zircons in these two samples were also analyzed for the U-Pb isotope composition during Lu-Hf isotope analyses by LASS-ICPMS. Although less precise, these LASS-ICPMS analyses yielded ages within analytical uncertainty of the ages obtained by the other methods (1840 ± 12 Ma, $n = 4$, MSWD = 0.50 and 1834.2 ± 6.1 Ma, $n = 12$, MSWD = 2.1, for 17SRB-J029A3 and 17SRB-M095A, respectively).

Samples 17SRB-A025A4 and 17SRB-A055A3 are along the pluton margin and have considerably more alteration than their counterparts that are slightly more interior in the pluton. Fayalite is rare, and when present, is commonly considerably altered to iddingsite and other iron-rich products. Mafic minerals less abundant by volume, though Fe-amphibole, magnetite, and ilmenite are still present. 17SRB-A055A3 which is still within error of age of the previous samples. 17SRB-A025A5 yielded a younger weighted average $^{207}\text{Pb}/^{206}\text{Pb}$ age, relative to 17SRB-M095A and 17SRB-J029A, of 1827.1 ± 2.6 Ma ($n = 35$, MSWD = 1.10 via LASS-ICPMS. This discrepancy may be a result of a calibration error in that analytical session. The secondary standard in that session (GJ1) yielded a $^{207}\text{Pb}/^{206}\text{Pb}$ age that was 11 Myr younger than the accepted value (Appendix 3), which suggests that the $^{207}\text{Pb}/^{206}\text{Pb}$ ages determined for sample 17SRB-A025A5 may be too young. The weighted mean of three robust ages in this study (17SRB-J029A3, 17SRB-M095A, and 17SRB-A055A3) give the best estimate for the emplacement age of the fayalite granite pluton, which is 1839.8 ± 2.8 Ma ($n=3$, MSWD = 1.4).

Charnockite

Five representative samples from the charnockite suite were analysed from the southwestern pluton (17SRB-D046A, 17SRB-D048A, 17SRB-L053A, 17SRB-L054A) and the southeastern pluton (17SRB-A018A). The zircons in the charnockite suite are abundant and large, up to 1 mm in length. The zircon morphology is consistent with the fayalite and hornblende-biotite granite suites, consisting mainly blocky fragments with little to minor oscillatory zonation. Samples 17SRB-D046A and 17SRB-D048A are both clinopyroxene-amphibole-orthopyroxene-biotite monzogranites, while 17SRB-L053A and 17SRB-L054A are both devoid of clinopyroxene and contain considerably less orthopyroxene and amphibole. The LASS-ICPMS $^{207}\text{Pb}/^{206}\text{Pb}$ weighted average ages determined for 17SRB-D046A (1831.6 ± 4.3 Ma, $n = 18$, MSWD = 1.2), 17SRB-D048A (1826.2 ± 6.4 Ma, $n = 20$, MSWD = 0.47), and 17SRB-L53A (1826.9 ± 4.8 Ma, $n = 15$, MSWD = 0.47) are within error of the hornblende-biotite granite suite, implying the southwest and southeast plutons were emplaced at a similar time. Sample 17SRB-L054A was dated by LA-ICPMS and yielded a concordia age of 1819.1 ± 5.5 Ma ($n = 25$, MSWD of concordance = 2.2) and a weighted average $^{207}\text{Pb}/^{206}\text{Pb}$ age of 1823.1 Ma ± 4.7 Ma (MSWD = 1.02). For consistency with other dated samples of this study, which are reported as weighted mean $^{207}\text{Pb}/^{206}\text{Pb}$ ages, I interpret 1823.1 Ma ± 4.7 Ma as the current best estimate of the crystallization age of this sample. Sample 17SRB-A018A has the highest plagioclase content in the charnockite suite and is the least altered, with fresh orthopyroxene and little chloritization of amphibole and biotite. Although clinopyroxene is absent, the mafic mineral content is considerably higher than 17SRB-L053A and 17SRB-L054A. 17SRB-A018A was the only charnockite sample that was dated from the southeast pluton, yielding a $^{207}\text{Pb}/^{206}\text{Pb}$ weighted average age of 1834.5 ± 4.3 Ma ($n = 18$, MSWD = 1.3), within error of other samples (17SRB-D046A, 17SRB-D048A) dated from the southwest pluton.

Hornblende-Biotite Granite

Four samples (17SRB-A015A3, 17SRB-R077B2, 17SRB-C047A, and 17SRB-R75A1) across the large SE pluton were selected for analysis, and all the zircon weighted average $^{207}\text{Pb}/^{206}\text{Pb}$ ages are in excellent agreement with one another. Sample 17SRB-R077B2 was dated via SHRIMP and yielded an age of 1826.4 ± 2.3 Ma, $n = 32$, MSWD = 1.19 (Regis, unpublished data), while 17SRB-A015A3 (1825.9 ± 3.3 Ma, $n = 51$, MSWD = 0.47), 17SRB-C047A (1829.9

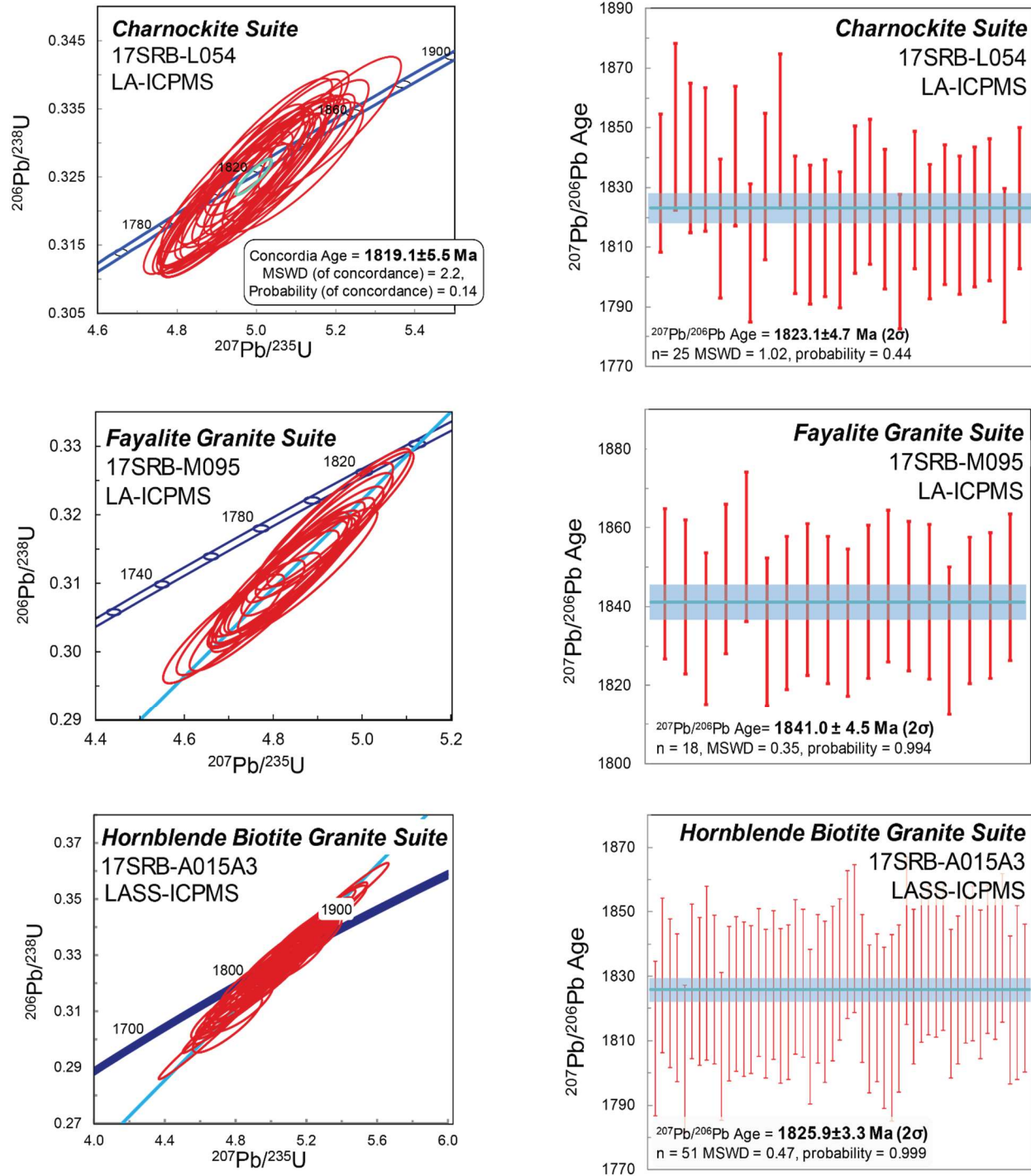


Figure 11a: Selected $^{207}\text{Pb}/^{206}\text{Pb}$ weighted average and Wetherill concordia diagrams for select samples of the charnockite, fayalite granite, and hornblende biotite granite suites. All results are from zircon analyses. All errors are reported to 2 σ unless otherwise stated.

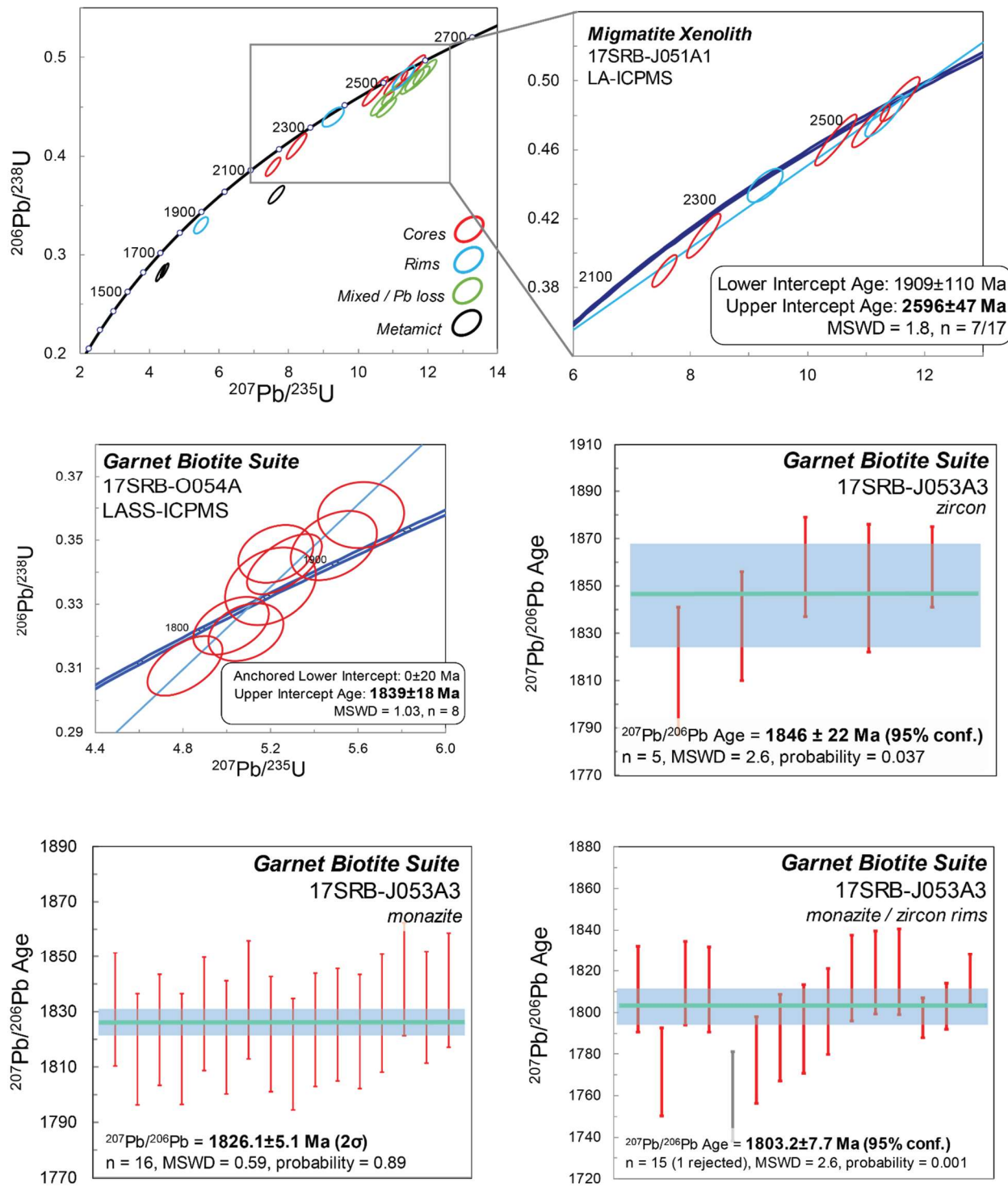


Figure 11b: Selected $^{207}\text{Pb}/^{206}\text{Pb}$ weighted average and Wetherill concordia diagrams for the monazite and zircon of the garnet biotite suite and zircons from the migmatite xenolith. All errors are reported to 2 σ unless otherwise stated.

± 6.6 Ma, $n = 14$, MSWD = 0.87), and 17SRB-R75A1 (1827.7 ± 3.6 Ma, $n = 19$, MSWD = 2.1) were determined using LASS-ICPMS. Similar to the fayalite granite suite, the zircon morphology of the hornblende-biotite granite suite consisted of large fragments lacking zonation; Elongated euhedral grains with coarse oscillatory zoning were more common, with some grains reaching sizes $>600 \mu\text{m}$. However, many of the zircons in the hornblende-biotite granite suite have considerably more fractures than the zircons of the other suites, and zircons in the hornblende-biotite granite suite do show the rare rim (Fig. 12b), indicating that some degree of late-stage zircon growth occurred locally in the pluton. These rims commonly proved too small for static spot analysis by LASS-ICPMS, however, a single rim spot analysis from 17SRB-R077B2 yielded a $^{207}\text{Pb}/^{206}\text{Pb}$ age of 1806 ± 20 Ma. This age is discussed further in connection with the garnet-biotite suite. The age of the migmatite xenoliths within the hornblende-biotite granite suite was also investigated via LA-ICPMS. Sample 17SRB-J051A is a fine-grained, biotite-rich granodiorite with minor hornblende, which was sampled from a large outcrop of migmatite material within a massive hornblende-biotite syenogranite. BSE imagery and zircon morphology was used to distinguish which analyses were likely metamorphic, metamict and igneous; these analyses are labelled on the concordia diagram of Fig. 11b. The oscillatory-zoned igneous cores yielded an upper intercept age of 2596 ± 47 Ma ($n = 7/17$, MSWD = 1.8).

Garnet-Biotite Suite

Two samples (17SRB-O054A and 17SRB-J053A) from the garnet-biotite suite were dated via LASS-ICPMS. Sample 17SRB-O054A is a fine-grained biotite monzogranite, with traces of garnet. Sample 17SRB-J053A is a garnet-biotite quartz monzonite, with abundant large monazite. The garnet biotite suite rocks showed a different zircon morphology from the other suites in the BFGC. Oscillatory zoned, elongated igneous zircon are corroded and mantled by secondary growth, giving a mottled appearance under CL imagery (Fig. 12d). The zircon cores also have more radiation damage and fractures, which resulted in a large number of discarded analyses due to higher ^{204}Pb counts ($^{206}\text{Pb}/^{204}\text{Pb}$ counts per second < 2000 , 9/27 analyses discarded across the two samples). Zircon rims, which are dark in CL images, have relatively low Th/U (< 0.3), compared to oscillatory zoned cores, which have Th/U > 2 . This difference in zircon composition highlights growth of cores and rims under different conditions. The zircon cores of 17SRB-O054A yielded an upper intercept age of 1839 ± 18 Ma ($n = 8$, MSWD = 7.1).

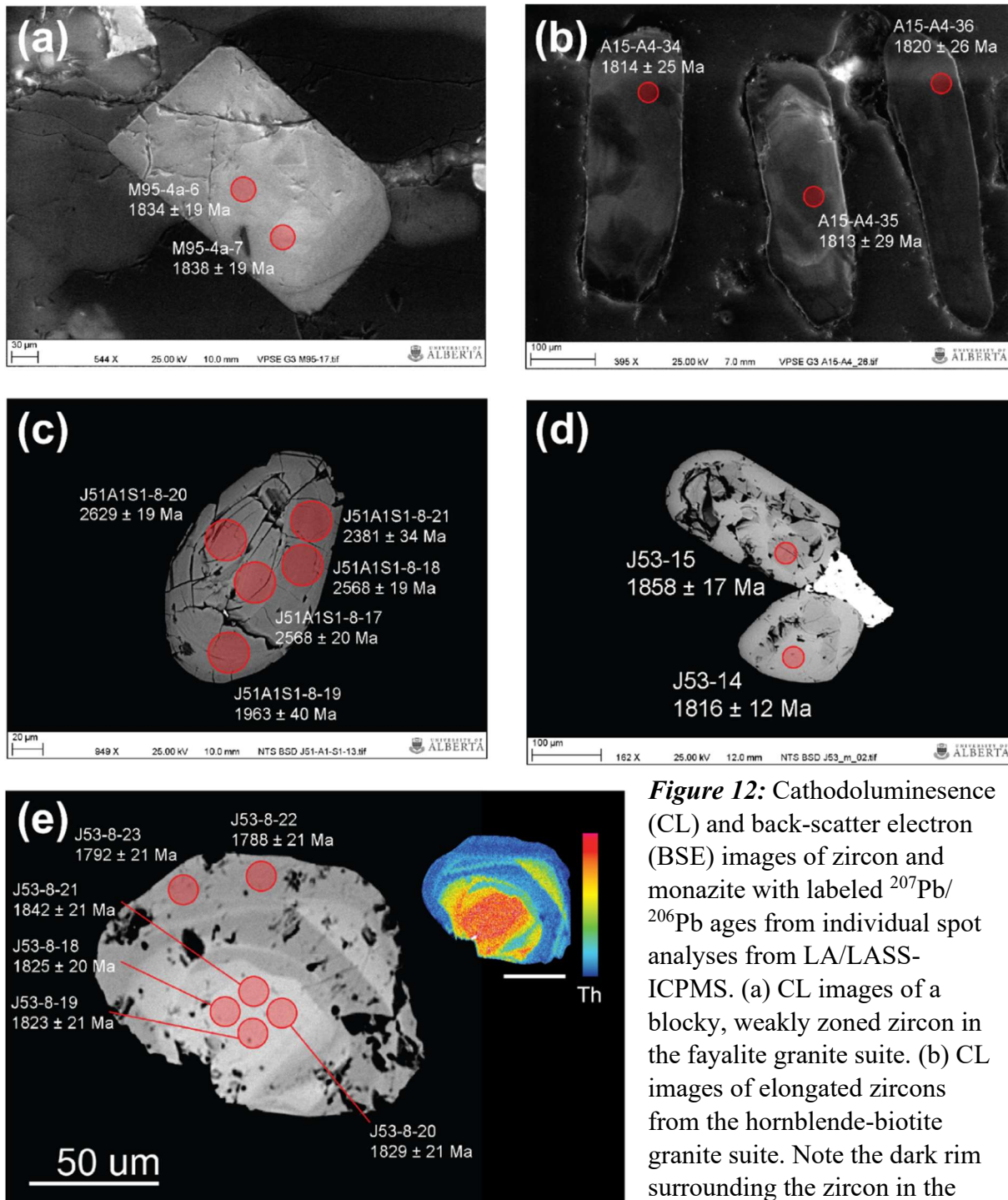


Figure 12: Cathodoluminescence (CL) and back-scatter electron (BSE) images of zircon and monazite with labeled $^{207}\text{Pb}/^{206}\text{Pb}$ ages from individual spot analyses from LA/LASS-ICPMS. (a) CL images of a blocky, weakly zoned zircon in the fayalite granite suite. (b) CL images of elongated zircons from the hornblende-biotite granite suite. Note the dark rim surrounding the zircon in the centre, discussed in text. (c) BSE

imagery showing complex zoning in zircon from a migmatite xenolith found in the hornblende-biotite suite. (d) BSE image of mottled zircons from the garnet-biotite suite, with younger rims indicative of later growth. (e) BSE image and Th X-ray map of a sector-zoned monazite in the garnet-biotite suite. Rims correspond to lower Th content and younger $^{207}\text{Pb}/^{206}\text{Pb}$ ages, while high Th cores corresponded to older ages.

Unfortunately, there were not enough analyses on the rims of the zircons to determine an age of later growth in this sample, but ages for both rims and cores of 17SRB-J053A were established. The zircon cores yielded a $^{207}\text{Pb}/^{206}\text{Pb}$ weighted average age of 1846 ± 22 Ma ($n = 5$, MSWD = 2.6). Three rim spots yielded a $^{207}\text{Pb}/^{206}\text{Pb}$ weighted average age of 1804.1 ± 6.2 Ma (MSWD = 3.0), a younger age than much of the BFGC.

Monazite shows similar core-rim age relationships as the zircons. Specifically, BSE images and Th X-Ray maps of monazite grains produced on the EMPA show an oscillatory zoned core of likely igneous origin and a relatively narrow rim, presumably of metamorphic origin (Fig. 12e). The oscillatory zoned portion of the grain, particularly its center, is characterized by high Th compared to the low Th rim (Fig 2e). In-situ U-Pb analyses of monazite rims via LA-ICPMS yield a younger $^{207}\text{Pb}/^{206}\text{Pb}$ age of 1799 ± 13 Ma (95% confidence, $n = 12$, MSWD = 3.9), compared to the cores, which yield an age similar to those obtained on zircon cores from the southeastern pluton (1826 ± 5.1 Ma, $n = 16$, MWSD = 0.59). Collectively, the rims of the monazite and zircons yielded an age of 1803.2 ± 7.7 Ma ($n = 14/15$, MSWD = 2.6). Given the relatively scattered nature of the U-Pb zircon data for the garnet-biotite suite granitoids, I interpret the monazite core age of 1826 ± 5.1 Ma to be our current best estimate of the crystallization age of the garnet-biotite suite magma.

Zircon Trace Elements

In addition to being an important geochronometer, trace elements in zircon, namely trivalent and tetravalent HFSE and REE that substitute easily into zircon's crystal structure, have been used to track magma fractionation processes (Nardi *et al.*, 2013; Breiter *et al.*, 2014), and discern the types of magmas from which zircons crystallized (Heaman *et al.*, 1990; Belousova *et al.*, 2002; Wang *et al.*, 2011). Zircons from 4 representative samples (17SRB-R075A, 17SRB-J053A1, 17SRB-L052A, 17SRB-J029A), one from each suite in the BFGC, were analysed for their trace-element composition to assess if each suite was derived from similar magmatic environments. This also included 5 rim analyses of zircon from sample 17SRB-J053A1 of the garnet-biotite suite. After screening the analyses for potential inclusions and fractures using BSE images, the average REE concentrations calculated from 4 to 15 analyses per sample are shown in Fig. 13 (normalized to C1 chondrite; McDonough and Sun, 1995). A full listing of zircon trace-element data is given in Appendix 5.

Although the cores of the zircons from all suites show traits typical of igneous zircon that crystallized from felsic magmas, such as a positive Ce anomaly, negative Eu anomaly, and greater abundance of HREE (Tb-Lu) relative to LREE (La-Pr) (Hoskin and Schaltegger, 2003), there are differences between suites that imply different sources and/or contrasting magma crystallization conditions. The zircon cores in the garnet-biotite suite have a less fractionated HREE pattern ($(\text{Gd}/\text{Yb})_N = 0.26$) than other suites ($(\text{Gd}/\text{Yb})_N = 0.067\text{-}0.096$) consistent with the presence of garnet in equilibrium with the zircons (Hoskin and Schaltegger, 2003). There is significantly higher HREE in zircon of the hornblende-biotite granite suite, and both the hornblende-biotite and garnet-biotite suites have higher LREE abundance than the fayalite granite and charnockite (Fig. 6a). In typical crustal zircon, LREEs (La-Pr, with exception to Ce) are less than 10 x chondritic abundance (Hoskin and Schaltegger, 2003), and higher LREE abundance in zircon is commonly attributed to alteration, whether that be the result of fluids infiltrating radiation damaged zones, metamorphism or hydrothermal regrowth (Hoskin and Schaltegger, 2003; Hoskin, 2005; Bell *et al.*, 2016). This is most apparent and likely the case with the garnet-biotite suite zircon rim analyses, which have the least fractionated overall REE

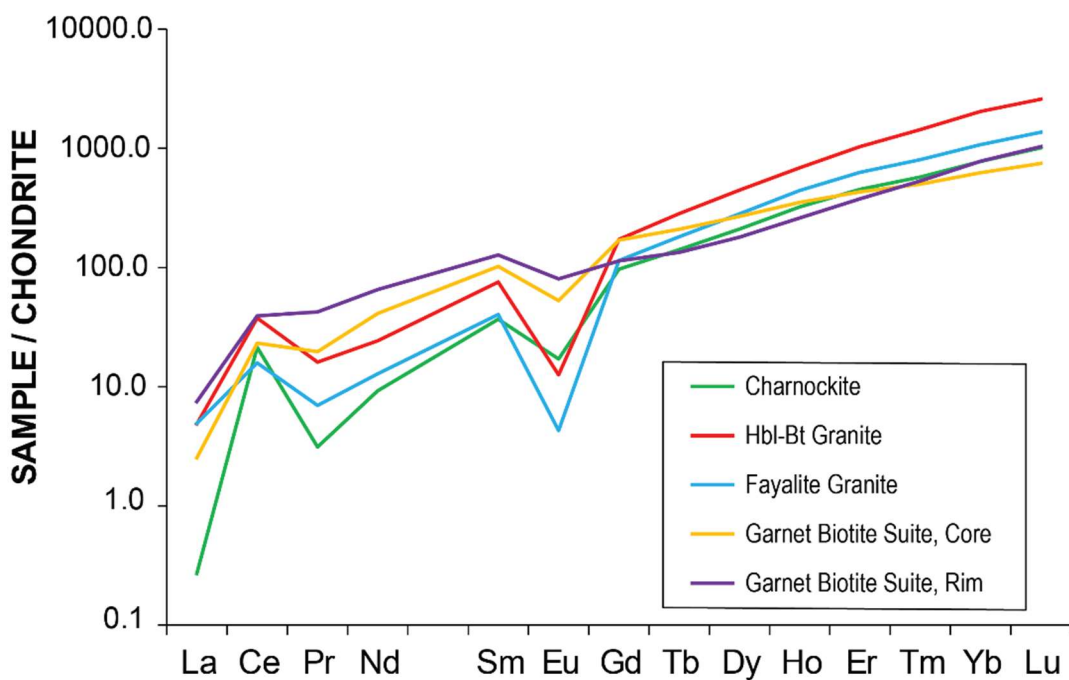


Figure 13: Chondrite normalized rare-earth-element plots of zircon for representative samples from the Boothia ferroan granitoid complex.

Table 6 : Average zircon trace element compositions of samples in the Boothia ferroan granitoid complex

Sample Name	17SRB-J29A1	17SRB-L52A	17SRB-R75B	17SRB-J53A1 (Core)	17SRB-J53A1 (Rim)
Rock Type	Fayalite Granite	Charnockite	Hbl-Bt Granite	Grt-Bt Suite	Grt-Bt Suite
<i>ppm</i>					
P	209	225	181	338	245
Sc	280	262	208	282	264
Ti	13.4	19.3	6.4	34.1	9.6
Y	695	481	1051	531	422
Nb	2.54	1.89	6.77	1.20	1.92
La	1.17	0.06	1.15	0.60	1.78
Ce	9.7	13.1	23.1	14.2	24.1
Pr	0.65	0.29	1.49	1.83	3.94
Nd	5.9	4.2	11.1	18.8	29.8
Sm	6.0	5.4	11.2	15.1	18.9
Eu	0.24	0.96	0.71	2.96	4.52
Gd	22.8	19.3	34.3	33.8	22.6
Tb	6.53	5.10	10.20	7.54	4.84
Dy	69.3	51.7	109.6	66.0	44.1
Ho	24.1	17.6	37.5	19.2	14.2
Er	100.7	72.3	165.4	68.9	60.3
Tm	19.84	14.14	35.39	12.33	13.10
Yb	172.8	124.6	327.6	100.5	125.4
Lu	33.6	24.8	63.5	18.4	25.4
Ta	1.16	0.67	3.59	0.40	0.87
Th	93.7	63.3	508.4	100.1	107.8
U	164.4	50.4	778.3	57.7	312.3
(wt. %) Hf	1.075	1.035	1.137	0.980	1.076
Th/U	0.570	1.257	0.653	1.733	0.345
Eu/Eu*	0.063	0.286	0.110	0.400	0.668
Ce/Ce*	2.707	23.259	4.262	3.291	2.205
(Gd/Lu)*	0.084	0.096	0.067	0.227	0.110

¹Eu/Eu* = Eu_N/√(Sm_N* Gd_N)

²Ce/Ce* = Ce_N/√(La_N * Pr_N)

³Normalized to chondritic values from McDonough and Sun (1995)

slopes ((La/Yb)_N = 0.0096), smallest negative Eu anomalies (0.66), and relatively low Th/U (< 0.3); all these traits paired with the rims enveloping corroded cores are typical of post-magmatic zircon growth (Hoskin and Schaltegger, 2003; Harley *et al.*, 2007; Wang *et al.*, 2011). However, hydrothermal growth or alteration is unlikely to be the cause of high LREE within the hornblende-biotite granite suite zircons, as the zircons yield near concordant U-Pb analyses,

indicating little radiogenic Pb loss and therefore proportionally little radiation damage; with little radiation damage and no post-intrusion metamorphism, there is little reason to suspect significant alteration to the zircons. Rather, the high LREE content in the hornblende-biotite granite suite zircons would directly reflect LREE enrichment in the magma from which it crystallized.

The Th/U of zircon has been a commonly used geochemical tool for distinguishing magmatic and metamorphic zircon and for inferring the magmatic environment in which the zircon is crystallized (Belousova *et al.*, 2002; Hoskin and Schaltegger, 2003; Wang *et al.*, 2011; Kirkland *et al.*, 2015). Although there is wide variability in the Th and U concentration of zircons, median Th/U values are typically lower ($\text{Th}/\text{U} < 1$) in lower-temperature felsic melts than in higher-temperature mafic melts (Wang *et al.*, 2011; Kirkland *et al.*, 2015). An interesting finding in this study is that there is a large range in Th/U values recorded in zircon from the four investigated felsic magma suites. Zircons in the fayalite and hornblende-biotite granite suites have the lowest average Th/U ratios (0.54 and 0.65, respectively), which is similar to that found in many granitoids. Zircons in the garnet-biotite suite has the highest Th/U, with values up to 2.1, which corresponds to the suite having lowest silica (56 – 63 wt.% SiO_2) and zircon Hf contents wt. % of the complex (Fig. 14b). The charnockite suite has Th/U ratios (average $\text{Th}/\text{U} = 1.3$) intermediate between the garnet-biotite and hornblende-biotite suites. Th/U ratios > 1 are uncommon for zircon that crystallized from felsic magmas, however zircon occurring in granitoids with a more alkaline character have been reported with high Th/U (Wang *et al.*, 2011).

Geochemical discrimination diagrams that utilize the HSFE and REE concentration of zircons can further our understanding of the melt compositions from which the BFGC zircons crystallized (Fig. 14). Various detrital zircon provenance studies have used discrimination diagrams to determine the zircon's source rock (Nardi *et al.*, 2013; Breiter *et al.*, 2014); Though the provenance of the zircons is obviously known in this study, discrimination diagrams can still be useful in establishing the degree of fractionation of each pluton and individual suites (Belousova *et al.*, 2002; Nardi *et al.*, 2013). Nb and Ta concentrations reflect the overall REE composition of the melt (Belousova *et al.*, 2002), as their abundances are controlled by the coupled substitution with trivalent REEs and Y (Hoskin and Schaltegger, 2003). A higher abundance of Nb, Y, and HREE is generally attributed to higher degree of fractionation. The hornblende-biotite suite granitoids show a clear enrichment in Nb, Ta, Y, and Lu in the

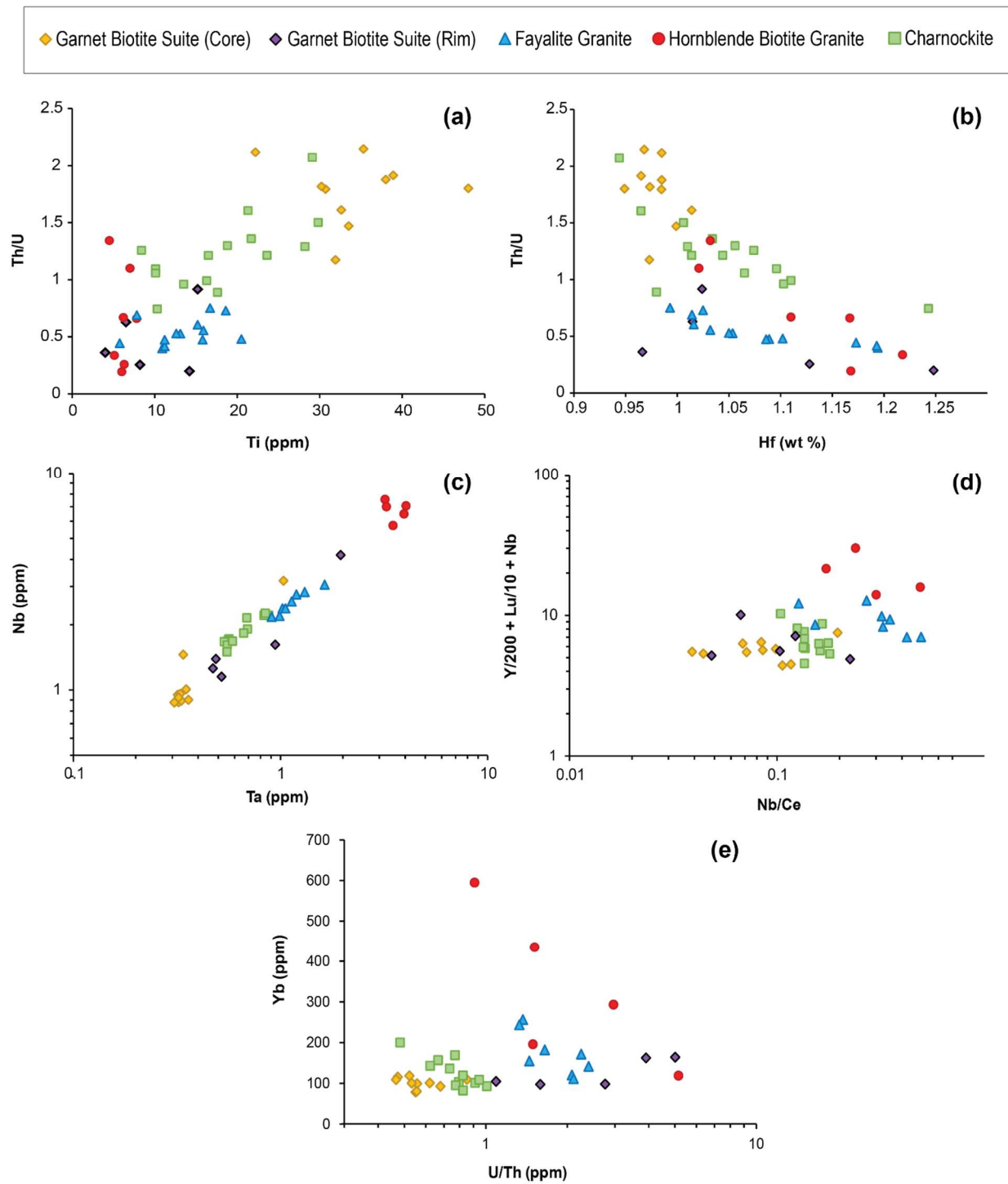


Figure 14: Zircon trace element plots for representative samples from the Boothia ferroan granitoid complex. a) Th/U vs Ti (ppm), b) Th/U vs Hf (wt %), c) Nb (ppm) vs Ta (ppm) after Belousova et al. (2002), d) Zircon trace element discrimination diagram for granitoids after Nardi et al. (2013), e) Yb vs U/Th zircon discrimination diagram after Breiter et al. (2014).

discrimination diagrams, confirming the high LREE content of the whole rock more likely reflects a highly fractionated magma composition rather than simple accumulation of LREE-enriched phases. In addition, the hornblende-biotite suite zircons show elevated Yb concentrations (Breiter *et al.*, 2014), which is unique to compared to the rest of the BFGC suites (Fig. 14e). Conversely, despite the garnet-biotite suite granitoids displaying the highest whole-rock incompatible element concentrations and whole-rock trace-element geochemistry displaying the highest concentration of incompatible elements thereby implying a high degree of fractionation, the trace-element concentrations in zircons from the garnet-biotite suite show the lowest degree of fractionation in these diagrams. This observation also correlates well with the high Th/U ratios (>1) and lower Hf wt. % (< 1 wt. %), indicative of less fractionation and a higher temperature melt.

Nd and Hf Isotope Compositions

The Sm-Nd and Lu-Hf isotopic systems are commonly used as sensitive tracers for the origin of granitoid suites. They can be a robust monitor of crustal evolution and differentiate between granite magmas derived from juvenile (mantle-like initial isotopic compositions) or evolved (re-working of older crust) sources. (Nelson and DePaolo, 1981; Patchett and Vervoort, 1996; LaFlamme *et al.*, 2014). The Sm-Nd isotopic system is useful as a crust versus mantle tracer due to the strong fractionation of parent and daughter elements during the mantle melting processes that result in the formation of juvenile continental crust. In contrast, these elements are less

Table 7: Summary of whole rock Sm-Nd, and Lu-Hf of zircon isotope analyses of the Boothia Ferroan Granite Complex

Sample Name	Age (Ma)	Sm (ppm)	Nd (ppm)	Measured $^{143}\text{Nd}/^{144}\text{Nd}$	$^{147}\text{Sm}/^{144}\text{Nd}$	Initial $^{143}\text{Nd}/^{144}\text{Nd}$	$\pm 2\sigma$	ϵ_{Nd}	$\pm 2\sigma$	T_{DM} (Sm/Nd)	n	Corrected $^{176}\text{Hf}/^{177}\text{Hf}$	Corrected $^{176}\text{Lu}/^{177}\text{Hf}$	Initial $^{176}\text{Hf}/^{177}\text{Hf}$	$\pm 2\sigma$	ϵ_{Hf}	$\pm 2\sigma$	$T_{\text{DM}*}$ (Lu/Hf)
Charnockite																		
17SRB-D048A	1826.2 ± 6.4	-	-	-	-	-	-	-	-	-	20	0.28133	0.00040	0.28132	0.00003	-10.6	0.3	2701
17SRB-L053A	1826.9 ± 4.8	-	-	-	-	-	-	-	-	-	15	0.28133	0.00032	0.28134	0.00002	-10.8	0.3	2713
17SRB-L054A	1819.1 ± 5.5	18.5	113.0	0.51104	0.099	0.50986	0.00002	-8.3	0.4	2775	-	-	-	-	-	-	-	
Hornblende Biotite Granite																		
17SRB-A015A3	1825.9 ± 3.3	18.6	142.7	0.51086	0.079	0.50991	0.00001	-7.1	0.4	2572	51	0.28141	0.00086	0.28138	0.00002	-8.5	0.2	2610
17SRB-R077B2	1826.4 ± 2.3	59.6	480.4	0.51082	0.075	0.50991	0.00001	-7.1	0.5	2546	-	-	-	-	-	-	-	
17SRB-C047A	1829.9 ± 6.6	-	-	-	-	-	-	-	-	-	14	0.28140	0.00040	0.28139	0.00004	-8.4	0.4	2604
Fayalite Granite																		
**17SRB-A025A4	1827.7 ± 3.6	10.3	55.3	0.51125	0.113	0.50988	0.00002	-7.5	0.3	2844	35	0.28137	0.00064	0.28135	0.00002	-9.3	0.2	2736
17SRB-J029A3	1841.1 ± 4.5	13.0	73.6	0.51118	0.107	0.50988	0.00002	-7.3	0.4	2792	5	0.28137	0.00040	0.28136	0.00007	-9.1	0.7	2720
Garnet Biotite Suite																		
17SRB-O054A	1840 ± 18	-	-	-	-	-	-	-	-	-	8	0.28135	0.00036	0.28134	0.00004	-9.8	0.5	2627

*Lu/Hf used for calculation an averaged whole rock Lu/Hf value of suite. Reference values for CHUR are given by Bouvier *et al.* (2008), and Depleted Mantle model and values based off Belousova *et al.* (2010)

**Secondary standard 10 myr younger

fractionated during reworking of pre-existing continental by intra-crustal melting processes. As such, the Sm-Nd system can be used to infer whether a particular granitoid magma was derived from rocks recently extracted from the mantle (i.e., juvenile rocks) or by re-melting of older crust. This isotopic system can in principle also provide insights on the time at which the source rocks were extracted from the mantle though the results can potentially be misconstrued should the magma in question be derived from multiple source rocks with differing isotopic compositions and different mantle extraction ages (Nelson and DePaolo, 1981).

The Lu-Hf isotopic system had in the past been less commonly applied than the Sm-Nd system in crustal evolution studies due to difficulty ionizing Hf via thermal ionization (i.e. TIMS) but has gained in popularity with the advent of ICP-MS (Dicken, 2018). The Lu-Hf isotopic system behaves much the same as Sm-Nd with a few crucial differences; the fractionation between Lu and Hf is larger during partial melting relative to Sm-Nd, thereby giving greater sensitivity to

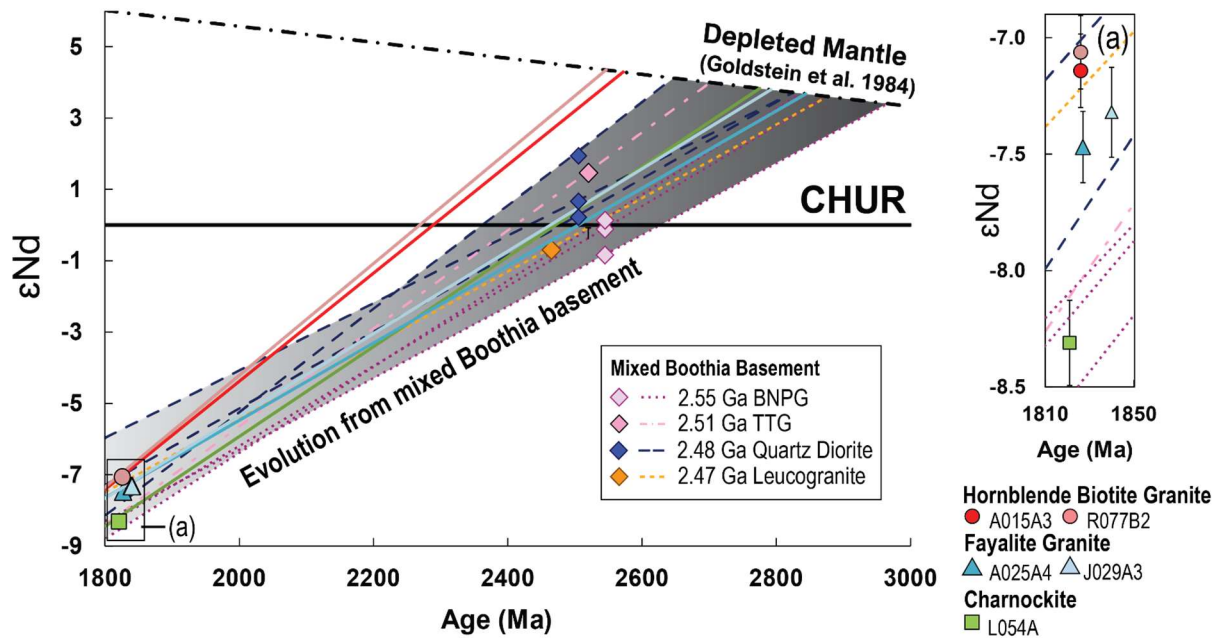


Figure 15: Nd isotopic evolution and (a) ϵ_{Nd} isotopic values of the Boothia ferroan granitoid complex. Depleted mantle reservoir values are derived from (Goldstein et al. 1984) and ϵ_{Nd} values are normalized to the chondritic uniform reservoir (CHUR). Coloured lines show evolution from depleted mantle of measured samples, and shaded region and dashed lines shows projected Nd evolution of mixed Boothia Basement to 1.83 Ga, including Boothia Neoarchean porphyroclastic granitoids (BNPG), 2.51 Ga tonalite-trondhjemite-gneiss (TTG), Boothia ca. 2.48 Ga mafic rocks, and leucogranite dominantly derived of BNPG material. Data from Boothia Peninsula-Somerset Island project (Sanborn Barrie et al., unpublished)

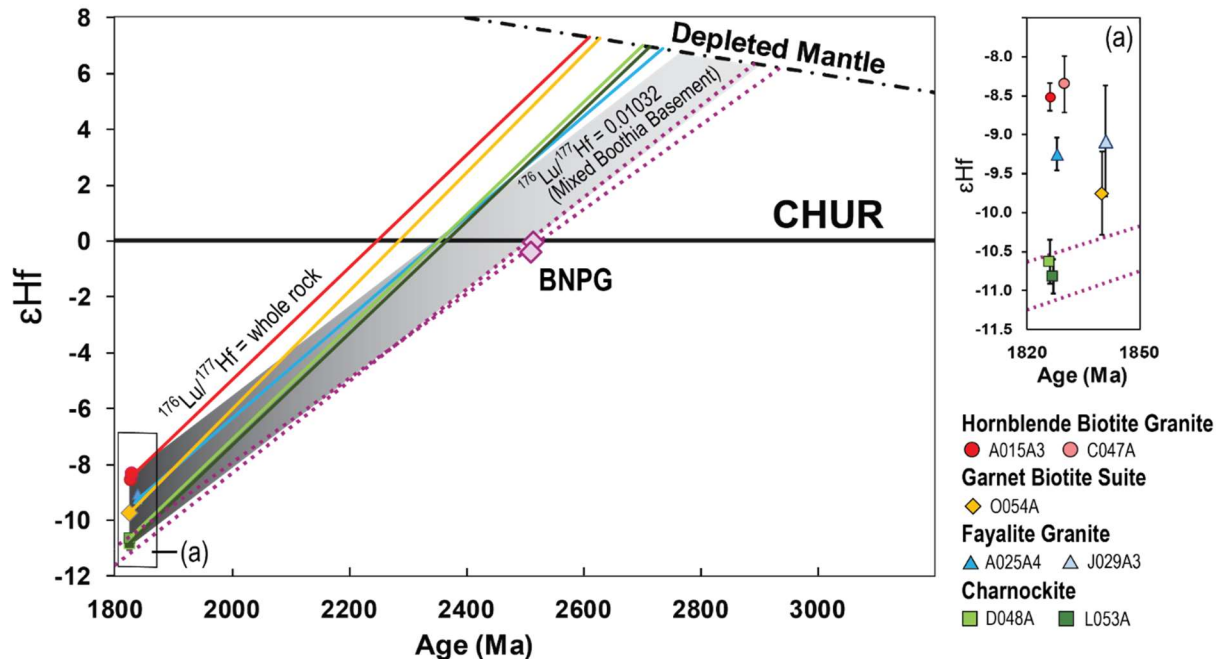


Figure 16: Hf isotopic evolution and (a) ϵHf isotopic values of the Boothia ferroan granitoid complex. Depleted mantle reservoir curve derived from (Belousova et al. 2010) and ϵHf values are normalized to the chondritic uniform reservoir (CHUR). Coloured lines show ϵHf evolution assuming $^{176}\text{Lu}/^{177}\text{Hf}$ values of the source rock, shaded region assumes source rock $^{176}\text{Lu}/^{177}\text{Hf}$ values are equal to that of a mixed Boothia Basement material (Boothia Neoarchean porphyroclastic granitoids and ca. 2.48 Ga Boothia mafic rocks).

differentiating magmatic suites using ϵHf values. The greatest advantage, however, to the using Lu-Hf isotopic system in granitoids is that, rather than analyzing whole rocks as with the Sm-Nd system, zircons can be used to more accurately constrain the initial isotopic composition of the magma. Hf is very similar geochemically to Zr and easily substitutes within zircon's mineral structure, which results in high Hf (wt. % level) as opposed to Lu (ppm level) concentrations. Consequently, the Lu/Hf ratios within zircons are very low (<0.01) and therefore, unlike whole rocks, the $^{176}\text{Hf}/^{177}\text{Hf}$ ratios of zircons do not change significantly from their initial values over time from the in-growth of radiogenic ^{176}Hf . In addition, because zircon is a robust mineral resistant to alteration and metamorphism, and because diffusion rates of Hf in zircon are exceedingly slow (Cherniak et al., 1997), its Hf isotope composition and evolution is unlikely to be disturbed by post-magmatic processes (Kemp et al., 2010). Collectively, these features of zircon enable it to provide a robust indication of the initial Hf isotope composition of the magma from which it crystallized.

To document the isotopic evolution of the Boothia ferroan granitoid complex from its source rocks, Sm-Nd and Lu-Hf isotope compositions at the initial time of pluton emplacement ($\epsilon\text{Nd}_{1.83\text{Ga}}$ and $\epsilon\text{Hf}_{1.83\text{Ga}}$) were calculated from measured present-day values of whole rock and zircon, respectively. Five whole-rock samples were analysed for their Nd isotope composition: one from the charnockite suite and two each from the hornblende-biotite and fayalite granite suites. Seven samples were analysed for their zircon Hf isotope compositions: one from the garnet-biotite suite and two each from the charnockite suite, fayalite granite suite, and hornblende-biotite granite suite. Three samples (17SRB-A015A3, 17SRB-A025A4, and 17SRB-J029A3) were analysed for both Nd and Hf, to allow comparison between these isotopic systems. Samples 17SRB-L053A and 17SRB-L054A were collected in close proximity with identical petrological and geochemical traits, so the isotopic results from these samples were expected to yield similar results. The Lu/Hf values derived from whole-rock analyses of these granitoids (Table 1) provide the minimum estimate of the Lu/Hf of the magma source rocks, which can then be used in combination with zircon $\epsilon\text{Hf}_{1.83\text{Ga}}$ values to calculate depleted mantle model ages ($T_{\text{DM(Hf)}}$) for each suite (Fig. 16). These zircon-based $T_{\text{DM(Hf)}}$ model ages can be compared to depleted mantle model ages derived from whole-rock Nd isotope analyses ($T_{\text{DM(Nd)}}$).

All suites exhibit negative $\epsilon\text{Nd}_{1.83\text{Ga}}$ (-7.1 to -8.3) and $\epsilon\text{Hf}_{1.83\text{Ga}}$ values (-8.4 to -10.8), much lower than primitive mantle (chondritic uniform reservoir or CHUR in Figure 15), which suggests derivation of these magmas dominantly from older crustal source rocks. Nevertheless, in detail, there is isotopic variation between suites, which suggests a more complex process than simple partial melting of single crustal source. The charnockite suite has the most negative $\epsilon\text{Nd}_{1.83\text{Ga}}$ (-8.3), being nearly a full Nd epsilon unit below the other suites. The $\epsilon\text{Nd}_{1.83\text{Ga}}$ of the hornblende-biotite granite suite (-7.1) is the least negative and overlaps with the fayalite granite suite (-7.3 to -7.5) within the calculated analytical error ($\pm 0.2 \epsilon\text{Nd}$). The Lu-Hf isotope system provides a more sensitive monitor of potential source differences due to stronger Lu/Hf relative to Sm/Nd fractionation during crustal melting. As expected, $\epsilon\text{Hf}_{1.83\text{Ga}}$ values show greater separation between suites than $\epsilon\text{Nd}_{1.83\text{Ga}}$. The hornblende-biotite granite suite has the least negative $\epsilon\text{Hf}_{1.83\text{Ga}}$ values (-8.4 to -8.5) while the charnockite has the most negative ($\epsilon\text{Hf}_{1.83\text{Ga}} = -10.6$ to -10.8), corroborating the results from Nd isotope system. Interestingly, the fayalite granite and garnet-biotite suites have identical $\epsilon\text{Hf}_{1.83\text{Ga}}$ within analytical uncertainty (-9.8 and -9.3, respectively).

Another notable characteristic of the Nd and Hf isotope compositions of the BFGC is the variation in depleted mantle model ages between suites. These model age calculations assume that Sm/Nd and Lu/Hf of the magma source is the same as that of the granitoids (i.e., there is no fractionation of these elements during crustal melting). In reality, the Sm/Nd and Lu/Hf of the source rocks are likely to have been higher than that of the granitoids, in which case the model ages would be minimum estimates of the age of crust extraction from the mantle. Since the hornblende-biotite granite suite has less negative ϵ Nd values and a lower $^{147}\text{Sm}/^{144}\text{Nd}$ than the fayalite granite or charnockite suites, it records a younger $T_{\text{DM(Nd)}}$ (~2.54-2.57 Ga vs. ~2.77-2.84 Ga). A lower $^{147}\text{Sm}/^{144}\text{Nd}$ is indicative of greater degree of fractionation of LREE during partial melting, however this is typically paired with more negative ϵ Nd values if the source rocks of each suite are the same. The Hf isotope results are similar with a minimum $T_{\text{DM(Hf)}} = \sim 2.60$ Ga for the hornblende-biotite suite as opposed to ~2.70-2.72 Ga for the fayalite and charnockite suites. While the Sm-Nd isotope composition of the garnet-biotite suite was not characterized, the $T_{\text{DM(Hf)}}$ was similar to that of the hornblende-biotite granite suite (~2.63 Ga).

DISCUSSION

Emplacement Ages of the Boothia Ferroan Granite Complex

Prior to the present study, there had been no reports of post-1.9 Ga magmatism within Boothia Peninsula. A detailed geochronological age study of the Boothia Ferroan Granite Complex was undertaken with the goal of establishing the connection to the Paleoproterozoic (1.85-1.80 Ga) granite ‘bloom’ within the Churchill Province, associated with the late stages of the Trans-Hudson orogen. The distribution of U-Pb ages indicates that magmatism occurred over and ~ 20 Myr period between ~1840 to 1823 Ma (Table 1). These ages were determined using three in-situ U-Pb methods; LA-ICPMS, LASS-ICPMS, and SHRIMP. The fayalite granite suite (1839.8 ± 2.8 ; n=3) is the oldest and was exclusively emplaced during the ~1840 Ma pulse of magmatism, which may explain the spatial separation between the fayalite granite, an isolated pluton, from the rest of the complex. The hornblende-biotite granite (1826.8 ± 1.6 Ma; n=4) and charnockite (1829.0 ± 5.9 Ma; n=5) suites generally overlap in their emplacement ages within analytical uncertainty. These two suites make up the southwest and southeast plutons, with a weighted mean of their emplacement 1827.6 ± 2.3 Ma (n=9, MSWD = 2.5) being the best estimate of the age of these younger plutons relative to the fayalite granite pluton (Fig. 17).

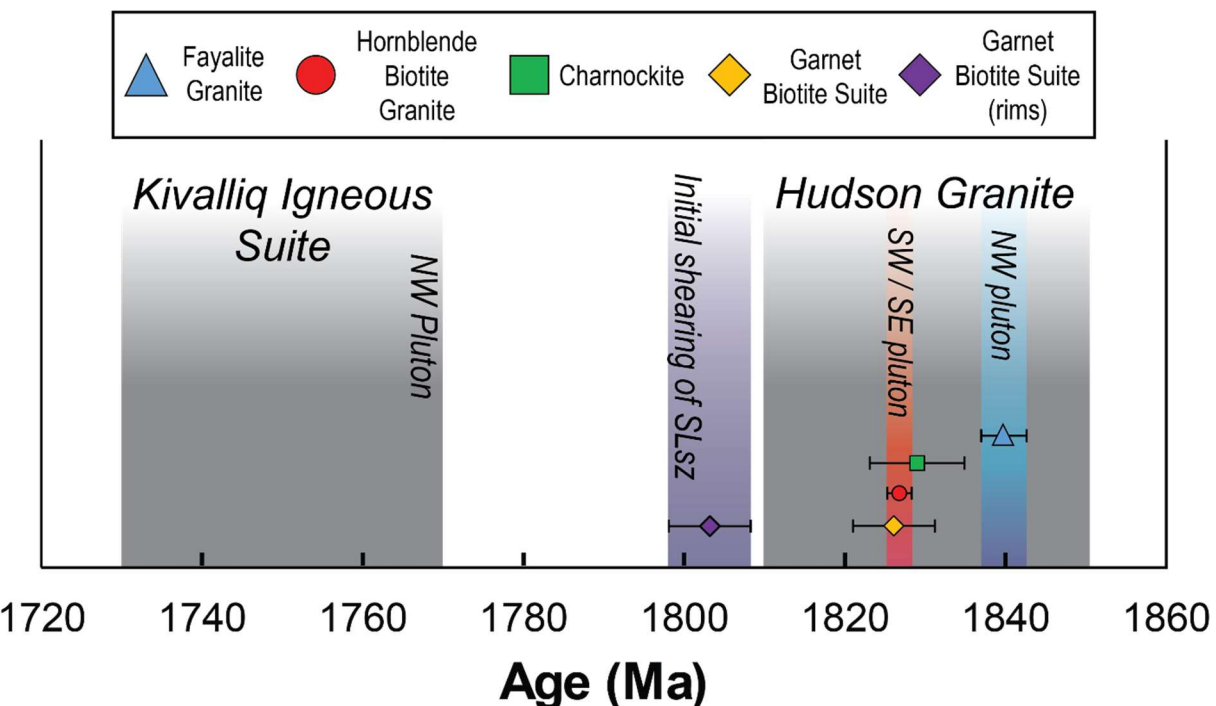


Figure 17: Summary and comparison of U-Pb ages of the BFGC plutons relative to widespread Paleoproterozoic magmatism within the Churchill Province. Symbols represent weighted mean of each suite using robust U-Pb geochronological analyses of this study (see discussion). Shaded regions represent best estimates magmatic emplacement and related Sanagak Lake shear zone (SLsz).

The only suite in the BFGC whose age of emplacement is not firmly established is the garnet-biotite suite. Although the zircon cores in two samples from this suite yield weighted average $^{207}\text{Pb}/^{206}\text{Pb}$ ages in agreement with the older pulse of magmatism (ca. 1.84-1.85 Ga), their corresponding age uncertainties are large and overlap both pulses. Spatially, the garnet-biotite suite is proximal to the younger, southern plutons of the BFGC, particularly the hornblende-biotite suite, which suggests that the garnet-biotite suite may be associated with the younger magmatic pulse. This hypothesis is supported by a U-Pb age of 1826.1 ± 5.1 Ma obtained on euhedral and concentrically zoned magmatic monazite grains from the garnet-biotite suite (Figs. 2 and 3), which is indistinguishable from the ages recorded by the hornblende-biotite suite (Table 1). Thus, I interpret the ca. 1826 Ma as the current best estimate of the emplacement age of the garnet-biotite suite. The more scattered ages obtained on zircons of this suite relative to the other plutonic suites of the BFGC suggest incorporation of a slightly older component either in the form of zircon xenocrysts (derived from totally unrelated rocks) or antecrysts (derived

from a slightly earlier crystallized garnet-biotite suite magma). These possibilities are discussed further as part of the petrogenesis of the garnet-biotite suite. Younger monazite and zircon rims (1803.2 ± 7.7 Ma, $n = 15$, MSWD = 2.5), are also exclusive to the garnet biotite suite. Why these rims are exclusive to the garnet-biotite suite is likely related to the suite's mineralogy; the partially skeletal texture of the garnets indicates mineral breakdown, which in turn would free some of the elements needed (REE, Zr, P) to allow latter stage growth of zircon and monazite (Rubatto, 2017). This age coincides with the growth of metamorphic titanite within the Sanagak Lake shear zone (SLsz), and which has been interpreted to record the initial age of shear zone development (Drayson *et al.*, in preparation). The relationship between the SLsz and the BFGC is discussed further in a later section.

The geochronological data obtained in the present study indicates that BFGC magmatism was contemporaneous with the intrusion of Hudson granites (1.85-1.81 Ga), which represent the most spatially widespread late Trans-Hudson magmatic activity in the Churchill Province (Fig. 17; Peterson *et al.*, 2002). The emplacement of the BFGC also broadly coincides with the intrusion (or eruption) of ultrapotassic rocks in the Churchill Province (Cousens *et al.*, 2001; Peterson *et al.*, 2002; Morelli *et al.*, 2009; Sandeman and Hadlari, 2010), and the intrusion of tholeiitic mafic dykes, the 1.827 Ga Sparrow dykes, in the western Rae craton (Bostock and van Breemen, 1992). The BFGC pre-dates intrusion of the 1.77-1.73 Ga anorogenic plutons of Kivalliq/Nuetlin suite, which, like the Hudson granites, are also widespread in the Churchill Province (Peterson *et al.*, 2015b).

Intensive Parameters

Temperature of emplacement

Three different geothermometers are available to constrain the temperatures at which the BFGC magmas were emplaced and crystallized. The temperatures indicated by each of these geothermometers is discussed below.

Amphibole-plagioclase geothermometers. Holland and Blundy (1994) formulated two geothermometer equilibria applicable to amphibole-plagioclase assemblages: 1) edenite + 4 quartz = tremolite + albite, and 2) edenite + albite = richterite + anorthite. Although both thermometers are in principle applicable to amphibole-bearing granitoids, I determined

equilibrium (2) was better suited for the BFGC because it does not require that the melt be quartz saturated during amphibole crystallization. If the melt was silica undersaturated at the time of amphibole crystallization, equilibrium (1), which assumes silica saturation, may record spuriously high temperatures (Holland and Blundy, 1994). Application of the amphibole-plagioclase thermometers to fayalite, charnockite and hornblende-biotite suite granitoids yield temperatures of 873 to 885 °C and 812 to 832 °C (\pm 35-40°C) with equilibria (1) and (2), respectively, calculated at an estimated magma emplacement pressure of 5-6 kbar (discussed further in the next section). As the garnet-biotite suite is not amphibole bearing, temperatures cannot be determined for this suite using this method.

Titanium in zircon. Ti concentrations were also determined in zircon from representative samples from each of the four granitoid suites (17SRB-R075A, 17SRB-J053A1, 17SRB-L052A, 17SRB-J029A) to constrain zircon crystallization temperatures. Apparent zircon crystallization temperatures in these samples were constrained with the Ti-in-zircon thermometer (Watson and Harrison, 2005) using the calibration of Ferry and Watson (2007). The initial calculations assumed that the activities of SiO_2 and TiO_2 components in the melt were unity ($a_{\text{SiO}_2} = a_{\text{TiO}_2} = 1$), which would imply that the melt was both quartz and rutile saturated during zircon crystallization. As none of the BFGC rocks contain primary rutile, the a_{TiO_2} of these melts must in fact be below unity. In such cases, Ti-in-zircon temperatures ($\mathbf{T}_{\text{Ti-Zircon}}$) calculated assuming $a_{\text{TiO}_2} = 1$ would be *minimum* estimates of the actual temperatures of zircon crystallization.

Although all the BFGC rocks are quartz bearing, it is not certain if these melts had reached silica saturation at the time that zircon crystallized (i.e., quartz crystallization may have begun at lower temperature than zircon crystallization). If this were the case then a_{SiO_2} of the melt would have been below unity during zircon crystallization and in turn $\mathbf{T}_{\text{Ti-Zircon}}$ provides a *maximum* estimate of the temperature of zircon crystallization. Understanding the cumulative impact of these competing effects on $\mathbf{T}_{\text{Ti-Zircon}}$ requires quantitative constraints on melt a_{SiO_2} and a_{TiO_2} during zircon crystallization. The most rigorous attempt at obtaining these constraints is that of Schiller and Finger (2019) who carried out thermodynamic modeling of a range of granitic melt compositions. They concluded that while both SiO_2 and TiO_2 activities are below unity over broad crystallization intervals of these melts, a_{TiO_2} is significantly less than a_{SiO_2} in many

ilmenite-bearing granitoids ($a_{\text{TiO}_2}/a_{\text{SiO}_2} \approx 0.5$). The net effect of these reduced activities is to raise $\mathbf{T}_{\text{Ti-Zircon}}$ on average by ~ 70 °C relative to calculations assuming that both activities are unity. Schiller and Finger (2019) also recommended that median values of $\mathbf{T}_{\text{Ti-Zircon}}$ be reported when multiple Ti analyses are conducted for zircon in a particular sample as this provides a reasonable estimate of the temperature at which the majority of the zircon in the sample crystallized. Following these recommendations, Fig. 18 shows both the median ‘uncorrected’ $\mathbf{T}_{\text{Ti-Zircon}}$ and the median ‘corrected’ $\mathbf{T}_{\text{Ti-Zircon}}$ that is 70 °C higher. Regardless of whether one takes the corrected or uncorrected values, it must be emphasized that $\mathbf{T}_{\text{Ti-Zircon}}$ reflects the temperatures of zircon crystallization, not the temperatures of magma generation or emplacement. Given the general absence of zircon inheritance in the BFGC, it is likely that these

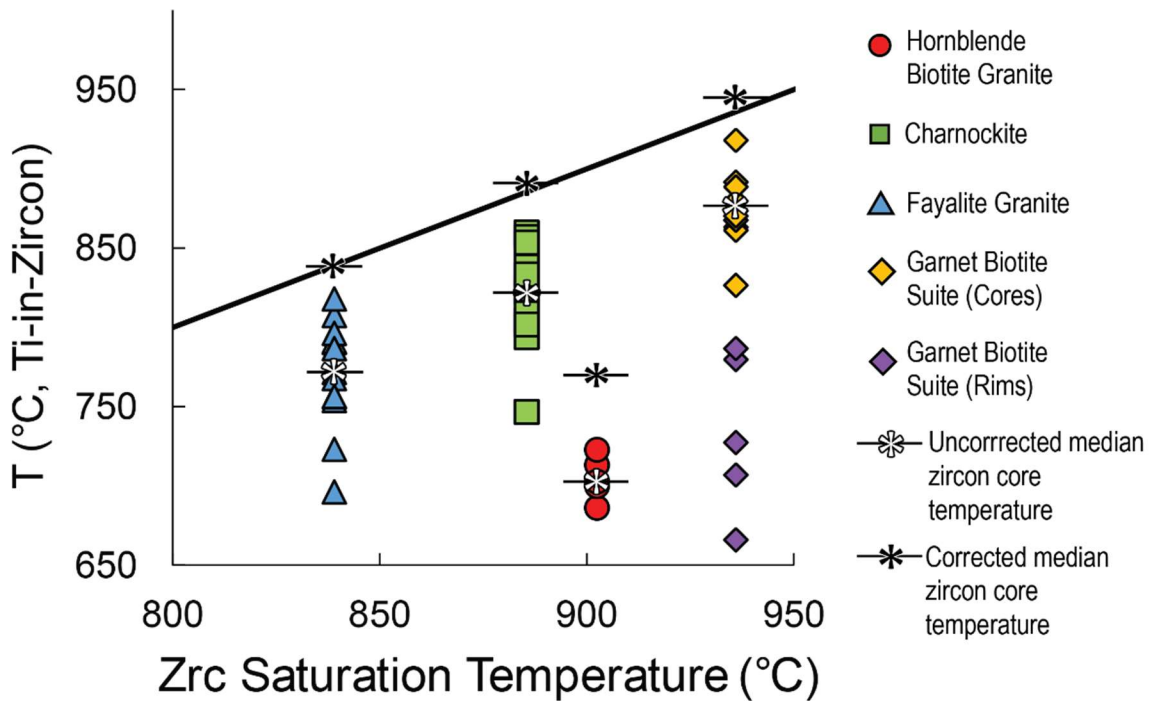


Figure 18: Zircon saturation temperatures compared to ‘uncorrected’ Ti-in-zircon thermometry (Ferry and Watson, 2007) for representative samples from each suite of the Boothia ferroan granitoid complex. Zircon saturation temperatures were calculated with the formulation from Watson and Harrison (1983) using whole-rock Zr content for each granitoid suite. The uncorrected Ti-in-zircon temperatures assume that the activity of both TiO_2 and SiO_2 in the magma was unity during zircon crystallization, which likely was not the case. The modeling of Schiller and Finger (2019) for ‘corrected’ median zircon core temperatures indicates that $a_{\text{TiO}_2}/a_{\text{SiO}_2} = \sim 0.5$ for most granitoids, which corresponds to ~ 70 °C higher temperature than indicated by the uncorrected temperature.

magmas were zircon undersaturated at their source and also when they were initially emplaced; zircon only formed after the magma had cooled and crystallized to some degree at the emplacement site. Thus, $T_{Ti-Zircon}$ represents minimum estimates of the temperatures of magma generation and emplacement. From their thermodynamic modeling, Schiller and Finger (2019) deduced that, in many cases, the peak magma temperature is ~ 30 - $50^{\circ}C$ higher than the median corrected $T_{Ti-Zircon}$.

Sample 17SRB-R075A (hornblende-biotite granite suite) records the lowest ‘uncorrected’ $T_{Ti-Zircon}$, ranging between 686 – $723^{\circ}C$, which corresponds to a corrected median temperature of $772^{\circ}C$. Samples 17SRB-J029A and 17SRB-L052A (fayalite and charnockite suites, respectively) show more variation and higher temperatures, with the corrected median $T_{Ti-Zircon}$ of J029A at $841^{\circ}C$ and of L052A at $892^{\circ}C$. The high charnockite temperature is consistent with the presence of inverted pigeonite within two charnockite samples (large augitic lamellae within an orthopyroxene host), as pigeonite requires temperatures $> 800^{\circ}C$ (Lindsley, 1983; Lindsley and Frost, 1992). Garnet-biotite suite sample 17SRB-J053A1 a marked difference between the core and rim $T_{Ti-Zircon}$ (Fig. 18). The core temperatures are the highest in the complex, with a corrected median of $946^{\circ}C$. The zircon rim uncorrected $T_{Ti-Zircon}$ range between 666 - $787^{\circ}C$ with a corrected median temperature of $797^{\circ}C$. It should be noted that α_{TiO_2} increases at near-solidus and sub-solidus temperatures (Schiller and Finger, 2019) and therefore the uncorrected temperatures may be more applicable to the zircon rims.

Zircon saturation temperatures. Additional temperature information for the BFGC can be obtained through the calculation of zircon saturation temperatures ($T_{ZircSat}$) (Watson and Harrison, 1983), which are derived from the whole-rock major-element composition and Zr content of each sample (Fig. 18). In the best case scenario, where the measured whole-rock composition reflects a true melt composition, $T_{ZircSat}$ would represent the temperature of initial zircon crystallization, which should approximately coincide with the maximum $T_{Ti-Zircon}$ obtained on the same sample. However, granitoid whole-rock compositions generally do not represent true melt compositions (e.g., Clemens and Stevens, 2012; Barnes et al., 2020) but rather magma compositions (melt plus crystals). In such cases, the measured Zr content of the whole-rock may be higher (zircon accumulation) or lower (accumulation of crystals other than zircon) than the Zr content of the part of the sample that represents the melt fraction of the magma. Thus, calculated

T_{ZircSat} in many granitoid samples can be either higher or lower than the temperature at which zircon began to crystallize in that sample. In short, temperatures indicated by the zircon saturation thermometer should not be taken at face value but rather interpreted in conjunction with other estimates of magma temperature available for the sample (Siégel *et al.*, 2018; Barnes *et al.*, 2020).

A further complication in the application of this thermometer is the different experimental calibrations of T_{ZircSat} that are available, which include the original calibration of Watson and Harrison (1983) and later calibrations by Boehnke *et al.* (2013) and Gervasoni *et al.* (2016). The various calibrations yield temperatures that differ by tens of degrees, with the Watson and Harrison (1983) calibration typically recording the highest temperatures. Schiller and Finger (2019) suggest that the original Watson and Harrison calibration is most in line with the results of some other granitic melting experiments and so I have chosen to use that calibration in the present study.

For the BFGC, the Watson and Harrison (1983) calibration yield T_{ZircSat} that range from 827°C - 972°C, with median temperatures of 839°C, 885°C, 903 °C, 937°C for the fayalite granite, charnockite, hornblende-biotite granite, and garnet-biotite suites, respectively. For three of the BFGC granitoid suites, there is a positive correlation between T_{ZircSat} and $T_{\text{Ti-Zircon}}$ (Figure 9). The notable exception is the hornblende-biotite suite, which had the second highest T_{ZircSat} despite having the lowest $T_{\text{Ti-Zircon}}$ among the four suites. The high T_{ZircSat} could reflect the accumulation of zircon in the hornblende-biotite suite samples in which case the high whole-rock Zr content does not reflect that of the melt and T_{ZircSat} is an overestimate of the temperature of zircon crystallization. Alternatively, the discrepancy between T_{ZircSat} and $T_{\text{Ti-Zircon}}$ in the hornblende-biotite suite could be related to a high fluorine content in the melt, which is evidenced by the very high F content of biotite and amphibole in this suite (Table 3) and the presence of post-magmatic fluorite. Fluorine increases the solubility of high-field-strength elements, including Zr, in the melt and thereby lowers the temperature at which zircon will begin to crystallize (Keppler, 1993; Hanchar and Watson, 2003); Accordingly, in these high F magmas, there may be a large difference between the magma emplacement temperature and the temperature marking the onset of zircon crystallization.

It should be noted that even in the three BFGC granitoid suites that show a general correlation between T_{ZircSat} and $T_{\text{Ti-Zircon}}$, the corrected median $T_{\text{Ti-Zircon}}$ is 3-10 °C higher than T_{ZircSat} . The discrepancy between $T_{\text{Ti-Zircon}}$ and T_{ZircSat} in these suites would be even larger if one of the other zircon saturation calibrations was used (see above). In cases where whole-rock granitoid compositions approximate melt compositions, median $T_{\text{Ti-Zircon}}$ should always be lower than

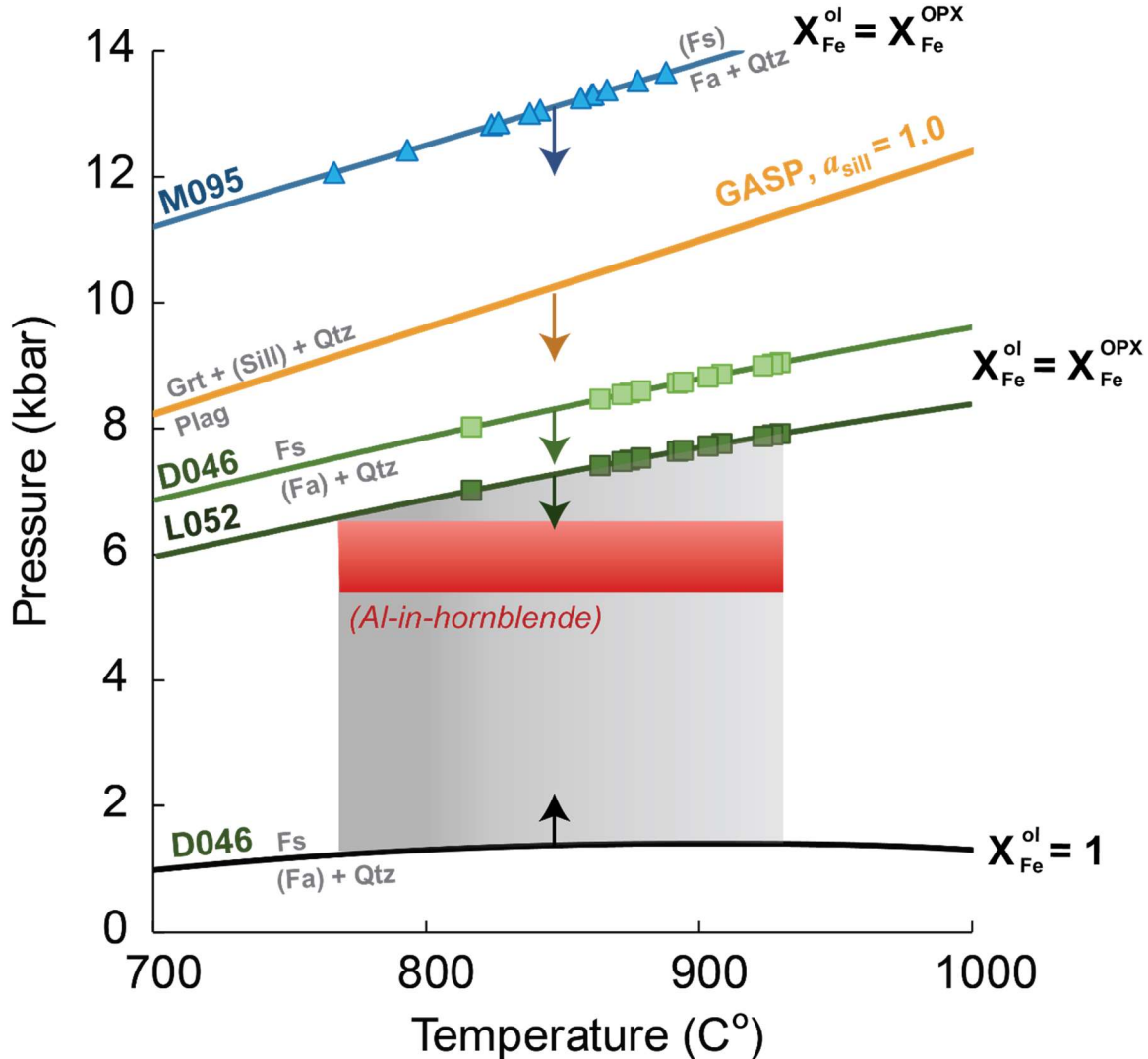


Figure 19: Pressure and temperature constraints of Boothia ferroan granitoid complex emplacement from various barometers. Because of missing phases within the fs-fa-quartz assemblages, the various mineral equilibria only provide upper or lower bounds on the pressure of magma emplacement. Temperature points are corrected $T_{\text{Ti-in-zircon}}$ of select sample in each suite. Minerals in brackets have assumed activities in the fayalite-ferrosilite-quartz reactions. Additional pressure constrains from the Al-in-hornblende barometer are shown in red.

T_{ZircSat} . That the two sets of temperature estimates are reversed for these three suites indicates either that their whole-rock compositions do not represent melt compositions or that the zircons in these samples are of xenocrystic (totally foreign to this granitoid) or antecrustic (crystallized at an earlier stage of magma evolution) origin (Siégel *et al.*, 2018). These possibilities are discussed within the petrogenesis of the garnet-biotite suite.

In summary, the available thermometers indicate that the crystallization temperatures of the BFGC magmas were certainly above 800°C, with $T_{\text{Ti-Zircon}}$ and T_{ZircSat} establishing temperatures of zircon crystallization between 840°C - 940°C for most suites. These crystallization temperature estimates provide a lower bound on the temperatures of BFGC magma generation and emplacement. Critically, the BFGC magmas are far hotter than minimum-melt granites, which form in the 650-750°C temperature range (Brown, 2007)

Pressure of emplacement

Constraining the emplacement pressures of the BFGC is difficult due to the lack of complete mineral assemblages required for the calculation of various geobarometer equilibria relevant to these granitoids. For example, fayalite and ferrosilite do not occur together in any of the suites, as is required for an exact pressure determination using the fayalite-quartz-ferrosilite equilibrium. Similarly, the absence of an aluminosilicate polymorph in the garnet-biotite suite rocks precludes calculation of the exact position of the garnet-aluminosilicate-silica-plagioclase (GASP) equilibrium in pressure-temperature space. Despite these difficulties, the mineral assemblages in these granitoids can still provide either maximum or minimum constraints on the pressure of magma emplacement. A widely-used granitoid geobarometer, the Al-in-hornblende barometer, is also applicable to the BFGC. However, as described further in this section, the accuracy of this barometer in ferroan granitoids has been called into question.

The positions of the fayalite-quartz-ferrosilite and GASP equilibria in P-T space were calculated using the THERMOCALC program and the DS62 thermodynamic dataset (White *et al.*, 2014), with the activities of end members calculated using mineral compositions determined by EPMA and the activity-composition (a-X) program associated with THERMOCALC.

For calculation of the GASP equilibrium, the activity of Al_2SiO_5 in fictive sillimanite was set to unity ($a_{\text{Al}_2\text{SiO}_5} = 1$). Given that no aluminosilicate polymorphs is in fact present in the garnet-

biotite suite rocks, $a_{\text{Al}_2\text{Si}_5\text{O}_8}$ is necessarily < 1 in these rocks. Therefore, assuming $a_{\text{Al}_2\text{Si}_5\text{O}_8} = 1$ only provides an upper pressure bound for the position of the GASP equilibrium (Fig. 10). Over the full temperature range determined from the uncorrected Ti-in-zircon geothermometer, including zircon rims (690°C - 960°C), the maximum pressure of emplacement indicated by the GASP geobarometer is ~8 to 12 kbar, which corresponds to lowermost crustal depths in normal thickness continental crust.

To obtain additional pressure constraints, the ferrosilite-fayalite-quartz geobarometer was utilized in the fayalite and charnockite suite samples. The activity of fictive orthopyroxene in the orthopyroxene-free fayalite granite samples was calculated assuming $X_{\text{Fe}(\text{opx})}$ equals the measured $X_{\text{Fe}(\text{ol})}$. In reality, $X_{\text{Fe}(\text{opx})} < X_{\text{Fe}(\text{ol})}$ when the two minerals co-exist at equilibrium (Bohlen *et al.*, 1980; Frost *et al.*, 1999). As such, the position of the ferrosilite-fayalite-quartz equilibrium shown in Fig. 10 is only an upper bound for the emplacement pressure of fayalite granite sample 17SRB-0M95. An analogous procedure can provide pressure constraints for the olivine-free charnockite samples. Specifically, the activity of fictive olivine in these samples was calculated assuming $X_{\text{Fe}(\text{ol})}$ equals the measured $X_{\text{Fe}(\text{opx})}$ when, in reality, $X_{\text{Fe}(\text{ol})} > X_{\text{Fe}(\text{opx})}$. Thus, the positions of the ferrosilite-fayalite-quartz equilibrium shown in Fig. 7 for charnockite samples 17SRB-D046 and 17SRB-L052 are again upper bounds for the emplacement pressures of these magmas. A lower pressure bound can be obtained for the charnockite samples by assuming the fictive olivine in these samples has a $X_{\text{Fe}(\text{ol})} = 1$.

These calculations of the ferrosilite-fayalite-quartz equilibrium yield maximum pressures between ~11 and 15 kbar for fayalite granite sample 17SRB-M095, which exceed the maximum pressures calculated using the GASP equilibrium for the garnet-biotite suite sample (Fig. 19). The charnockite samples 17SRB-D046A and 17SRB-L052A, however, yield significantly lower maximum pressure constraints from 6.6 – 9.2 kbar and 5.3 – 7.3 kbar, respectively. The lower pressure bound for the charnockite samples is between 0.43 - 1.5 kbar for 17SRB-D046 and < 1 kbar for 17SRB-L052A. Collectively, the tightest constraints in Fig. 19 suggest pressures between ~1.5 and 7 kbar, which corresponds to emplacement of the BFGC at mid- to upper-crustal depths.

Whereas many of the amphibole-bearing rocks of the BFGC have the complete mineral assemblage required for application of the Al-in-hornblende geobarometer (e.g., Mutch *et al.*, 2016), it may not be appropriate to apply this barometer to the BFGC for two reasons: First,

analyses are ideally obtained on amphibole rims in contact with plagioclase for the purposes of amphibole-plagioclase thermometry to determine if the mineral assemblage equilibrated at temperatures near the granite solidus (725 ± 75 °C, Mutch *et al.*, 2016). If the temperature is well above the solidus, the pressures recorded by the Al-in-hornblende barometer could have been established as the magmas were rising from their source region rather than at the crustal level of final magma emplacement. Though no obvious intra-grain compositional zoning was detected in the amphibole of the hornblende-biotite suite at the time of writing, paired analyses from the very rim of amphibole grains and immediately adjacent plagioclase have not been obtained; such analyses would be needed to firmly establish that pressures recorded by the Al-in-hornblende are those of final magma emplacement.

Secondly, existing experimental and empirical calibrations of the Al-in-amphibole barometer were done on amphiboles with $X_{Fe} < 0.65$. As noted by Anderson and Smith (1995), more ferroan amphiboles typically crystallize in low fO_2 melts with little Fe^{3+} , which allows for additional Al^{3+} to substitute in the amphibole. In turn, the high Al content results in spuriously high pressure estimates using prior calibrations of the Al-in-hornblende barometer such as the widely-used calibration of Schmidt (1992). To illustrate the problem, Anderson and Smith (1995) noted that the Nain Plutonic Complex (Emslie and Stirling, 1993), which contains ferroan granitoids broadly similar in composition to the BFGC, yielded Al-in-hornblende pressures of > 6 kbar with the Schmidt (1992) calibration, whereas pressures deduced from metamorphic mineral assemblages in the contact aureole of that complex are significantly lower (3.5–5 kbar; McFarlane *et al.*, 2003 and references cited therein). In this regard, application of the Johnson and Rutherford (1989) and the new Mutch *et al.* (2016) calibration of the Al-in-hornblende barometer to granitoid amphibole compositions reported for the Nain Complex (Emslie and Stirling, 1993) results in an average pressure of 4.0 kbar, which is in good agreement with the metamorphic pressure estimates. This finding suggests that, despite the high X_{Fe} of the BFGC amphiboles, the new calibration of the barometer may yield appropriate pressures for these amphiboles.

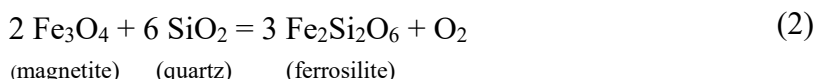
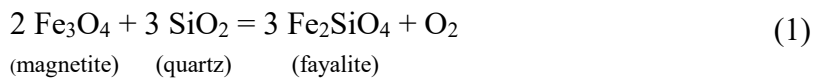
Application of the Mutch *et al.* (2016) calibration of the Al-in-hornblende barometer to the BFGC amphibole compositions listed in Table 5 results in pressures between 5.4 – 6.3 kbar with an average of 5.8 kbar. These pressure estimates are consistent with the upper pressure constraint

indicated by the ferrosilite-fayalite-quartz equilibrium for the charnockite suite (Fig. 19). They are also consistent with pressures derived from ca. 1.84 Ga pelitic mineral assemblages from the Committee Bay Belt (5.1-6.3 kbar), located approximately 200 km south of the BFGC (Berman *et al.*, 2005; Kraft, 2006).

Collectively, the various pressure estimates suggest that the BFGC plutons were emplaced at mid-crustal levels corresponding to depths between ~ 19 – 22 km. This observation has important implications for the thickness of Boothia Peninsula crust at the time of BFGC magmatism. The BFGC plutons were likely the last geological event in the Boothia Peninsula area in which significant magmatic underplating could have occurred, which in turn implies that the thickness of the crust in the area at the time of pluton emplacement would encompass the present-day crustal thickness with an additional overlying ~20 km. If we assume a present-day thickness of 30-40 km, typical of stable continental crust, this signifies the crust of Boothia Peninsula was overthickened to 50-60 km at 1.83 Ga.

Oxygen Fugacity

Oxygen fugacity is an important parameter in identifying the nature of the magma source rocks and the conditions of magma generation for ferroan-type granitoids (Frost and Frost, 2011). Using the mineral assemblage fayalite/ferrosilite-quartz-magnetite present in the fayalite and charnockite suite samples, the following reactions can be used to determine oxygen fugacity:



Calculations were done using THERMOCALC software and the DS62 dataset (White *et al.*, 2014) and an assumed pressure of 5 kbar. Activities were derived from an on-sites mixing model using the measured X_{Fe} of each mineral. Reintegrated titanomagnetite compositions were used where possible. The calculated $f\text{O}_2$ of three samples (17SRB-L052A, 17SRB-M095, 17SRB-D046) are reported as $\Delta \log f\text{O}_2$, which are positive or negative log unit deviations from the fayalite-magnetite-quartz (FMQ) buffer (Fig. 20). Also shown for reference in Fig. 20 are the positions of the Ni-NiO and ferrosilite-magnetite-quartz (fsMQ) buffers. The calculated $\Delta \log f\text{O}_2$

values of samples 17SRB-M095 (fayalite granite) and 17SRB-D046 (cpx-charnockite), both of which have exsolved titanomagnetite grains whose original composition could be reintegrated, are -1.64 and -1.41, respectively. In contrast to these strongly reduced values, charnockite sample 17SRB-L052A records a significantly higher $\Delta \log fO_2$ value of +0.43. Notably, this sample, unlike the other two, contains no exsolved grains of titanomagnetite suitable for compositional reintegration. It is possible that this charnockite formed at much more oxidizing conditions than the other samples. However, an alternative and more likely explanation is that the magnetite in this rock underwent post-magmatic, Fe-Ti exchange with the abundant ilmenite in the sample. The occurrence of such a re-equilibration process is evidenced by the very low temperature ($T < 400^\circ\text{C}$) indicated by the two-oxide geothermometer (Ghiorso and Sack, 1991) for the ilmenite and magnetite compositions measured for this sample. Because ilmenite is much more abundant than magnetite in the sample, its composition did not change greatly during retrograde Fe-Ti exchange. In contrast, the re-equilibration process caused magnetite to become significantly

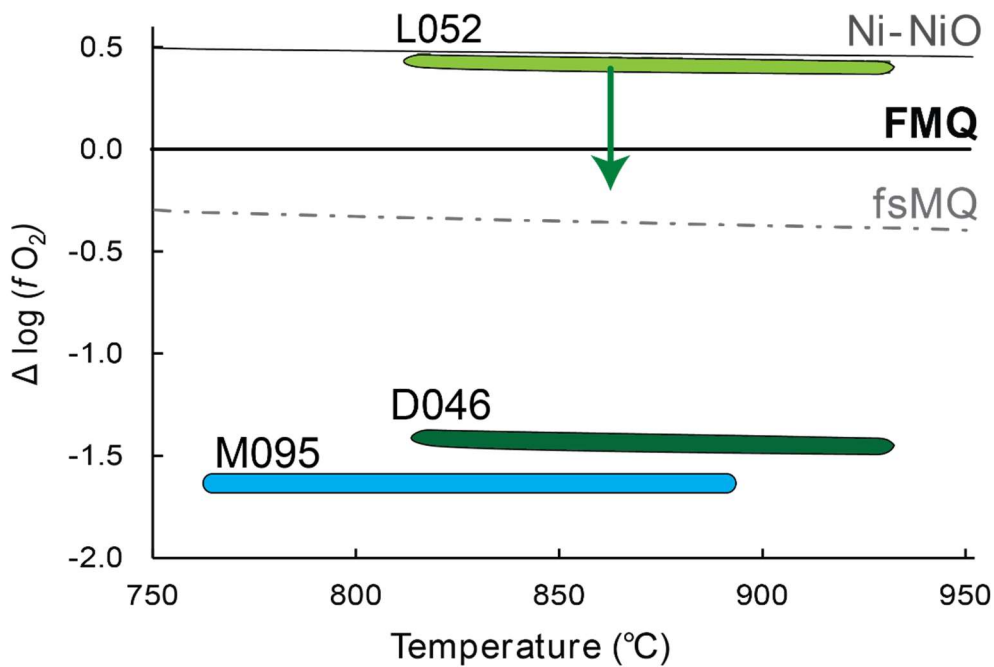


Figure 20: Oxygen fugacity relative to the fayalite-magnetite-quartz (FMQ) buffer of representative samples of the fayalite granite (blue, M095) and charnockite (green, D046 and L052) suites. Other oxygen buffer reactions included as comparison are ferrosilite-magnetite-quartz (fsMQ) and Ni-NiO. Temperature ranges given by the corrected $T_{\text{Ti-in-zircon}}$. Arrow indicates L052 is considered an upper bound on oxygen fugacity (see text for discussion).

depleted in ulvöspinel component relative to its original igneous composition. Given the effects of the low-temperature re-equilibration on magnetite composition, the calculated $\Delta \log fO_2$ value for sample 17SRB-L052A must be regarded as an upper bound of its fO_2 at magmatic conditions.

Petrogenesis of the Boothia Ferroan Granite Complex

Frost and Frost (1997; 2011) suggest three models for the origin of ferroan granites: 1) partial melting of quartzofeldspathic crustal rocks; 2) extensive fractional crystallization of tholeiitic magmas or partial melting of recently underplated tholeiitic magmas; and 3) a combination of (1) and (2), where mantle-derived mafic melts incorporate a significant amount of crustal material. Given the strongly negative initial ϵ_{Hf} and ϵ_{Nd} values of the BFGC, we can eliminate the possibility that these granites formed solely by model (2) as tholeiitic magmas recently derived from depleted or chondritic mantle would have produced granitoids with epsilon values greater than or equal to zero (e.g., Bouvier *et al.*, 2008). Additionally, ferroan granites that are fractional crystallization or partial melting products of tholeiitic magmas have exclusively metaluminous compositions (Frost and Frost, 2011) whereas the BFGC includes both metaluminous and weakly to moderately peraluminous granitoids. Below, I consider potential source rocks for the BFGC granitoids and the ability of these source rocks to explain both the isotopic and chemical composition of the granitoids.

Source rock characteristics

It is important to note that the different granitoid suites of the BFGC have small but significant differences in their Nd and Hf isotope compositions (Fig. 5.6). Thus, these suites cannot simply be related to each other by magmatic differentiation processes but must have been derived from different source rocks or have assimilated different rocks during magma ascent or emplacement. In considering potential crustal sources for the BFGC, the Sm-Nd and/or Lu-Hf isotope compositions of the dominant basement rocks in the area were determined as part of the Boothia Peninsula-Somerset Project (Appendix 4). These basement rocks (Fig. 2) include the ca. 2.52–2.56 Ga Boothia Neoarchean porphyroclastic granitoids (BNPG, lilac unit), 2.51 Ga biotite tonalite-trondhjemite-gneiss (TTG, pink unit), 2.47 Ga garnet leucogranite derived from granulite-grade metapelite (brown unit), and 2.48 Ga Boothia mafic to intermediate rocks (blue units, map). The BNPG is an orthopyroxene-garnet-biotite granodiorite to monzogranite, with 1–10 cm alkali-feldspar porphyroclasts. The 2.48 Boothia mafic-intermediate rocks encompass

gabbro, quartz diorites, and gabbroic anorthosites, although the most common lithologies are biotite-hornblende-clinopyroxene quartz diorite ($n = 4$) and gabbroic anorthosite ($n = 2$). These rocks have intermediate silica contents (53 - 65 wt. %), are dominantly metaluminous, and have compositions that straddle compositions the ferroan-magnesian boundary in the Frost *et al.* (2001) discrimination diagram (Fig 3a,c).

Epsilon Nd values of the Boothia basement rocks at the time of BFGC magmatism (~ 1.83 Ga) were calculated by extrapolating their present-day whole-rock Nd isotope compositions back to 1.83 Ga along evolution trajectories given by the rocks' $^{147}\text{Sm}/^{144}\text{Nd}$ ratios (Fig. 15). The $\epsilon\text{Hf}_{1.83\text{Ga}}$ values of the BNPG basement rocks were calculated by combining their initial ϵHf values ($\epsilon\text{Hf}_{2.55\text{Ga}}$), which were determined by isotopic analysis of zircon, with their whole-rock $^{176}\text{Lu}/^{177}\text{Hf}$ to project forward in time to the Hf isotope composition these rocks would have had at the time of BFGC magma generation. This approach results in calculated $\epsilon\text{Nd}_{1.83\text{Ga}}$ values of -8.6 to -8.1 and $\epsilon\text{Hf}_{1.83\text{Ga}}$ values of -11.5 to -10.8 for the BNPG. The Nd isotopic compositions of the 2.48 Ga mafic-intermediate rocks span a broader range than the BNPG, with $\epsilon\text{Nd}_{1.83\text{Ga}}$ values between -5.8 and -7.8. The $\epsilon\text{Nd}_{1.83\text{Ga}}$ values of the 2.51 Ga TTG (-8.1) and 2.47 Ga leucogranite (-7.3) are bracketed between the BNPG and 2.48 Ga Boothia mafic-intermediate rocks. As such, the likely Nd isotope composition of magma derived by partial melting of Boothia basement would have $\epsilon\text{Nd}_{1.83\text{Ga}}$ values between -5.8 and -8.6 (Fig. 15).

Unfortunately, no Hf isotope data are currently available for the Boothia basement mafic-intermediate rocks, the 2.51 Ga TTG or the 2.47 Ga leucogranite. However, (Vervoort *et al.*, 1999) showed that there is a strong positive correlation between ϵNd and ϵHf values in terrestrial samples, which define a so-called terrestrial array, A linear equation fit to this array ($\epsilon\text{Hf} = 1.36 * \epsilon\text{Nd} + 2.95$) can be used to infer the ϵHf values of samples for which ϵNd values are known. With this approach, the $\epsilon\text{Nd}_{1.83\text{Ga}}$ values of the Boothia basement rocks for which there are presently no measured Hf isotope data translate to $\epsilon\text{Hf}_{1.83\text{Ga}}$ values of ~ -5 to -8. It must be emphasized that these calculated $\epsilon\text{Hf}_{1.83\text{Ga}}$ values are only serve as a crude approximation until zircons from these basement rocks can be analyzed for their Hf isotope composition.

Petrogenesis of the Fayalite, Charnockite and Hornblende-Biotite Suites

The Nd and Hf isotope compositions of the BNPG at 1.83 Ga fit well with those of the charnockite suite granitoids, which have the most negative ϵ_{Nd} and ϵ_{Hf} values in the BFGC. However, partial melting of solely BNPG rocks cannot adequately account for the less negative $\epsilon_{\text{Nd}_{1.83\text{Ga}}}$ and $\epsilon_{\text{Hf}_{1.83\text{Ga}}}$ of the other BFGC suites. Thus, the BFGC magmas must have been derived from at least two distinct source rocks. In this regard, magmas derived from a combination of BNPG and Boothia basement mafic-intermediate source rocks can explain the full spectrum of Nd isotope compositions observed in the BFGC (Fig. 15). The Hf isotope constraints are less clear because of the absence of directly measured Hf isotope data for some of the basement rocks but, on the basis of the calculated $\epsilon_{\text{Hf}_{1.83\text{Ga}}}$ values (see above), mixtures of these two basement source rocks could also account for the full range of Hf isotope compositions observed in the BFGC granitoids.

In addition to accounting for their Nd and Hf isotope compositions, the geochemical composition of these two putative Boothia basement source rocks are also broadly consistent with the major-element compositions of the fayalite, charnockite and hornblende-biotite suite granitoids of the BFGC. As detailed in a subsequent section, the garnet-biotite suite granitoids require an additional source rock to account for their more peraluminous composition. Dehydration melting experiments have shown that melts produced from both quartzofeldspathic and mafic source rocks are typically more ferroan (higher Fe/Mg) than their source rocks (e.g., Skjerlie and Johnston, 1993; Rapp *et al.*, 2003). Given that the Boothia mafic-intermediate basement rocks straddle the ferroan-magnesian boundary and the BNPG are just on the magnesian side of that boundary (Fig. 3c), it is reasonable to conclude that the magmas derived by partial melting of these source rocks are likely to be ferroan (see also Frost and Frost, 2011). Additionally, because the BNPG is peraluminous and the basement mafic-intermediate rocks are dominantly metaluminous, magmas derived from varying proportions of these two source rocks are likely to include both metaluminous and peraluminous varieties, as is the case with the BFGC granitoids.

The Nd and Hf isotope and major-element compositions of the hornblende-biotite suite granitoids, like the charnockite and fayalite suite granitoids, can in general terms be attributed to melting of the Boothia basement rocks. However, it is unclear whether these two source rocks can, by themselves, also account for the very high concentration of LREE and other incompatible

trace elements found in this granite suite (Fig. 9). For example, the La concentration of the average hornblende-biotite suite granitoid is ~ 1400 times chondrite whereas the BNPG and mafic-intermediate basement rocks only average ~ 200-250 times chondrite. A batch melting model (Allègre and Minster, 1978) was used to determine a hypothetical concentration of La within a partial melt derived from mixed Boothia basement rocks. Even with conservative estimates for La mineral-melt partition coefficients (K_D) for minerals in the melt residue (Nash and Crecraft, 1985; Rollinson, 1993) and a very low melt fraction ($F = 0.05$), the La concentrations within a melt derived from mixed Boothia basement material would only be ~ 800 – 900 times chondrite. Additionally, it is unlikely that such a low melt fraction (0.05) could produce the volume of melt within the hornblende-biotite suite, which is the most regionally extensive suite within the BFGC. Therefore the high La contents of the hornblende-biotite granite suite cannot simply be attributed to melting of known Boothia basement rocks.

One possible explanation for the strong incompatible-element enriched nature of the hornblende-biotite suite whole-rock composition is that it reflects an accumulation of incompatible-element enriched accessory minerals rather than an actual enrichment of these elements in the melt phase. However, the zircons in this suite are enriched in LREE (Fig. 13), as well as Yb, Nb, and Ta (Fig. 14). This enrichment suggests the zircons crystallized from a highly incompatible-element enriched magma. If that is correct, it is not immediately apparent if the source rocks responsible for generating the BFGC magmas are solely confined to the Boothia basement rocks outcropping at the present erosional level. Some additional incompatible-element enriched source rock(s), present at deeper crustal levels, are required to explain the trace-element composition of the hornblende-biotite suite. Importantly, this cryptic additional source rock needs to have Nd and Hf isotope compositions broadly comparable to those of the exposed Boothia basement rocks in order to account for the overall similarity in isotopic compositions between those basement rocks and the hornblende-biotite suite.

Petrogenesis of the Garnet-Biotite Suite

The granitoids of the garnet-biotite suite differ from the other granitoids of the BFGC, not only in the presence of garnet but also in their field relationships and major-element compositions. In particular, the garnet-biotite suite has a greater frequency of country-rock xenoliths, some of which show evidence of migmatization (Fig. 1g-k). This suite is also exclusively peraluminous

whereas the other suites of the BFGC include both metaluminous and peraluminous varieties. The garnet-biotite suite granitoids have some connection to the hornblende-biotite suite; these two suites are spatially associated (Fig. 2), are contemporaneous based on the monazite U-Pb age of 1826.1 ± 5.1 Ma, and have similar, strongly enriched trace-element patterns (Fig. 4). Given these similarities, I propose that the petrogenesis of the garnet-biotite suite magma reflects assimilation of semi-pelitic country rock (Fig. 2) or incorporation of partial melts derived from these country rocks by the hornblende-biotite suite magma. This hypothesis can account for the more peraluminous composition of the garnet-biotite suite as well as the similar trace-element characteristics of the two suites.

There are some complications associated with this assimilation model. Zircon trace-element geochemical discrimination diagrams indicate the zircons of the garnet-biotite suite crystallized from the least evolved melt of the BFGC, which is at odds with the strongly incompatible-element enriched whole-rock compositions of this suite (cf. Figs. 4 and 8). There are a limited number of scenarios to account for these seemingly contradictory observations. The zircons within the garnet-biotite suite could be xenocrystic, formed in an older, unrelated rock, which was then incorporated into the garnet-biotite suite magma, as evidenced by the scattered $^{207}\text{Pb}/^{206}\text{Pb}$ ages recorded by zircon. However, many of these ages are still broadly comparable to those of the rest of the BFGC granitoids, which requires that the U-Pb isotope systematics of these putative xenocrystic zircons must have been extensively reset at the time of magma emplacement or are not unequivocally derived from a totally foreign rock. Secondly, the less HREE-enriched nature of the zircon cores of the garnet-biotite suite relative to zircons found in the other BFGC suites (Fig. 7) is consistent with these zircons having crystallized in equilibrium with garnet, which in turn suggests that the zircons do have some connection to their host rock.

An alternative explanation for the discrepancy in incompatible-element concentrations between the zircon and the whole-rock is that the rock compositions of the garnet-biotite suite may represent those of a cumulate rather than a melt. The zircons in this scenario would be antecrustic, defined as crystallizing during an earlier phase of magma evolution, prior to the suite achieving its present whole-rock composition either by crystal accumulation or further magma differentiation. If the zircons crystallized in an early stage of magma differentiation, the zircons cores would still retain their less fractionated Th/U and low Hf contents (Kirkland *et al.*, 2015;

Siégel *et al.*, 2018). The antecrustic nature of the zircons is also consistent with the temperatures indicated by the two zircon thermometers, as corrected Ti-in-zircon temperatures are somewhat higher than the zircon saturation temperatures (Siégel *et al.*, 2018). Although antecrustic origin for the zircons is preferred for the garnet-biotite suite on the basis of their trace-element composition, neither model can at present be ruled out.

Another apparent problem with the assimilation model for the origin of the garnet-biotite suite magma is the large difference in $T_{Ti-Zircon}$ between the garnet-biotite and hornblende-biotite suite zircons, with the latter recording much lower temperature. As noted previously, the low $T_{Ti-Zircon}$ of hornblende-biotite suite zircons can be attributed to the high F content of these magmas, which may have delayed zircon crystallization. In contrast, if the initial phase of garnet-biotite suite magma generation involved partial melting of semi-pelitic rocks, these melts may have been lower in F and higher in SiO_2 and Al_2O_3 than the hornblende-biotite suite magma and thereby reached zircon saturation at higher temperatures.

Heat Trigger and Mantle Input

-There are two scenarios that would provide the heat required to trigger partial melting within continental collisional settings: 1) radiogenic heat production as a result of crustal thickening (England and Thompson, 1984; Patino-Douce *et al.*, 1990) and 2) introduction of mantle heat from underplating or upwelling of mafic magmas (Brown, 2007).

As previously discussed, the BFGC represents high-temperature, reduced magmas emplaced within an overthickened crust. Indeed, if the BFGC were generated at the lower crustal levels of a 50-60 km crust, then crustal thickening and associated radioactive heating could contribute a significant portion of the heat required for partial melting. In Boothia Peninsula, crustal thickening may have occurred during the ~ 1.93 Ga Thelon orogeny (Sanborn-Barrie and Regis, 2020) and/or as a far-field effect of collision during the ~1.9-1.8 Ga Trans-Hudson orogeny. However, relying solely on crustal thickening to generate the thermal conditions required to explain the high-temperature BFGC magmas is problematic. Numerical modeling of the thermal effects of crustal thickening indicates that temperatures as high as 900°C are only achieved at the very base of 55 km-thick crust (Patino-Douce *et al.*, 1990). At these depths, partial melting would occur under eclogite-facies conditions, leaving large amounts of garnet in the melt residue

(e.g., Nair and Chacko, 2008). The resulting melts would be severely HREE depleted ($\text{Yb}_N < 5$), which is inconsistent with the only moderate degrees of HREE depletion present in the BFGC granitoids ($\text{Yb}_N > 20$). These observations suggest that BFGC magma generation occurred at shallower levels in this thickened crust and in turn that crustal thickening cannot be the sole means of heat generation; additional mantle heating is required.

Although there seems to be a need for mantle heat to generate the BFGC magmas, that does not necessarily translate into the direct input of mantle-derived material to those magmas. In this regard, there is a notable absence at the current exposure level of mafic-felsic magma-mingling textures or coeval mafic dykes associated with the BFGC. Thus, if there was an influx of mantle-derived mafic magmas that partially melted or assimilated Boothia basement rocks, those processes must have occurred at deeper crustal levels. One argument in favour of a mantle contribution to some of the BFGC magmas is the extreme enrichment in LREE in the hornblende-biotite suite granitoids noted previously, which seem to require contributions from an additional source rock or magma with greater incompatible-element enrichment than characterizes the exposed Boothia basement rocks. One potential source rock/magma with these characteristics is the ca. 1.83 Ga ultrapotassic mafic and intermediate rocks (e.g., minettes, spessartites, monzodiorites, monzonites, syenites) that have been documented over broad swaths of both the Rae and Hearne cratons (Peterson *et al.*, 1994; 2002; Cousens *et al.*, 2001; Sandeman and Hadlari, 2010). Notably, some of these rocks show strong LREE enrichment. In addition, their initial ε_{Nd} values, which range from ~ -6 to -11 but are commonly between -7 and -9 , show nearly complete overlap with the ε_{Nd} values reported here for the BFGC. It should be noted that the more primitive endmembers of this alkali-rich magma suite are quite magnesian and thus not suitable as a major contributor to the ferroan BFGC magmas. However, more evolved versions of these magmas are less magnesian and therefore plausible contributors. These contributions could come directly through mixing of these enriched mantle-derived magmas with melts of the basement rocks or, as suggested by Frost and Frost (1997) for other ferroan granitoids, earlier-formed mafic magma underplates could be partially melted by later intrusions to generate more ferroan felsic magmas that could interact with the overlying crust.

Whereas these ca. 1.83 Ga ultrapotassic mafic magmas are widespread further south in the Rae and Hearne cratons, it is not clear if they extend as far north as the Boothia Peninsula. If they do,

the challenge will be to find additional geochemical or isotopic tracers that will enable magmas derived solely from Boothia basement rocks to be distinguished from those that have received contributions from these enriched mantle-derived magmas with crust-like Nd isotope signatures. One potentially diagnostic tracer is the Rb-Sr isotope system; the available data for the least-altered ultrapotassic rocks of the Churchill Province indicate initial $^{87}\text{Sr}/^{86}\text{Sr}$ (at 1.83 Ga) mostly between ~ 0.705 and 0.706 (Peterson *et al.*, 1994; Cousens *et al.*, 2001) whereas the Boothia basement rocks are predicted to have supported a much wider range of $^{87}\text{Sr}/^{86}\text{Sr}$ at 1.83 Ga because of the low and high Rb/Sr of the Boothia basement mafic rocks and BNPG, respectively.

Location of magmatism

It is unclear if the BFGC magmas exploited a pre-existing zone of weakness within the crust to facilitate their emplacement as there are limited field data available immediately south of the southeast pluton. An indication that there may be a geological boundary present is the 2596 ± 47 Ma zircon age that has been obtained for the migmatite xenolith within the hornblende-biotite granite suite records. Granitoid ages of ~ 2.6 Ga are common within the Rae craton (Hinchey *et al.*, 2011) but notably absent from Boothia Peninsula (Regis, unpublished data, Sanborn-Barrie and Regis, 2020). However, the migmatite xenolith and BNPG have identical whole-rock compositions. In addition, the large error in the migmatite U-Pb age overlaps the 2.56 Ga age range of the felsic basement material of Boothia Peninsula, therefore the migmatite and basement rocks from Boothia Peninsula cannot be confidently distinguished. More detailed work would be needed to determine if such a terrane boundary as associated deformation zone exists immediately to the south of the BFGC plutons and served as a conduit for the BFGC magmas.

The NE-SW distribution and sense of elongation of the BFGC plutons broadly coincides with the orientation of the Sanagak Lake shear zone (SLsz), a strike-slip structure that defines the fabric across a ~ 40 km zone of deformation centred at the SLsz core (Fig. 2). Crystallization of metamorphic titanite within the dominant high-strain fabric indicates that the initial stages of shearing occurred at ca. 1805 Ma (Drayson *et al.*, in prep.). In addition, there is no evidence that the shear zone developed along a pre-existing structure (Drayson *et al.*, in prep.). Thus, BFGC pluton emplacement preceded shearing, which is consistent with the observation that some of the granitoids display a weak fabric whose orientation broadly coincides with that of the shear fabric in the SLsz. The rims of garnet-biotite suite zircons and monazite may document temperatures

within the BFGC at the time of shearing; These rims record an age (1803.2 ± 7.7 Ma) correlative of suspected movement of the shear zone and titanium-in-zircon temperatures near 700°C , coincident with temperature estimates of within-fabric titanite growth in the SLSz (Drayson *et al.*, *in prep.*). Despite the high temperatures of the BFGC plutons at the time, the strain was localized north of the BFGC (Drayson *et al.*, *in prep.*). The low degree of strain reflected in the BFGC plutons relative to their country rocks could be due to competency differences between lithologies, which localized strain in rheologically weaker rocks north of the plutons.

Since intrusion of the BFGC granitoids preceded shearing in the SLSz, this particular shear zone could not have served as the mechanism of magma emplacement. However, it remains unclear if other shear zones more proximal to the BFGC may have facilitated magma transport. In this regard, it is interesting to note that the northwest coastline of the Gulf of Boothia, which forms part of the southern boundary of the southeast pluton of the BFGC, is a pronounced linear feature that runs approximately parallel to the elongation of the pluton and to the orientation of the SLSz (Fig. 2). Thus, a deformation zone may lie submerged in the Gulf of Boothia and also buried by Phanerozoic rocks and sediment farther to the southwest. Unfortunately, there are limited field data and samples from the southern margin of the BFGC to evaluate this possibility. Although the exact relationship between the SLSz and other shear zones and the BFGC are still unclear, many ca. 1.83 Ga post-tectonic plutons show similar associations with large-scale shear zones across the Churchill Province (e.g. Wager Bay shear zone, Therriault *et al.*, 2018; Amer shear zone, Sanborn-Barrie *et al.* 2014).

Tectonic Models

The tectonic mechanisms for generating late- to post-collisional magmas in orogenic belts has long been debated within the scientific community (Brown, 2007), with numerous tectonic models developed to explain the underlying causes of this magmatism. The Churchill Province has abundant plutonic and volcanic rocks associated with the latter stages (ca. 1.85-1.81 Ga) of the Trans-Hudson orogen (Peterson *et al.*, 2002; Corrigan *et al.*, 2009), and also post-dating the orogen (1.77-1.73 Ga; Peterson *et al.*, 2002; 2015b). Of these igneous suites, the BFGC is the most distal to the Trans-Hudson orogenic front. Indeed, the BFGC is located > 250 km north of where Corrigan *et al.* (2009) placed the northernmost limit of Trans-Hudson tectonothermal overprinting. Although there are similarities between the BFGC and other late Trans-Hudson

magmatic suites and the tectonic mechanisms proposed for their petrogenesis, it is crucial to note the BFGC also shows some unique characteristics relative to the other suites that should be considered prior to determining if these suites had similar origins. A full comparison between the BFGC and other late- to post-collisional magmatic rocks in the Churchill Province can be found in Appendix 7.

In the case of the BFGC, any successful petrogenetic model must be able to account for the following features: 1) the generation of high-temperature, reduced, relatively H₂O-poor, ferroan granitoid magmas with strongly negative initial ϵ_{Nd} and ϵ_{Hf} values, 2) the emplacement of these magmas at mid-crustal levels in overthickened (50-60 km) crust, 3) the spatial and possible genetic association of the magmas with shear zones, and 4) emplacement ages that correspond to the late-accretion/terminal-collision phases of the Trans-Hudson orogen. Here, I will evaluate two mechanisms that can generate increased heat flux into continental crust during continental collision (Magni *et al.*, 2013): slab failure (also referred to as slab break-off), and lithospheric delamination.

Slab Failure

Slab failure is a mechanism whereby the leading edge of the dense subducting oceanic slab detaches from the remaining oceanic lithosphere, typically in the terminal collision phase of an orogeny (e.g. Peninsular Ranges Batholith, Hildebrand and Whalen, 2014). In the case of shallow slab break-off, as the slab tears and descends into the mantle, melts from the underlying asthenosphere rise and interact with the mantle lithosphere of the over-riding plate (Davies and von Blanckenburg, 1995). Slab failure deeper within the asthenosphere is proposed to trigger dehydration melting of the oceanic crust portion of the detached slab (Hildebrand and Whalen, 2014; Freeburn *et al.*, 2017). These felsic melts then rise and interact with the lithosphere of the over-riding plate.

Slab failure is commonly invoked to explain the influx of mantle heat to the crust in the terminal phases of collisional orogens (Davies and von Blanckenburg, 1995; Whalen and Hildebrand, 2019). Given that a heating mechanism in addition to intra-crustal radioactive heating appears to be required to explain the high temperature of BFGC granitoids, the slab failure model is worth examining in the context of the BFGC. In particular, this mechanism provides a means to rapidly

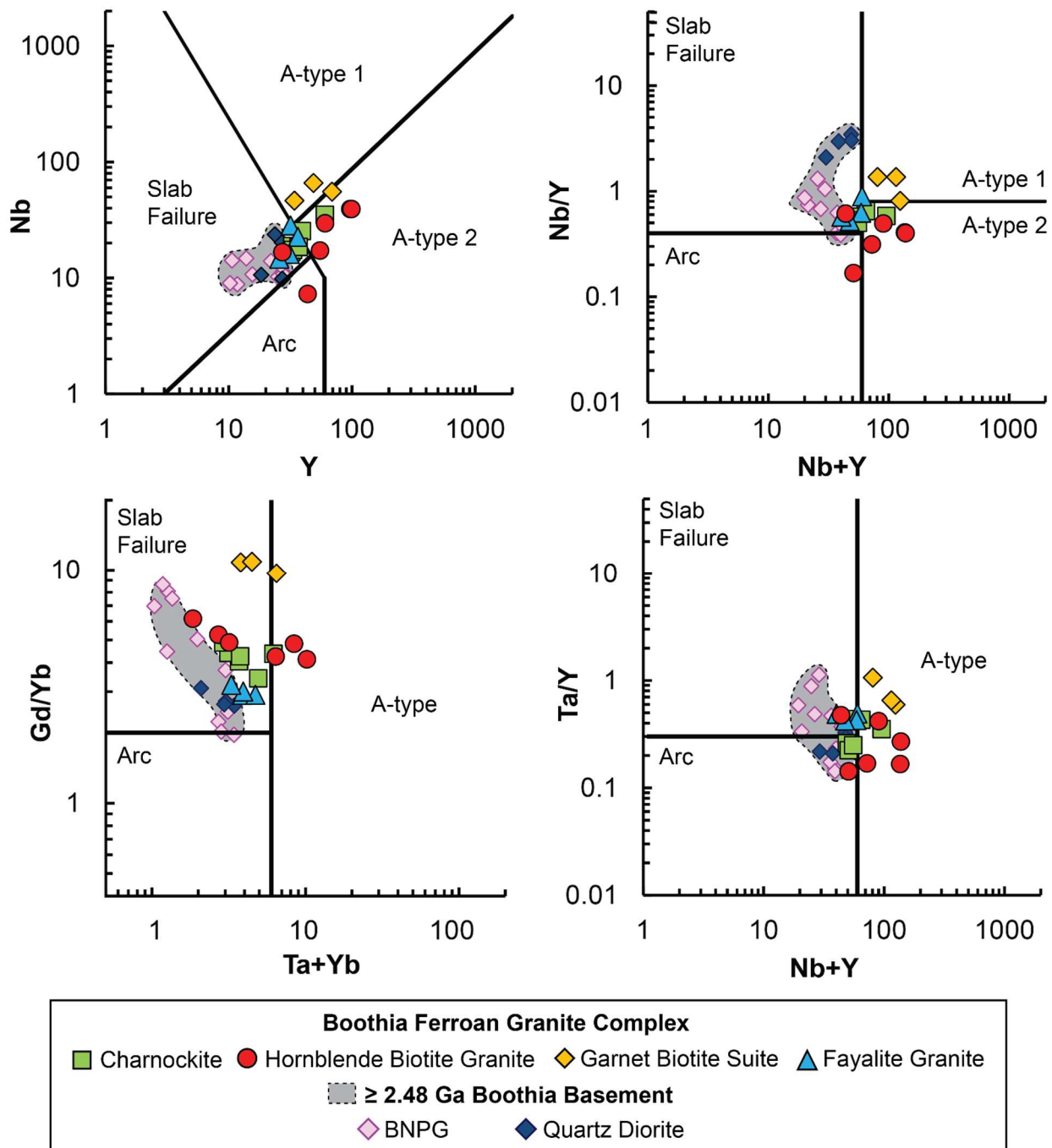


Figure 21: Select trace-element discrimination diagrams for slab-failure, arc, and anorogenic (a-type) granites after Whalen and Hildebrand (2019). Note the ambiguity of where the Boothia ferroan granite complex samples plot between each diagram, and the close association of the dominant source rocks (shaded region) and the fayalite granite and charnockite suites.

advect mantle heat, likely in the form of mantle-derived magmas, to the crust and thereby trigger or enhance partial melting of crust during collisional orogenesis. Additionally, because these mantle magmas will tend to focus and ascend along zones of structural weakness, this tectonic model may also be able to explain the occurrence of the BFGC plutons along a broadly linear belt.

Select modified trace-element discrimination diagrams developed to distinguish so-called slab-failure granitoids from “A-type” and arc granitoids (Whalen and Hildebrand, 2019) were used to establish the feasibility of the slab-failure mechanism for generation of the BFGC magmas (Fig. 21). The tectonic setting of the BFGC is ambiguous in these discrimination diagrams. The hornblende-biotite granite suite and garnet-biotite suite granitoids mostly plot in the A-type fields whereas the charnockite and fayalite suite granitoids straddle the boundary between the slab failure and A-type fields on many diagrams. Notably, the fayalite and charnockite suite granitoids partially overlap with the composition of the Boothia basement rocks, which plot entirely within the slab-failure field. This implies that these individual trace-element abundances of the BFGC granitoids are partly or largely controlled by the source rocks (Pearce, 1996). Thus, while the Boothia basement rocks may have formed in a slab-failure tectonic setting given their relatively juvenile isotopic compositions, the discrimination diagrams do not necessarily demonstrate that the BFGC magmas formed in that setting at 1.83 Ga.

A slab-failure mechanism for formation of the BFGC implies the presence of a subducted slab at depth underneath Boothia Peninsula lithosphere. Commonly, slab failure magmatism occurs close to the collisional plate boundary, proximal to the previous arc magmatism. The BFGC plutons are not situated on any type of ca. 1.83 Ga collisional boundary, nor associated with younger (typically 10-40 My prior) arc magmatism. Though it is possible for subducting slabs to travel 100s or 1000s of km beyond the plate boundary should the subduction angle be shallow enough, magmatism associated with slab failure would be expected to show temporal changes within the hinterland (Li and Li, 2007). As the BFGC and late-accretion magmatism (i.e. Hudson granite) are broadly contemporaneous, a far-travelled flat slab from the Trans-Hudson orogen is unlikely. In addition, geodynamic modelling suggests that slab-failure, particularly at deeper levels in the mantle, does not trigger significant melting within the lithospheric mantle, which is crucial to the petrogenesis of many of the Trans-Hudson late- to post-collisional magmas

(Cousens *et al.*, 2001; Peterson *et al.*, 2002, 2015b). Despite the late- to post-collisional timing of the BFGC, the trace-element discrimination plots, the distal location of the Boothia Peninsula relative to the plate margin, and the contemporaneous relationship with Hudson granite late-accretion magmatism do not support a slab-failure model for BFGC magmatism.

Partial Lithospheric Delamination

Lithospheric delamination is a process that removes subcontinental lithospheric mantle (SCLM), either in its entirety or the lowermost portions, and brings hot asthenosphere closer to the thickened crust and thereby induces melting in the remaining SCLM and/or the overlying crust (Bird, 1979). The most common mechanism proposed to remove part or all of the SCLM within collisional orogens is delamination of thickened continental crust that has become eclogitized at its base causing it and the underlying SCLM to sink into the asthenosphere (Kay and Kay, 1991). Delamination is interpreted as the dominant mechanism in asthenosphere upwelling and associated decompression melting, triggering post-orogenic magmatism and orogenic collapse (Dewey, 1988). In a complete lithospheric delamination scenario, upwelling mantle will typically lead to bimodal magmatism; however, the amount of melt generated depends on how much SCLM is lost. Partial lithospheric delamination can introduce mantle heat with advecting mantle material upwelling no further than the base of the crust (Kay and Mahlburg Kay, 1993). For the BFGC, this is crucial, as mafic material would remain at the base or lowermost crust which may explain the lack of mafic material at the emplacement level of the BFGC.

Lithospheric delamination or stretching and associated SCLM reworking is proposed to have taken place within the Churchill Province during and after Trans-Hudson collision (Cousens *et al.*, 2001). Mantle upwelling following delamination potentially provided heat for generation of 1.83 Ga minette magmas from the SCLM and coeval crustal-derived Hudson granites (Cousens *et al.*, 2001; Peterson *et al.*, 2002; van Breemen *et al.*, 2005). As noted previously, these ultrapotassic mafic magmas have strongly negative initial ϵ_{Nd} values that overlap those of the Hudson granites (-6 and -11). Cousens et al. (2001) proposed that these ultrapotassic magmas were derived from Churchill Province lithospheric mantle that had been metasomatically enriched over broad areas during Neoarchean flat subduction. The long time interval between metasomatism and minette-magma generation allowed the ϵ_{Nd} of the enriched mantle to evolve

to strongly negative values. Lithospheric delamination thereby can generate melts with strongly negative ϵ Nd and ϵ Hf values required for the BFGC.

Similarly, 1.77 Ga mantle upwelling is proposed to be the trigger of both mafic and felsic magmatism of the Kivalliq/Nueltin suites (Peterson *et al.*, 2015a). Liu *et al.* (2016) interpreted a peak in Os model ages between 1.7 and 1.9 Ga obtained on peridotite xenoliths from Pelly Bay at the southern end of Boothia Peninsula to reflect formation of Paleoproterozoic lithosphere replacing metasomatized Archean lithosphere. Thus the mantle-derived magmas of the Kivalliq/Nueltin suites and the mantle lithosphere formation may be part of the same overall event (Peterson *et al.*, 2015b; Liu *et al.*, 2016). Notably, the felsic magmatism within the Kivalliq/Nueltin suites share many geochemical and isotopic characteristics with the BFGC (Fig. 8-10; Appendix 7), suggesting broadly similar source rocks and petrogenetic processes for these magmas. However, given the temporal association between Hudson granites and minette-related magmas derived from metasomatized Archean lithospheric melts, it may be that the initial phases of lithospheric delamination in parts of the Churchill Province started prior to the Kivalliq/Nueltin events during the late stages of the Trans-Hudson orogen. This implies the Churchill Paleoproterozoic granite ‘blooms’ were largely formed by the same protracted event of partial lithospheric delamination followed by formation of new Paleoproterozoic lithosphere, contemporaneous with generation of the BFGC.

If partial lithospheric delamination triggered generation of the Hudson granite and Kivalliq/Nueltin suites, it may also be an appropriate mechanism for generating the BFGC magmas. However, the mechanism that generated the BFGC magmas as well as the widespread ca. 1.85-1.81 Ga Hudson granite magmatism in the Churchill Province should also have a close association with shear zone development. All the shear zones spatially associated with ca. 1.8 Ga magmatism within the Churchill province are generated in a transpressional setting, however mantle upwelling following delamination typically will develop extensional shear zones associated with post-orogenic collapse (Kay and Mahlburg Kay, 1993). Krystopowicz and Currie (2013) modeled lithospheric delamination occurring during orogenic evolution. In cases with rapidly thickening crust (such as a continental collision event), the lithosphere delaminates rapidly across a wide area associated with a weak lower crust (deemed stationary delamination).

In this model, deformation, uplift, and heating was prevalent concurrently across the full width of the orogen. This is opposed to so-called retreating delamination, where deformation and magmatism would ‘migrate’ across the orogen, thereby creating a temporal gradient of magmatism and shearing (i.e. not contemporaneous across the orogen). In the stationary model of delamination, widespread magmatism would be contemporaneous across the orogen and with compressional deformation (i.e. shear zone development), as we see in the Churchill Province. For the BFGC, further work would be necessary to establish why the known shear zone in the area developed after rather than during magma emplacement, however these delamination models suggest the potential for cogenetic association between shear zone development and magmatism during lithospheric delamination within a collisional orogen.

CONCLUSIONS

A new component of the Trans-Hudson late-collisional granite ‘bloom’ was documented as a part of the reconnaissance regional mapping within Boothia Peninsula, NU, herein called the Boothia Ferroan Granite Complex. This complex, composed of three regionally extensive plutons, extends the tectonothermal effects of the Trans-Hudson orogen by >250 km from its previously known northernmost limit (Corrigan, 2009). In this study, I report petrographic, U-Pb geochronological, geochemical, radiogenic isotope, and mineral composition data to establish the petrogenesis of these plutons. This study has determined:

- The BFGC was emplaced within a constrained ~20 Myr period (1841-1823 Ma), and consists of massive to weakly deformed granitoids, with subordinate granodiorites and quartz monzonite.
- The BFGC magmas are characterized by their major- and trace-element chemistry, namely the BFGC is ferroan, potassium rich, with both peraluminous and metaluminous compositions, and incompatible element enriched.
- The strongly negative initial ϵ_{Nd} and ϵ_{Hf} values indicate the BFGC are derived from dominantly older crustal sources. Notably, variation in these epsilon values between suites suggests the BFGC magmas were not derived solely on a single source rock.
- The presence of anhydrous mafic minerals such as fayalite, orthopyroxene, and inverted pigeonite, as well as various geothermometric constraints (amphibole-plagioclase, titanium-

in-zircon and zircon saturation thermometers) indicate that the BFGC comprises high-temperature magmas that exceeded at least 800 and possibly 900 °C upon emplacement.

These high emplacement temperatures require the input of mantle heat along with radioactive heating associated with crustal thickening to trigger melting.

- Various geobarometric constraints (fayalite-ferrosilite-quartz, Al-in-hornblende, garnet-aluminosilicate-quartz-plagioclase) indicates that the BFGC magmas were generated in an over-thickened (50-60 km) crust, and subsequently emplaced at the mid-crustal depths of ~20 km.

The BFGC was likely caused by partial lithospheric delamination in the hinterland of the Trans-Hudson orogen, which triggered partial melting of enriched Churchill Province SCLM that had been incompatible-element enriched through metasomatism at 2.7-2.8 Ga and thereby acquired crust-like Nd isotope signatures by ca. 1.83 Ga. These mantle-derived LREE-, K-enriched magmas both heated and interacted with the Boothia crust to produce the high-temperature BFGC magmas. The chemical and isotopic composition of these magmas are consistent with their derivation from three sources, the 2.56-2.52 Ga Boothia porphyroclastic granites, the 2.48 Ga Boothia basement mafic rocks and LREE-enriched mantle-derived mafic rocks or their differentiates. The garnet-biotite suite granitoids of the BFGC reflect an additional process, namely the assimilation of semi-pelitic country rocks by BFGC magmas at their final mid-crustal level emplacement site. The far-field stress of the Trans-Hudson coupled with partial lithospheric delamination may have generated laterally extensive shear zones (e.g., the Sanagak Lake shear zone), some of which may have facilitated magma transport and emplacement in discrete belts. The data obtained in this thesis for the BFGC in conjunction with previously acquired data on ca. 1.83 Ga magmatic rocks from across the Churchill Province provide important insights on the nature of late- to post-collisional magmatism. Crustal thickening across an orogenic plateau coupled with subsequent partial delamination of the mantle lithosphere beneath that plateau can produce synchronous magmatism over a very broad area. For example, although the BFGC is located more than > 1000 km distal to the Trans-Hudson orogenic front, the combined thermal effects of thickening and delamination was nevertheless able to trigger high-temperature partial melting of the thickened crust in this distal region, possibly accompanied by additional contributions from magmas derived from enriched lithospheric mantle. Similar post-collisional

magmatic processes may be occurring in the present-day at deeper crustal levels of the Tibetan Plateau. The BFGC affords an opportunity to study these processes at the surface.

REFERENCES

- Allègre, C. J. & Minster, J. F. (1978). Quantitative models of trace element behavior in magmatic processes. *Earth and Planetary Science Letters* **38**, 1–25.
- Anderson, J. L. & Smith, R. D. (1995). The effects of temperature and fO₂ on the Al-in-hornblende barometer. *American Mineralogist* **80**, 549–559.
- Ashton, K. E., Hartlaub, R. P., Bethune, K. M., Heaman, L. M., Rayner, N. & Niebergall, G. R. (2013). New depositional age constraints for the Murmac Bay group of the southern Rae craton, Canada. *Precambrian Research*. Elsevier B.V. **232**, 70–88.
- Ashton, K. E., Heaman, L. M., Lewry, J. F., Hartlaub, R. P. & Shi, R. (1999). Age and origin of the Jan Lake Complex: A glimpse at the buried Archean craton of the Trans-Hudson Orogen. *Canadian Journal of Earth Sciences* **36**, 185–208.
- Aspler, L. B., Cousens, B. L. & Chiarenzelli, J. R. (2002). Griffin gabbro sills (2.11 Ga), Hurwitz Basin, Nunavut, Canada: Long-distance lateral transport of magmas in western Churchill Province crust. *Precambrian Research* **117**, 269–294.
- Aspler, L. B., Wisotzek, I. E., Chiarenzelli, J. R., Losonczy, M. F., Cousens, B. L., McNicoll, V. J. & Davis, W. J. (2001). Paleoproterozoic intracratonic basin processes, from breakup of Kenorland to assembly of Laurentia: Hurwitz Basin, Nunavut, Canada. *Sedimentary Geology* **141–142**, 287–318.
- Barnes, C. G., Werts, K., Memeti, V. & Ardill, K. (2020). Most granitoid rocks are cumulates: Deductions from hornblende compositions and zircon saturation. *Journal of Petrology* **60**, 2240–2277.
- Barros, M. A. de S. A., Júnior, F. C., Nardi, L. V. S. & Lima, E. F. (2009). Paleoproterozoic bimodal post-collisional magmatism in the southwestern Amazonian Craton, Mato Grosso, Brazil: Geochemistry and isotopic evidence. *Journal of South American Earth Sciences* **27**, 11–23.
- Bell, E. A., Boehnke, P. & Harrison, T. M. (2016). Recovering the primary geochemistry of Jack Hills zircons through quantitative estimates of chemical alteration. *Geochimica et*

Cosmochimica Acta **191**, 187–202.

Belousova, E. A., Griffin, W. L., O'Reilly, S. Y. & Fisher, N. I. (2002). Igneous zircon: Trace element composition as an indicator of source rock type. *Contributions to Mineralogy and Petrology* **143**, 602–622.

Berman, R. G., Davis, W., Sanborn-Barrie, M., Whalen, J., Taylor, B. E., McMartin, I., McCurdy, M. W., Mitchell, R. K., Ma, S., Coyle, M., Roberts, B., Craven, J. A. (2018). Report of activities for the GEM-2 Chantrey-Thelon activity: Thelon tectonic zone project , Nunavut GEOLOGICAL SURVEY OF CANADA OPEN FILE 8372

Berman, R. G., Davis, W. J. & Pehrsson, S. J. (2007). Collisional Snowbird tectonic zone resurrected: Growth of Laurentia during the 1 . 9 Ga accretionary phase of the Hudsonian orogeny. *Geology* **35**, 911–914.

Berman, R. G., Pehrsson, S. J., Davis, W. J., Ryan, J. J., Qui, H. & Ashton, K. E. (2013). The Arrowsmith orogeny: Geochronological and thermobarometric constraints on its extent and tectonic setting in the Rae craton, with implications for pre-Nuna supercontinent reconstruction. *Precambrian Research*. Elsevier B.V. **232**, 44–69.

Berman, R. G., Sanborn-Barrie, M., Stern, R. A. & Carson, C. J. (2005). Tectonometamorphism at ca. 2.35 and 1.85 Ga in the rae domain, western Churchill Province, Nunavut, Canada: Insights from structural, metamorphic and in situ geochronological analysis of the southwestern Committee Bay Belt. *Canadian Mineralogist* **43**, 409–442.

Blackadar, R. G. (1967). Precambrian Geology of Boothia Peninsula, Somerset Island, and Prince of Wales Island, District of Franklin. *Geological Survey of Canada Bulletin* **1**.

Boehnke, P., Watson, E. B., Trail, D., Harrison, T. M. & Schmitt, A. K. (2013). Zircon saturation re-revisited. *Chemical Geology*. Elsevier B.V. **351**, 324–334.

Bohlen, S. R., Essene, E. J. & Boettcher, A. L. (1980). Reinvestigation and application of olivine-quartz-orthopyroxene barometry. *Earth and Planetary Science Letters* **47**, 1–10.

Bonin, B. (2004). Do coeval mafic and felsic magmas in post-collisional to within-plate regimes necessarily imply two contrasting, mantle and crustal, sources? A review. *Lithos* **78**, 1–24.

- Bostock, H. H. & Van Breemen, O. (1992). The timing of emplacement, and distribution of the Sparrow diabase dyke swarm, District of Mackenzie, Northwest Territories. *Radiogenic age and isotopic studies: Report 6*.
- Bouvier, A., Vervoort, J. D. & Patchett, P. J. (2008). The Lu-Hf and Sm-Nd isotopic composition of CHUR: Constraints from unequilibrated chondrites and implications for the bulk composition of terrestrial planets. *Earth and Planetary Science Letters* **273**, 48–57.
- Breiter, K., Lamarão, C. N., Borges, R. M. K. & Dall'Agnol, R. (2014). Chemical characteristics of zircon from A-type granites and comparison to zircon of S-type granites. *Lithos*. Elsevier B.V. **192–195**, 208–225.
- Brown, M. (2007). Crustal melting and melt extraction, ascent and emplacement in orogens: mechanisms and consequences. *Journal of the Geological Society* **164**, 709–730.
- Brown, M. (2013). Granite: From genesis to emplacement. *Bulletin of the Geological Society of America* **125**, 1079–1113.
- Chacko, T., De, S. K., Creaser, R. A. & Muehlenbachs, K. (2000). Tectonic setting of the Taltson magmatic zone at 1.9–2.0 Ga: a granitoid-based perspective. *Canadian Journal of Earth Sciences* **37**, 1597–1609.
- Cherniak, D. J., Hanchar, J. M. & Watson, E. B. (1997). Rare-earth diffusion in zircon. *Chemical Geology* **134**, 289–301.
- Corrigan, D., Pehrsson, S., Wodicka, N. & de Kemp, E. (2009). The Palaeoproterozoic Trans-Hudson Orogen: A prototype of modern accretionary processes. *Geological Society Special Publication* **327**, 457–479.
- Corrigan, D., Scott, D. & St-Onge, M. (2001). Geology of the northern margin of the Trans-Hudson Orogen (Foxe Fold Belt), central Baffin Island, Nunavut. *Current Research 2001-C23*.
- Cousens, B. L., Aspler, L. B., Chiarenzelli, J. R., Donaldson, J. A., Sandeman, H. A., Peterson, T. D. & Lecheminant, A. N. (2001). Enriched Archean lithospheric mantle beneath western Churchill Province tapped during Paleoproterozoic orogenesis. *Geology* **29**, 827–830.

- Davies, J. H. F. L. & von Blanckenburg, F. (1995). Slab breakoff: A model of lithosphere detachment and its test in the magmatism and deformation of collisional orogens. *Earth and Planetary Science Letters* **129**, 85–102.
- Drayson, D., Camacho, A., Sanborn-barrie, M., Regis, D. & Larson, K. ((n.d.)). Deformation history and significance of the Sanagak Lake shear zone , Boothia Peninsula , Nunavut. .
- Eklund, O., Konopelko, D., Rutanen, H., Fröjdö, S. & Shebanov, A. D. (1998). 1.8 Ga Svecofennian post-collisional shoshonitic magmatism in the Fennoscandian shield. *Lithos* **45**, 87–108.
- Emslie, R. F. & Stirling, J. A. R. (1993). Rapakivi and related granitoids of the Nain plutonic suite: geochemistry, mineral assemblages and fluid equilibria. *Canadian Mineralogist* **31**, 821–847.
- England, P. C. & Thompson, A. B. (1984). Pressure - temperature - time paths of regional metamorphism I. heat transfer during the evolution of regions of thickened continental crust. *Journal of Petrology* **25**, 894–928.
- Evans, D. A. D. & Mitchell, R. N. (2011). Assembly and breakup of the core of Paleoproterozoic-Mesoproterozoic supercontinent Nuna. *Geology* **39**, 443–446.
- Fisher, C. M., Hanchar, J. M., Samson, S. D., Dhuime, B., Blichert-Toft, J., Vervoort, J. D. & Lam, R. (2011). Synthetic zircon doped with hafnium and rare earth elements: A reference material for in situ hafnium isotope analysis. *Chemical Geology*. Elsevier B.V. **286**, 32–47.
- Fisher, C. M., Vervoort, J. D. & Dufrane, S. A. (2014). Accurate Hf isotope determinations of complex zircons using the “laser ablation split stream” method. *Geochemistry, Geophysics, Geosystems* **15**, 121–139.
- Freeburn, R., Bouilhol, P., Maunder, B., Magni, V. & van Hunen, J. (2017). Numerical models of the magmatic processes induced by slab breakoff. *Earth and Planetary Science Letters* **478**, 203–213.
- Frisch, T. & Hunt, P. A. (1993). Reconnaissance U-Pb geochronology of the crystalline core of the Boothia Uplift, District of Franklin, Northwest Territories. *Radiogenic Age and Isotopic*

Studies: Report 7; Geological Survey of Canada.

- Frost, C. D. & Frost, R. B. (1997). Reduced rapakivi-type granites: The tholeiite connection. *Geology* **25**, 647–650.
- Frost, C. D. & Frost, R. B. (2011). On ferroan (A-type) granitoids: Their compositional variability and modes of origin. *Journal of Petrology* **52**, 39–53.
- Frost, C. D., Frost, R. B., Chamberlain, K. R. & Edwards, B. R. (1999). *Petrogenesis of the 1.43 Ga Sherman batholith, SE Wyoming, USA: a reduced, rapakivi-type anorogenic granite.* *Journal of Petrology*.
- Frost, R. B., Barnes, C. G., Collins, W. J., Arculus, R. J., Ellis, D. J. & Frost, C. D. (2001). A Geochemical Classification for Granitic Rocks. *Journal of Petrology* **42**, 2033–2048.
- Fu, B., Page, F. Z., Cavosie, A. J., Fournelle, J., Kita, N. T., Lackey, J. S., Wilde, S. A. & Valley, J. W. (2008). Ti-in-zircon thermometry: Applications and limitations. *Contributions to Mineralogy and Petrology* **156**, 197–215.
- Gervasoni, F., Klemme, S., Rocha-Júnior, E. R. V. & Berndt, J. (2016). Zircon saturation in silicate melts: a new and improved model for aluminous and alkaline melts. *Contributions to Mineralogy and Petrology*. Springer Berlin Heidelberg **171**, 1–12.
- Ghiorso, M. S. & Sack, O. (1991). Fe-Ti oxide geothermometry: thermodynamic formulation and the estimation of intensive variables in silicic magmas. *Contributions to Mineralogy and Petrology* **108**, 485–510.
- Griffin, T. J., Page, R. W., Sheppard, S. & Tyler, I. M. (2000). Tectonic implications of Palaeoproterozoic post-collisional, high-K felsic igneous rocks from the Kimberley region of northwestern Australia. *Precambrian Research* **101**, 1–23.
- Hanchar, J. M. & Watson, E. B. (2003). Zircon saturation thermometry. *Reviews in Mineralogy and Geochemistry* **53**, 89–112.
- Harley, S. L., Kelly, N. M. & Möller, A. (2007). Zircon behaviour and the thermal histories of mountain chains. *Elements* **3**, 25–30.

- Hartlaub, R. P., Heaman, L. M., Chacko, T. & Ashton, K. E. (2007). Circa 2.3-Ga Magmatism of the Arrowsmith Orogeny, Uranium City Region, Western Churchill Craton, Canada. *Journal of Geology* **115**, 181–195.
- Hawkesworth, C., Cawood, P. A., Kemp, T., Storey, C. & Dhuime, B. (2009). A matter of preservation. *Science* **323**, 49–50.
- Heaman, L. M., Bowins, R. & Crocket, J. (1990). The chemical composition of igneous zircon suites: implications for geochemical tracer studies. *Geochimica et Cosmochimica Acta* **54**, 1597–1607.
- Heaman, L. M. & LeCheminant, A. N. (1993). Paragenesis and U-Pb systematics of baddeleyite (ZrO_2). *Chemical Geology* **110**, 95–126.
- Hildebrand, R. S. & Whalen, J. B. (2014). Arc and Slab-failure magmatism in Cordilleran Batholiths II - The Cretaceous Peninsula Ranges Batholith of Southern and Baja California. *Geoscience Canada* **41**, 399–458.
- Hinchey, A. M., Davis, W. J. & Ryan, J. J. (2011). Neoarchean high-potassium granites of the Boothia mainland area , Rae domain , Churchill Province: U – Pb zircon and Sm – Nd whole rock isotopic constraints. *Canadian Journal of Earth Sciences* **48**, 247–279.
- Hoffman, P. F. (1988). United Plates of America, the Birth of a Craton: Early Proterozoic Assembly and Growth of Laurentia. *Annual Reviews in Earth Planetary Sciences* **16**, 543–603.
- Holland, T. & Blundy, J. (1994). Non-ideal interactions in calcic amphiboles and their bearing on amphibole-plagioclase thermometry. *Contributions to Mineralogy and Petrology* **116**, 433–447.
- Horstwood, M. S. A. *et al.* (2016). Community-Derived Standards for LA-ICP-MS U-(Th)-Pb Geochronology – Uncertainty Propagation, Age Interpretation and Data Reporting. *Geostandards and Geoanalytical Research* **40**, 311–332.
- Hoskin, P. W. O. (2005). Trace-element composition of hydrothermal zircon and the alteration of Hadean zircon from the Jack Hills, Australia. *Geochimica et Cosmochimica Acta* **69**, 637–

- Hoskin, P. W. O. & Schaltegger, U. (2003). The composition of zircon and igneous and metamorphic petrogenesis. *Reviews in Mineralogy and Geochemistry* **53**, 27–62.
- Huang, H., Li, X., Li, W. & Li, Z. (2011). Formation of high $\delta^{18}\text{O}$ fayalite-bearing A-type granite by high-temperature melting of granulitic metasedimentary rocks, southern China. *Geology* **39**, 903–906.
- Ickert, R. B. (2013). Algorithms for estimating uncertainties in initial radiogenic isotope ratios and model ages. *Chemical Geology*. Elsevier B.V. **340**, 131–138.
- Jackson, S. E., Pearson, N. J., Griffin, W. L. & Belousova, E. A. (2004). The application of laser ablation-inductively coupled plasma-mass spectrometry to in situ U-Pb zircon geochronology. *Chemical Geology* **211**, 47–69.
- Johnson, M. C. & Rutherford, M. J. (1989). Experimental calibration of the aluminum-in-hornblende geobarometer with application of Long Valley caldera (California) volcanic rocks. *Geology* **17**, 837–841.
- Kay, R. W. & Mahlburg Kay, S. (1993). Delamination and delamination magmatism. *Tectonophysics* **219**, 177–189.
- Kemp, A. I. S., Wilde, S. A., Hawkesworth, C. J., Coath, C. D., Nemchin, A., Pidgeon, R. T., Vervoort, J. D. & DuFrane, S. A. (2010). Hadean crustal evolution revisited: New constraints from Pb-Hf isotope systematics of the Jack Hills zircons. *Earth and Planetary Science Letters* **296**, 45–56.
- Keppler, H. (1993). Influence of fluorine on the enrichment of high field strength trace elements in granitic rocks. *Contributions to Mineralogy and Petrology* **114**, 479–488.
- Kerr, J. W. & Christie, R. L. (1965). Tectonic History of Boothia Uplift and Cornwallis Fold Belt, Arctic Canada. *Bulletin of the American Association of Petroleum Geologists* **49**, 905–926.
- Kirkland, C. L., Smithies, R. H., Taylor, R. J. M., Evans, N. & McDonald, B. (2015). Zircon Th/U ratios in magmatic environs. *Lithos* **212–215**, 397–414.

Kraft, J. (2006). Petrology , geochronology and tectonometamorphism of the Paleoproterozoic Northern Chantrey Group , northern Rae Domain , Churchill Province , Nunavut. .

Krystopowicz, N. J. & Currie, C. A. (2013). Crustal eclogitization and lithosphere delamination in orogens. *Earth and Planetary Science Letters* **361**, 195–207.

LaFlamme, C., McFarlane, C. R. M. & Corrigan, D. (2014). U–Pb , Lu–Hf and REE in zircon from 3.2 to 2.6 Ga Archean gneisses of the Repulse Bay block, Melville Peninsula , Nunavut. *Precambrian Research*. Elsevier B.V. **252**, 223–239.

LeCheminant, A. N., Miller, A. R. & LeCheminant, G. M. (1987). Early Proterozoic alkaline igneous rocks, District of Keewatin, Canada: petrogenesis and mineralization. *Geochemistry and Mineralization of Proterozoic Volcanic Suites* **33**, 219–240.

Li, Z. X. & Li, X. H. (2007). Formation of the 1300-km-wide intracontinental orogen and postorogenic magmatic province in Mesozoic South China: A flat-slab subduction model. *Geology* **35**, 179–182.

Lindsley, D. H. (1983). Pyroxene thermometry. *American Mineralogist* **68**, 477–493.

Lindsley, D. H. & Frost, R. B. (1992). Equilibria among Fe-Ti oxides, pyroxenes, olivine, and quartz: Part 1. Theory. *American Mineralogist* **77**, 987–1003.

Liu, J., Riches, A. J. V., Pearson, D. G., Luo, Y., Kienlen, B., Kjarsgaard, B. A., Stachel, T. & Armstrong, J. P. (2016). Age and evolution of the deep continental root beneath the central Rae craton, northern Canada. *Precambrian Research*. Elsevier B.V. **272**, 168–184.

Magni, V., Faccenna, C., Van Hunen, J. & Funiciello, F. (2013). Delamination vs. break-off: The fate of continental collision. *Geophysical Research Letters* **40**, 285–289.

Mahan, K. H. & Williams, M. L. (2005). Reconstruction of a large deep-crustal terrane: Implications for the Snowbird tectonic zone and early growth of Laurentia. *Geology* **33**, 385–388.

Maurice, C., David, J., O’Neil, J. & Francis, D. (2009). Age and tectonic implications of Paleoproterozoic mafic dyke swarms for the origin of 2.2Ga enriched lithosphere beneath the Ungava Peninsula, Canada. *Precambrian Research* **174**, 163–180.

- McDonough, W. F. & Sun, S. -s. (1995). The Composition of the Earth. *Chemica* **120**, 223–253.
- McFarlane, C. R. M., Carlson, W. D. & Connelly, J. N. (2003). Prograde, peak, and retrograde P-T paths from aluminium in orthopyroxene: High-temperature contact metamorphism in the aureole of the Makhavinekh Lake Pluton, Nain Plutonic Suite, Labrador. *Journal of Metamorphic Geology* **21**, 405–423.
- Morelli, R. M., Hartlaub, R. P., Ashton, K. E. & Ansdell, K. M. (2009). Evidence for enrichment of subcontinental lithospheric mantle from Paleoproterozoic intracratonic magmas: Geochemistry and U-Pb geochronology of Martin Group igneous rocks, western Rae Craton, Canada. *Precambrian Research* **175**, 1–15.
- Mutch, E. J. F., Blundy, J. D., Tattitch, B. C., Cooper, F. J. & Brooker, R. A. (2016). An experimental study of amphibole stability in low-pressure granitic magmas and a revised Al-in-hornblende geobarometer. *Contributions to Mineralogy and Petrology*. Springer Berlin Heidelberg **171**, 1–27.
- Nair, R. & Chacko, T. (2008). Role of oceanic plateaus in the initiation of subduction and origin of continental crust. *Geology* **36**, 583–586.
- Nardi, L. V. S., Formoso, M. L. L., Müller, I. F., Fontana, E., Jarvis, K. & Lamarão, C. (2013). Zircon/rock partition coefficients of REEs, Y, Th, U, Nb, and Ta in granitic rocks: Uses for provenance and mineral exploration purposes. *Chemical Geology* **335**, 1–7.
- Nash, W. P. & Crecraft, H. R. (1985). Partition coefficients for trace elements in silicic magmas. *Geochimica et Cosmochimica Acta* **49**, 2309–2322.
- Nelson, B. K. & Depaolo, D. J. (1981). Nd isotopic evidence from the basement of the North American mid-continent. *Geological Society Of America Bulletin* **96**, 746–754.
- Paces, J. B. & Miller, J. D. (1993). Precise U-Pb Ages of the Duluth Complex and Related Mafic Intrusions, Northeastern Minnesota: Geochronological Insights to Physical, Petrogenetic, Paleomagnetic, and Tectonomagmatic Processes Associated with the 1.1 Ga Midcontinent Rift System. *Journal of Geophysical Research* **98**, 13997–14013.
- Patchett, P. J. & Vervoort, J. D. (1996). Behavior of hafnium and neodymium isotopes in the

- crust: Constraints from Precambrian crustally derived granites. *Geochimica et Cosmochimica Acta* **60**, 3717–3733.
- Patino-Douce, A. E., Humphreys, E. D. & Johnston, A. D. (1990). Anatexis and metamorphism in tectonically thickened continental crust exemplified by the Sevier hinterland, western North America. *Earth and Planetary Science Letters* **97**, 290–315.
- Paton, C., Hellstrom, J., Paul, B., Woodhead, J. & Hergt, J. (2011). Iolite: Freeware for the visualisation and processing of mass spectrometric data. *Journal of Analytical Atomic Spectrometry* **26**, 2508–2518.
- Patterson, J. G. & Heaman, L. M. (1991). New geochronologic limits on the depositional age of the Hurwitz Group, Trans-Hudson hinterland, Canada. *Geology* **19**, 1137–1140.
- Pearce, J. (1996). Sources and Settings of Granitic Rocks. *Episodes* **19**.
- Pearce, J., Harris, N. B. W. & Tindle, A. G. (1984). Trace element distribution diagrams for the tectonic interpretation of granitic rocks. *Journal of Petrology* **25**, 956–983.
- Peprsson, S. J., Berman, R. G. & Davis, W. J. (2013a). Paleoproterozoic orogenesis during Nuna aggregation: A case study of reworking of the Rae craton, Woodburn Lake, Nunavut. *Precambrian Research* **232**, 167–188.
- Peprsson, S. J., Berman, R. G., Eglington, B. & Rainbird, R. (2013b). Two Neoarchean supercontinents revisited: The case for a Rae family of cratons. *Precambrian Research* **232**, 27–43.
- Peters, B. J. & Day, J. M. (2014). Assessment of relative Ti, Ta, and Nb (TITAN) enrichments in ocean islands basalts. *Geochemistry, Geophysics, Geosystems* **15**, 4424–4444.
- Peterson, T. D., Esperanca, S. & LeCheminant, A. N. (1994). Geochemistry and origin of the Proterozoic ultrapotassic rocks of the Churchill Province, Canada. *Mineralogy and Petrology* **51**, 251–276.
- Peterson, T. D., Jefferson, C. W. & Anand, A. (2015a). Geological setting and geochemistry of the ca. 2.6 Ga Snow Island Suite in the central Rae Domain of the Western Churchill Province, Nunavut - Report: Geological Survey of Canada Open File 7841

Peterson, T. D. & Pehrsson, S. J. (2010). Proterozoic (1.85-1.7 Ga) igneous suites of the Western Churchill Province: constraints on tectonic assembly and crust-mantle dynamics. *GeoCanada 2010 Abstracts* 1–4.

Peterson, T. D., Scott, J. M. J., LeCheminant, A. N., Jefferson, C. W. & Pehrsson, S. J. (2015b). The Kivalliq Igneous Suite: Anorogenic bimodal magmatism at 1.75Ga in the western Churchill Province, Canada. *Precambrian Research*. Elsevier B.V. **262**, 101–119.

Peterson, T. D., Van Breemen, O., Sandeman, H. A. & Cousens, B. L. (2002). Proterozoic (1.85–1.75 Ga) igneous suites of the Western Churchill Province: Granitoid and ultrapotassic magmatism in a reworked Archean hinterland. *Precambrian Research* **119**, 73–100.

Rainbird, R. H., Davis, W. J., Pehrsson, S. J., Wodicka, N., Rayner, N. & Skulski, T. (2010). Early Paleoproterozoic supracrustal assemblages of the Rae domain , Nunavut , Canada : Intracratonic basin development during supercontinent break-up and assembly. *Precambrian Research* **181**, 167–186.

Rapp, R. P., Shimizu, N. & Norman, M. D. (2003). Growth of early continental crust by partial melting of eclogite. *Nature* **425**, 605–609.

Regan, S. P., Williams, M. L., Mahan, K. H., Dumond, G., Jercinovic, M. J. & Orlandini, O. F. (2017). Neoarchean arc magmatism and subsequent collisional orogenesis along the eastern Rae domain, western Churchill Province: Implications for the early growth of Laurentia. *Precambrian Research*.

Richard, P., Shimizu, N. & Allegre, C. J. (1976). $^{143}\text{Nd}/^{146}\text{Nd}$, A natural tracer: an application to oceanic basalts. *Earth and Planetary Science Letters* **31**, 269–278.

Rollinson, H. R. (1993). *Using Geochemical Data Evaluation, Presentation, Interpretation..*

Rubatto, D. (2017). Zircon : The Metamorphic Mineral. *Reviews in Mineralogy and Geochemistry* **83**, 261–295.

Ryan, J. J., Nadeau, L., Hinckley, A. M., James, D. T., Sandeman, H. A., Schetselaar, E. M., Davis, W. J. & Berman, R. G. (2009). Bedrock geology of the southern Boothia mainland area (Pelly Bay-Rae Strait-Spence Bay map areas), Kitikmeot region, Nunavut. *Geological*

Survey of Canada Current Research, 1–18.

- Sanborn-Barrie, M., Camacho, A. & Berman, R. G. (2019). High-pressure, ultrahigh-temperature 1.9 Ga metamorphism of the Kramanituar Complex, Snowbird Tectonic Zone, Rae Craton, Canada. *Contributions to Mineralogy and Petrology*. Springer Berlin Heidelberg **174**, 1–26.
- Sanborn-Barrie, M., Davis, W. J., Berman, R. G., Rayner, N., Skulski, T. & Sandeman, H. A. (2014). Neoarchean continental crust formation and Paleoproterozoic deformation of the central Rae craton, Committee Bay belt, Nunavut. *Canadian Journal of Earth Sciences*. NRC Research Press **51**, 635–667.
- Sanborn-Barrie, M. & Regis, D. (2020). 2.56 to 1.87 Ga evolution of the Rae cratonic margin: micro- to macro-scale constraints from Boothia Peninsula-Somerset Island, Nunavut. *Geoconvention Abstract* 1–2.
- Sanborn-Barrie, M., Regis, D., Ford, A., Osinchuk, A. & Drayson, D. (2018). Report of activities for the GEM-2 Boothia Peninsula – Somerset Island Project : integrated geoscience of the Northwest Passage , Nunavut GEOLOGICAL SURVEY OF CANADA OPEN FILE 8339
- Sandeman, H. A. & Hadlari, T. (2010). Insights into the origin of calc-alkaline lamprophyres an oblique Paleoproterozoic crustal section through the northern Hearne Province , Nunavut. *GeoCanada 2010 Abstracts* 1–4.
- Schiller, D. & Finger, F. (2019). Application of Ti-in-zircon thermometry to granite studies: problems and possible solutions. *Contributions to Mineralogy and Petrology*. Springer Berlin Heidelberg **174**, 1–16.
- Schmidt, M. W. (1992). Amphibole composition in tonalite as a function of pressure: an experimental calibration of the Al-in-hornblende barometer. *Contributions to Mineralogy and Petrology* **110**, 304–310.
- Schultz, M. E. J. (2007). The Queen Maud Block, Nunavut - Genesis of a large felsic igneous province in the earliest Paleoproterozoic and implications for Laurentian geotectonic models. University of Alberta.
- Schultz, M. E. J., Chacko, T., Heaman, L. M., Sandeman, H. A., Simonetti, A. & Creaser, R. A.

- (2007). Queen Maud block: A newly recognized Paleoproterozoic (2.4–2.5 Ga) terrane in northwest Laurentia. *Geology* **35**, 707–710.
- Scott, J. M. J., Peterson, T. D., Davis, W. J., Jefferson, C. W. & Cousens, B. L. (2015). Petrology and geochronology of Paleoproterozoic intrusive rocks, Kiggavik uranium camp, Nunavut. *Canadian Journal of Earth Sciences* **52**, 495–518.
- Siégel, C., Bryan, S. E., Allen, C. M. & Gust, D. A. (2018). Use and abuse of zircon-based thermometers: A critical review and a recommended approach to identify antecrustic zircons. *Earth-Science Reviews*. Elsevier **176**, 87–116.
- Simonetti, A., Heaman, L. M., Chacko, T. & Banerjee, N. R. (2006). In situ petrographic thin section U-Pb dating of zircon, monazite, and titanite using laser ablation-MC-ICP-MS. *International Journal of Mass Spectrometry* **253**, 87–97.
- Skjerlie, K. P. & Johnston, A. D. (1993). Fluid-absent melting behavior of an F-rich tonalitic gneiss at mid-crustal pressures: Implications for the generation of anorogenic granites. *Journal of Petrology* **34**, 785–815.
- Sláma, J. et al. (2008). Plešovice zircon - A new natural reference material for U-Pb and Hf isotopic microanalysis. *Chemical Geology* **249**, 1–35.
- Söderlund, U. & Johansson, L. (2002). A simple way to extract baddeleyite (ZrO_2) . *Geochemistry, Geophysics, Geosystems* **3**, 1 of 7–7.
- Stern, R. A., Bodorkos, S., Kamo, S. L., Hickman, A. H. & Corfu, F. (2009). Measurement of SIMS of Pb isotopes during Zircon dating. *Geostandards and Geoanalytical Research* **33**, 145–168.
- Tersmette, D. (2012). Geology, geochronology, thermobarometry, and tectonic evolution of the Queen Maud block, Churchill craton, Nunavut, Canada. .
- Theriault, I., Steenkamp, H. M., Larson, K. P. & Cottle, J. M. (2018). Geochronological constraints on deformation in the Wager shear zone, northwestern Hudson Bay, Nunavut. .
- Thomas, M. D. (2018). *Definition of magnetic domains within the Rae Craton, mainland Canadian Shield, Nunavut, Northwest Territories, Saskatchewan, and Alberta: their*

magnetic signatures and relationship to geology. Geological Survey of Canada, Open File 8343.

Thompson, P. H. (1989). An empirical model for metamorphic evolution of the Archaean Slave Province and adjacent Thelon Tectonic Zone, north-western Canadian Shield. *Geological Society Special Publication* **43**, 245–263.

van Breemen, O., Peterson, T. D. & Sandeman, H. A. (2005). U-Pb zircon geochronology and Nd isotope geochemistry of Proterozoic granitoids in the western Churchill Province: intrusive age pattern and Archean source domains. *Canadian Journal of Earth Sciences* **42**, 339–377.

Ver Hoeve, T. J., Scoates, J. S., Wall, C. J., Weis, D. & Amini, M. (2018). Evaluating downhole fractionation corrections in LA-ICP-MS U-Pb zircon geochronology. *Chemical Geology*. Elsevier **483**, 201–217.

Vervoort, J. D., Patchett, P. J., Blichert-Toft, J. & Albarède, F. (1999). Relationships between Lu-Hf and Sm-Nd isotopic systems in the global sedimentary system. *Earth and Planetary Science Letters* **168**, 79–99.

Wang, X., Griffin, W. L., Chen, J., Huang, P. & Li, X. (2011). U and Th Contents and the Th/U Ratios of Zircon in Felsic and Mafic Magmatic Rocks: Improved Zircon-Melt Distribution Coefficients. *Acta Geological Sinica* **85**, 164–174.

Watson, E. B. & Harrison, T. M. (1983). Zircon saturation revisited: temperature and composition effects in a variety of crustal magma types. *Earth and Planetary Science Letters* **64**, 295–304.

Watson, E. B. & Harrison, T. M. (2005). Zircon thermometer reveals minimum melting conditions on earliest earth. *Science* **308**, 841–844.

Weller, O. M. & St-Onge, M. R. (2017). Record of modern-style plate tectonics in the Palaeoproterozoic Trans-Hudson orogen. *Nature Geoscience* **10**, 305–311.

Whalen, J. B. & Hildebrand, R. S. (2019). Trace element discrimination of arc, slab failure, and A-type granitic rocks. *Lithos* **348–349**.

- Whalen, J. B., Wodicka, N., Taylor, B. E. & Jackson, G. D. (2010). Cumberland batholith, Trans-Hudson Orogen, Canada: Petrogenesis and implications for Paleoproterozoic crustal and orogenic processes. *Lithos* **117**, 99–118.
- White, R. W., Powell, R., Holland, T. J. B., Johnson, T. E. & Green, E. C. R. (2014). New mineral activity – composition relations for thermodynamic calculations in metapelitic systems. *Journal of Metamorphic Geology* **32**, 261–286.
- Wiedenbeck, M., Alle, P., Corfu, F., Griffin, W. L., Meier, M., Oberli, F., Von Quadt, A., Roddick, J. C. & Spiegel, W. (1995). Three Natural Zircon Standards for U-Th-Pb, Lu-Hf, Trace Element and REE Analyses. *Geostandards Newsletter* **19**, 1–23.
- Wiedenbeck, M., Hanchar, J. M., Peck, W. H., Sylvester, P., Valley, J., Whitehouse, M., Kronz, A., Morishita, Y. & Nasdala, L. (2004). Further Characterisation of the 91500 Zircon Crystal. *Geost* **28**, 9–39.
- Zhao, G., Sun, M., Wilde, S. A. & Li, S. (2004). A Paleo-Mesoproterozoic supercontinent: Assembly, growth and breakup. *Earth-Science Reviews* **67**, 91–123.

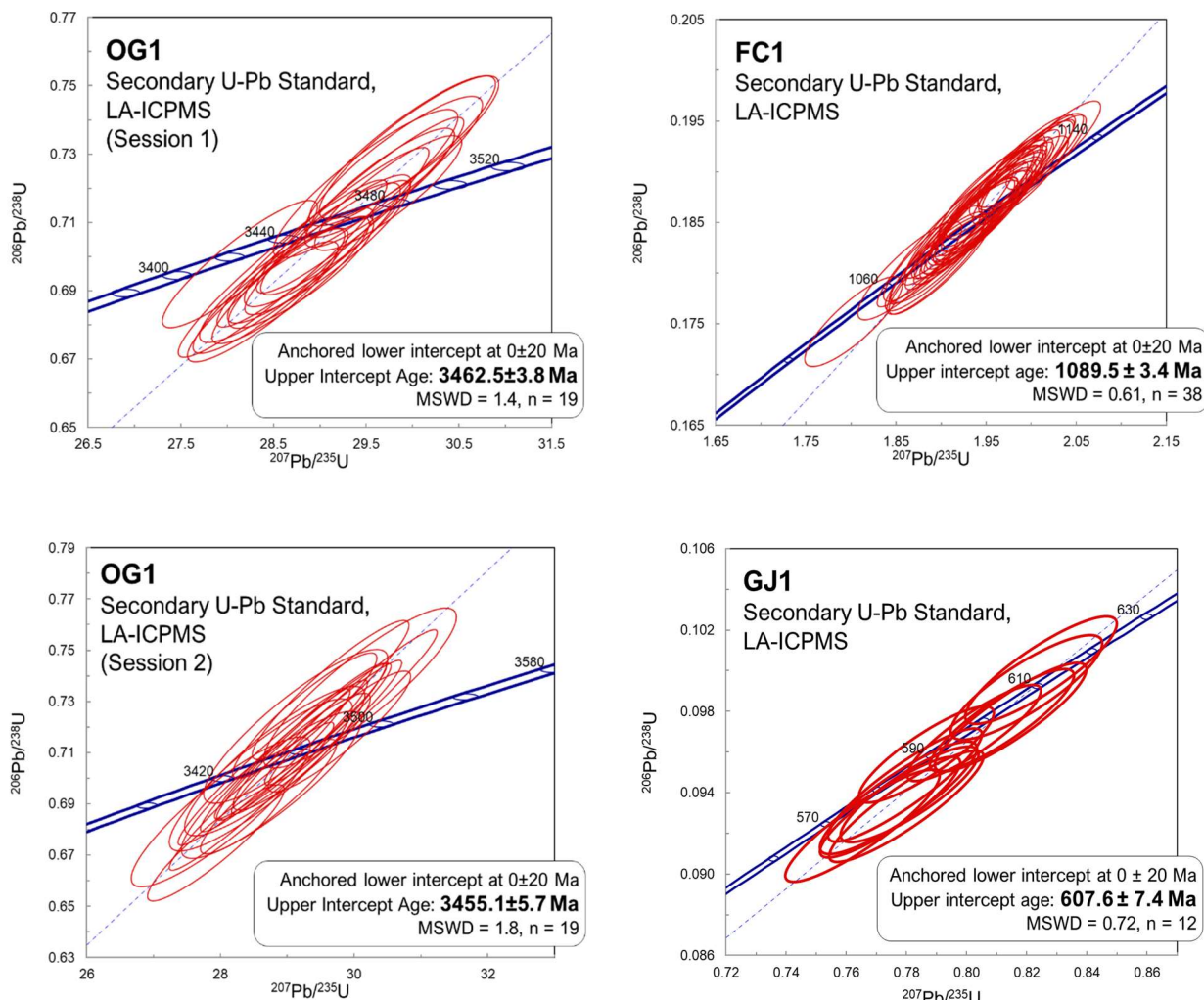
APPENDIX 1: LA/LASS-ICPMS OPERATION PARAMETERS AND STANDARD VERIFICATION

Appendix 1, Table 1: LA-ICPMS operating parameters for zircon

Laboratory and Sample Preparation	
<i>Laboratory Name</i>	Canadian Center for Isotopic Microanalysis, Department of Earth and Atmospheric Science, University of Alberta
<i>Sample type/Mineral</i>	In-situ zircon and separated zircon
<i>Sample Preparation</i>	Polished Thin Section, ~30 µm thickness, and polished 1-inch epoxy rounds
<i>Imaging</i>	CL, High Contrast BSE on Zeiss EVO SEM with Variable Pressure aperture
Laser Ablation System	
<i>Make, Model, and Type</i>	ESI / New Wave Research UP213 Nd YAG
<i>Ablation Cell and Volume</i>	ESI / New Wave Research Supercell, 33 cm ³ volume
<i>Laser Wavelength (nm)</i>	213 nm
<i>Pulse Width</i>	< 4 ns
<i>Fluence</i>	1.5-2.5 J/cm ²
<i>Repetition Rate</i>	4 Hz
<i>Ablation Duration</i>	41 s
<i>Ablation pit depth/ablation rate</i>	~15 µm pit depth, estimated via optical microscope. Equivalent to 0.063 µm/pulse
<i>Spot Diameter</i>	25-30 µm
<i>Sampling Mode</i>	Static Spot Ablation
<i>Carrier Gas</i>	100% He, with Ar make-up gas combined at Nu Instruments DSN100
<i>Cell Carrier Gas Flow</i>	1 L/min
ICP-MS Instrument	
<i>Make, Model, and type</i>	Nu Plasma I Multi-Collector ICP-MS
<i>Sample Introduction</i>	Ablation aerosol combined with co-aspiration of 0.5 ppb Tl tracer solution
<i>RF Power</i>	1300 W
<i>Make-up gas flow</i>	Sourced from Nu instrument DSN-100 desolvating nebuliser, nebuliser pressure ~30 psi Ar
<i>Detection System</i>	Mixed Faraday and electron multiplier ion counting array
<i>Masses Measured</i>	203 – 207, 235, 238
<i>Total Integration Time (per data point)</i>	1 s (30 points total)
<i>Ion Counter dead time</i>	7.9 ns (IC0), 10.7 ns (IC1), and 9.8 ns (IC2)
Data Processing	
<i>Blanks</i>	<ul style="list-style-type: none"> • 2% HNO₃ + Gas Blank done prior to each sample (Blank 1) • 0.5 ppb Tl Solution + Gas + 2% HNO₃ Blank done prior to unknowns (Blank 2) and every subsequent 10 spot analyses (Blank ≥3). Blank corrections are done if necessary, to account for instrument drift and any Tl solution inconstancies
<i>Calibration Strategy</i>	LH9415 used as primary reference material; FC1, OG1, GJ1 used as validation (exception to 17SRB-L54, GJ1 used as primary)
<i>Reference Material Information</i>	LH9415 (Aston et al., (1998)) FC1 (Paces and Miller, (1993)) GJ1 (Jackson et al. (2004)) OG1 (Stern et al., (2009))

Appendix 1, Table 1 cont.

<i>Mass discrimination</i>	Tl tracer solution used for mass bias correction of Pb isotopes $^{206}\text{Pb}/^{238}\text{U}$ normalized to primary reference material
<i>Common Pb correction</i>	No common Pb correction applied, common Pb influenced data ($^{206}\text{Pb}/^{204}\text{Pb}$ below 1000) rejected
<i>Uncertainty level and propagation</i>	Uncertainty reported as 2s absolute, error propagation by quadratic addition. If SD of the mean was >0.005, a combined constant external error and SD of the mean of 0.005 was used prior to quadratic addition.
<i>QC/Validation</i>	FC1: 1089.7 ± 3.8 Ma OG1: 3462.5 ± 3.4 Ma GJ1: $607. \pm 9$ Ma



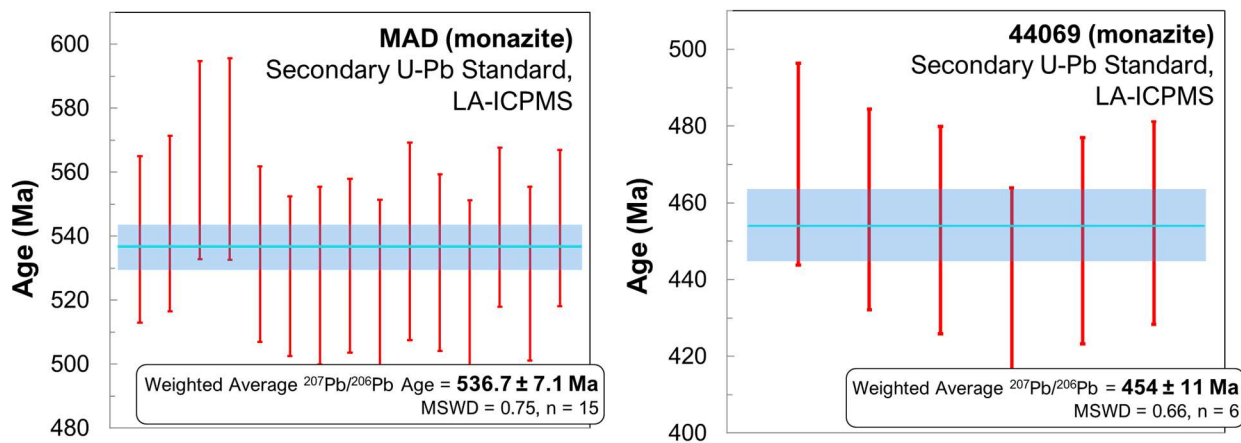
Appendix 1, Figure 1: U-Pb Wetherill Concordia Diagrams of secondary standards for LA-ICPMS of zircon, constructed with Isoplot v4.15 from Ludwig (2004). All error ellipses shown are 2σ . Standards were measured across three sessions with three unknowns. Standard OG1 for Session 2 was analysed along side sample 17SRB-O009A3.

Appendix 1, Table 2: LA-ICPMS operating parameters for monazite

<i>Laboratory and Sample Preparation</i>	
<i>Laboratory Name</i>	Canadian Center for Isotopic Microanalysis, Department of Earth and Atmospheric Science, University of Alberta
<i>Sample type/Mineral</i>	In-situ monazite
<i>Sample Preparation</i>	Polished Thin Section, ~30 µm thickness
<i>Imaging</i>	High Contrast BSE on Zeiss EVO SEM with Variable Pressure aperture
<i>Laser Ablation System</i>	
<i>Make, Model, and Type</i>	ESI / New Wave Research UP213 Nd YAG
<i>Ablation Cell and Volume</i>	ESI / New Wave Research Supercell, 33 cm ³ volume
<i>Laser Wavelength (nm)</i>	213 nm
<i>Pulse Width</i>	< 4 ns
<i>Fluence</i>	1.5-2 J/cm ²
<i>Repetition Rate</i>	4 Hz
<i>Ablation Duration</i>	41 s
<i>Ablation pit depth/ablation rate</i>	~15 µm pit depth, estimated via optical microscope. Equivalent to 0.063 µm/pulse
<i>Spot Diameter</i>	12 µm
<i>Sampling Mode</i>	Static Spot Ablation
<i>Carrier Gas</i>	100% He, with Ar make-up gas combined at Nu Instruments DSN100
<i>Cell Carrier Gas Flow</i>	1 L/min
<i>ICP-MS Instrument</i>	
<i>Make, Model, and type</i>	Nu Plasma I Multi-Collector ICP-MS
<i>Sample Introduction</i>	Ablation aerosol combined with co-aspiration of 0.5 ppb Tl solution
<i>RF Power</i>	1300 W
<i>Make-up gas flow</i>	Sourced from Nu instrument DSN-100 desolvating nebuliser, nebuliser pressure ~30 psi Ar
<i>Detection System</i>	Mixed Faraday and electron multiplier ion counting array
<i>Masses Measured</i>	203 – 207, 235, 238
<i>Total Integration Time (per data point)</i>	1 s (30 points total)
<i>Ion Counter dead time</i>	7.9 ns (IC0), 10.7 ns (IC1), and 9.8 ns (IC2)
<i>Data Processing</i>	
<i>Blanks</i>	<ul style="list-style-type: none"> • 2% HNO₃ + Gas Blank done prior to each sample (Blank 1) • 0.5 ppb Tl Solution + Gas + 2% HNO₃ Blank done prior to unknowns (Blank 2) and every subsequent 10 spot analyses (Blank ≥3). • Blank corrections are done if necessary, to account for instrument drift and any Tl solution inconstancies
<i>Calibration Strategy</i>	Western Australia (WA) used as primary reference material; Madagascar (MAD) and 44069 used as validation (For sessions 1 and 2 respectively)
<i>Reference Material Information</i>	Western Australia (Simonetti et al., 2006; Heaman et al., unpublished data) Madagascar (Simonetti et al., 2006; Heaman et al., unpublished data) 44069 (Aleinikoff et al. 2006)

Appendix 1, Table 2 cont.

<i>Data Processing</i>	In-house spreadsheet for data normalisation, uncertainty propagation and age calculation. Isoplot v4.15 (Ludwig, 2012) used for weighted average age calculation and U-Pb Concordia plot construction
<i>Mass discrimination</i>	Tl tracer solution used for mass bias correction of Pb isotopes
<i>Common Pb correction</i>	206Pb/238 U normalized to primary reference material
<i>Uncertainty level and error propagation</i>	No common Pb correction applied, common Pb influenced data (206 Pb/204 Pb counts below 1000) rejected
<i>QC/Validation</i>	Uncertainty reported as 2s absolute, error propagation by quadratic addition. If SD of the mean was >0.005, a combined constant external error and SD of the mean of 0.005 was used prior to quadratic addition. MAD: 537.2 Ma \pm 6.8 Ma 44069: 454 \pm 11 Ma



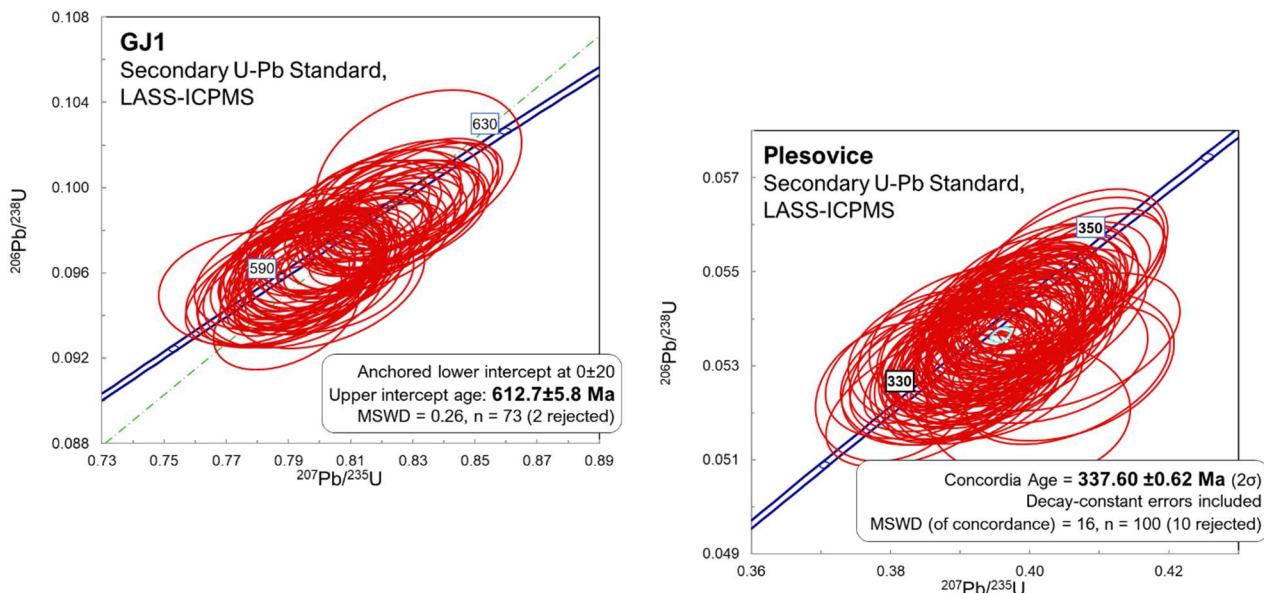
Appendix 1, Figure 2: U-Pb Wetherill Concordia Diagrams of secondary standards for LA-ICPMS of monazite, constructed with Isoplot v4.15 from Ludwig (2004). All error ellipses shown are 2σ .

Appendix 1, Table 3: LASS-ICPMS operating parameters

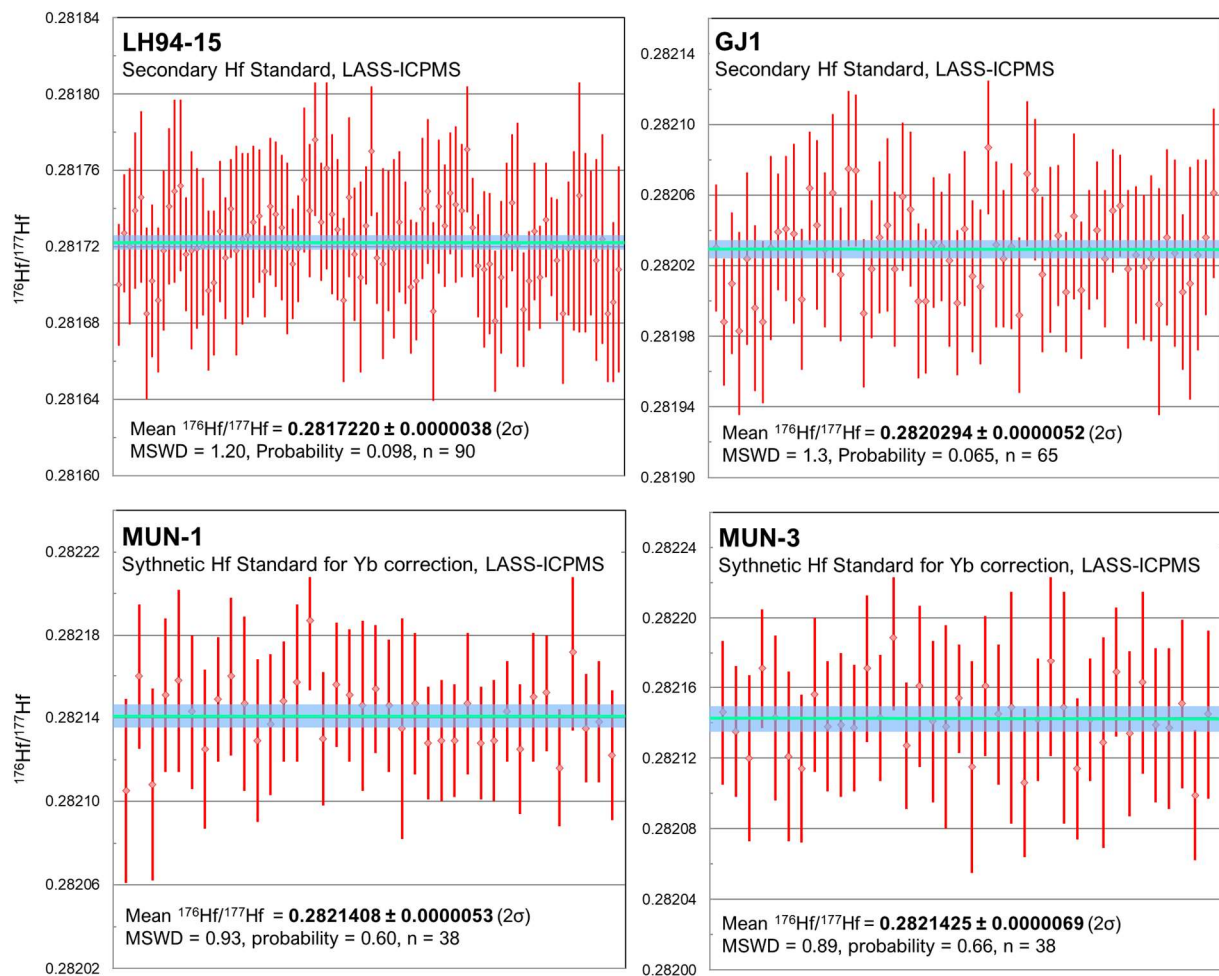
Laboratory and Sample Preparation		
Laboratory Name	Artic Resources Laboratory, Department of Earth and Atmospheric Science, University of Alberta	
Sample type/Mineral	In-situ zircon and separated zircon	
Sample Preparation	Polished 1-inch epoxy rounds and Polished Thin Section, ~30 µm thickness	
Imaging	CL, High Contrast BSE on Zeiss EVO SEM with Variable Pressure aperture	
Laser Ablation System		
Make, Model, and Type	Resonetics M-50 LR	
Ablation Cell	Laurin Technic S155 two-volume (2 cm ³ inner cell funnel to 380 cm ³ cell box)	
Laser Wavelength (nm)	193 nm	
Pulse Width	< 4 ns	
Fluence	5 J/cm ²	
Repetition Rate	10 Hz	
Ablation Duration	45 s	
Ablation pit depth/ablation rate	~35-40 µm pit depth, estimated via optical microscope. Equivalent to 0.78 µm/pulse	
Spot Diameter	33 µm	
Sampling Mode	Static Spot Ablation	
Carrier Gas	100% He, mixed with N ₂ gas (5mL/min) and prior to split and with Ar make-up gas prior to instrument introduction	
Cell Carrier Gas Flow	1.2 L/min	
Instruments		
	Lu-Hf	U-Pb
Make, Model, and type	Thermo Neptune Plus MC-ICP-MS	
Sample Introduction	Ablation aerosol (He, N ₂) split with "Y" connector to separate instruments and mixed with Ar sample gas	
RF Power	1200 W	
Make-up gas flow	Cool/Plasma (Ar) 16 L/min Auxiliary (Ar) 0.85 L/min Nebulizer (Ar) 0.6 L/min	Cool/Plasma (Ar) 0.85 L/min Auxiliary (Ar) 0.85 L/min Nebulizer (Ar) 1 L/min
Detection System	Faraday Detectors	
Masses Measured	171, 173, 175 – 180, 182	
Total Integration Time (per data point)	1 s	
Data Processing		
Blanks	<ul style="list-style-type: none"> • Baseline measured 15s prior to each analysis • Auto-Baseline integration line from Iolite from primary reference materials used for corrections in all samples 	
Calibration Strategy	LH9415 used as primary reference material for U-Pb; GJ1, Plesovice used as validation	

Appendix 1, Table 3 cont.

Calibration Strategy (cont.)	Plesovice used as a primary reference material for Lu-Hf; GJ1, LH94-15 used as validation MUN-1 and MUN-3 used to correct for Yb interference on mass 176.
Reference Material Information	LH9415 (Aston et al., 1998, no published literature value for Hf ratios) GJ1 (Jackson et al., 2004) Plesovice (Sláma et al., 2008)
Data Processing	Iolite for mass bias correction, data normalisation, integration time selection Isoplot v4.15 (Ludwig, 2012) used for weighted average of ϵ_{Hf} values, weighted average age calculation, and U-Pb Concordia plot construction
Mass discrimination	206Pb/238U normalized to primary reference material
Common Pb correction	No common Pb correction applied, common Pb influenced data (206 Pb/204 Pb counts below 1000) rejected
Uncertainty level and propagation	Spreadsheet by Ickert (2013) used for individual ϵ_{Hf} error propagation, using a model 1 solution to 2s absolute errors. U-Pb uncertainty reported as 2s absolute, error propagation by quadratic addition.
QC/Validation	GJ1: 612.7 ± 5.8 Ma, $^{176}\text{Hf}/^{177}\text{Hf} = 0.2820294 \pm 0.0000052$ Plesovice: 337.60 ± 0.62 Ma LH94-15: $^{176}\text{Hf}/^{177}\text{Hf} = 0.2817220 \pm 0.0000038$



Appendix 1, Figure 3: U-Pb Wetherill Concordia Diagrams of secondary standards for LASS-ICPMS of zircon, constructed with Isoplot v4.15 from Ludwig (2004). All error ellipses shown are 2 σ . Standards were measured across 6 sessions, one of which was a U-Pb only session.



Appendix 1, Figure 4: $^{176}\text{Hf}/^{177}\text{Hf}$ weighted averages of secondary standards for LASS-ICPMS Lu-Hf of zircon, constructed with Isoplot v4.15 from Ludwig (2004). All red error bars shown are 2 σ , and the shaded blue region shows 2 σ error in the weighted mean. Standards were measured across 5 sessions.

APPENDIX 2: COMPILED U-PB GEOCHRONOLOGY RESULTS

Table 1: Compiled U-Pb Geochronology Results for the Boothia Ferroan Granitoid Complex

Sample Name, Preperation and Method	Spot Name	Model Ages (Ma)																		
		206Pb (cps)	204Pb (cps)	$^{207}\text{Pb}/^{206}\text{Pb}$		$^{207}\text{Pb}/^{235}\text{U}$		$^{206}\text{Pb}/^{238}\text{U}$		ρ value	$^{207}\text{Pb}/^{206}\text{Pb}$		$^{207}\text{Pb}/^{235}\text{U}$		disc %					
				$\pm 2\sigma$	$\pm 2\sigma$	$\pm 2\sigma$	$\pm 2\sigma$	$\pm 2\sigma$	$\pm 2\sigma$		$\pm 2\sigma$	$\pm 2\sigma$	$\pm 2\sigma$	$\pm 2\sigma$						
17SRB-A018A (Charnockite, SE pluton)																				
<i>Thin Section, Zircon</i>																				
<i>LA-ICPMS</i>																				
	A18S1-1-1	273491	27	0.1129	0.0012	4.8986	0.1410	0.3147	0.0084	0.93	1847	19	1802	24	1764	41	4.72			
	A18S1-2-2	193530	38	0.1121	0.0012	4.8662	0.1350	0.3148	0.0081	0.93	1834	19	1796	23	1764	39	3.95			
	A18S1-2-3	174665	30	0.1124	0.0012	4.9699	0.1314	0.3208	0.0078	0.92	1838	19	1814	22	1793	38	2.49			
	A18S1-3-1	177303	25	0.1116	0.0012	4.7886	0.1358	0.3111	0.0082	0.93	1826	19	1783	24	1746	40	4.59			
	A18S1-3-5	206536	55	0.1117	0.0012	4.8182	0.1366	0.3129	0.0082	0.93	1827	19	1788	24	1755	40	4.08			
	A18S1-4a-6	153832	51	0.1130	0.0012	4.9242	0.1417	0.3160	0.0084	0.93	1848	19	1806	24	1770	41	4.39			
	A18S1-4b-7	292077	36	0.1116	0.0012	4.8761	0.1543	0.3170	0.0095	0.95	1825	19	1798	26	1775	46	2.81			
	A18S1-5-8	333934	47	0.1128	0.0012	4.8074	0.1379	0.3092	0.0082	0.93	1844	19	1786	24	1737	40	6.20			
	A18S1-6-9	208312	32	0.1125	0.0012	4.7860	0.1418	0.3085	0.0086	0.94	1840	19	1782	25	1734	42	6.15			
	A18S1-6-10	217563	34	0.1125	0.0012	4.8286	0.1371	0.3113	0.0082	0.93	1840	19	1790	24	1747	40	5.33			
	A18S1-7-11	302336	28	0.1125	0.0012	4.9629	0.1439	0.3198	0.0087	0.93	1841	19	1813	24	1789	42	2.90			
	A18S1-8-12	561010	52	0.1124	0.0012	4.9404	0.1436	0.3187	0.0087	0.93	1839	19	1809	24	1783	42	3.14			
	A18S1-12a-13	244135	40	0.1110	0.0012	4.7487	0.1442	0.3101	0.0088	0.94	1817	19	1776	25	1741	43	4.32			
	A18S1-13-14	330508	33	0.1128	0.0012	4.8252	0.1337	0.3103	0.0080	0.93	1844	19	1789	23	1742	39	5.86			
	A18S1-13-15	308045	32	0.1124	0.0012	4.9516	0.1450	0.3194	0.0087	0.93	1839	19	1811	24	1787	42	2.92			
	A18S1-14-16	526106	36	0.1112	0.0011	4.7473	0.1352	0.3096	0.0082	0.93	1819	19	1776	24	1739	40	4.63			
	A18S1-2-17	168115	37	0.1125	0.0012	4.8513	0.1322	0.3128	0.0079	0.92	1840	19	1794	23	1755	38	4.84			
	A18S1-3-18	166614	17	0.1108	0.0011	4.6896	0.1305	0.3068	0.0079	0.93	1813	19	1765	23	1725	39	5.11			
17SRB-D046A (Charnockite, SW pluton)																				
<i>Thin Section, Zircon</i>																				
<i>LASS-ICPMS</i>																				
	D46 - 1	61900	5	0.1114	0.0014	5.2410	0.1200	0.3387	0.0061	0.51	1820	22	1859	20	1880	30	-3.19			
	D46 - 3	52000	22	0.1122	0.0012	5.0140	0.1200	0.3245	0.0058	0.70	1832	20	1821	21	1811	28	1.16			
	D46 - 5	76100	25	0.1114	0.0012	5.1300	0.1400	0.3334	0.0068	0.78	1820	20	1839	24	1854	33	-1.83			
	D46 - 6	73200	21	0.1119	0.0010	5.1180	0.1100	0.3312	0.0055	0.50	1832	18	1838	18	1844	27	-0.65			

Model Ages (Ma)																	
Sample Name, Preperation and Method	Spot Name	206Pb (cps)	204Pb (cps)	207Pb/ 206Pb ± 2σ	207Pb/ 235U ± 2σ	206Pb/ 238U ± 2σ	p value	207Pb/ 206Pb ± 2σ	207Pb/ 235U ± 2σ	206Pb/ 238U ± 2σ	disc %						
	D46 - 7	87000	13	0.1131	0.0013	5.2380	0.1300	0.3372	0.0070	0.74	1847	20	1858	21	1873	34	-1.39
	D46 - 8	53200	17	0.1128	0.0014	5.3340	0.1200	0.3437	0.0057	0.47	1842	23	1874	20	1904	27	-3.26
	D46 - 9	150000	73	0.1123	0.0008	5.1360	0.1300	0.3340	0.0065	0.90	1836	13	1841	22	1857	31	-1.13
	D46 - 10	59800	21	0.1128	0.0012	5.1590	0.1200	0.3312	0.0055	0.58	1842	20	1845	20	1844	27	-0.11
	D46 - 13	66500	5	0.1116	0.0010	4.9370	0.1100	0.3211	0.0051	0.58	1823	16	1808	18	1795	25	1.56
	D46 - 14	64900	20	0.1117	0.0013	5.2150	0.1400	0.3402	0.0071	0.80	1825	21	1854	23	1887	34	-3.29
	D46 - 15	75100	9	0.1130	0.0012	5.2120	0.1200	0.3354	0.0059	0.68	1846	19	1854	20	1864	28	-0.97
	D46 - 16	85000	28	0.1115	0.0009	5.1630	0.1100	0.3370	0.0055	0.58	1822	15	1846	19	1872	27	-2.67
	D46 - 18	79200	36	0.1122	0.0012	5.2200	0.1300	0.3393	0.0062	0.81	1832	19	1855	22	1883	30	-2.71
	D46 - 19	111700	32	0.1122	0.0012	5.2110	0.1200	0.3367	0.0058	0.53	1834	19	1854	19	1871	28	-1.98
	D46 - 24	50020	8	0.1134	0.0012	5.2160	0.1200	0.3352	0.0062	0.71	1852	19	1854	21	1863	30	-0.59
	D46 - 25	149700	-8	0.1114	0.0011	5.1180	0.1200	0.3346	0.0061	0.69	1820	17	1839	20	1861	29	-2.20
	D46 - 26	83700	-8	0.1123	0.0012	5.3810	0.1200	0.3474	0.0063	0.62	1834	19	1881	20	1922	30	-4.58
	D46 - 27	127500	23	0.1116	0.0009	5.1970	0.1100	0.3369	0.0053	0.46	1823	15	1852	18	1871	25	-2.57
17SRB-D048A (Charnockite, SW pluton)																	
<i>Thin Section, Zircon</i>																	
<i>LASS-ICPMS</i>																	
	D48 - 1	111100	24	0.1104	0.0018	5.2590	0.1600	0.3474	0.0085	0.34	1804	30	1861	25	1922	41	-6.14
	D48 - 3	99860	46	0.1125	0.0018	5.2090	0.1500	0.3375	0.0085	0.52	1838	29	1853	25	1874	41	-1.92
	D48 - 4	45700	-29	0.1109	0.0021	5.1100	0.1500	0.3358	0.0081	0.49	1811	34	1837	25	1866	39	-2.95
	D48 - 5	40450	-33	0.1112	0.0029	5.2900	0.1800	0.3473	0.0094	0.50	1815	47	1867	28	1921	45	-5.52
	D48 - 6	83700	-13	0.1128	0.0016	5.1680	0.1400	0.3336	0.0074	0.56	1843	26	1847	23	1856	36	-0.70
	D48 - 7	182000	61	0.1125	0.0016	5.2560	0.1600	0.3397	0.0083	0.08	1839	26	1861	25	1885	40	-2.44
	D48 - 8	164500	32	0.1105	0.0015	5.1690	0.1400	0.3399	0.0076	0.31	1806	24	1847	23	1886	36	-4.24
	D48 - 9	55600	-8	0.1111	0.0017	5.2130	0.1500	0.3412	0.0081	0.48	1815	28	1854	24	1892	39	-4.07
	D48 - 12	31810	1	0.1116	0.0021	5.0140	0.1500	0.3271	0.0075	0.15	1821	34	1820	26	1824	36	-0.16
	D48 - 13	61900	13	0.1102	0.0016	5.0820	0.1400	0.3343	0.0076	0.45	1805	26	1832	24	1859	36	-2.90
	D48 - 14	80400	4	0.1122	0.0017	5.1990	0.1500	0.3362	0.0081	0.48	1833	27	1852	24	1868	39	-1.87
	D48 - 15	152100	24	0.1113	0.0014	5.0990	0.1400	0.3323	0.0076	0.36	1819	24	1835	23	1849	37	-1.62
	D48 - 17	75900	25	0.1124	0.0020	5.1870	0.1500	0.3347	0.0086	0.51	1836	32	1850	25	1861	41	-1.34

Model Ages (Ma)																		
Sample Name, Preperation and Method	Spot Name	206Pb (cps)	204Pb (cps)	$^{207}\text{Pb}/^{206}\text{Pb}$		$^{207}\text{Pb}/^{235}\text{U}$		$^{206}\text{Pb}/^{238}\text{U}$		ρ value	$^{207}\text{Pb}/^{206}\text{Pb}$		$^{207}\text{Pb}/^{235}\text{U}$		$^{206}\text{Pb}/^{238}\text{U}$		$\pm 2\sigma$	disc %
	D48 - 18	53300	3	0.1119	0.0018	4.9240	0.1400	0.3191	0.0075	0.42	1828	29	1805	24	1785	37	2.41	
	D48 - 19	73600	26	0.1120	0.0019	5.1770	0.1500	0.3352	0.0077	0.53	1829	30	1848	24	1863	37	-1.83	
	D48 - 20	41790	15	0.1131	0.0019	5.1420	0.1600	0.3296	0.0079	0.16	1847	30	1842	26	1836	38	0.60	
	D48 - 21	90500	36	0.1115	0.0017	5.1100	0.1500	0.3314	0.0079	0.44	1822	27	1837	25	1845	38	-1.25	
	D48 - 23	74200	8	0.1132	0.0020	5.4200	0.2100	0.3498	0.0110	0.16	1848	32	1885	33	1932	51	-4.35	
	D48 - 25	90600	-6	0.1119	0.0015	5.1980	0.1400	0.3373	0.0075	0.39	1828	25	1852	24	1873	36	-2.40	
	D48 - 28	81600	10	0.1128	0.0019	4.9330	0.1500	0.3173	0.0078	0.31	1843	31	1807	25	1776	38	3.77	
17SRB-L053A (Charnockite, SW pluton)																		
<i>Grain Mount, Zircon</i>																		
<i>LASS-ICPMS</i>																		
	L53 - 2	264900	59	0.1115	0.0011	5.0430	0.1300	0.3278	0.0066	0.78	1823	18	1826	21	1827	32	-0.22	
	L53 - 4	161400	22	0.1135	0.0012	4.9490	0.1100	0.3179	0.0057	0.52	1855	19	1813	17	1780	28	4.21	
	L53 - 6	239000	36	0.1116	0.0009	4.9740	0.1100	0.3246	0.0057	0.84	1824	15	1815	17	1812	28	0.66	
	L53 - 9	127600	54	0.1124	0.0013	4.8910	0.1100	0.3175	0.0061	0.67	1836	21	1800	19	1777	30	3.32	
	L53 - 10	238000	85	0.1111	0.0011	5.0960	0.1200	0.3336	0.0064	0.83	1816	18	1835	20	1855	31	-2.10	
	L53 - 16	106100	48	0.1127	0.0012	5.0900	0.1200	0.3276	0.0062	0.69	1841	20	1833	20	1826	30	0.82	
	L53 - 17	98300	40	0.1119	0.0011	5.0130	0.1200	0.3260	0.0062	0.40	1828	18	1820	19	1819	30	0.49	
	L53 - 18	138900	-12	0.1117	0.0010	5.0170	0.1100	0.3268	0.0058	0.79	1825	17	1822	19	1823	28	0.11	
	L53 - 19	136000	-7	0.1123	0.0010	4.9940	0.1100	0.3233	0.0058	0.47	1835	16	1818	18	1805	28	1.66	
	L53 - 20	95200	20	0.1130	0.0011	4.9290	0.1100	0.3163	0.0060	0.80	1846	18	1807	19	1772	29	4.18	
	L53 - 21	164200	25	0.1120	0.0010	5.0160	0.1100	0.3250	0.0058	0.86	1831	16	1822	18	1814	28	0.95	
	L53 - 26	98600	43	0.1110	0.0012	5.0390	0.1100	0.3284	0.0062	0.66	1813	19	1825	19	1830	30	-0.93	
	L53 - 30	210000	40	0.1108	0.0009	4.9350	0.1000	0.3223	0.0055	0.55	1812	15	1808	17	1801	27	0.62	
	L53 - 32	42200	19	0.1112	0.0014	5.2110	0.1200	0.3387	0.0069	0.60	1817	23	1854	20	1880	33	-3.35	
	L53 - 33	130200	44	0.1124	0.0013	4.9910	0.1100	0.3212	0.0063	0.67	1836	21	1817	19	1795	31	2.28	
17SRB-L054A (Charnockite, SW Pluton)																		
<i>Thin Section, Zircon</i>																		
<i>LA-ICPMS</i>																		
	L54S1-1a-1	106917	33	0.1120	0.0014	5.0447	0.1439	0.3268	0.0083	0.89	1831	23	1827	24	1823	40	0.48	
	L54S1-1a-2	91353	41	0.1131	0.0018	5.0919	0.1452	0.3264	0.0078	0.84	1850	28	1835	24	1821	38	1.60	
	L54S1-1a-3	132185	53	0.1125	0.0016	5.1015	0.1490	0.3289	0.0084	0.88	1840	25	1836	25	1833	41	0.36	
	L54S1-1a-4	133703	45	0.1124	0.0015	5.0618	0.1443	0.3265	0.0082	0.88	1839	24	1830	24	1821	40	0.99	

		Model Ages (Ma)															
Sample Name, Preperation and Method	Spot Name	206Pb (cps)	204Pb (cps)	$^{207}\text{Pb}/^{206}\text{Pb}$		$^{207}\text{Pb}/^{235}\text{U}$		$^{206}\text{Pb}/^{238}\text{U}$		ρ value	$^{207}\text{Pb}/^{206}\text{Pb}$		$^{207}\text{Pb}/^{235}\text{U}$		$^{206}\text{Pb}/^{238}\text{U}$		disc %
	L54S1-1b-1	109378	34	0.1110	0.0014	5.0519	0.1480	0.3300	0.0087	0.90	1816	23	1828	25	1838	42	-1.20
	L54S1-3-2	123472	41	0.1125	0.0015	5.0511	0.1612	0.3256	0.0095	0.91	1841	23	1828	27	1817	46	1.30
	L54S1-5a-1	175502	28	0.1105	0.0014	4.8772	0.1312	0.3200	0.0076	0.88	1808	23	1798	22	1790	37	1.01
	L54S1-5b-1	63560	22	0.1119	0.0015	4.9932	0.1512	0.3237	0.0088	0.89	1830	25	1818	25	1808	42	1.26
	L54S1-5b-2	128518	38	0.1131	0.0016	5.1855	0.1474	0.3327	0.0082	0.86	1849	26	1850	24	1851	39	-0.12
	L54S1-5c-1	195195	23	0.1111	0.0014	5.0324	0.1503	0.3285	0.0089	0.90	1818	23	1825	25	1831	43	-0.75
	L54S1-5c-2	79155	13	0.1109	0.0014	4.9729	0.1402	0.3252	0.0082	0.89	1814	23	1815	24	1815	40	-0.05
	L54S1-6-1	111853	23	0.1110	0.0014	4.9411	0.1486	0.3228	0.0088	0.91	1816	23	1809	25	1803	43	0.73
	L54S1-7-1	177283	24	0.1108	0.0014	4.9426	0.1568	0.3236	0.0094	0.92	1812	23	1810	26	1807	46	0.29
	L54S1-9a-1	72579	21	0.1116	0.0015	4.9792	0.1506	0.3235	0.0087	0.89	1826	25	1816	25	1807	42	1.04
	L54S1-9b-1	52256	24	0.1118	0.0015	5.0223	0.1511	0.3259	0.0088	0.89	1829	24	1823	25	1818	42	0.56
	L54S1-10a-1	93752	24	0.1112	0.0014	4.9153	0.1353	0.3205	0.0078	0.88	1819	23	1805	23	1792	38	1.51
	L54S1-10b-1	420608	25	0.1103	0.0014	4.9420	0.1483	0.3248	0.0089	0.91	1805	23	1809	25	1813	43	-0.45
	L54S1-11-1	121912	22	0.1116	0.0014	4.9261	0.1380	0.3201	0.0080	0.89	1826	23	1807	23	1790	39	1.99
	L54S1-12a-1	148889	22	0.1110	0.0014	4.9150	0.1441	0.3212	0.0085	0.90	1815	23	1805	24	1796	41	1.08
	L54S1-12b-1	116764	25	0.1113	0.0014	4.9961	0.1500	0.3255	0.0088	0.90	1821	23	1819	25	1817	43	0.23
	L54S1-14-1	135055	33	0.1111	0.0014	4.9460	0.1543	0.3229	0.0092	0.91	1817	23	1810	26	1804	45	0.74
	L54S1-14-2	121659	27	0.1113	0.0014	4.9573	0.1572	0.3231	0.0093	0.91	1820	23	1812	26	1805	45	0.83
	L54S1-16-1	92757	28	0.1114	0.0015	4.9792	0.1781	0.3241	0.0108	0.93	1823	24	1816	30	1810	52	0.71
	L54S1-17-1	773320	35	0.1105	0.0014	5.0299	0.1318	0.3302	0.0076	0.88	1807	22	1824	22	1839	37	-1.74
	L54S1-18-1	64161	28	0.1116	0.0015	4.9760	0.1743	0.3232	0.0105	0.93	1826	24	1815	29	1806	51	1.16

17SRB-A025A5 (Fayalite Granite, NE pluton)

Grain Mount, Zircon

LASS-ICPMS

A25-A5 - 1	273100	59	0.1117	0.0009	5.0290	0.1100	0.3253	0.0058	0.87	1826	15	1824	18	1815	28	0.60
A25-A5 - 2	1610000	106	0.1126	0.0009	5.3240	0.1100	0.3422	0.0059	0.86	1840	14	1873	18	1897	29	-3.00
A25-A5 - 3	1290000	68	0.1112	0.0009	4.9270	0.1200	0.3197	0.0068	0.95	1819	15	1806	20	1788	33	1.71
A25-A5 - 4	646000	61	0.1125	0.0009	5.1570	0.1100	0.3323	0.0059	0.91	1839	14	1845	19	1849	29	-0.56
A25-A5 - 5	304000	83	0.1121	0.0010	5.0990	0.1200	0.3294	0.0066	0.89	1832	16	1835	20	1835	32	-0.17
A25-A5 - 6	217000	61	0.1122	0.0010	5.0920	0.1100	0.3280	0.0062	0.91	1835	16	1834	19	1828	30	0.36
A25-A5 - 7	518000	47	0.1114	0.0009	5.1460	0.1100	0.3338	0.0062	0.90	1822	15	1843	19	1857	30	-1.90
A25-A5 - 8	538000	46	0.1121	0.0009	5.1670	0.1100	0.3333	0.0060	0.93	1832	14	1847	19	1854	29	-1.18

Model Ages (Ma)																	
Sample Name, Preperation and Method	Spot Name	206Pb (cps)	204Pb (cps)	$^{207}\text{Pb}/^{206}\text{Pb}$		$^{207}\text{Pb}/^{235}\text{U}$		$^{206}\text{Pb}/^{238}\text{U}$		ρ value	$^{207}\text{Pb}/^{206}\text{Pb}$		$^{207}\text{Pb}/^{235}\text{U}$		$^{206}\text{Pb}/^{238}\text{U}$		disc %
	A25-A5 - 9	178000	57	0.1122	0.0010	5.1170	0.1200	0.3297	0.0069	0.90	1833	17	1838	20	1836	33	-0.16
	A25-A5 - 10	832000	55	0.1121	0.0009	5.2400	0.1100	0.3383	0.0062	0.95	1833	14	1859	19	1878	30	-2.42
	A25-A5 - 11	320000	79	0.1111	0.0010	5.1210	0.1100	0.3336	0.0061	0.88	1816	16	1840	18	1855	29	-2.11
	A25-A5 - 12	222000	61	0.1111	0.0010	5.1970	0.1200	0.3397	0.0067	0.91	1815	16	1851	21	1884	32	-3.64
	A25-A5 - 13	335000	62	0.1118	0.0009	5.1420	0.1100	0.3334	0.0059	0.90	1828	15	1843	19	1855	29	-1.46
	A25-A5 - 14	538000	64	0.1117	0.0009	5.1400	0.1100	0.3332	0.0062	0.94	1826	14	1842	19	1854	30	-1.54
	A25-A5 - 15	170500	60	0.1116	0.0010	5.0740	0.1100	0.3301	0.0060	0.82	1824	16	1831	19	1839	29	-0.82
	A25-A5 - 16	569000	54	0.1112	0.0009	5.1730	0.1100	0.3364	0.0061	0.90	1819	16	1848	18	1869	30	-2.69
	A25-A5 - 17	229000	96	0.1106	0.0010	5.1410	0.1100	0.3362	0.0059	0.45	1807	17	1843	18	1868	28	-3.28
	A25-A5 - 21	562000	50	0.1113	0.0009	5.0880	0.1100	0.3312	0.0060	0.92	1820	14	1834	19	1846	28	-1.40
	A25-A5 - 22	375000	28	0.1115	0.0009	5.0710	0.1100	0.3300	0.0059	0.89	1823	15	1831	18	1838	29	-0.82
	A25-A5 - 23	443000	31	0.1101	0.0009	5.0640	0.1000	0.3333	0.0057	0.67	1800	15	1830	17	1854	28	-2.93
	A25-A5 - 24	310300	42	0.1114	0.0009	5.0930	0.1100	0.3320	0.0059	0.87	1821	15	1834	19	1848	29	-1.46
	A25-A5 - 25	870000	49	0.1118	0.0009	5.3480	0.1100	0.3469	0.0062	0.90	1827	14	1876	18	1920	30	-4.82
	A25-A5 - 26	148600	46	0.1125	0.0011	5.2280	0.1200	0.3374	0.0063	0.36	1839	18	1856	19	1874	30	-1.87
	A25-A5 - 27	235300	38	0.1123	0.0009	5.1070	0.1100	0.3308	0.0060	0.86	1835	15	1837	19	1842	29	-0.36
	A25-A5 - 28	267000	51	0.1114	0.0009	5.1040	0.1100	0.3330	0.0058	0.84	1821	15	1836	18	1853	28	-1.73
	A25-A5 - 29	377000	58	0.1118	0.0009	5.0840	0.1100	0.3310	0.0058	0.86	1827	15	1834	18	1843	28	-0.87
	A25-A5 - 32	350000	85	0.1116	0.0009	5.1070	0.1100	0.3321	0.0058	0.86	1825	15	1838	18	1848	28	-1.26
	A25-A5 - 33	347500	73	0.1115	0.0009	5.0960	0.1100	0.3315	0.0059	0.88	1823	15	1835	18	1845	29	-1.19
	A25-A5 - 34	403800	53	0.1117	0.0009	5.1350	0.1100	0.3333	0.0059	0.89	1826	14	1842	18	1854	29	-1.52
	A25-A5 - 35	182300	38	0.1117	0.0010	5.1310	0.1100	0.3332	0.0058	0.56	1826	17	1841	18	1854	28	-1.50
	A25-A5 - 36	260800	44	0.1118	0.0009	5.1070	0.1100	0.3308	0.0061	0.90	1828	15	1838	18	1844	29	-0.88
	A25-A5 - 37	425000	43	0.1124	0.0009	5.1690	0.1100	0.3335	0.0058	0.86	1838	15	1847	18	1855	28	-0.93
	A25-A5 - 38	548000	83	0.1111	0.0009	5.2400	0.1100	0.3413	0.0061	0.74	1817	15	1859	18	1893	29	-4.04
	A25-A5 - 39	235900	60	0.1126	0.0009	5.1110	0.1100	0.3284	0.0059	0.85	1841	15	1838	18	1830	29	0.61
	A25-A5 - 40	202000	52	0.1122	0.0010	5.1300	0.1100	0.3323	0.0061	0.87	1835	15	1840	19	1849	30	-0.77
17SRB-A055A3 (Fayalite Granite, NE pluton)																	
Thin Section, Zircon																	
LA-ICPMS																	
	A55-A3-1a-1	168799	26	0.1119	0.0012	4.7966	0.1352	0.3108	0.0081	0.93	1831	19	1784	23	1745	40	4.95
	A55-A3-1a-2	211159	37	0.1127	0.0012	4.8087	0.1321	0.3096	0.0079	0.92	1843	19	1786	23	1739	39	5.99

Model Ages (Ma)																	
Sample Name, Preperation and Method	Spot Name	206Pb (cps)	204Pb (cps)	$^{207}\text{Pb}/^{206}\text{Pb}$		$^{207}\text{Pb}/^{235}\text{U}$		$^{206}\text{Pb}/^{238}\text{U}$		p value	$^{207}\text{Pb}/^{206}\text{Pb}$		$^{207}\text{Pb}/^{235}\text{U}$		$^{206}\text{Pb}/^{238}\text{U}$		disc %
	A55-A3-1a-3	222555	57	0.1133	0.0015	4.8288	0.1441	0.3091	0.0082	0.89	1853	24	1790	25	1736	40	6.70
	A55-A3-1b-4	192999	40	0.1124	0.0012	4.8688	0.1380	0.3142	0.0083	0.93	1838	19	1797	24	1761	40	4.38
	A55-A3-1b-5	192974	31	0.1121	0.0012	4.8669	0.1365	0.3149	0.0082	0.93	1833	19	1797	23	1765	40	3.88
	A55-A3-1b-6	216953	33	0.1121	0.0012	4.8761	0.1396	0.3156	0.0084	0.93	1833	19	1798	24	1768	41	3.67
	A55-A3-1c-7	281129	35	0.1118	0.0011	4.9297	0.1414	0.3199	0.0086	0.93	1828	19	1807	24	1789	42	2.16
	A55-A3-2-9	182887	39	0.1126	0.0012	4.9962	0.1441	0.3219	0.0087	0.93	1841	19	1819	24	1799	42	2.34
	A55-A3-2-10	224168	33	0.1119	0.0012	4.9349	0.1419	0.3197	0.0086	0.93	1831	19	1808	24	1788	42	2.39
	A55-A3-5-12	270721	21	0.1120	0.0012	4.8540	0.1351	0.3144	0.0081	0.93	1832	19	1794	23	1762	40	3.94
	A55-A3-5-13	277611	21	0.1122	0.0012	4.9302	0.1364	0.3187	0.0082	0.93	1835	19	1807	23	1783	40	2.92
17SRB-J029A (Fayalite Granite, NE pluton)																	
<i>Thin Section, Zircon</i>																	
<i>LASS-ICPMS</i>																	
	J29 - 1	245700	77	0.1133	0.0014	5.2600	0.1500	0.3360	0.0079	0.23	1852	23	1862	24	1867	38	-0.80
	J29 - 4	201400	20	0.1120	0.0014	5.2440	0.1400	0.3395	0.0076	0.22	1834	22	1859	23	1884	37	-2.65
	J29 - 5	150000	19	0.1124	0.0015	5.3290	0.1400	0.3432	0.0075	0.50	1836	24	1873	23	1902	36	-3.47
	J29 - 6	115000	0	0.1127	0.0017	5.3880	0.1600	0.3457	0.0078	0.03	1840	28	1882	25	1914	37	-3.87
17SRB-M095 (Fayalite Granite, NE pluton)																	
<i>Thin Section, Zircon</i>																	
<i>LA-ICPMS</i>																	
	M95-1-1	206738	56	0.1128	0.0012	4.7587	0.1205	0.3058	0.0070	0.91	1846	19	1778	21	1720	35	7.30
	M95-2a-2	261482	51	0.1126	0.0012	4.8876	0.1307	0.3147	0.0077	0.91	1842	20	1800	22	1764	38	4.46
	M95-2b-3	242118	46	0.1121	0.0012	4.9236	0.1510	0.3184	0.0092	0.94	1834	19	1806	26	1782	45	2.94
	M95-3c-4	187579	51	0.1129	0.0012	4.8262	0.1366	0.3100	0.0081	0.93	1847	19	1789	24	1741	40	6.12
	M95-3d-5	311510	78	0.1134	0.0012	4.8768	0.1281	0.3118	0.0075	0.92	1855	19	1798	22	1750	37	6.03
	M95-4a-6	246883	56	0.1121	0.0012	4.6882	0.1114	0.3034	0.0065	0.90	1834	19	1765	20	1708	32	7.35
	M95-4a-7	288902	57	0.1124	0.0012	4.7262	0.1179	0.3050	0.0069	0.90	1838	19	1772	21	1716	34	7.12
	M95-4b-8	226716	59	0.1126	0.0012	4.7993	0.1206	0.3091	0.0070	0.90	1842	19	1785	21	1736	35	6.07
	M95-4c-9	300442	71	0.1124	0.0012	4.9141	0.1261	0.3170	0.0074	0.91	1839	19	1805	21	1775	36	3.62
	M95-5-10	315069	52	0.1122	0.0012	4.8175	0.1250	0.3113	0.0074	0.92	1836	19	1788	22	1747	36	5.08
	M95-6-11	228652	73	0.1126	0.0012	4.8105	0.1271	0.3100	0.0075	0.91	1841	19	1787	22	1740	37	5.79
	M95-7-12	203531	68	0.1128	0.0012	4.8275	0.1284	0.3104	0.0076	0.92	1845	19	1790	22	1742	37	5.90
	M95-7-13	282763	57	0.1126	0.0012	4.8414	0.1243	0.3117	0.0073	0.91	1843	19	1792	21	1749	36	5.35

Sample Name, Preperation and Method		Model Ages (Ma)														
		206Pb (cps)	204Pb (cps)	$^{207}\text{Pb}/^{206}\text{Pb}$		$^{207}\text{Pb}/^{235}\text{U}$		$^{206}\text{Pb}/^{238}\text{U}$		ρ value	$^{207}\text{Pb}/^{206}\text{Pb}$		$^{207}\text{Pb}/^{235}\text{U}$		$^{206}\text{Pb}/^{238}\text{U}$	
M95-8a-14	155968	69	0.1126	0.0012	4.8192	0.1284	0.3105	0.0075	0.91	1841	20	1788	22	1743	37	5.62
M95-8b-15	467144	70	0.1119	0.0012	4.9135	0.1273	0.3183	0.0075	0.92	1831	19	1805	22	1782	37	2.79
M95-8c-16	339400	69	0.1124	0.0012	4.9507	0.1345	0.3194	0.0080	0.92	1839	19	1811	23	1787	39	2.93
M95-10-17	329351	66	0.1125	0.0012	4.8424	0.1331	0.3122	0.0080	0.93	1840	19	1792	23	1751	39	5.08
M95-3c-19	208997	66	0.1128	0.0012	4.8626	0.1345	0.3127	0.0080	0.93	1845	19	1796	23	1754	39	5.20
<i>Thin Section, Zircon</i>																
<i>LASS-ICPMS</i>																
M95 - 1	189900	22	0.1133	0.0009	5.2360	0.1300	0.3368	0.0066	0.89	1852	14	1857	22	1871	32	-1.02
M95 - 2	135400	33	0.1113	0.0011	5.2520	0.1300	0.3440	0.0065	0.82	1819	17	1861	22	1906	31	-4.56
M95 - 3	383000	44	0.1118	0.0010	5.3530	0.1100	0.3478	0.0056	0.50	1828	17	1880	22	1924	27	-4.99
M95 - 4	172000	57	0.1120	0.0007	5.2270	0.1100	0.3390	0.0061	0.84	1830	11	1857	19	1882	29	-2.76
M95 - 5	171000	38	0.1121	0.0010	5.3150	0.1100	0.3437	0.0057	0.53	1832	15	1871	18	1904	27	-3.78
M95 - 6	208000	-20	0.1120	0.0009	5.3740	0.1100	0.3470	0.0055	0.63	1831	14	1881	18	1920	26	-4.64
M95 - 7	160000	10	0.1126	0.0009	5.2930	0.1200	0.3400	0.0058	0.78	1840	14	1867	19	1886	28	-2.44
M95 - 8	164000	26	0.1114	0.0008	5.3830	0.1200	0.3492	0.0060	0.76	1820	13	1882	19	1930	29	-5.70
M95 - 9	198700	3	0.1119	0.0007	5.1620	0.1100	0.3350	0.0054	0.77	1829	12	1846	18	1863	26	-1.83
M95 - 10	129460	7	0.1127	0.0013	5.3950	0.1200	0.3473	0.0061	0.49	1841	20	1884	19	1921	29	-4.16
M95 - 11	219500	22	0.1133	0.0010	5.5690	0.1200	0.3542	0.0055	0.45	1852	17	1911	18	1954	26	-5.22
M95 - 12	278800	48	0.1124	0.0005	5.4600	0.1300	0.3523	0.0066	0.92	1838	8	1894	20	1945	32	-5.50
17SRB-A015A4 (Hbl-Bt Granite, SE pluton)																
<i>Grain Mount, Zircon</i>																
<i>LASS-ICPMS</i>																
A15-A4 - 1	527000	46	0.1108	0.0014	4.8950	0.1500	0.3197	0.0075	0.83	1811	24	1801	26	1788	37	1.27
A15-A4 - 2	464000	75	0.1120	0.0015	5.0850	0.1600		0.0082	0.90	1830	24	1834	25	1830	40	0.02
A15-A4 - 3	1130000	48	0.1116	0.0014	5.1960	0.1600	0.3367	0.0081	0.94	1825	23	1851	27	1871	39	-2.47
A15-A4 - 4	1210000	51	0.1114	0.0014	5.2070	0.1700	0.3380	0.0088	0.96	1820	23	1852	27	1876	42	-2.97
A15-A4 - 5	1800000	73	0.1104	0.0014	5.0320	0.1600	0.3298	0.0083	0.95	1804	23	1824	27	1837	40	-1.78
A15-A4 - 6	1133000	54	0.1118	0.0014	5.0450	0.1500	0.3267	0.0076	0.86	1828	24	1827	26	1822	37	0.35
A15-A4 - 7	810000	58	0.1117	0.0014	5.2290	0.1800	0.3385	0.0098	0.97	1825	23	1855	28	1878	47	-2.81
A15-A4 - 8	161000	65	0.1120	0.0017	5.1500	0.1900	0.3321	0.0093	0.90	1831	27	1842	30	1848	45	-0.92
A15-A4 - 10	1810000	38	0.1117	0.0014	5.3360	0.1700	0.3453	0.0087	0.95	1826	23	1873	27	1912	42	-4.50
A15-A4 - 11	1050000	45	0.1106	0.0014	4.7200	0.1400	0.3087	0.0071	0.85	1808	23	1771	25	1734	35	4.28

Sample Name, Preperation and Method	Spot Name	Model Ages (Ma)															
		206Pb (cps)	204Pb (cps)	$^{207}\text{Pb}/^{206}\text{Pb}$		$^{207}\text{Pb}/^{235}\text{U}$		$^{206}\text{Pb}/^{238}\text{U}$		p value	$^{207}\text{Pb}/^{206}\text{Pb}$		$^{207}\text{Pb}/^{235}\text{U}$		$^{206}\text{Pb}/^{238}\text{U}$		disc %
				$\pm 2\sigma$	$\pm 2\sigma$	$\pm 2\sigma$	$\pm 2\sigma$	$\pm 2\sigma$	$\pm 2\sigma$		$\pm 2\sigma$	$\pm 2\sigma$	$\pm 2\sigma$	$\pm 2\sigma$	$\pm 2\sigma$		
A15-A4 - 12	279000	45	0.1114	0.0015	4.6100	0.2000	0.2992	0.0110	0.98	1821	24	1743	39	1684	57	8.16	
A15-A4 - 13	1060000	68	0.1116	0.0015	5.2700	0.1700	0.3417	0.0095	0.97	1825	24	1862	27	1894	45	-3.66	
A15-A4 - 14	1130000	34	0.1114	0.0014	5.1960	0.1700	0.3371	0.0089	0.97	1823	24	1850	28	1872	43	-2.63	
A15-A4 - 15	1640000	58	0.1115	0.0014	5.0930	0.1700	0.3303	0.0089	0.96	1823	23	1833	28	1839	43	-0.88	
A15-A4 - 16	1073000	53	0.1118	0.0014	5.0960	0.1600	0.3297	0.0079	0.92	1828	23	1835	26	1836	38	-0.43	
A15-A4 - 17	900000	37	0.1114	0.0014	5.0890	0.1600	0.3302	0.0079	0.92	1822	23	1834	27	1839	38	-0.95	
A15-A4 - 18	910000	57	0.1117	0.0014	4.9170	0.1600	0.3159	0.0084	0.97	1827	23	1803	27	1777	46	2.83	
A15-A4 - 19	909000	65	0.1114	0.0015	5.0200	0.1600	0.3260	0.0085	0.91	1821	24	1822	28	1819	41	0.10	
A15-A4 - 20	465000	34	0.1115	0.0015	4.7450	0.1500	0.3085	0.0083	0.94	1822	24	1774	27	1732	41	5.19	
A15-A4 - 21	901000	44	0.1120	0.0015	5.1370	0.1600	0.3321	0.0086	0.94	1830	24	1841	27	1848	41	-0.98	
A15-A4 - 22	2010000	53	0.1118	0.0014	5.0680	0.1500	0.3279	0.0077	0.89	1828	23	1830	26	1828	37	-0.01	
A15-A4 - 23	538000	47	0.1110	0.0015	4.8330	0.1500	0.3153	0.0078	0.88	1814	24	1790	27	1766	38	2.74	
A15-A4 - 24	1240000	65	0.1117	0.0014	5.1860	0.1600	0.3359	0.0081	0.91	1826	23	1850	26	1866	39	-2.14	
A15-A4 - 25	310000	61	0.1115	0.0015	4.8490	0.1600	0.3148	0.0086	0.92	1822	25	1792	28	1763	42	3.35	
A15-A4 - 26	2070000	10	0.1118	0.0015	5.0200	0.1900	0.3240	0.0110	0.99	1828	24	1823	31	1814	52	0.76	
A15-A4 - 27	1340000	68	0.1120	0.0014	5.1440	0.1700	0.3326	0.0091	0.97	1832	22	1842	28	1850	44	-0.97	
A15-A4 - 28	1166000	29	0.1126	0.0014	5.1680	0.1600	0.3316	0.0083	0.96	1840	23	1847	27	1845	40	-0.28	
A15-A4 - 29	2578000	55	0.1127	0.0014	4.9750	0.1500	0.3194	0.0076	0.94	1842	23	1815	26	1787	37	3.06	
A15-A4 - 30	1013000	48	0.1117	0.0014	4.9970	0.1600	0.3235	0.0083	0.96	1826	23	1818	27	1806	41	1.12	
A15-A4 - 31	1590000	43	0.1111	0.0014	4.6970	0.1600	0.3058	0.0087	0.97	1817	23	1764	29	1719	43	5.69	
A15-A4 - 32	2530000	18	0.1113	0.0014	5.1970	0.1600	0.3375	0.0079	0.90	1820	23	1852	26	1875	38	-2.92	
A15-A4 - 34	250000	36	0.1110	0.0015	4.7840	0.1700	0.3119	0.0088	0.94	1814	25	1779	31	1749	44	3.72	
A15-A4 - 35	175000	44	0.1111	0.0017	4.9600	0.2300	0.3240	0.0140	0.97	1814	29	1802	41	1801	69	0.72	
A15-A4 - 36	369000	67	0.1114	0.0016	4.9900	0.1800	0.3243	0.0100	0.95	1820	26	1813	30	1809	50	0.61	
A15-A4 - 38	169600	47	0.1126	0.0016	4.7540	0.1600	0.3053	0.0082	0.86	1841	26	1776	28	1717	40	7.22	
A15-A4 - 40	1460000	80	0.1118	0.0015	5.2550	0.1700	0.3402	0.0085	0.92	1827	24	1861	27	1887	41	-3.19	
A15-A4 - 41	1990000	50	0.1121	0.0014	5.4570	0.1700	0.3521	0.0088	0.97	1832	23	1893	27	1944	42	-5.74	
A15-A4 - 42	2300000	66	0.1122	0.0014	5.0370	0.1500	0.3241	0.0077	0.94	1835	23	1825	26	1809	38	1.43	
A15-A4 - 43	1970000	58	0.1122	0.0014	5.1770	0.1600	0.3328	0.0080	0.94	1834	23	1848	26	1852	39	-0.96	
A15-A4 - 44	2328000	51	0.1123	0.0014	5.1640	0.1600	0.3326	0.0081	0.94	1836	23	1846	26	1851	39	-0.79	
A15-A4 - 45	1670000	64	0.1114	0.0014	5.2490	0.1600	0.3403	0.0080	0.94	1822	23	1860	26	1890	37	-3.62	
A15-A4 - 46	1440000	65	0.1117	0.0014	5.2390	0.1700	0.3392	0.0083	0.94	1826	23	1858	27	1883	40	-3.04	
A15-A4 - 47	1681000	72	0.1121	0.0014	5.3440	0.1600	0.3449	0.0081	0.92	1832	23	1875	26	1910	39	-4.07	

Model Ages (Ma)																	
Sample Name, Preperation and Method	Spot Name	206Pb (cps)	204Pb (cps)	$^{207}\text{Pb}/^{206}\text{Pb}$		$^{207}\text{Pb}/^{235}\text{U}$		$^{206}\text{Pb}/^{238}\text{U}$		p value	$^{207}\text{Pb}/^{206}\text{Pb}$		$^{207}\text{Pb}/^{235}\text{U}$		$^{206}\text{Pb}/^{238}\text{U}$		
	A15-A4 - 48	391000	59	0.1122	0.0015	5.1800	0.2100	0.3342	0.0120	0.99	1834	24	1846	35	1856	59	-1.19
	A15-A4 - 49	708000	77	0.1118	0.0014	5.1630	0.1600	0.3338	0.0079	0.88	1828	23	1846	26	1856	38	-1.54
	A15-A4 - 50	3000000	55	0.1123	0.0014	5.2040	0.1600	0.3353	0.0077	0.78	1835	23	1853	26	1864	37	-1.54
	A15-A4 - 51	3800000	49	0.1122	0.0014	5.0540	0.1500	0.3257	0.0074	0.85	1834	23	1828	25	1818	36	0.88
	A15-A4 - 52	2881000	76	0.1125	0.0014	5.1320	0.1500	0.3300	0.0075	0.76	1839	23	1841	25	1838	36	0.03
	A15-A4 - 53	2090000	103	0.1113	0.0014	5.0970	0.1800	0.3313	0.0095	0.99	1820	23	1833	29	1843	46	-1.28
	A15-A4 - 54	372000	67	0.1117	0.0017	4.8180	0.1600	0.3121	0.0079	0.75	1825	27	1790	25	1751	39	4.23
	A15-A4 - 55	615000	35	0.1115	0.0014	4.8300	0.1500	0.3135	0.0080	0.95	1823	23	1789	27	1757	39	3.77
17SRB-C047A (Hbl-Bt Granite, NE pluton)																	
<i>Thin Section, Zircon</i>																	
<i>LASS-ICPMS</i>																	
	C47 - 1	109000	8	0.1119	0.0018	5.0650	0.1400	0.3290	0.0084	0.67	1828	30	1830	24	1833	41	-0.27
	C47 - 2	156800	6	0.1120	0.0016	5.0170	0.1400	0.3251	0.0072	0.64	1830	26	1822	23	1815	35	0.83
	C47 - 4	197800	36	0.1113	0.0014	5.0510	0.1400	0.3297	0.0073	0.42	1819	23	1827	23	1836	35	-0.93
	C47 - 5	131600	59	0.1121	0.0016	5.1330	0.1400	0.3324	0.0074	0.34	1832	25	1841	24	1850	36	-0.97
	C47 - 6	205000	41	0.1122	0.0013	4.9710	0.1400	0.3216	0.0077	0.11	1834	21	1813	25	1797	38	2.06
	C47 - 7	236000	36	0.1127	0.0014	5.3740	0.1500	0.3462	0.0079	0.51	1842	23	1880	24	1916	38	-3.86
	C47 - 9	255000	47	0.1119	0.0014	5.1730	0.1400	0.3353	0.0079	0.50	1828	23	1848	23	1863	38	-1.88
	C47 - 10	554000	77	0.1109	0.0013	5.0020	0.1300	0.3275	0.0069	0.54	1812	21	1820	22	1826	33	-0.76
	C47 - 11	132300	31	0.1132	0.0014	5.0740	0.1400	0.3240	0.0072	0.40	1851	22	1831	23	1809	35	2.32
	C47 - 12	266000	27	0.1124	0.0013	5.3080	0.1400	0.3431	0.0077	0.40	1837	21	1870	23	1901	37	-3.36
	C47 - 13	192200	11	0.1117	0.0015	5.2680	0.1500	0.3428	0.0086	0.34	1825	24	1863	24	1900	42	-3.95
	C47 - 14	218800	11	0.1113	0.0014	5.1910	0.1400	0.3380	0.0073	0.42	1819	22	1851	23	1877	35	-3.09
	C47 - 16	124600	10	0.1123	0.0023	5.1940	0.1600	0.3356	0.0079	0.43	1834	37	1851	26	1865	38	-1.66
17SRB-R075A1 (Hbl-Bt Granite, SE pluton)																	
<i>Thin Section, Zircon</i>																	
<i>LASS-ICPMS</i>																	
	R75 - 1	569200	27	0.1113	0.0008	5.2210	0.1100	0.3426	0.0060	0.83	1819	13	1858	15	1899	29	-4.21
	R75 - 2	614500	2	0.1114	0.0005	5.1210	0.1200	0.3373	0.0062	0.91	1821	9	1839	21	1874	30	-2.84
	R75 - 3	550000	61	0.1110	0.0007	5.0670	0.1100	0.3327	0.0057	0.79	1814	12	1830	18	1852	28	-2.05
	R75 - 4	241000	51	0.1115	0.0007	5.2400	0.1500	0.3426	0.0078	0.96	1823	11	1858	24	1899	38	-4.00
	R75 - 5	439000	33	0.1114	0.0007	5.0320	0.1200	0.3304	0.0057	0.84	1821	11	1824	19	1840	28	-1.03
	R75 - 6	627000	38	0.1115	0.0005	5.1920	0.1200	0.3400	0.0066	0.96	1824	8	1850	21	1886	32	-3.31

Sample Name, Preperation and Method		Model Ages (Ma)															
		206Pb (cps)	204Pb (cps)	$^{207}\text{Pb}/^{206}\text{Pb}$		$^{207}\text{Pb}/^{235}\text{U}$		$^{206}\text{Pb}/^{238}\text{U}$		p value	$^{207}\text{Pb}/^{206}\text{Pb}$		$^{207}\text{Pb}/^{235}\text{U}$		$^{206}\text{Pb}/^{238}\text{U}$		
Spot Name					$\pm 2\sigma$				$\pm 2\sigma$			$\pm 2\sigma$		$\pm 2\sigma$		$\pm 2\sigma$	
R75 - 7		526000	46	0.1119	0.0006	5.0880	0.1300	0.3328	0.0069	0.95	1829	10	1833	22	1851	33	-1.20
R75 - 8		649000	102	0.1125	0.0006	5.3460	0.1200	0.3469	0.0059	0.85	1839	9	1876	19	1920	28	-4.24
R75 - 9		2897000	27	0.1113	0.0006	5.1860	0.1200	0.3420	0.0067	0.95	1820	9	1850	21	1896	32	-4.03
R75 - 10		515000	70	0.1117	0.0006	5.3100	0.1100	0.3465	0.0058	0.82	1826	10	1870	19	1918	28	-4.80
R75 - 11		1037000	88	0.1124	0.0005	5.2060	0.1300	0.3388	0.0065	0.95	1838	8	1853	21	1880	31	-2.23
R75 - 12		1097000	51	0.1117	0.0007	5.2350	0.1300	0.3431	0.0072	0.95	1826	11	1857	22	1901	35	-3.95
R75 - 13		533000	82	0.1123	0.0007	5.2430	0.1200	0.3410	0.0067	0.86	1836	12	1859	19	1891	32	-2.91
R75 - 14		1297000	84	0.1118	0.0005	5.1060	0.1300	0.3348	0.0073	0.97	1828	8	1836	22	1861	35	-1.76
R75 - 15		311600	35	0.1123	0.0008	5.0340	0.1200	0.3269	0.0064	0.89	1836	12	1824	20	1823	31	0.71
R75 - 16		1810000	117	0.1122	0.0007	4.9330	0.1200	0.3203	0.0071	0.93	1833	11	1807	22	1791	35	2.35
R75 - 18		573000	95	0.1116	0.0008	5.0670	0.1100	0.3296	0.0068	0.89	1825	13	1834	22	1836	33	-0.60
R75 - 19		408000	58	0.1129	0.0010	5.2440	0.1200	0.3390	0.0060	0.80	1845	16	1860	19	1882	29	-1.97
R75 - 20		706000	26	0.1119	0.0007	4.9480	0.1300	0.3252	0.0069	0.95	1830	11	1810	23	1815	34	0.83
17SRB-J053A1 (Grt-Bt Suite, SE pluton)																	
<i>Thin Section, Zircon, Cores</i>																	
<i>LASS-ICPMS</i>																	
J53 - 1		40000	-4	0.1111	0.0017	5.0970	0.1300	0.3334	0.0063	0.51	1814	27	1834	21	1855	31	-2.21
J53 - 2		46200	-17	0.1123	0.0014	5.2640	0.1300	0.3407	0.0065	0.71	1833	23	1861	22	1890	32	-3.02
J53 - 3		63400	-1	0.1138	0.0013	5.2540	0.1300	0.3359	0.0056	0.61	1858	21	1861	21	1867	27	-0.48
J53 - 6		115600	20	0.1132	0.0017	5.7300	0.2200	0.3700	0.0120	0.91	1849	27	1933	33	2027	58	-8.78
J53 - 15		198000	55	0.1137	0.0011	5.7100	0.1600	0.3624	0.0074	0.89	1858	17	1931	25	1993	35	-6.77
<i>Thin Section, Zircon, Rims</i>																	
<i>LASS-ICPMS</i>																	
J53 - 12		392400	5	0.1100	0.0006	5.0830	0.1300	0.3352	0.0067	0.94	1797	10	1832	22	1863	32	-3.53
J53 - 13		960000	217	0.1103	0.0007	5.6300	0.2200	0.3690	0.0130	0.98	1803	11	1917	34	2023	60	-10.87
J53 - 14		333100	0	0.1111	0.0008	5.1000	0.1100	0.3319	0.0061	0.88	1816	12	1836	19	1847	30	-1.68
<i>Thin Section, Monazite, Cores</i>																	
<i>LA-ICPMS</i>																	
J53-2-1		924187	3	0.1119	0.0013	5.0780	0.0969	0.3291	0.0050	0.80	1831	20	1832	16	1834	24	-0.16
J53-2-2		1009558	3	0.1110	0.0012	5.1217	0.0952	0.3345	0.0050	0.80	1816	20	1840	16	1860	24	-2.36
J53-2-3		384263	1	0.1115	0.0012	5.2224	0.1055	0.3398	0.0057	0.83	1823	20	1856	17	1886	27	-3.30
J53-2-4		649468	1	0.1110	0.0012	5.0826	0.0945	0.3320	0.0050	0.80	1816	20	1833	16	1848	24	-1.70
J53-3-8		206641	19	0.1118	0.0013	4.8015	0.0906	0.3114	0.0047	0.80	1829	21	1785	16	1748	23	4.66

Model Ages (Ma)																	
Sample Name, Preperation and Method	Spot Name	206Pb (cps)	204Pb (cps)	$^{207}\text{Pb}/^{206}\text{Pb}$		$^{207}\text{Pb}/^{235}\text{U}$		$^{206}\text{Pb}/^{238}\text{U}$		p value	$^{207}\text{Pb}/^{206}\text{Pb}$		$^{207}\text{Pb}/^{235}\text{U}$		$^{206}\text{Pb}/^{238}\text{U}$		disc %
	J53-3-9	231293	22	0.1113	0.0013	4.7703	0.0925	0.3109	0.0049	0.81	1821	20	1780	16	1745	24	4.34
	J53-3-10	231976	25	0.1121	0.0013	4.8839	0.0935	0.3159	0.0047	0.78	1834	21	1799	16	1770	23	3.67
	J53-5-13	205821	16	0.1114	0.0013	4.8300	0.0929	0.3145	0.0048	0.80	1822	21	1790	16	1763	24	3.34
	J53-5-14	248731	16	0.1109	0.0012	4.9067	0.0932	0.3208	0.0049	0.81	1815	20	1803	16	1794	24	1.16
	J53-5-15	195616	11	0.1115	0.0013	4.9269	0.0954	0.3206	0.0050	0.81	1823	20	1807	16	1793	25	1.72
	J53-8-18	276240	80	0.1116	0.0013	4.7574	0.0894	0.3092	0.0046	0.80	1825	20	1777	16	1737	23	5.08
	J53-8-19	214258	92	0.1114	0.0013	4.8504	0.0931	0.3157	0.0049	0.80	1823	21	1794	16	1769	24	3.06
	J53-8-20	189643	74	0.1118	0.0013	4.9684	0.0983	0.3222	0.0051	0.80	1829	21	1814	17	1801	25	1.61
	J53-8-21	209279	28	0.1126	0.0013	4.8330	0.0936	0.3113	0.0049	0.81	1842	21	1791	16	1747	24	5.43
	J53-9-27	180410	26	0.1120	0.0013	4.8128	0.0929	0.3117	0.0049	0.81	1832	20	1787	16	1749	24	4.71
	J53-9-28	215806	53	0.1124	0.0013	4.8148	0.0939	0.3108	0.0049	0.81	1838	21	1787	16	1745	24	5.34
<i>Thin Section, Monazite, Rims LA-ICPMS</i>																	
	J53-2-5	165047	61	0.1107	0.0013	4.6702	0.0919	0.3059	0.0049	0.81	1811	21	1762	16	1721	24	5.28
	J53-2-6	129214	22	0.1083	0.0013	4.4685	0.0854	0.2992	0.0045	0.80	1771	21	1725	16	1687	23	4.99
	J53-2-7	186984	44	0.1109	0.0013	4.6509	0.0906	0.3042	0.0048	0.82	1814	20	1758	16	1712	24	5.97
	J53-3-11	168303	29	0.1107	0.0013	4.6271	0.0874	0.3031	0.0046	0.80	1811	21	1754	16	1707	22	6.11
	J53-3-12	143367	26	0.1076	0.0013	4.3470	0.0839	0.2929	0.0045	0.79	1760	21	1702	16	1656	22	6.26
	J53-5-17	137162	32	0.1087	0.0013	4.5460	0.0868	0.3034	0.0046	0.80	1777	21	1739	16	1708	23	4.03
	J53-8-22	109077	13	0.1093	0.0013	4.1979	0.0820	0.2785	0.0044	0.81	1788	21	1674	16	1584	22	12.88
	J53-8-23	116959	8	0.1096	0.0013	4.2661	0.0857	0.2824	0.0046	0.81	1792	21	1687	16	1604	23	11.76
	J53-5-16	238670	23	0.1101	0.0013	4.8342	0.0914	0.3186	0.0048	0.80	1800	21	1791	16	1783	23	0.99
	J53-9-25	142530	10	0.1110	0.0013	4.5138	0.0852	0.2948	0.0044	0.79	1817	21	1734	16	1665	22	9.08
	J53-9-26	208656	27	0.1112	0.0012	4.6591	0.0865	0.3038	0.0045	0.80	1819	20	1760	15	1710	22	6.38
	J53-9-24	164624	17	0.1112	0.0013	4.4957	0.0853	0.2931	0.0044	0.79	1820	21	1730	16	1657	22	9.83
17SRB-O054A (Grt-Bt Suite, SE pluton)																	
<i>Thin Section, Zircon LASS-ICPMS</i>																	
	O54 - 1	456200	92	0.1123	0.0014	5.0200	0.1400	0.3233	0.0074	0.42	1836	22	1822	24	1805	36	1.72
	O54 - 2	547000	76	0.1094	0.0013	5.2240	0.1400	0.3457	0.0074	0.26	1789	22	1856	23	1914	36	-6.53
	O54 - 12	378000	117	0.1150	0.0016	5.0880	0.1400	0.3213	0.0074	0.30	1879	25	1834	24	1796	36	4.62
	O54 - 14	428000	141	0.1127	0.0018	5.2000	0.1700	0.3356	0.0099	0.29	1841	29	1852	28	1865	48	-1.29

Sample Name, Preperation and Method		Model Ages (Ma)															
		206Pb (cps)	204Pb (cps)	$^{207}\text{Pb}/^{206}\text{Pb}$		$^{207}\text{Pb}/^{235}\text{U}$		$^{206}\text{Pb}/^{238}\text{U}$		ρ value	$^{207}\text{Pb}/^{206}\text{Pb}$		$^{207}\text{Pb}/^{235}\text{U}$		$^{206}\text{Pb}/^{238}\text{U}$		disc %
Spot Name				$\pm 2\sigma$	$\pm 2\sigma$	$\pm 2\sigma$	$\pm 2\sigma$	$\pm 2\sigma$	$\pm 2\sigma$	$\pm 2\sigma$	$\pm 2\sigma$	$\pm 2\sigma$	$\pm 2\sigma$	$\pm 2\sigma$	$\pm 2\sigma$	$\pm 2\sigma$	
054 - 8		525000	29	0.1105	0.0016	4.8090	0.1400	0.3108	0.0076	0.54	1806	26	1786	24	1744	37	3.56
054 - 9		295000	59	0.1136	0.0014	5.6130	0.1600	0.3578	0.0084	0.06	1856	23	1917	25	1971	40	-5.83
054 - 11		762000	55	0.1116	0.0013	5.2630	0.1400	0.3425	0.0077	0.60	1824	20	1864	22	1902	35	-4.11
054 - 13		290000	126	0.1146	0.0015	5.4890	0.1600	0.3483	0.0088	0.36	1873	24	1898	25	1926	42	-2.75
17SRB-J051A1 (Migmatite Xenolith, SE pluton)																	
<i>Thin Section, Zircon</i>																	
<i>LA-ICPMS</i>																	
1	J51A1S1-1-1	1187111	81	0.1539	0.0020	7.6578	0.1845	0.3608	0.0074	0.85	2390	22	2192	21	1986	35	20.33
2	J51A1S1-1-2	1248060	80	0.1133	0.0012	4.4320	0.1026	0.2838	0.0058	0.88	1852	20	1718	19	1611	29	15.01
3	J51A1S1-1-3	833830	89	0.1112	0.0013	4.3165	0.1158	0.2814	0.0068	0.90	1820	21	1697	22	1599	34	13.84
4	J51A1S1-2a-4	454089	135	0.1634	0.0017	10.4842	0.2938	0.4654	0.0121	0.93	2491	18	2479	26	2464	53	1.11
5	J51A1S1-3-6	330525	28	0.1407	0.0017	7.5564	0.1735	0.3894	0.0076	0.85	2236	21	2180	20	2120	35	5.48
6	J51A1S1-3-7	676727	64	0.1723	0.0019	11.0129	0.2665	0.4635	0.0100	0.89	2580	18	2524	22	2455	44	5.11
7	J51A1S1-4-8	261704	30	0.1455	0.0018	8.2249	0.2364	0.4099	0.0106	0.90	2294	21	2256	26	2214	48	3.60
8	J51A1S1-4-9	324645	29	0.1716	0.0018	11.5786	0.2762	0.4893	0.0105	0.90	2574	18	2571	22	2568	45	0.24
9	J51A1S1-5b-11	551343	94	0.1696	0.0018	11.0797	0.2650	0.4737	0.0102	0.90	2554	17	2530	22	2500	44	2.16
10	J51A1S1-5b-12	231256	99	0.1781	0.0019	11.9120	0.2771	0.4851	0.0101	0.89	2635	17	2598	22	2550	44	3.36
11	J51A1S1-6-13	599046	182	0.1761	0.0020	11.5449	0.2750	0.4754	0.0100	0.88	2617	19	2568	22	2507	43	4.38
12	J51A1S1-6-14	623542	366	0.1747	0.0018	10.8207	0.2280	0.4493	0.0082	0.87	2603	17	2508	19	2392	36	8.81
13	J51A1S1-8-17	336963	250	0.1711	0.0020	10.6909	0.2735	0.4532	0.0103	0.89	2568	20	2497	23	2410	46	6.58
14	J51A1S1-8-18	167356	20	0.1710	0.0020	11.3073	0.2675	0.4795	0.0099	0.87	2568	19	2549	22	2525	43	1.69
15	J51A1S1-8-19	418065	229	0.1204	0.0027	5.4784	0.1702	0.3299	0.0070	0.68	1963	40	1897	26	1838	34	6.78
16	J51A1S1-8-20	383978	313	0.1774	0.0021	11.7002	0.2808	0.4783	0.0101	0.88	2629	19	2581	22	2520	44	4.31
17	J51A1S1-8-21	171090	22	0.1532	0.0031	9.2757	0.2504	0.4393	0.0079	0.67	2381	34	2366	24	2347	35	1.45

$$\text{disc \%} = \text{Percent discordance} = [(\text{}^{207}\text{Pb}/\text{}^{206}\text{Pb Age} / \text{}^{206}\text{Pb}/\text{}^{235}\text{U Age}) - 1] * 100$$

Table 1 cont.: Compiled U-Pb Geochronology Results for Boothia Neoarchean Porphyroclastic Unit

Sample Name, Preperation, and Method	Spot Name	Model Ages (Ma)															
		206Pb (cps)	204Pb (cps)	207Pb/ 206Pb	± 2σ	207Pb/ 235U	± 2σ	206Pb/ 238U	± 2σ	p value	207Pb/ 206Pb	207Pb/ 235U	± 2σ	206Pb/ 238U	± 2σ	disc %	
17SRB-C008A																	
<i>Thin Section, Zircon</i>																	
<i>LA-ICPMS</i>																	
	C8-S1-1-1	859469	111	0.1376	0.0015	6.6025	0.1470	0.3479	0.0068	0.88	2198	18	2060	19	1925	32	14.17
	C8-S1-1-2	465059	33	0.1338	0.0015	6.7908	0.1456	0.3681	0.0068	0.86	2149	19	2085	19	2020	32	6.35
	C8-S1-2-3	331221	25	0.1571	0.0017	9.5295	0.2311	0.4400	0.0096	0.90	2425	18	2390	22	2351	43	3.15
	C8-S1-2-4	207062	19	0.1398	0.0020	7.4572	0.1831	0.3868	0.0078	0.82	2225	24	2168	22	2108	36	5.55
	C8-S1-3a-5	827280	44	0.1581	0.0017	9.5324	0.2438	0.4372	0.0102	0.91	2436	18	2391	23	2338	45	4.19
	C8-S1-3b-6	224342	22	0.1393	0.0015	7.4172	0.1866	0.3860	0.0088	0.91	2219	18	2163	22	2104	41	5.45
	C8-S1-3b-7	503749	25	0.1594	0.0016	9.8764	0.2239	0.4494	0.0091	0.89	2449	17	2423	21	2392	40	2.38
	C8-S1-4a-8	586987	37	0.1612	0.0031	10.0713	0.2983	0.4532	0.0102	0.76	2468	32	2441	27	2410	45	2.42
	C8-S1-4a-9	502521	34	0.1618	0.0017	10.2404	0.2503	0.4589	0.0102	0.91	2475	17	2457	22	2435	45	1.65
	C8-S1-4c-11	389961	39	0.1514	0.0020	8.8305	0.1974	0.4230	0.0076	0.81	2362	22	2321	20	2274	35	3.87
	C8-S1-5a-12	286308	26	0.1512	0.0018	8.7708	0.2064	0.4208	0.0085	0.86	2359	21	2314	21	2264	38	4.20
	C8-S1-5b-13	608277	38	0.1535	0.0026	9.1518	0.3098	0.4324	0.0127	0.87	2385	29	2353	31	2317	57	2.97
	C8-S1-6b-14	651238	40	0.1628	0.0017	10.3332	0.2743	0.4603	0.0112	0.92	2485	17	2465	24	2441	49	1.82
	C8-S1-6b-15	433683	45	0.1616	0.0017	9.9697	0.2423	0.4476	0.0098	0.90	2472	17	2432	22	2384	44	3.68
	C8-S1-7-17	1284950	615	0.1396	0.0015	7.5913	0.1998	0.3945	0.0095	0.92	2222	18	2184	23	2144	44	3.64
	C8-S1-9-21	354288	24	0.1565	0.0019	9.5427	0.2787	0.4422	0.0117	0.91	2418	21	2392	26	2360	52	2.45
	C8-S1-9-22	235240	20	0.1492	0.0016	8.4428	0.2036	0.4105	0.0089	0.90	2337	18	2280	22	2217	40	5.40
	C8-S1-10a-23	1359050	77	0.1531	0.0027	8.8532	0.3709	0.4195	0.0160	0.91	2381	29	2323	38	2258	72	5.43
	C8-S1-10b-24	401362	35	0.1577	0.0017	9.9201	0.3197	0.4561	0.0139	0.94	2431	18	2427	29	2422	61	0.37
	C8-S1-10d-26	284397	26	0.1347	0.0017	6.9717	0.2045	0.3754	0.0100	0.91	2160	21	2108	26	2055	47	5.12
	C8-S1-10e-27	388156	84	0.1605	0.0020	9.9191	0.2823	0.4482	0.0115	0.90	2461	21	2427	26	2387	51	3.10
	C8-S1-10f-28	703831	62	0.1606	0.0017	9.8778	0.2261	0.4461	0.0091	0.89	2462	18	2423	21	2378	40	3.54
	C8-S1-10f-29	372070	26	0.1557	0.0020	9.3722	0.2839	0.4365	0.0120	0.90	2410	22	2375	27	2335	53	3.21
	C8-S1-10f-30	716275	39	0.1618	0.0017	10.1260	0.2203	0.4538	0.0087	0.88	2475	17	2446	20	2412	38	2.62
	C8-S1-9-31	331399	33	0.1625	0.0017	10.3556	0.2605	0.4621	0.0105	0.91	2482	18	2467	23	2449	46	1.35
	C8-S1-9-32	510452	38	0.1480	0.0019	8.6708	0.2107	0.4248	0.0087	0.84	2323	22	2304	22	2282	39	1.80
	C8-S1-9-33	401121	36	0.1509	0.0019	8.8277	0.1993	0.4243	0.0079	0.82	2356	22	2320	20	2280	36	3.34
	C8-S1-9-34	446105	36	0.1620	0.0017	10.2611	0.2227	0.4594	0.0087	0.88	2476	18	2459	20	2437	38	1.61
	C8-S1-9-35	398916	33	0.1609	0.0017	10.0351	0.2345	0.4524	0.0094	0.89	2465	18	2438	21	2406	41	2.44
	C8-S1-9-36	330020	32	0.1577	0.0016	9.6731	0.2633	0.4448	0.0112	0.92	2431	18	2404	25	2372	50	2.50

Model Ages (Ma)																
Sample Name, Preperation, and Method	Spot Name	206Pb (cps)	204Pb (cps)	207Pb/ 206Pb	± 2σ	207Pb/ 235U	± 2σ	206Pb/ 238U	± 2σ	p value	207Pb/ 206Pb	207Pb/ 235U	206Pb/ 238U	± 2σ	disc %	
17SRB-C031A																
<i>Thin Section, Zircon</i>																
<i>LA-ICPMS</i>																
C31-S1-1-1	1334898	662	0.1381	0.0027	6.4548	0.1732	0.3390	0.0062	0.69	2203	34	2040	23	1882	30	17.07
C31-S1-1-2	737291	84	0.1450	0.0019	8.3439	0.2837	0.4173	0.0131	0.92	2288	22	2269	30	2248	59	1.75
C31-S1-2-3	444765	63	0.1485	0.0016	8.5429	0.2271	0.4174	0.0101	0.91	2328	19	2290	24	2248	46	3.55
C31-S1-2-4	130002	52	0.1347	0.0015	6.9513	0.1889	0.3743	0.0092	0.91	2160	20	2105	24	2050	43	5.37
C31-S1-3b-5	317266	49	0.1521	0.0034	8.9598	0.3824	0.4271	0.0155	0.85	2370	38	2334	38	2293	70	3.38
C31-S1-4-6	1304166	65	0.1254	0.0013	5.8104	0.1407	0.3361	0.0073	0.90	2034	19	1948	21	1868	35	8.89
C31-S1-4-7	959217	136	0.1358	0.0016	6.9296	0.1568	0.3701	0.0071	0.85	2174	20	2102	20	2030	34	7.13
C31-S1-4-8	366360	74	0.1320	0.0017	6.7167	0.1719	0.3691	0.0082	0.87	2124	22	2075	22	2025	38	4.88
C31-S1-6-9	372750	57	0.1244	0.0017	6.0005	0.1416	0.3498	0.0066	0.80	2021	25	1976	20	1934	32	4.50
C31-S1-6-10	342458	54	0.1228	0.0014	5.9567	0.1384	0.3518	0.0071	0.86	1997	21	1970	20	1943	34	2.80
C31-S1-8b-11	816019	131	0.1449	0.0015	7.9170	0.1761	0.3964	0.0078	0.88	2286	18	2222	20	2152	36	6.22
C31-S1-9-13	390023	82	0.1584	0.0017	9.4941	0.2668	0.4346	0.0113	0.93	2439	18	2387	25	2326	51	4.85
C31-S1-10a-14	121411	65	0.1445	0.0016	7.5799	0.1766	0.3805	0.0077	0.87	2282	19	2182	21	2078	36	9.78
C31-S1-10a-15	300953	47	0.1524	0.0016	8.8533	0.2212	0.4212	0.0095	0.91	2373	18	2323	23	2266	43	4.74
C31-S1-10b-16	1230101	215	0.1402	0.0019	6.6009	0.2616	0.3415	0.0127	0.94	2229	24	2059	34	1894	61	17.72
C31-S1-10b-17	179113	24	0.1572	0.0019	9.1575	0.2010	0.4226	0.0077	0.83	2425	20	2354	20	2272	35	6.73
C31-S1-12a-18	447234	78	0.1607	0.0017	9.9636	0.2719	0.4497	0.0113	0.92	2463	18	2431	25	2394	50	2.90
C31-S1-12b-19	241104	50	0.1424	0.0016	7.6612	0.1996	0.3901	0.0092	0.90	2257	19	2192	23	2123	42	6.31
C31-S1-13-20	946104	72	0.1344	0.0017	6.9639	0.1653	0.3758	0.0075	0.84	2156	22	2107	21	2057	35	4.83
C31-S1-13-22	569107	40	0.1634	0.0018	10.6038	0.2697	0.4706	0.0108	0.91	2491	18	2489	23	2486	47	0.20
17SRB-D042A1																
<i>Thin Section, Zircon</i>																
<i>LA-ICPMS</i>																
D42A1S1-1-1	1460716	127	0.1570	0.0018	9.6525	0.2379	0.4459	0.0097	0.88	2424	20	2402	22	2377	43	1.97
D42A1S1-1-2	2140969	72	0.1584	0.0018	9.8102	0.2750	0.4491	0.0115	0.92	2439	19	2417	26	2391	51	1.99
D42A1S1-1-3	507646	174	0.1585	0.0018	9.8166	0.2438	0.4492	0.0099	0.89	2440	19	2418	23	2392	44	2.00
D42A1S1-1-4	363159	113	0.1593	0.0021	9.5112	0.2764	0.4329	0.0112	0.89	2449	22	2389	26	2319	50	5.60
D42A1S1-1-5	471534	47	0.1589	0.0019	9.7443	0.2228	0.4448	0.0087	0.86	2444	20	2411	21	2372	39	3.04
D42A1S1-2b-7	451003	45	0.1591	0.0018	10.2376	0.3162	0.4666	0.0134	0.93	2446	19	2456	28	2469	59	-0.90
D42A1S1-4a-8	835824	108	0.1617	0.0019	9.9441	0.2220	0.4460	0.0084	0.85	2474	20	2430	20	2377	37	4.06
D42A1S1-5-9	263162	40	0.1578	0.0018	9.5606	0.2377	0.4394	0.0097	0.89	2432	19	2393	23	2348	43	3.60
D42A1S1-7-10	288483	46	0.1628	0.0019	10.1696	0.2461	0.4530	0.0096	0.88	2485	19	2450	22	2408	43	3.19
D42A1S1-7-11	262222	37	0.1463	0.0018	7.9378	0.1817	0.3936	0.0075	0.83	2303	22	2224	20	2140	35	7.61

Model Ages (Ma)																
Sample Name, Preperation, and Method	Spot Name	206Pb (cps)	204Pb (cps)	207Pb/ 206Pb	± 2σ	207Pb/ 235U	± 2σ	206Pb/ 238U	± 2σ	p value	207Pb/ 206Pb	207Pb/ 235U	206Pb/ 238U	± 2σ	disc %	
D42A1S1-7-12	385746	45	0.1608	0.0019	9.8120	0.2309	0.4426	0.0091	0.87	2464	19	2417	21	2362	40	4.30
D42A1S1-7-13	288950	24	0.1630	0.0019	10.1071	0.2274	0.4498	0.0086	0.85	2487	20	2445	21	2395	38	3.84
D42A1S1-8a-14	551330	54	0.1627	0.0018	10.2361	0.2725	0.4564	0.0110	0.91	2484	19	2456	24	2423	49	2.49
D42A1S1-8b-15	194805	36	0.1533	0.0018	8.8793	0.2128	0.4201	0.0088	0.88	2383	19	2326	22	2261	40	5.41
D42A1S1-9-16	493290	68	0.1537	0.0018	8.9358	0.2265	0.4217	0.0095	0.89	2387	19	2331	23	2268	43	5.25
D42A1S1-10-17.1	163818	31	0.1419	0.0017	7.5958	0.2101	0.3883	0.0097	0.91	2250	20	2184	25	2115	45	6.39
D42A1S1-11a-19	195189	50	0.1231	0.0015	5.7924	0.1654	0.3414	0.0089	0.91	2001	21	1945	24	1893	42	5.68
D42A1S1-11a-20	432940	62	0.1302	0.0016	6.4115	0.1546	0.3571	0.0075	0.87	2101	21	2034	21	1968	35	6.73
D42A1S1-11b-21	848035	47	0.1644	0.0018	10.4523	0.2392	0.4612	0.0092	0.87	2501	19	2476	21	2445	41	2.30
D42A1S1-13a-22	815083	154	0.1610	0.0018	10.0022	0.2206	0.4506	0.0086	0.86	2466	19	2435	20	2398	38	2.86
D42A1S1-13b-23	518056	60	0.1530	0.0018	9.1871	0.2307	0.4355	0.0097	0.88	2380	20	2357	23	2331	43	2.10
D42A1S1-13c-24	173998	50	0.1633	0.0019	10.2131	0.3034	0.4537	0.0124	0.92	2490	19	2454	27	2412	55	3.24
D42A1S1-15-25	566097	51	0.1516	0.0022	8.8970	0.2586	0.4256	0.0107	0.87	2364	25	2327	26	2286	48	3.44
D42A1S1-17a-26	160302	48	0.1523	0.0025	8.7807	0.2349	0.4181	0.0088	0.79	2372	28	2315	24	2252	40	5.35
D42A1S1-17b-27	843287	49	0.1654	0.0021	10.7980	0.3364	0.4736	0.0135	0.92	2511	21	2506	29	2499	59	0.49
D42A1S1-18-28	576489	122	0.1540	0.0019	8.6943	0.1968	0.4095	0.0077	0.83	2391	21	2306	20	2213	35	8.05
17SRB-L032A																
<i>Thin Section, Zircon</i>																
<i>LA-ICPMS</i>																
L32AS2-1-1	403210	20	0.1633	0.0017	10.4855	0.3622	0.4656	0.0153	0.95	2491	17	2479	32	2464	67	1.08
L32AS2-1-2	444385	27	0.1635	0.0017	10.3759	0.3224	0.4602	0.0135	0.94	2493	17	2469	28	2440	59	2.15
L32AS1-2-3	828582	71	0.1509	0.0017	8.8176	0.2966	0.4238	0.0134	0.94	2356	20	2319	30	2278	60	3.44
L32AS1-3-4	551700	38	0.1575	0.0020	10.0746	0.3407	0.4638	0.0145	0.93	2429	22	2442	31	2456	64	-1.11
L32AS1-3-5	376837	16	0.1582	0.0016	9.9458	0.3151	0.4560	0.0136	0.94	2437	17	2430	29	2422	60	0.61
L32AS1-3b-6	308820	19	0.1581	0.0017	9.7043	0.3197	0.4453	0.0138	0.94	2435	19	2407	30	2374	61	2.56
L32AS1-3b-7	529290	25	0.1609	0.0017	10.2401	0.3285	0.4615	0.0140	0.95	2466	17	2457	29	2446	62	0.80
L32AS1-4a-8	242196	17	0.1604	0.0018	9.9427	0.3300	0.4494	0.0140	0.94	2460	19	2429	30	2393	62	2.82
L32AS1-5a-9	1400838	91	0.1404	0.0016	6.8791	0.2237	0.3553	0.0108	0.93	2233	20	2096	28	1960	51	13.93
L32AS1-5a-10	553621	25	0.1398	0.0015	7.8725	0.2846	0.4083	0.0141	0.96	2225	18	2217	32	2207	64	0.80
L32AS1-6a-11	479616	34	0.1624	0.0018	10.3793	0.3470	0.4636	0.0147	0.95	2481	18	2469	31	2455	64	1.02
L32AS1-7-12	842426	126	0.1637	0.0017	10.3852	0.3472	0.4602	0.0146	0.95	2494	17	2470	31	2441	64	2.18
L32AS1-7-14	746821	130	0.1314	0.0015	6.7693	0.2186	0.3736	0.0113	0.94	2117	19	2082	28	2046	53	3.44
L32AS1-7-15	1083191	125	0.1606	0.0017	9.9292	0.3254	0.4483	0.0139	0.95	2462	17	2428	30	2388	62	3.11

Model Ages (Ma)																	
Sample Name, Preperation, and Method	Spot Name	206Pb (cps)	204Pb (cps)	207Pb/ 206Pb	± 2σ	207Pb/ 235U	± 2σ	206Pb/ 238U	± 2σ	p value	207Pb/ 206Pb	207Pb/ 235U	206Pb/ 238U	± 2σ	disc %		
L32AS1-7-13	L32AS1-7-13	1741838	126	0.1326	0.0015	5.9636	0.1885	0.3262	0.0096	0.93	2133	20	1971	27	1820	46	17.17
	L32AS1-7-16	367815	14	0.1542	0.0017	9.2605	0.2981	0.4355	0.0132	0.94	2393	18	2364	29	2331	59	2.68
	L32AS1-7-17	733601	193	0.1519	0.0016	8.9109	0.2911	0.4254	0.0132	0.95	2368	18	2329	29	2285	59	3.62
	L32AS1-7-18	365100	37	0.1629	0.0017	10.2258	0.3384	0.4552	0.0143	0.95	2486	17	2455	30	2418	63	2.82
	L32AS1-8-19	399015	40	0.1611	0.0017	10.2187	0.3410	0.4602	0.0146	0.95	2467	18	2455	30	2440	64	1.08
	L32AS1-9-20	740623	39	0.1621	0.0017	10.1874	0.3432	0.4557	0.0146	0.95	2478	17	2452	31	2421	64	2.36
	L32AS2-9-21	1304226	15	0.1509	0.0016	9.0720	0.3029	0.4361	0.0138	0.95	2356	18	2345	30	2333	62	0.98
	L32AS2-12-22	448712	19	0.1318	0.0021	6.3776	0.2224	0.3510	0.0108	0.88	2122	28	2029	30	1939	51	9.42
	L32AS2-3-23	756353	16	0.1545	0.0022	9.5969	0.3692	0.4506	0.0161	0.93	2396	24	2397	35	2398	71	-0.06
	L32AS2-3-24	801835	15	0.1619	0.0017	10.4643	0.3456	0.4687	0.0147	0.95	2476	17	2477	30	2478	64	-0.09
17SRB-0009A3																	
<i>Grain Mount, Zircon</i>																	
<i>LA-ICPMS</i>																	
17SRB09	17SRB09-1	792199	193	0.1544	0.0015	9.3645	0.3504	0.4398	0.0159	0.96	2395	17	2374	34	2350	71	1.94
	17SRB09-2	364807	49	0.1616	0.0016	10.1016	0.3744	0.4535	0.0162	0.96	2472	17	2444	34	2411	71	2.55
	17SRB09-3	1519962	50	0.1619	0.0016	10.4828	0.3772	0.4696	0.0163	0.96	2476	16	2478	33	2482	71	-0.25
	17SRB09-4	1711171	45	0.1601	0.0016	10.5494	0.3878	0.4779	0.0169	0.96	2457	16	2484	34	2518	73	-2.44
	17SRB09-5	501375	159	0.1519	0.0020	8.8552	0.3574	0.4227	0.0162	0.95	2368	22	2323	36	2273	73	4.19
	17SRB09-6	597654	98	0.1594	0.0016	9.9153	0.3756	0.4512	0.0165	0.97	2449	17	2427	34	2400	73	2.03
	17SRB09-7	627353	60	0.1315	0.0015	6.7800	0.2562	0.3739	0.0135	0.95	2118	20	2083	33	2048	63	3.45
	17SRB09-8	564833	103	0.1493	0.0015	8.7319	0.3356	0.4241	0.0158	0.97	2338	17	2310	34	2279	71	2.61
	17SRB09-9	639746	12	0.1627	0.0016	10.4017	0.3886	0.4636	0.0167	0.97	2484	16	2471	34	2455	73	1.18
	17SRB09-10	1013725	53	0.1617	0.0016	10.2965	0.3785	0.4618	0.0164	0.96	2473	16	2462	33	2448	72	1.06
	17SRB09-11	736475	58	0.1516	0.0015	8.7983	0.3379	0.4210	0.0156	0.97	2364	17	2317	34	2265	71	4.35
	17SRB09-12	633247	148	0.1345	0.0017	6.9215	0.2767	0.3732	0.0141	0.95	2158	22	2101	35	2045	66	5.53
	17SRB09-13.1	317802	74	0.1484	0.0023	8.2412	0.3562	0.4028	0.0162	0.93	2327	26	2258	38	2182	74	6.67
	17SRB09-14	189803	53	0.1509	0.0018	8.4219	0.3042	0.4048	0.0138	0.94	2356	21	2278	32	2191	63	7.54
	17SRB09-15	1097061	158	0.1579	0.0016	9.7260	0.3644	0.4468	0.0161	0.96	2433	17	2409	34	2381	71	2.18
	17SRB09-16	436853	53	0.1597	0.0015	9.6315	0.3405	0.4375	0.0149	0.97	2452	15	2400	32	2340	67	4.80
	17SRB09-17	1779454	125	0.1529	0.0015	9.2374	0.3316	0.4381	0.0152	0.96	2379	16	2362	32	2342	68	1.55
	17SRB09-18	789199	102	0.1475	0.0017	8.2907	0.3030	0.4078	0.0142	0.95	2317	19	2263	33	2205	65	5.07
	17SRB09-19	373834	42	0.1526	0.0016	8.8346	0.3156	0.4198	0.0143	0.95	2375	18	2321	32	2260	65	5.12
	17SRB09-20	534611	17	0.1613	0.0015	10.0716	0.3732	0.4528	0.0163	0.97	2470	15	2441	34	2407	72	2.58
	17SRB09-21	815514	69	0.1566	0.0016	9.3255	0.3291	0.4319	0.0146	0.96	2419	17	2371	32	2314	65	4.52
	17SRB09-22	979490	32	0.1615	0.0015	10.1644	0.3626	0.4566	0.0157	0.97	2471	15	2450	32	2424	69	1.93
	17SRB09-24	718962	47	0.1436	0.0016	7.7955	0.2825	0.3938	0.0136	0.95	2271	19	2208	32	2141	63	6.08

Model Ages (Ma)																	
Sample Name, Preperation, and Method	Spot Name	206Pb (cps)	204Pb (cps)	207Pb/ 206Pb	± 2σ	207Pb/ 235U	± 2σ	206Pb/ 238U	± 2σ	p value	207Pb/ 206Pb	207Pb/ 235U	206Pb/ 238U	± 2σ	disc %		
	17SRBO9-25	1180623	45	0.1546	0.0015	9.5068	0.3465	0.4460	0.0157	0.97	2397	16	2388	33	2377	70	0.84
	17SRBO9-26	375481	67	0.1550	0.0015	9.2644	0.3513	0.4334	0.0159	0.97	2402	16	2365	34	2321	71	3.49
	17SRBO9-27	746263	55	0.1618	0.0015	10.5155	0.4089	0.4713	0.0178	0.97	2475	16	2481	35	2489	78	-0.57
	17SRBO9-28	588929	42	0.1492	0.0015	8.5437	0.3163	0.4154	0.0148	0.96	2336	17	2291	33	2240	67	4.33
	17SRBO9-29	455905	18	0.1619	0.0015	10.1493	0.3656	0.4547	0.0158	0.97	2476	16	2448	33	2416	70	2.46
	17SRBO9-30	1061439	53	0.1531	0.0014	9.1609	0.3413	0.4341	0.0157	0.97	2380	16	2354	34	2324	70	2.42
	17SRBO9-31	1037333	86	0.1453	0.0031	8.3161	0.3336	0.4150	0.0141	0.85	2292	36	2266	36	2238	64	2.40
	17SRBO9-32	945648	100	0.1521	0.0014	9.0657	0.3375	0.4322	0.0156	0.97	2370	16	2345	33	2316	70	2.35
	17SRBO9-33	386590	60	0.1478	0.0015	8.1769	0.3078	0.4013	0.0146	0.97	2320	17	2251	34	2175	67	6.67
	17SRBO9-34	1184650	411	0.1404	0.0014	7.6827	0.2724	0.3970	0.0135	0.96	2232	18	2195	31	2155	62	3.55
	17SRBO9-35	526767	72	0.1491	0.0014	8.5966	0.3255	0.4183	0.0153	0.97	2335	16	2296	34	2253	69	3.66
	17SRBO9-36	584071	160	0.1573	0.0016	9.4097	0.3516	0.4338	0.0156	0.96	2427	17	2379	34	2323	70	4.50
	17SRBO9-37	750389	197	0.1432	0.0014	7.9624	0.3144	0.4032	0.0154	0.97	2266	17	2227	35	2184	70	3.77
	17SRBO9-38	840406	169	0.1443	0.0014	8.1033	0.2954	0.4074	0.0143	0.96	2279	17	2243	32	2203	65	3.47
	17SRBO9-40	639165	79	0.1494	0.0015	8.4333	0.2997	0.4093	0.0140	0.96	2340	17	2279	32	2212	64	5.78
	17SRBO9-41	390529	43	0.1516	0.0016	8.8290	0.3527	0.4223	0.0163	0.96	2364	18	2320	36	2271	73	4.13
	17SRBO9-42	1230777	21	0.1501	0.0014	8.8474	0.3266	0.4275	0.0152	0.97	2347	16	2322	33	2295	68	2.28
	17SRBO9-43	774437	46	0.1611	0.0015	10.1383	0.3702	0.4565	0.0161	0.97	2467	15	2447	33	2424	71	1.76
	17SRBO9-44	414125	2	0.1605	0.0015	9.7450	0.3645	0.4402	0.0160	0.97	2461	16	2411	34	2352	71	4.67
	17SRBO9-45	1075792	65	0.1568	0.0014	9.6535	0.3717	0.4464	0.0167	0.97	2422	16	2402	35	2379	74	1.78
	17SRBO9-46	2039931	133	0.1557	0.0014	9.7309	0.3446	0.4532	0.0155	0.97	2410	16	2410	32	2409	68	0.01
	17SRBO9-47	1145989	142	0.1614	0.0015	10.3076	0.3699	0.4633	0.0161	0.97	2470	15	2463	33	2454	70	0.66
	17SRBO9-48	2079663	161	0.1600	0.0015	10.3708	0.3706	0.4702	0.0162	0.97	2455	15	2468	33	2484	71	-1.18
	17SRBO9-49	1384815	283	0.1561	0.0014	9.5617	0.3534	0.4444	0.0159	0.97	2413	16	2393	33	2370	71	1.83
	17SRBO9-50	678005	57	0.1555	0.0015	9.7878	0.3639	0.4564	0.0164	0.97	2408	16	2415	34	2424	72	-0.65
	17SRBO9-51	520227	21	0.1628	0.0015	10.4492	0.3868	0.4655	0.0167	0.97	2485	15	2475	34	2464	73	0.86
	17SRBO9-52	847821	68	0.1546	0.0014	9.2324	0.3314	0.4331	0.0150	0.97	2398	16	2361	32	2319	67	3.37
	17SRBO9-53	714157	153	0.1553	0.0014	9.0734	0.3317	0.4237	0.0150	0.97	2405	16	2345	33	2277	67	5.63
	17SRBO9-54	638571	45	0.1616	0.0015	10.0416	0.3760	0.4506	0.0164	0.97	2473	15	2439	34	2398	72	3.12
	17SRBO9-55	485298	102	0.1525	0.0017	8.7066	0.3150	0.4140	0.0142	0.95	2375	19	2308	32	2233	65	6.34
	17SRBO9-56	469837	132	0.1378	0.0013	7.0562	0.2682	0.3715	0.0137	0.97	2199	16	2119	33	2036	64	8.01
	17SRBO9-57	1086880	24	0.1560	0.0014	9.1029	0.3293	0.4232	0.0148	0.97	2413	15	2348	33	2275	67	6.05
	17SRBO9-59	429423	1	0.1408	0.0014	7.5429	0.2678	0.3884	0.0132	0.96	2238	17	2178	31	2116	61	5.77
	17SRBO9-58	404486	91	0.1530	0.0015	8.9458	0.3223	0.4241	0.0147	0.96	2380	17	2332	32	2279	66	4.41
	17SRBO9-61	952496	26	0.1470	0.0015	8.0446	0.2874	0.3969	0.0136	0.96	2311	18	2236	32	2155	62	7.26
	17SRBO9-62	1505249	0	0.1425	0.0013	7.8747	0.2989	0.4007	0.0147	0.97	2258	16	2217	34	2172	67	3.98

Model Ages (Ma)																	
Sample Name, Preperation, and Method	Spot Name	206Pb (cps)	204Pb (cps)	207Pb/ 206Pb	± 2σ	207Pb/ 235U	± 2σ	206Pb/ 238U	± 2σ	p value	207Pb/ 206Pb	207Pb/ 235U	206Pb/ 238U	± 2σ	disc %		
	17SRBO9-63	300107	0	0.1661	0.0016	10.6459	0.3997	0.4650	0.0169	0.97	2518	16	2493	34	2461	74	2.31
	17SRBO9-64	803715	0	0.1582	0.0015	10.4065	0.4466	0.4771	0.0200	0.98	2436	16	2472	39	2515	87	-3.11
	17SRBO9-65	1047839	0	0.1562	0.0014	9.5175	0.3455	0.4419	0.0155	0.97	2415	15	2389	33	2359	69	2.36
	17SRBO9-66	745231	0	0.1541	0.0015	9.2757	0.3581	0.4367	0.0163	0.97	2391	16	2366	35	2336	73	2.38
	17SRBO9-67	983061	0	0.1574	0.0016	9.7446	0.3579	0.4489	0.0159	0.96	2428	17	2411	33	2390	70	1.58
	17SRBO9-68	648790	0	0.1370	0.0013	7.1251	0.2629	0.3772	0.0134	0.97	2190	17	2127	32	2063	63	6.15
	17SRBO9-69	295903	0	0.1614	0.0015	9.8240	0.3734	0.4415	0.0163	0.97	2470	16	2418	34	2357	72	4.80
	17SRBO9-70	706819	0	0.1554	0.0015	9.0020	0.3629	0.4202	0.0165	0.97	2406	16	2338	36	2261	74	6.41
	17SRBO9-71	749371	182	0.1584	0.0015	9.4227	0.3477	0.4313	0.0154	0.97	2439	16	2380	33	2312	69	5.50
	17SRBO9-72	1189493	102	0.1615	0.0015	9.9176	0.3574	0.4453	0.0155	0.97	2472	15	2427	33	2374	69	4.11
	17SRBO9-73	958595	220	0.1605	0.0016	9.7592	0.3579	0.4410	0.0156	0.96	2461	16	2412	33	2355	69	4.49
	17SRBO9-74	709526	151	0.1611	0.0016	9.5514	0.3600	0.4300	0.0157	0.97	2467	16	2393	34	2306	70	7.01
	17SRBO9-75	1887198	387	0.1426	0.0024	7.8558	0.3353	0.3995	0.0157	0.92	2259	29	2215	38	2167	72	4.27
	17SRBO9-76	1069300	151	0.1472	0.0016	8.4955	0.3284	0.4186	0.0155	0.96	2314	19	2285	35	2254	70	2.64
	17SRBO9-77	840781	130	0.1589	0.0014	10.1523	0.3802	0.4633	0.0168	0.97	2444	15	2449	34	2454	74	-0.39
	17SRBO9-78	1377740	75	0.1576	0.0014	10.0716	0.3701	0.4635	0.0165	0.97	2430	15	2441	33	2455	72	-1.02
	17SRBO9-79	1431624	125	0.1558	0.0015	9.9074	0.3703	0.4611	0.0167	0.97	2411	16	2426	34	2445	73	-1.38
	17SRBO9-80	868121	95	0.1585	0.0014	10.1307	0.3694	0.4635	0.0164	0.97	2440	15	2447	33	2455	72	-0.62
	17SRBO9-81	846320	101	0.1603	0.0015	10.2432	0.3830	0.4635	0.0168	0.97	2459	15	2457	34	2455	74	0.15
	17SRBO9-82	849771	33	0.1576	0.0014	9.8069	0.3629	0.4514	0.0162	0.97	2430	15	2417	34	2401	72	1.18
	17SRBO9-83	543790	41	0.1198	0.0012	5.5898	0.2186	0.3385	0.0128	0.97	1953	17	1915	33	1879	61	3.93
	17SRBO9-84	818312	107	0.1350	0.0013	7.1642	0.2667	0.3850	0.0139	0.97	2163	16	2132	33	2100	64	3.04
	17SRBO9-85	833722	67	0.1478	0.0014	8.6066	0.3116	0.4222	0.0148	0.97	2321	16	2297	32	2271	67	2.23
	17SRBO9-86	707924	60	0.1489	0.0015	8.8868	0.3429	0.4328	0.0161	0.97	2334	17	2326	35	2318	72	0.67
	17SRBO9-87	678752	75	0.1513	0.0016	8.8095	0.3164	0.4224	0.0145	0.96	2360	18	2318	32	2271	65	3.91
	17SRBO9-88	3293023	76	0.1471	0.0016	8.5896	0.3305	0.4235	0.0157	0.96	2312	18	2295	34	2276	71	1.58
	17SRBO9-89	1009679	75	0.1514	0.0014	9.2986	0.3325	0.4453	0.0154	0.96	2362	16	2368	32	2375	68	-0.52
	17SRBO9-90	893053	98	0.1537	0.0014	9.2315	0.3359	0.4355	0.0153	0.97	2388	16	2361	33	2331	68	2.46
	17SRBO9-91	783395	61	0.1600	0.0015	10.1526	0.3741	0.4602	0.0164	0.97	2456	15	2449	33	2440	72	0.62
	17SRBO9-92	3707109	89	0.1521	0.0014	9.4536	0.3349	0.4507	0.0154	0.97	2370	16	2383	32	2398	68	-1.19
	17SRBO9-93	877193	67	0.1461	0.0016	8.2333	0.3223	0.4088	0.0153	0.96	2301	19	2257	35	2209	70	4.13
	17SRBO9-94	851696	16	0.1480	0.0014	8.9601	0.3211	0.4392	0.0152	0.97	2322	16	2334	32	2347	68	-1.05
	17SRBO9-95	965771	36	0.1610	0.0015	10.2258	0.3720	0.4606	0.0162	0.97	2466	15	2455	33	2442	71	0.98
	17SRBO9-96	1076199	45	0.1591	0.0017	9.9513	0.3834	0.4536	0.0168	0.96	2446	18	2430	35	2411	74	1.46

Sample Name, Preperation, and Method		Model Ages (Ma)															
		206Pb (cps)	204Pb (cps)	$^{207}\text{Pb}/^{206}\text{Pb}$		$^{207}\text{Pb}/^{235}\text{U}$		$^{206}\text{Pb}/^{238}\text{U}$		$^{207}\text{Pb}/^{206}\text{Pb}$		$^{207}\text{Pb}/^{235}\text{U}$		$^{206}\text{Pb}/^{238}\text{U}$		disc %	
Spot Name				$\pm 2\sigma$	$\pm 2\sigma$	$\pm 2\sigma$	$\pm 2\sigma$	$\pm 2\sigma$	p value	$\pm 2\sigma$	$\pm 2\sigma$	$\pm 2\sigma$	$\pm 2\sigma$				
17SRBO9-97		1760865	114	0.1519	0.0014	8.7340	0.3166	0.4169	0.0146	0.96	2368	16	2311	32	2247	66	5.39
17SRBO9-98		457857	38	0.1605	0.0015	10.1428	0.3732	0.4584	0.0163	0.97	2461	16	2448	33	2432	72	1.17
17SRBO9-99		1038376	57	0.1332	0.0013	7.1063	0.2628	0.3870	0.0138	0.96	2140	17	2125	32	2109	64	1.50
17SRBO9-100		748134	28	0.1562	0.0015	9.4298	0.3714	0.4379	0.0167	0.97	2415	17	2381	36	2341	74	3.13
17SRBO9-101		1178337	37	0.1417	0.0014	7.7030	0.2752	0.3944	0.0135	0.96	2248	17	2197	32	2143	62	4.88
17SRBO9-102		901105	54	0.1555	0.0015	9.3039	0.3275	0.4341	0.0147	0.96	2407	16	2368	32	2324	66	3.56
17SRBO9-103		553951	22	0.1499	0.0016	8.3932	0.3055	0.4061	0.0142	0.96	2345	18	2274	33	2197	65	6.72
17SRBO9-104		2451284	732	0.1590	0.0015	9.5412	0.3384	0.4352	0.0148	0.96	2445	16	2392	32	2329	66	4.97
17SRBO9-105		594665	18	0.1562	0.0015	9.8979	0.3725	0.4595	0.0167	0.97	2415	16	2425	34	2437	73	-0.90
17SRBO9-106		10116993	89	0.1494	0.0014	8.7473	0.3200	0.4246	0.0150	0.97	2339	16	2312	33	2281	68	2.55
17SRBO9-107		1172014	54	0.1617	0.0015	10.3887	0.3803	0.4660	0.0165	0.97	2473	15	2470	33	2466	72	0.31
17SRBO9-108		1030315	28	0.1613	0.0015	10.4764	0.3821	0.4711	0.0166	0.97	2469	15	2478	33	2488	72	-0.77
17SRBO9-109		468310	28	0.1600	0.0015	10.1598	0.3886	0.4604	0.0171	0.97	2456	15	2449	35	2441	75	0.60
17SRBO9-110		604873	50	0.1622	0.0015	10.2537	0.3784	0.4584	0.0164	0.97	2479	15	2458	34	2432	72	1.93
17SRBO9-111		817737	37	0.1449	0.0013	8.2296	0.3136	0.4120	0.0152	0.97	2286	16	2257	34	2224	69	2.79
17SRBO9-112		927468	53	0.1551	0.0018	9.4197	0.3394	0.4406	0.0150	0.95	2403	20	2380	33	2353	67	2.10
17SRBO9-113		858329	12	0.1625	0.0015	10.2998	0.3658	0.4597	0.0158	0.97	2482	15	2462	32	2438	69	1.78
17SRBO9-114		566614	27	0.1204	0.0012	5.6437	0.2059	0.3401	0.0120	0.96	1962	17	1923	31	1887	57	3.96
17SRBO9-115		731263	41	0.1501	0.0014	8.4957	0.3119	0.4105	0.0146	0.97	2347	16	2285	33	2217	66	5.86
17SRBO9-116		1789460	66	0.1616	0.0015	10.3821	0.3682	0.4661	0.0160	0.97	2472	15	2469	32	2466	70	0.23
17SRBO9-117		1198094	32	0.1441	0.0013	7.8848	0.2803	0.3968	0.0136	0.97	2277	16	2218	32	2154	63	5.71
17SRBO9-118		981343	12	0.1613	0.0015	10.1527	0.3619	0.4565	0.0157	0.97	2469	16	2449	32	2424	69	1.86
17SRBO9-119		1060336	48	0.1356	0.0014	7.0736	0.2524	0.3782	0.0129	0.95	2172	18	2121	31	2068	60	5.05
17SRBO9-120		829178	6	0.1626	0.0015	10.1870	0.3714	0.4543	0.0160	0.97	2483	15	2452	33	2414	71	2.85
17SRBO9-121		1089428	18	0.1609	0.0015	10.1395	0.3665	0.4571	0.0160	0.97	2465	16	2448	33	2427	70	1.59
17SRBO9-122		741010	1	0.1475	0.0014	8.4568	0.3262	0.4157	0.0156	0.97	2318	16	2281	34	2241	71	3.43
17SRBO9-123		959740	0	0.1465	0.0026	8.1048	0.3162	0.4012	0.0140	0.89	2305	30	2243	35	2175	64	6.01
17SRBO9-124		1306710	1	0.1581	0.0016	9.8620	0.3665	0.4525	0.0162	0.96	2435	17	2422	34	2406	71	1.19
17SRBO9-125		710145	9	0.1436	0.0019	7.7644	0.3106	0.3921	0.0148	0.95	2271	22	2204	35	2133	68	6.48
17SRBO9-126		447360	8	0.1634	0.0015	10.0746	0.3707	0.4472	0.0159	0.97	2491	16	2442	33	2383	70	4.54
17SRBO9-127		1085263	13	0.1595	0.0015	9.6350	0.3392	0.4381	0.0149	0.96	2450	16	2401	32	2342	66	4.61
17SRBO9-128		1414687	4	0.1614	0.0015	9.9847	0.3501	0.4486	0.0152	0.97	2471	15	2433	32	2389	67	3.42
17SRBO9-129		1058303	9	0.1606	0.0015	9.8248	0.3494	0.4436	0.0152	0.97	2462	15	2418	32	2367	68	4.05
17SRBO9-130		469747	0	0.1387	0.0013	7.1413	0.2658	0.3734	0.0135	0.97	2211	16	2129	33	2046	63	8.09

Model Ages (Ma)																	
Sample Name, Preperation, and Method	Spot Name	206Pb (cps)	204Pb (cps)	207Pb/ 206Pb	± 2σ	207Pb/ 235U	± 2σ	206Pb/ 238U	± 2σ	p value	207Pb/ 206Pb	207Pb/ 235U	206Pb/ 238U	± 2σ	disc %		
	17SRB09-131	787832	3	0.1642	0.0015	10.2658	0.3736	0.4534	0.0160	0.97	2499	16	2459	33	2410	70	3.70
	17SRB09-132	607128	4	0.1612	0.0015	9.7009	0.3479	0.4366	0.0151	0.97	2468	15	2407	32	2335	68	5.68
	17SRB09-133	602175	6	0.1575	0.0015	9.2719	0.3275	0.4270	0.0146	0.97	2429	16	2365	32	2292	65	5.95
	17SRB09-134	2274368	34	0.1575	0.0014	9.8411	0.3616	0.4531	0.0161	0.97	2429	15	2420	33	2409	71	0.83
	17SRB09-135	1320308	2	0.1570	0.0015	9.7470	0.3427	0.4502	0.0152	0.96	2424	16	2411	32	2396	67	1.14
	17SRB09-136	1312383	96	0.1521	0.0016	8.7394	0.3153	0.4167	0.0144	0.96	2370	18	2311	32	2246	65	5.53
	17SRB09-138	1342600	72	0.1359	0.0015	7.2516	0.2731	0.3869	0.0139	0.95	2176	20	2143	33	2108	64	3.21
	17SRB09-139	726394	27	0.1482	0.0016	8.2018	0.2933	0.4013	0.0137	0.96	2326	18	2254	32	2175	63	6.94
	17SRB09-140	1400145	34	0.2441	0.0027	19.0934	0.7247	0.5673	0.0206	0.96	3147	17	3047	36	2897	84	8.64
	17SRB09-141	732614	59	0.1580	0.0016	9.8071	0.3552	0.4502	0.0156	0.96	2434	18	2417	33	2396	69	1.60
	17SRB09-142	755571	5	0.1555	0.0016	8.9714	0.3180	0.4183	0.0142	0.96	2408	18	2335	32	2253	64	6.88
	17SRB09-143	2119606	62	0.1578	0.0016	9.5930	0.3416	0.4409	0.0150	0.96	2432	17	2397	32	2355	67	3.30
	17SRB09-144	1103856	26	0.1549	0.0016	9.1047	0.3236	0.4262	0.0145	0.95	2401	18	2349	32	2288	65	4.93
	17SRB09-145	897726	30	0.1621	0.0017	9.8595	0.3557	0.4412	0.0152	0.96	2477	18	2422	33	2356	68	5.15
	17SRB09-146	501231	16	0.1597	0.0017	9.6785	0.3495	0.4396	0.0152	0.96	2452	18	2405	33	2349	68	4.42
	17SRB09-147	756105	24	0.1587	0.0017	9.4485	0.3413	0.4319	0.0149	0.95	2442	18	2383	33	2314	67	5.51
	17SRB09-148	5345690	30	0.1399	0.0015	7.6699	0.2760	0.3975	0.0136	0.95	2227	19	2193	32	2157	63	3.20
17SRB-0009A3																	
<i>Grain Mount, Zircon</i>																	
<i>LASS-ICPMS</i>																	
	O9-1	833000	231	0.1621	0.0010	11.2500	0.3800	0.5020	0.0160	0.98	2479	9	2540	32	2620	67	-5.39
	O9-2	893000	82	0.1570	0.0008	8.1800	0.3000	0.3800	0.0130	0.99	2422	9	2242	35	2074	60	16.80
	O9-3	624000	90	0.1540	0.0009	9.1730	0.2100	0.4320	0.0089	0.65	2389	10	2355	21	2314	40	3.25
	O9-4	568000	75	0.1616	0.0009	10.8000	0.2900	0.4862	0.0120	0.95	2471	10	2504	25	2553	52	-3.20
	O9-5	784000	53	0.1546	0.0009	9.1000	0.2300	0.4272	0.0097	0.91	2396	10	2347	23	2292	44	4.54
	O9-6	460000	43	0.1565	0.0013	9.7200	0.2400	0.4492	0.0110	0.85	2417	14	2408	23	2391	49	1.09
	O9-7	762000	129	0.1444	0.0007	8.1200	0.2300	0.4073	0.0100	0.97	2279	8	2242	26	2201	47	3.56
	O9-8	1082000	92	0.1615	0.0010	10.5000	0.2500	0.4726	0.0110	0.88	2470	11	2481	24	2494	49	-0.96
	O9-9	768000	59	0.1631	0.0007	10.9390	0.2600	0.4861	0.0100	0.90	2487	8	2517	22	2553	45	-2.60
	O9-10	629000	40	0.1615	0.0009	10.5200	0.2500	0.4714	0.0110	0.87	2471	10	2481	22	2489	46	-0.72
	O9-11	594000	89	0.1605	0.0007	10.3740	0.2400	0.4678	0.0099	0.88	2460	8	2468	21	2474	43	-0.55
	O9-12	350000	128	0.1438	0.0009	8.3800	0.2400	0.4221	0.0120	0.94	2272	11	2269	26	2267	53	0.22
	O9-13	598000	155	0.1613	0.0011	10.5900	0.2600	0.4747	0.0099	0.78	2468	12	2486	23	2504	43	-1.44
	O9-14	343400	51	0.1471	0.0015	8.7000	0.2300	0.4286	0.0098	0.76	2311	17	2306	24	2299	45	0.52
	O9-15	626000	70	0.1634	0.0009	11.2600	0.3300	0.4994	0.0140	0.97	2490	9	2542	27	2609	59	-4.58
	O9-16	490000	59	0.1478	0.0013	9.2400	0.2700	0.4533	0.0130	0.85	2320	15	2360	26	2408	57	-3.65

Sample Name, Preperation, and Method		Model Ages (Ma)															
		206Pb (cps)	204Pb (cps)	$^{207}\text{Pb}/^{206}\text{Pb}$		$^{207}\text{Pb}/^{235}\text{U}$		$^{206}\text{Pb}/^{238}\text{U}$		$^{207}\text{Pb}/^{206}\text{Pb}$		$^{207}\text{Pb}/^{235}\text{U}$		$^{206}\text{Pb}/^{238}\text{U}$		disc %	
Spot Name				$\pm 2\sigma$		$\pm 2\sigma$		$\pm 2\sigma$		p value		$\pm 2\sigma$		$\pm 2\sigma$			
O9-17		352000	59	0.1578	0.0009	10.1700	0.2800	0.4665	0.0120	0.96	2431	9	2447	25	2466	53	-1.44
O9-18		203000	90	0.1220	0.0010	6.1750	0.1600	0.3663	0.0089	0.80	1984	14	2000	22	2011	42	-1.34
O9-19		557000	97	0.1560	0.0008	10.2400	0.2500	0.4753	0.0110	0.94	2412	9	2456	23	2505	48	-3.73
O9-20		704000	80	0.1548	0.0009	9.7500	0.2400	0.4566	0.0100	0.86	2398	10	2410	23	2424	45	-1.08
O9-21		414000	53	0.1561	0.0012	9.7000	0.2600	0.4497	0.0100	0.83	2412	13	2405	25	2393	46	0.79
O9-22		830000	71	0.1585	0.0010	9.4700	0.2400	0.4330	0.0096	0.92	2439	11	2384	24	2319	43	5.17
O9-23		754000	72	0.1611	0.0007	10.3040	0.2400	0.4639	0.0097	0.86	2466	7	2462	21	2457	43	0.35
O9-24		450000	73	0.1562	0.0008	9.7660	0.2300	0.4522	0.0094	0.84	2414	8	2412	21	2404	42	0.41
O9-25		399000	117	0.1554	0.0014	9.3300	0.2600	0.4340	0.0110	0.78	2405	16	2370	25	2323	51	3.53
O9-26		703000	50	0.1620	0.0007	10.6270	0.2500	0.4745	0.0100	0.91	2475	7	2490	22	2503	45	-1.11
O9-27		702000	102	0.1574	0.0016	10.3100	0.2900	0.4731	0.0110	0.83	2426	17	2462	26	2496	50	-2.80
O9-28		464000	22	0.1573	0.0011	10.0640	0.2400	0.4633	0.0099	0.79	2426	11	2440	22	2454	44	-1.14
O9-29		539000	68	0.1453	0.0013	8.4700	0.2300	0.4211	0.0110	0.88	2291	15	2282	24	2265	51	1.15
O9-30		925000	104	0.1546	0.0008	9.5400	0.2400	0.4466	0.0110	0.93	2396	9	2391	23	2379	48	0.73
O9-31		831000	58	0.1622	0.0008	10.7700	0.2600	0.4810	0.0100	0.89	2478	8	2503	22	2535	48	-2.25
O9-32		452000	118	0.1489	0.0015	10.2300	0.3400	0.4958	0.0140	0.94	2332	18	2452	32	2594	59	-10.10
O9-33		439000	39	0.1611	0.0010	9.9930	0.2300	0.4491	0.0093	0.53	2465	10	2434	22	2391	41	3.11
O9-34		314000	36	0.1265	0.0009	6.4960	0.1600	0.3725	0.0081	0.83	2048	12	2044	22	2040	38	0.39
O9-35		672000	50	0.1617	0.0007	10.9600	0.2700	0.4917	0.0110	0.95	2472	7	2519	23	2577	48	-4.06
O9-36		758000	50	0.1488	0.0009	9.0040	0.2100	0.4386	0.0092	0.74	2331	10	2338	21	2344	41	-0.55
O9-37		594000	97	0.1607	0.0008	10.5200	0.2600	0.4744	0.0110	0.93	2462	9	2481	22	2502	48	-1.60
O9-38		512000	147	0.1501	0.0013	7.8300	0.2300	0.3808	0.0094	0.93	2345	14	2210	27	2080	44	12.74
O9-39		1354000	128	0.1579	0.0009	9.7630	0.2200	0.4483	0.0096	0.90	2432	9	2412	21	2387	43	1.87
O9-40		529000	26	0.1544	0.0008	10.7800	0.2800	0.5062	0.0130	0.96	2395	9	2503	24	2639	54	-9.26
O9-41		2890000	80	0.1503	0.0014	8.0200	0.2300	0.3869	0.0093	0.89	2347	16	2232	27	2108	44	11.34
O9-42		816000	85	0.1358	0.0014	6.8820	0.1700	0.3680	0.0077	0.48	2172	18	2096	22	2020	36	7.52
O9-43		202000	15	0.1319	0.0015	7.5700	0.2000	0.4160	0.0098	0.67	2122	19	2181	23	2242	45	-5.35
O9-44		637000	81	0.1485	0.0009	8.6690	0.2000	0.4224	0.0090	0.77	2327	10	2304	21	2271	41	2.48

														Model Ages (Ma)					
Sample Name, Preperation, and Method	Spot Name	206Pb (cps)	204Pb (cps)	207Pb/ 206Pb	± 2σ	207Pb/ 235U	± 2σ	206Pb/ 238U	± 2σ	p value	207Pb/ 206Pb	± 2σ	207Pb/ 235U	± 2σ	206Pb/ 238U	± 2σ	disc %		
18SRB-O112A1																			
<i>Grain Mount, Zircon</i>																			
<i>LASS-ICPMS</i>																			
O112 - 1		2787000	105	0.1437	0.0008	7.7470	0.1900	0.3903	0.0081	0.86	2270	10	2201	22	2124	38	6.89		
O112 - 3		1303000	99	0.1584	0.0008	9.6500	0.2500	0.4416	0.0110	0.95	2438	8	2401	25	2357	47	3.42		
O112 - 4		668000	59	0.1615	0.0010	10.4700	0.2500	0.4696	0.0100	0.82	2470	11	2476	23	2481	45	-0.44		
O112 - 5		1220000	149	0.1582	0.0009	8.2300	0.3300	0.3810	0.0150	0.99	2435	9	2247	36	2074	69	17.41		
O112 - 6		598000	45	0.1610	0.0009	10.4300	0.2700	0.4712	0.0120	0.91	2465	10	2472	24	2487	51	-0.90		
O112 - 7		883000	348	0.1575	0.0011	9.4110	0.2200	0.4319	0.0089	0.73	2428	11	2378	22	2314	40	4.93		
O112 - 8		405000	221	0.1638	0.0011	11.5400	0.2800	0.5117	0.0120	0.86	2495	11	2567	22	2663	51	-6.31		
O112 - 9		644000	117	0.1581	0.0009	10.0720	0.2400	0.4627	0.0100	0.79	2434	10	2441	22	2451	44	-0.69		
O112 - 10		613900	120	0.1565	0.0010	9.8540	0.2300	0.4574	0.0096	0.72	2417	10	2421	21	2428	42	-0.47		
O112 - 11		613000	90	0.1533	0.0008	9.4300	0.2400	0.4462	0.0100	0.94	2382	9	2379	24	2377	47	0.20		
O112 - 12		851000	92	0.1577	0.0009	9.8200	0.2400	0.4514	0.0110	0.91	2430	10	2417	23	2401	47	1.19		
O112 - 13		1141000	119	0.1533	0.0012	8.9500	0.2400	0.4214	0.0100	0.89	2381	13	2331	24	2270	47	4.89		
O112 - 14		641000	439	0.1647	0.0021	12.5600	0.4500	0.5530	0.0160	0.91	2502	21	2643	34	2836	66	-11.78		
O112 - 15		923000	161	0.1566	0.0014	9.6280	0.2300	0.4447	0.0100	0.70	2418	16	2400	22	2371	45	1.98		
O112 - 16		1155000	208	0.1545	0.0012	6.3200	0.1800	0.2991	0.0077	0.94	2396	13	2020	25	1686	38	42.11		
O112 - 17		871000	172	0.1399	0.0010	7.6900	0.2600	0.3989	0.0110	0.99	2224	12	2191	31	2162	53	2.87		
O112 - 18		854000	357	0.1654	0.0011	10.4740	0.2500	0.4599	0.0095	0.74	2511	11	2477	22	2439	42	2.95		
O112 - 19		662000	144	0.1676	0.0010	11.4500	0.3200	0.4967	0.0120	0.94	2532	10	2559	26	2599	52	-2.56		
O112 - 20		450000	80	0.1627	0.0007	11.7800	0.3900	0.5260	0.0170	0.99	2483	7	2581	32	2719	72	-8.70		
O112 - 21		388000	88	0.1568	0.0009	10.0300	0.2900	0.4649	0.0120	0.96	2420	10	2435	26	2459	54	-1.60		
O112 - 22		1600000	375	0.1473	0.0012	8.2200	0.3300	0.4030	0.0140	0.98	2314	14	2250	37	2182	65	6.05		
O112 - 23		791000	405	0.1640	0.0012	9.8570	0.2300	0.4358	0.0097	0.73	2496	12	2421	22	2332	44	7.03		
O112 - 24		878000	182	0.1507	0.0010	7.6000	0.2600	0.3692	0.0120	0.97	2352	12	2184	30	2023	55	16.26		
O112 - 25		655000	107	0.1502	0.0009	8.6300	0.2400	0.4164	0.0098	0.92	2347	10	2298	25	2243	44	4.61		
O112 - 26		563000	46	0.1564	0.0010	9.8600	0.2700	0.4585	0.0110	0.93	2415	11	2420	25	2432	50	-0.70		

Sample Name, Preperation, and Method	Spot Name	Model Ages (Ma)															
		206Pb (cps)	204Pb (cps)	$\frac{^{207}\text{Pb}}{^{206}\text{Pb}}$		$\frac{^{207}\text{Pb}}{^{235}\text{U}}$		$\frac{^{206}\text{Pb}}{^{238}\text{U}}$		p value	$\frac{^{207}\text{Pb}}{^{206}\text{Pb}}$		$\frac{^{207}\text{Pb}}{^{235}\text{U}}$		$\frac{^{206}\text{Pb}}{^{238}\text{U}}$		
		$\pm 2\sigma$	$\pm 2\sigma$	$\pm 2\sigma$	$\pm 2\sigma$	$\pm 2\sigma$	$\pm 2\sigma$	$\pm 2\sigma$	$\pm 2\sigma$	$\pm 2\sigma$	$\pm 2\sigma$	$\pm 2\sigma$	$\pm 2\sigma$	$\pm 2\sigma$	disc %		
17SRB-S058A																	
<i>Thin Section, Zircon</i>																	
<i>LA-ICPMS</i>																	
	S58S1-4a-2	853322	52	0.1349	0.0015	6.9975	0.1565	0.3762	0.0073	0.87	2163	19	2111	20	2058	34	5.07
	S58S1-4b-3	558155	27	0.1508	0.0016	9.0689	0.2210	0.4363	0.0096	0.91	2355	18	2345	22	2334	43	0.88
	S58S1-4b-4	344072	34	0.1629	0.0017	10.5487	0.2436	0.4697	0.0097	0.89	2486	18	2484	21	2482	42	0.14
	S58S1-7a-5	849845	188	0.1573	0.0017	9.7416	0.2063	0.4492	0.0083	0.87	2427	18	2411	19	2392	37	1.46
	S58S1-7a-6	726330	24	0.1582	0.0017	10.5306	0.3214	0.4827	0.0138	0.94	2437	18	2483	28	2539	60	-4.02
	S58S1-8-7	1076725	30	0.1594	0.0017	10.1217	0.2395	0.4606	0.0098	0.90	2449	18	2446	22	2442	43	0.27
	S58S1-9a-8	2009143	71	0.1526	0.0016	8.6004	0.1741	0.4089	0.0071	0.86	2375	18	2297	18	2210	32	7.46
	S58S1-9b-9	672131	17	0.1623	0.0019	10.2657	0.2314	0.4588	0.0088	0.85	2479	20	2459	21	2434	39	1.85
	S58S1-10-10	478845	10	0.1575	0.0019	9.5714	0.2408	0.4408	0.0097	0.87	2429	21	2394	23	2354	43	3.15
	S58S1-12-11	359642	20	0.1627	0.0017	10.4108	0.3560	0.4640	0.0151	0.95	2484	18	2472	31	2457	66	1.09
	S58S1-12-12	341758	17	0.1575	0.0017	9.6373	0.2241	0.4439	0.0092	0.89	2429	18	2401	21	2368	41	2.56
	S58S1-12-14	432450	89	0.1466	0.0017	8.4853	0.1890	0.4199	0.0080	0.85	2306	20	2284	20	2260	36	2.04
	S58S1-15-15	659828	214	0.1578	0.0019	9.7159	0.2423	0.4465	0.0097	0.87	2432	21	2408	23	2380	43	2.20
	S58S1-15-16	458290	10	0.1571	0.0019	9.8535	0.2351	0.4550	0.0093	0.86	2424	20	2421	22	2417	41	0.29
	S58S1-16-17	1420983	156	0.1512	0.0017	9.0668	0.2478	0.4349	0.0108	0.91	2360	19	2345	25	2328	48	1.38
	S58S1-17-18	353126	8	0.1514	0.0018	9.1344	0.2657	0.4376	0.0116	0.91	2362	20	2352	26	2340	52	0.94
	S58S1-18-19	385225	12	0.1619	0.0017	10.5368	0.3423	0.4720	0.0145	0.94	2476	18	2483	30	2492	63	-0.66
	S58S1-19-20	370574	8	0.1605	0.0017	10.2808	0.2466	0.4647	0.0100	0.90	2460	17	2460	22	2460	44	0.00
	S58S1-21b-21	498520	12	0.1615	0.0017	10.3298	0.2721	0.4638	0.0112	0.92	2472	18	2465	24	2456	49	0.62
	S58S1-21b-22	1220142	19	0.1178	0.0012	5.6372	0.1300	0.3469	0.0071	0.89	1924	18	1922	20	1920	34	0.19
	S58S1-21b-23	1512597	18	0.1395	0.0015	7.9309	0.1878	0.4122	0.0087	0.89	2221	19	2223	21	2225	40	-0.16
	S58S1-21b-24	1164105	14	0.1517	0.0016	9.3559	0.2083	0.4473	0.0087	0.87	2365	18	2374	20	2383	39	-0.77
17SRB-D042A1																	
<i>Thin Section, Monazite Grain 1</i>																	
<i>LA-ICPMS</i>																	
	D42A1S1-m4c-1	268207	32	0.1175	0.0013	5.4232	0.1038	0.3347	0.0053	0.83	1919	19	1889	16	1861	26	3.11
	D42A1S1-m4c-2	281701	39	0.1176	0.0013	5.4722	0.1196	0.3376	0.0064	0.87	1919	19	1896	19	1875	31	2.36
	D42A1S1-m4c-3	406334	83	0.1180	0.0013	5.6961	0.1288	0.3501	0.0070	0.88	1926	19	1931	19	1935	33	-0.45
	D42A1S1-m13-4	185451	44	0.1165	0.0012	5.2557	0.1022	0.3271	0.0053	0.84	1904	19	1862	16	1824	26	4.35
<i>Thin Section, Monazite Grain 2</i>																	
<i>LA-ICPMS</i>																	
	D42A1S1-m14-5	282833	53	0.1522	0.0016	8.8511	0.1625	0.4219	0.0063	0.82	2370	18	2323	17	2269	29	4.47

														Model Ages (Ma)						
Sample Name, Preperation, and Method	Spot Name	206Pb	204Pb	$^{207}\text{Pb}/^{206}\text{Pb}$		$^{207}\text{Pb}/^{235}\text{U}$		$^{206}\text{Pb}/^{238}\text{U}$		p value	$^{207}\text{Pb}/^{206}\text{Pb}$		$^{207}\text{Pb}/^{235}\text{U}$		$^{206}\text{Pb}/^{238}\text{U}$		disc %			
		(cps)	(cps)	$\pm 2\sigma$	$\pm 2\sigma$	$\pm 2\sigma$	$\pm 2\sigma$	$\pm 2\sigma$	$\pm 2\sigma$		$\pm 2\sigma$	$\pm 2\sigma$	$\pm 2\sigma$	$\pm 2\sigma$	$\pm 2\sigma$					
	D42A1S1-m14-6	288382	48	0.1497	0.0016	8.7961	0.1662	0.4261	0.0067	0.83	2343	18	2317	17	2288	30	2.37			
	D42A1S1-m14-7	249147	48	0.1529	0.0016	9.0946	0.1672	0.4313	0.0065	0.82	2379	18	2348	17	2312	29	2.91			
	D42A1S1-m14-8	246598	51	0.1519	0.0017	9.0262	0.1747	0.4310	0.0068	0.82	2367	19	2341	18	2310	31	2.46			
	D42A1S1-m14-9	255005	40	0.1508	0.0016	8.9131	0.1655	0.4288	0.0066	0.83	2355	18	2329	17	2300	30	2.36			
	D42A1S1-m14-10	249313	39	0.1516	0.0016	8.9794	0.1670	0.4294	0.0066	0.82	2365	18	2336	17	2303	30	2.67			
	D42A1S1-m14-11	236280	50	0.1518	0.0016	9.0623	0.1680	0.4331	0.0066	0.82	2366	18	2344	17	2320	30	1.99			
	D42A1S1-m14-12	267667	32	0.1510	0.0016	8.8419	0.1694	0.4247	0.0068	0.83	2357	18	2322	17	2282	31	3.32			
17SRB-S058A																				
<i>Thin Section, Monazite</i>																				
<i>LA-ICPMS</i>																				
	S58S1-m3-1	373194	18	0.1164	0.0012	5.3093	0.1198	0.3309	0.0066	0.88	1901	19	1870	19	1843	32	3.19			
	S58S1-m3-2	561293	22	0.1156	0.0012	5.4861	0.1274	0.3442	0.0071	0.89	1889	19	1898	20	1907	34	-0.93			
	S58S1-m3-3	526821	17	0.1166	0.0012	5.4646	0.1229	0.3399	0.0067	0.88	1905	19	1895	19	1886	32	1.01			
	S58S1-m3-4	432581	23	0.1160	0.0012	5.5034	0.1258	0.3440	0.0070	0.89	1896	19	1901	19	1906	33	-0.54			
	S58S1-m6-5	874111	21	0.1138	0.0012	5.4543	0.1295	0.3475	0.0074	0.90	1862	19	1893	20	1923	35	-3.17			
	S58S1-m6-6	791526	12	0.1136	0.0012	5.3571	0.1308	0.3420	0.0075	0.90	1858	19	1878	21	1896	36	-2.01			
	S58S1-m6-7	726793	20	0.1135	0.0012	5.3717	0.1224	0.3433	0.0070	0.89	1856	19	1880	19	1903	33	-2.47			
	S58S1-m6-8	640418	8	0.1137	0.0013	5.3364	0.1251	0.3405	0.0070	0.88	1859	20	1875	20	1889	34	-1.62			
	S58S1-m6-9	593413	13	0.1140	0.0012	5.3406	0.1218	0.3397	0.0069	0.89	1865	19	1875	19	1885	33	-1.10			
	S58S1-m6-10	374423	12	0.1158	0.0012	5.4024	0.1258	0.3383	0.0070	0.89	1892	19	1885	20	1879	34	0.73			
	S58S1-m6-11	371641	6	0.1160	0.0012	5.5143	0.1291	0.3447	0.0072	0.89	1896	19	1903	20	1909	34	-0.70			
	S58S1-m6-12	395895	7	0.1164	0.0012	5.5280	0.1271	0.3445	0.0070	0.89	1901	19	1905	20	1908	34	-0.37			
	S58S1-m6-13	375788	6	0.1152	0.0012	5.3862	0.1239	0.3392	0.0069	0.89	1883	19	1883	20	1883	33	0.00			
	S58S1-m6-14	430188	2	0.1135	0.0012	5.2463	0.1250	0.3352	0.0071	0.89	1856	19	1860	20	1864	34	-0.40			
	S58S1-m6-15	479773	3	0.1142	0.0012	5.3244	0.1222	0.3382	0.0069	0.89	1867	19	1873	19	1878	33	-0.56			
	S58S1-m6-16	745634	9	0.1117	0.0012	5.1735	0.1251	0.3360	0.0073	0.90	1827	19	1848	20	1867	35	-2.15			
	S58S1-m7a-17	397506	1	0.1134	0.0012	5.1123	0.1160	0.3268	0.0066	0.89	1855	19	1838	19	1823	32	1.77			
	S58S1-m7a-18	395892	0	0.1154	0.0012	5.3179	0.1224	0.3343	0.0068	0.89	1886	19	1872	19	1859	33	1.45			
	S58S1-m7a-19	534012	3	0.1160	0.0012	5.5930	0.1299	0.3496	0.0072	0.89	1896	19	1915	20	1933	34	-1.91			
	S58S1-m7b-20	377648	1	0.1109	0.0012	4.8854	0.1117	0.3194	0.0065	0.88	1815	19	1800	19	1787	31	1.58			
	S58S1-m7b-21	392052	3	0.1111	0.0012	4.9104	0.1123	0.3204	0.0065	0.89	1818	19	1804	19	1792	32	1.48			
	S58S1-m7b-22	397449	1	0.1134	0.0012	5.1620	0.1178	0.3301	0.0067	0.89	1855	19	1846	19	1839	32	0.87			
	S58S1-m7b-23	376691	3	0.1166	0.0012	5.4728	0.1249	0.3403	0.0069	0.89	1905	19	1896	19	1888	33	0.92			
	S58S1-m7b-24	367936	3	0.1165	0.0012	5.4559	0.1271	0.3396	0.0070	0.89	1903	19	1894	20	1885	34	0.98			

Model Ages (Ma)																	
Sample Name, Preperation, and Method	Spot Name	206Pb (cps)	204Pb (cps)	207Pb/ 206Pb	± 2σ	207Pb/ 235U	± 2σ	206Pb/ 238U	± 2σ	p value	207Pb/ 206Pb	± 2σ	207Pb/ 235U	± 2σ	206Pb/ 238U	± 2σ	disc %
	S58S1-m7b-25	397264	4	0.1156	0.0012	5.3555	0.1214	0.3360	0.0067	0.88	1889	19	1878	19	1867	32	1.19
	S58S1-m7b-26	391988	1	0.1168	0.0012	5.4711	0.1245	0.3398	0.0069	0.89	1908	19	1896	19	1886	33	1.17
	S58S1-m7b-27	376327	4	0.1153	0.0012	5.2672	0.1192	0.3315	0.0066	0.89	1884	19	1864	19	1845	32	2.08
	S58S1-m7c-28	382452	0	0.1149	0.0012	5.2950	0.1198	0.3342	0.0067	0.88	1878	19	1868	19	1859	32	1.04
	S58S1-m7c-29	385857	6	0.1146	0.0013	5.2485	0.1199	0.3322	0.0066	0.87	1874	20	1861	19	1849	32	1.34
	S58S1-m7c-30	407159	2	0.1165	0.0012	5.5226	0.1258	0.3438	0.0070	0.89	1903	19	1904	19	1905	33	-0.07
	S58S1-m7c-31	379871	5	0.1122	0.0012	5.0045	0.1155	0.3235	0.0066	0.89	1835	19	1820	19	1807	32	1.57
	S58S1-m7c-32	350187	3	0.1153	0.0013	5.2638	0.1197	0.3310	0.0066	0.88	1885	19	1863	19	1843	32	2.25
	S58S1-m22-33	916581	3	0.1150	0.0012	5.5452	0.1288	0.3496	0.0072	0.89	1880	19	1908	20	1933	35	-2.72
	S58S1-m22-34	720757	1	0.1151	0.0012	5.4790	0.1281	0.3453	0.0072	0.89	1881	19	1897	20	1912	34	-1.63
	S58S1-m22-35	429857	0	0.1140	0.0012	5.0773	0.1166	0.3230	0.0066	0.89	1864	19	1832	19	1804	32	3.34
	S58S1-m22-36	449686	0	0.1151	0.0012	5.2026	0.1170	0.3279	0.0065	0.88	1881	19	1853	19	1828	32	2.88
	S58S1-m22-37	612942	0	0.1149	0.0012	5.4133	0.1236	0.3416	0.0069	0.89	1879	19	1887	19	1894	33	-0.81
	S58S1-m22-38	486287	1	0.1137	0.0012	5.1859	0.1179	0.3307	0.0067	0.89	1860	19	1850	19	1842	32	0.96
17SRB-L032A																	
<i>Thin Section, Monazite</i>																	
<i>LA-ICPMS</i>																	
	L32AS1-m4c-1	467417	40	0.1177	0.0013	5.5312	0.1067	0.3407	0.0053	0.81	1922	20	1905	16	1890	26	1.68
	L32AS1-m4c-2	273701	32	0.1176	0.0013	5.3755	0.1036	0.3314	0.0051	0.80	1921	20	1881	16	1845	25	4.09
	L32AS1-m4c-3	161453	43	0.1180	0.0014	5.2935	0.1097	0.3254	0.0055	0.81	1926	21	1868	18	1816	27	6.05
	L32AS1-m6a-4	181919	42	0.1182	0.0014	5.5199	0.1059	0.3388	0.0052	0.80	1929	20	1904	16	1881	25	2.55
	L32AS1-m6a-5	141577	37	0.1179	0.0014	5.5958	0.1075	0.3442	0.0053	0.80	1925	21	1915	16	1907	25	0.97
	L32AS1-m6a-6	131209	32	0.1173	0.0014	5.2529	0.1030	0.3247	0.0051	0.81	1916	21	1861	17	1813	25	5.70
	L32AS1-m6a-7	125631	40	0.1167	0.0014	5.2974	0.1035	0.3293	0.0051	0.79	1906	21	1868	17	1835	25	3.87
	L32AS1-m6a-8	129235	32	0.1172	0.0014	5.2584	0.1014	0.3253	0.0050	0.79	1914	21	1862	16	1816	24	5.43
	L32AS1-m6a-9	133079	29	0.1183	0.0014	5.4952	0.1058	0.3369	0.0052	0.80	1931	21	1900	16	1872	25	3.15
	L32AS1-m6a-10	112654	43	0.1180	0.0014	5.4077	0.1043	0.3323	0.0051	0.79	1927	21	1886	16	1849	24	4.17
	L32AS1-m6a-11	160571	32	0.1173	0.0013	5.3414	0.1016	0.3302	0.0050	0.80	1916	20	1876	16	1839	24	4.15
	L32AS1-m6a-12	115469	18	0.1183	0.0014	5.3896	0.1046	0.3305	0.0051	0.80	1930	21	1883	16	1841	25	4.88
	L32AS1-m6a-13	102948	26	0.1185	0.0014	5.3842	0.1034	0.3295	0.0051	0.80	1934	20	1882	16	1836	25	5.35
	L32AS1-m6b-14	128429	27	0.1165	0.0014	5.2583	0.1029	0.3274	0.0051	0.80	1903	21	1862	17	1826	25	4.26
	L32AS1-m6b-15	138585	40	0.1167	0.0014	5.2870	0.1034	0.3285	0.0050	0.78	1907	22	1867	17	1831	24	4.15
	L32AS1-m6b-16	117274	15	0.1167	0.0014	5.3439	0.1029	0.3320	0.0051	0.80	1907	21	1876	16	1848	25	3.16

Model Ages (Ma)																	
Sample Name, Preperation, and Method	Spot Name	206Pb (cps)	204Pb (cps)	207Pb/ 206Pb	± 2σ	207Pb/ 235U	± 2σ	206Pb/ 238U	± 2σ	p value	207Pb/ 206Pb	± 2σ	207Pb/ 235U	± 2σ	206Pb/ 238U	± 2σ	disc %
	L32AS1-m6b-17	104761	24	0.1177	0.0015	5.3803	0.1058	0.3316	0.0051	0.78	1921	22	1882	17	1846	25	4.09
	L32AS1-m6c-19	147721	22	0.1186	0.0014	5.4650	0.1061	0.3343	0.0052	0.80	1935	21	1895	17	1859	25	4.07
	L32AS1-m9-20	130085	19	0.1174	0.0014	4.9208	0.0960	0.3041	0.0047	0.79	1916	21	1806	16	1712	23	11.96
	L32AS1-m9-21	164958	14	0.1174	0.0014	5.1923	0.0995	0.3208	0.0049	0.80	1917	21	1851	16	1794	24	6.86
	L32AS1-m9-22	115814	14	0.1171	0.0014	4.6813	0.0914	0.2899	0.0046	0.80	1913	21	1764	16	1641	23	16.56
	L32AS1-m10-23	94297	8	0.1161	0.0014	5.1597	0.1006	0.3223	0.0050	0.80	1897	21	1846	16	1801	25	5.32
	L32AS1-m10-23.1	110466	18	0.1169	0.0014	5.2346	0.1014	0.3249	0.0050	0.79	1909	21	1858	16	1813	24	5.26
	L32AS1-m10-25	78547	20	0.1185	0.0014	5.4443	0.1071	0.3331	0.0052	0.79	1934	21	1892	17	1854	25	4.35
	L32AS1-m10-26	85261	10	0.1182	0.0015	5.4487	0.1094	0.3342	0.0053	0.79	1930	22	1893	17	1859	26	3.81
	L32AS1-m10-27	99675	17	0.1180	0.0014	5.4909	0.1073	0.3374	0.0053	0.80	1927	21	1899	17	1874	25	2.81
	L32AS1-m10-28	97340	15	0.1156	0.0014	5.1420	0.1014	0.3226	0.0051	0.80	1889	21	1843	17	1802	25	4.84
	L32AS1-m10-29	120824	18	0.1170	0.0014	5.3525	0.1065	0.3317	0.0053	0.80	1911	21	1877	17	1847	26	3.49
	L32AS1-m10-30	110858	32	0.1190	0.0015	5.3842	0.1091	0.3282	0.0051	0.77	1941	23	1882	17	1830	25	6.06
	L32AS1-m10-31	97776	12	0.1185	0.0014	5.5435	0.1136	0.3394	0.0056	0.81	1933	21	1907	17	1884	27	2.62
	L32AS1-m10-32	95765	14	0.1161	0.0014	5.1882	0.1024	0.3242	0.0051	0.80	1897	21	1851	17	1810	25	4.79

$$\text{disc \%} = \text{Percent discordance} = [(\text{207Pb}/\text{206Pb Age}) / (\text{206Pb}/\text{235U Age}) - 1] * 100$$

APPENDIX 3: COMPILED U-PB GEOCHRONOLOGY STANDARD

Appendix 3, Table 1: Compiled LA-ICPMS Secondary Standards for Zircon

Sample Name and Spot Session	Name	^{206}Pb (CPS)	^{204}Pb (CPS)	$^{207}\text{Pb}/^{206}\text{Pb}$		$^{207}\text{Pb}/^{235}\text{U}$		$^{206}\text{Pb}/^{238}\text{U}$		p value	Model Ages (Ma)								
				$\pm 2\sigma$	$\pm 2\sigma$	$\pm 2\sigma$	$\pm 2\sigma$	$\pm 2\sigma$	$\pm 2\sigma$		$^{207}\text{Pb}/^{206}\text{Pb}$	$\pm 2\sigma$	$^{207}\text{Pb}/^{235}\text{U}$	$\pm 2\sigma$	$^{206}\text{Pb}/^{238}\text{U}$	$\pm 2\sigma$			
Session 1 (17SRB-L054)																			
<i>OG-1 (3465.4 ± 0.6 Ma)</i>																			
og1-1	251644	39	0.2925	0.0031	28.1376	0.6841	0.6978	0.0152	0.8974	3431	17	3424	24	3412	58	0.54			
og1-2	321544	15	0.2985	0.0031	29.6465	0.6595	0.7202	0.0142	0.8845	3463	16	3475	22	3497	53	-0.98			
og1-3	230156	12	0.3001	0.0031	29.7352	0.6469	0.7187	0.0137	0.8773	3471	16	3478	21	3491	51	-0.59			
<i>LH94-15 (1830 ± 1 Ma)</i>																			
lh9415-1	254080	25	0.1117	0.0015	5.2883	0.1301	0.3433	0.0072	0.8474	1827	23	1867	21	1903	34	-3.96			
lh9415-2	341518	27	0.1110	0.0014	5.1966	0.1296	0.3397	0.0073	0.8667	1815	22	1852	21	1885	35	-3.70			
lh9415-3	208982	18	0.1113	0.0014	5.0817	0.1342	0.3311	0.0077	0.8777	1821	23	1833	22	1844	37	-1.22			
lh9415-4	839034	30	0.1107	0.0014	5.2641	0.1413	0.3449	0.0082	0.8865	1811	22	1863	23	1910	39	-5.20			
Session 2 (17SRB-M095)																			
<i>FC-1 (1099.0 + 0.6 Ma)</i>																			
fc1-1	305104	24	0.0762	0.0008	2.0247	0.0429	0.1926	0.0036	0.8695	1101	21	1124	14	1135	19	-3.00			
fc1-2	278204	15	0.0757	0.0008	1.9850	0.0440	0.1901	0.0037	0.8736	1088	21	1110	15	1122	20	-2.97			
fc1-3	281230	9	0.0762	0.0008	1.9882	0.0432	0.1891	0.0036	0.8753	1101	21	1111	15	1117	19	-1.39			
<i>GJ1 (608.5 ± 0.4 Ma)</i>																			
gj1-1	99616	15	0.0600	0.0008	0.8199	0.0206	0.0992	0.0021	0.8420	602	29	608	11	610	12	-1.24			
gj1-2	102171	12	0.0598	0.0008	0.8247	0.0206	0.1000	0.0022	0.8636	596	27	611	11	615	13	-3.00			
gj1-3	100293	27	0.0605	0.0007	0.8147	0.0206	0.0977	0.0022	0.8809	620	26	605	11	601	13	3.19			
gj1-4	97731	17	0.0603	0.0007	0.8118	0.0196	0.0976	0.0021	0.8738	616	25	603	11	600	12	2.63			
Session 3 (17SRB-A018)																			
<i>FC-1 (1099.0 + 0.6 Ma)</i>																			
fc1-1	828066	67	0.0760	0.0008	1.9385	0.0509	0.1849	0.0045	0.9192	1096	21	1094	17	1094	24	0.15			
fc1-2	869234	60	0.0759	0.0008	1.9365	0.0477	0.1850	0.0041	0.9094	1093	20	1094	16	1094	23	-0.15			
fc1-3	831569	52	0.0760	0.0008	1.9521	0.0481	0.1864	0.0042	0.9073	1094	21	1099	16	1102	23	-0.66			
fc1-4	804489	69	0.0758	0.0008	1.9280	0.0470	0.1845	0.0041	0.9074	1090	20	1091	16	1091	22	-0.14			
fc1-5	798589	59	0.0759	0.0008	1.9570	0.0464	0.1870	0.0040	0.9021	1092	20	1101	16	1105	22	-1.17			
Session 4 (17SRB-A055)																			
<i>FC-1 (1099.0 + 0.6 Ma)</i>																			
fc1-1	916419	37	0.0758	0.0008	1.9534	0.0528	0.1869	0.0047	0.9267	1090	20	1100	18	1104	25	-1.29			
fc1-2	873043	34	0.0759	0.0008	1.9495	0.0542	0.1863	0.0048	0.9292	1092	20	1098	18	1101	26	-0.80			
fc1-3	875799	33	0.0761	0.0008	1.9455	0.0525	0.1855	0.0046	0.9229	1097	21	1097	18	1097	25	-0.04			
<i>GJ1 (608.5 ± 0.4 Ma)</i>																			
gj1-4	173948	59	0.0595	0.0007	0.7866	0.0183	0.0959	0.0019	0.8641	586	25	589	10	590	11	-0.78			
gj1-1	162735	55	0.0603	0.0008	0.7810	0.0188	0.0939	0.0019	0.8504	615	27	586	11	579	11	6.22			
gj1-2	160953	50	0.0602	0.0007	0.7745	0.0190	0.0933	0.0020	0.8832	611	25	582	11	575	12	6.30			
gj1-3	168157	46	0.0600	0.0006	0.8025	0.0182	0.0969	0.0019	0.8815	605	23	598	10	596	11	1.44			

Sample Name and Session	Spot Name	^{206}Pb (CPS)	^{204}Pb (CPS)	$^{207}\text{Pb}/^{206}\text{Pb}$		$^{207}\text{Pb}/^{235}\text{U}$		$^{206}\text{Pb}/^{238}\text{U}$		p value	Model Ages (Ma)								
				$\pm 2\sigma$	$\pm 2\sigma$	$\pm 2\sigma$	$\pm 2\sigma$	$\pm 2\sigma$	$\pm 2\sigma$		$^{207}\text{Pb}/^{206}\text{Pb}$	$\pm 2\sigma$	$^{207}\text{Pb}/^{235}\text{U}$	$\pm 2\sigma$	$^{206}\text{Pb}/^{238}\text{U}$	$\pm 2\sigma$			
Session 5 (17SRB-C008)																			
<i>FC-1 (1099.0 + 0.6 Ma)</i>																			
	fc1-1	628923	59	0.0757	0.0008	1.9600	0.0521	0.1878	0.0046	0.9215	1087	21	1102	18	1109	25	-1.98		
	fc1-2	639247	57	0.0757	0.0008	1.9664	0.0532	0.1884	0.0047	0.9239	1087	21	1104	18	1113	25	-2.26		
	fc1-3	595321	43	0.0756	0.0008	1.9527	0.0530	0.1874	0.0047	0.9260	1084	20	1099	18	1107	26	-2.12		
	fc1-4	602577	33	0.0758	0.0008	1.9226	0.0510	0.1839	0.0045	0.9209	1090	21	1089	18	1088	24	0.20		
<i>OG-1 (3465.4 ± 0.6 Ma)</i>																			
	og1-1	325361	33	0.2965	0.0037	29.4931	0.8137	0.7214	0.0178	0.8926	3452	19	3470	27	3501	66	-1.40		
	og1-2	316309	28	0.2966	0.0037	29.8890	0.8221	0.7309	0.0180	0.8931	3453	19	3483	27	3537	67	-2.38		
	og1-3	350545	26	0.2975	0.0037	29.7956	0.7831	0.7263	0.0168	0.8826	3458	19	3480	25	3519	63	-1.76		
	og1-4	310458	21	0.2969	0.0037	29.9611	0.7920	0.7319	0.0171	0.8841	3454	19	3486	26	3541	63	-2.45		
Session 6 (17SRB-C031)																			
<i>FC-1 (1099.0 + 0.6 Ma)</i>																			
	fc1-1	299856	13	0.0759	0.0008	1.9363	0.0415	0.1850	0.0034	0.8633	1093	22	1094	14	1094	19	-0.07		
	fc1-2	300527	19	0.0761	0.0008	1.9458	0.0445	0.1855	0.0038	0.8893	1097	21	1097	15	1097	20	0.00		
	fc1-3	301732	25	0.0759	0.0008	1.9503	0.0447	0.1863	0.0038	0.8876	1093	21	1099	15	1102	21	-0.80		
	fc1-4	306759	63	0.0753	0.0008	1.9504	0.0426	0.1879	0.0036	0.8698	1076	21	1099	15	1110	19	-3.02		
	fc1-5	306879	16	0.0756	0.0008	1.9593	0.0440	0.1880	0.0037	0.8848	1085	21	1102	15	1110	20	-2.32		
	fc1-6	299283	21	0.0757	0.0008	1.9244	0.0467	0.1844	0.0040	0.8998	1087	21	1090	16	1091	22	-0.36		
	fc1-7	326831	33	0.0758	0.0008	1.8969	0.0435	0.1815	0.0037	0.8827	1089	21	1080	15	1075	20	1.30		
<i>OG-1 (3465.4 ± 0.6 Ma)</i>																			
	og1-1	164512	15	0.3002	0.0031	28.6842	0.6917	0.6931	0.0151	0.9029	3471	16	3443	23	3394	57	2.26		
	og1-2	160833	27	0.2994	0.0031	28.7875	0.6413	0.6974	0.0138	0.8874	3467	16	3446	22	3411	52	1.64		
	og1-4	258190	24	0.3002	0.0031	29.0822	0.7285	0.7027	0.0160	0.9108	3471	16	3456	24	3431	60	1.17		
	og1-5	500843	40	0.2995	0.0031	29.1694	0.6618	0.7064	0.0143	0.8918	3468	16	3459	22	3445	54	0.66		
Session 7 (17SRB-L032)																			
<i>FC-1 (1099.0 + 0.6 Ma)</i>																			
	fc1-1	270199	50	0.0762	0.0008	1.8995	0.0468	0.1808	0.0040	0.9010	1100	21	1081	16	1072	22	2.64		
	fc1-2	274371	46	0.0761	0.0008	1.8960	0.0457	0.1808	0.0039	0.8975	1097	21	1080	16	1071	21	2.42		
	fc1-3	280761	51	0.0754	0.0008	1.8908	0.0446	0.1819	0.0038	0.8947	1078	21	1078	16	1078	21	0.08		
	fc1-4	275343	38	0.0759	0.0008	1.8934	0.0452	0.1810	0.0038	0.8902	1092	22	1079	16	1072	21	1.85		
<i>OG-1 (3465.4 ± 0.6 Ma)</i>																			
	og1-1	258388	52	0.2997	0.0031	28.3825	0.6649	0.6868	0.0144	0.8956	3469	16	3432	23	3371	55	2.91		
	og1-2	304588	42	0.2992	0.0031	28.4674	0.6835	0.6900	0.0149	0.9016	3466	16	3435	23	3383	57	2.47		
	og1-3	235703	21	0.2987	0.0032	28.4835	0.6392	0.6916	0.0137	0.8823	3463	16	3436	22	3389	52	2.21		

Sample Name and Spot Session	Name	^{206}Pb (CPS)	^{204}Pb (CPS)	$^{207}\text{Pb}/^{206}\text{Pb}$		$^{207}\text{Pb}/^{235}\text{U}$		$^{206}\text{Pb}/^{238}\text{U}$		p value	Model Ages (Ma)								
				$\pm 2\sigma$	$\pm 2\sigma$	$\pm 2\sigma$	$\pm 2\sigma$	$\pm 2\sigma$	$\pm 2\sigma$		$^{207}\text{Pb}/^{206}\text{Pb}$	$\pm 2\sigma$	$^{207}\text{Pb}/^{235}\text{U}$	$\pm 2\sigma$	$^{206}\text{Pb}/^{238}\text{U}$	$\pm 2\sigma$			
Session 8 (17SRB-D042)																			
<i>FC-1 (1099.0 + 0.6 Ma)</i>																			
fc1-1	291580	23	0.0760	0.0008	1.9476	0.0634	0.1859	0.0057	0.9461	1095	21	1098	22	1099	31	-0.41			
fc1-2	286153	25	0.0757	0.0008	1.9193	0.0630	0.1840	0.0057	0.9473	1086	21	1088	22	1089	31	-0.22			
fc1-3	299794	29	0.0759	0.0008	1.9697	0.0639	0.1881	0.0058	0.9447	1094	21	1105	22	1111	31	-1.57			
fc1-4	296242	11	0.0753	0.0008	1.9377	0.0632	0.1866	0.0058	0.9461	1077	21	1094	22	1103	31	-2.29			
fc1-5	288157	8	0.0752	0.0008	1.9047	0.0620	0.1836	0.0057	0.9475	1075	21	1083	21	1087	31	-1.09			
fc1-6	285667	7	0.0755	0.0008	1.9338	0.0621	0.1857	0.0056	0.9421	1082	21	1093	21	1098	30	-1.47			
<i>OG-1 (3465.4 ± 0.6 Ma)</i>																			
og1-1	258388	52	0.2997	0.0031	28.3825	0.6649	0.6868	0.0144	0.8956	3469	16	3432	23	3371	55	2.91			
og1-2	304588	42	0.2992	0.0031	28.4674	0.6835	0.6900	0.0149	0.9016	3466	16	3435	23	3383	57	2.47			
og1-3	235703	21	0.2987	0.0032	28.4835	0.6392	0.6916	0.0137	0.8823	3463	16	3436	22	3389	52	2.21			
Session 9 (17SRB-J051)																			
<i>FC-1 (1099.0 + 0.6 Ma)</i>																			
fc1-1	281680	22	0.0760	0.0008	1.9998	0.0475	0.1908	0.0040	0.8906	1096	21	1115	16	1126	22	-2.66			
fc1-2	289749	23	0.0762	0.0008	2.0026	0.0474	0.1907	0.0040	0.8914	1100	21	1116	16	1125	22	-2.27			
fc1-3	281814	15	0.0758	0.0008	1.9937	0.0433	0.1906	0.0036	0.8690	1091	21	1113	15	1125	19	-3.01			
fc1-4	293206	15	0.0757	0.0008	1.9949	0.0441	0.1910	0.0037	0.8757	1088	21	1114	15	1127	20	-3.44			
<i>OG-1 (3465.4 ± 0.6 Ma)</i>																			
og1-1	324484	55	0.3003	0.0033	28.7968	0.6404	0.6954	0.0134	0.8656	3472	17	3447	22	3403	51	2.01			
og1-2	275468	28	0.2999	0.0034	28.3169	0.6895	0.6848	0.0148	0.8873	3470	17	3430	24	3363	56	3.18			
og1-3	387284	23	0.2993	0.0033	29.0289	0.6888	0.7035	0.0148	0.8842	3467	17	3454	23	3434	56	0.95			
Session 10 (17SRB-S058)																			
<i>FC-1 (1099.0 + 0.6 Ma)</i>																			
fc1-1	68923	35	0.0757	0.0010	1.8383	0.0458	0.1761	0.0038	0.8622	1087	25	1059	16	1046	21	3.94			
fc1-2	71297	32	0.0751	0.0010	1.8651	0.0473	0.1802	0.0040	0.8654	1070	25	1069	17	1068	22	0.17			
fc1-3	61809	28	0.0746	0.0010	1.8029	0.0444	0.1752	0.0036	0.8362	1058	27	1046	16	1041	20	1.70			
<i>OG-1 (3465.4 ± 0.6 Ma)</i>																			
og1-1	350721	33	0.2986	0.0031	29.4339	0.9164	0.7150	0.0210	0.9438	3463	16	3468	30	3477	78	-0.41			
og1-2	237187	7	0.2978	0.0031	28.5958	0.9209	0.6964	0.0212	0.9463	3459	16	3440	31	3407	80	1.52			
og1-3	228335	5	0.2984	0.0031	29.0323	0.9330	0.7056	0.0215	0.9468	3462	16	3455	31	3442	81	0.59			

$$\text{disc \%} = \text{Percent discordance} = [(\frac{\text{207Pb}}{\text{206Pb}} \text{ Age} / \frac{\text{206Pb}}{\text{235U}} \text{ Age}) - 1] * 100$$

Appendix 3, Table 2: Compiled LA-ICPMS Secondary Standards for Monazite

Sample Name and Spot Session	Name	^{206}Pb (CPS)	^{204}Pb (CPS)	$^{207}\text{Pb}/^{206}\text{Pb}$		$^{207}\text{Pb}/^{235}\text{U}$		$^{206}\text{Pb}/^{238}\text{U}$		p value	Model Ages (Ma)						
				$\pm 2\sigma$	$\pm 2\sigma$	$\pm 2\sigma$	$\pm 2\sigma$	$\pm 2\sigma$	$\pm 2\sigma$		$^{207}\text{Pb}/^{206}\text{Pb}$	$\pm 2\sigma$	$^{207}\text{Pb}/^{235}\text{U}$	$\pm 2\sigma$			
Session 1 (17SRB-S058-m)																	
MAD (514.6 ± 1.1 Ma)																	
mad-1	113503	30	0.0582	0.0007	0.6543	0.0153	0.0815	0.0016	0.8580	539	26	511	9	505	10	6.74	
mad-2	112831	27	0.0584	0.0007	0.6435	0.0151	0.0799	0.0016	0.8424	544	27	504	9	496	9	9.71	
mad-3	116348	23	0.0589	0.0008	0.6520	0.0159	0.0803	0.0016	0.8093	564	31	510	10	498	9	13.25	
mad-4	105383	25	0.0589	0.0009	0.6434	0.0158	0.0792	0.0016	0.8049	564	31	504	10	491	9	14.81	
mad-6	123552	6	0.0581	0.0007	0.6497	0.0153	0.0811	0.0016	0.8425	534	27	508	9	503	10	6.34	
mad-7	121630	3	0.0579	0.0007	0.6430	0.0147	0.0805	0.0016	0.8652	527	25	504	9	499	9	5.71	
Session 2 (17SRB-L032-m)																	
MAD (514.6 ± 1.1 Ma)																	
mad-1	116843	30	0.0579	0.0007	0.6344	0.0126	0.0794	0.0012	0.7651	528	28	499	8	493	7	7.12	
mad-2	117740	31	0.0580	0.0007	0.6395	0.0126	0.0799	0.0012	0.7743	531	27	502	8	496	7	7.09	
mad-3	115199	66	0.0578	0.0008	0.6305	0.0129	0.0791	0.0012	0.7409	521	30	496	8	491	7	6.17	
mad-4	113030	43	0.0582	0.0008	0.6427	0.0134	0.0801	0.0012	0.7296	538	31	504	8	496	7	8.44	
mad-5	120403	22	0.0581	0.0007	0.6410	0.0127	0.0801	0.0012	0.7680	532	28	503	8	497	7	7.06	
mad-6	118562	26	0.0578	0.0007	0.6360	0.0126	0.0798	0.0012	0.7661	524	28	500	8	495	7	5.84	
Session 3 (17SRB-D042-m)																	
MAD (514.6 ± 1.1 Ma)																	
mad-1	121813	38	0.0583	0.0007	0.6500	0.0122	0.0808	0.0012	0.7923	543	25	508	7	501	7	8.34	
mad-2	123344	34	0.0580	0.0007	0.6459	0.0126	0.0808	0.0012	0.7664	528	27	506	8	501	7	5.43	
mad-3	125154	43	0.0583	0.0007	0.6491	0.0122	0.0807	0.0012	0.8013	543	24	508	7	500	7	8.46	
Session 4 (17SRB-J053)																	
44069 (424.9 ± 0.4 Ma)																	
44069-1	174589	21	0.0564	0.0007	0.5044	0.0097	0.0648	0.0010	0.7840	470	26	415	7	405	6	16.12	
44069-2	172484	24	0.0561	0.0007	0.5077	0.0097	0.0656	0.0010	0.7840	458	26	417	7	409	6	11.93	
44069-3	174941	70	0.0560	0.0007	0.5101	0.0100	0.0660	0.0010	0.7810	453	27	419	7	412	6	9.85	
44069-4	179235	39	0.0556	0.0007	0.5076	0.0098	0.0662	0.0010	0.7799	437	27	417	7	413	6	5.81	
44069-5	160727	49	0.0559	0.0007	0.5130	0.0101	0.0665	0.0010	0.7826	450	27	420	7	415	6	8.44	
44069-6	168492	62	0.0561	0.0007	0.5132	0.0104	0.0664	0.0011	0.8041	455	26	421	7	414	7	9.74	

$$\text{disc \%} = \text{Percent discordance} = [(\text{Age}_{^{207}\text{Pb}}/\text{Age}_{^{206}\text{Pb}}) / (\text{Age}_{^{206}\text{Pb}}/\text{Age}_{^{235}\text{U}}) - 1] * 100$$

Appendix 3, Table 3: Compiled LASS-ICPMS U-Pb Secondary Standard Analyses

Sample Name and Session	Spot Name	Model Ages (Ma)																
		$^{207}\text{Pb}/^{206}\text{Pb}$			$^{207}\text{Pb}/^{235}\text{U}$			$^{206}\text{Pb}/^{238}\text{U}$			p value	$^{207}\text{Pb}/^{206}\text{Pb}$		$^{207}\text{Pb}/^{235}\text{U}$		$^{206}\text{Pb}/^{238}\text{U}$		disc %
		$\pm 2\sigma$	$\pm 2\sigma$	$\pm 2\sigma$	$\pm 2\sigma$	$\pm 2\sigma$	$\pm 2\sigma$	$\pm 2\sigma$	$\pm 2\sigma$	$\pm 2\sigma$		$\pm 2\sigma$	$\pm 2\sigma$	$\pm 2\sigma$				
Session 1 (17SRB-0009, 18SRB-0112)																		
<i>GJ1 (608.5 ± 0.4 Ma)</i>																		
GJ1 - 1	0.0605	0.0006	0.8131	0.0190	0.0976	0.0020	0.4287	616	21	604	11	601	12	2.56				
GJ1 - 2	0.0602	0.0005	0.7973	0.0190	0.0962	0.0020	0.3894	605	20	595	11	592	12	2.18				
GJ1 - 3	0.0599	0.0006	0.7991	0.0190	0.0967	0.0020	0.4788	596	21	596	11	595	12	0.22				
GJ1 - 4	0.0596	0.0005	0.8020	0.0190	0.0974	0.0020	0.5238	587	18	598	11	599	12	-1.99				
GJ1 - 5	0.0601	0.0006	0.8029	0.0190	0.0967	0.0020	0.1772	604	23	598	11	595	12	1.51				
GJ1 - 6	0.0595	0.0006	0.7999	0.0190	0.0972	0.0020	0.0858	581	21	597	11	598	12	-2.88				
GJ1 - 7	0.0593	0.0007	0.7972	0.0190	0.0973	0.0022	0.4087	575	26	595	11	599	13	-3.93				
GJ1 - 8	0.0596	0.0006	0.7943	0.0190	0.0965	0.0021	0.4495	584	23	593	11	594	12	-1.63				
GJ1 - 9	0.0600	0.0006	0.8005	0.0190	0.0965	0.0021	0.5683	601	21	597	11	594	13	1.21				
GJ1 - 10	0.0600	0.0008	0.7960	0.0200	0.0958	0.0022	0.4235	597	29	594	11	590	13	1.27				
GJ1 - 11	0.0601	0.0006	0.7954	0.0190	0.0958	0.0020	0.4033	605	21	594	11	590	12	2.56				
GJ1 - 12	0.0605	0.0005	0.8011	0.0190	0.0961	0.0020	0.3923	619	19	597	11	592	12	4.61				
GJ1 - 13	0.0601	0.0007	0.7963	0.0190	0.0964	0.0021	0.5011	601	24	594	11	594	12	1.14				
GJ1 - 14	0.0602	0.0007	0.7985	0.0190	0.0964	0.0022	0.2221	607	25	596	11	593	13	2.29				
GJ1 - 15	0.0608	0.0006	0.7892	0.0190	0.0939	0.0020	0.4079	631	21	591	11	579	12	9.06				
GJ1 - 16	0.0601	0.0009	0.7927	0.0200	0.0958	0.0022	0.2998	605	30	592	11	590	13	2.63				
<i>Plesovice (337.1 ± 0.4 Ma)</i>																		
Plesovice - 1	0.0534	0.0006	0.3988	0.0098	0.0543	0.0011	0.4422	339	26	341	7	341	7	0.00				
Plesovice - 2	0.0535	0.0005	0.3966	0.0093	0.0537	0.0011	0.3434	348	20	339	7	337	7	0.56				
Plesovice - 3	0.0533	0.0005	0.3945	0.0092	0.0538	0.0011	0.1270	339	21	338	7	338	7	-0.09				
Plesovice - 4	0.0534	0.0005	0.4013	0.0096	0.0544	0.0011	0.5619	344	22	343	7	342	7	0.29				
Plesovice - 5	0.0535	0.0005	0.4004	0.0095	0.0542	0.0011	0.3353	346	21	342	7	340	7	0.47				
Plesovice - 6	0.0533	0.0005	0.3986	0.0092	0.0541	0.0011	0.3050	337	21	341	7	340	7	0.26				
Plesovice - 7	0.0532	0.0005	0.3997	0.0095	0.0542	0.0011	0.3424	332	23	341	7	340	7	0.41				
Plesovice - 8	0.0531	0.0006	0.3954	0.0095	0.0540	0.0011	0.3556	328	24	338	7	339	7	-0.21				
Plesovice - 9	0.0536	0.0006	0.4002	0.0099	0.0535	0.0011	0.3890	356	23	342	7	336	7	1.64				
Plesovice - 10	0.0533	0.0005	0.3958	0.0094	0.0539	0.0011	0.4595	339	21	339	7	338	7	0.06				
Plesovice - 11	0.0534	0.0006	0.3949	0.0095	0.0535	0.0011	0.3011	342	24	338	7	336	7	0.60				
Plesovice - 12	0.0528	0.0005	0.3898	0.0092	0.0535	0.0011	0.3635	320	22	334	7	336	7	-0.45				
Plesovice - 13	0.0531	0.0005	0.3954	0.0093	0.0538	0.0011	0.4401	328	20	338	7	338	7	0.15				
Plesovice - 14	0.0529	0.0005	0.3916	0.0093	0.0535	0.0012	0.6133	321	21	335	7	336	7	-0.24				
Plesovice - 15	0.0530	0.0004	0.3974	0.0091	0.0544	0.0011	0.3833	327	18	340	7	341	7	-0.44				
Plesovice - 16	0.0535	0.0004	0.3966	0.0092	0.0537	0.0011	0.4043	348	18	339	7	337	7	0.65				
Plesovice - 17	0.0537	0.0005	0.3908	0.0095	0.0528	0.0012	0.5692	361	21	335	7	332	7	0.90				
Plesovice - 18	0.0534	0.0005	0.3915	0.0093	0.0531	0.0011	0.6883	344	19	335	7	333	7	0.63				
Plesovice - 19	0.0540	0.0005	0.3962	0.0093	0.0532	0.0011	0.5069	371	19	339	7	334	7	1.35				
Plesovice - 20	0.0535	0.0005	0.3911	0.0094	0.0532	0.0011	0.4912	347	23	335	7	334	7	0.36				
Plesovice - 21	0.0530	0.0004	0.3872	0.0090	0.0531	0.0011	0.6843	327	18	332	7	334	7	-0.42				
Plesovice - 22	0.0536	0.0005	0.3892	0.0094	0.0528	0.0011	0.2521	351	20	334	7	332	7	0.66				
Plesovice - 23	0.0527	0.0007	0.3806	0.0093	0.0524	0.0012	0.2178	312	30	327	7	329	7	-0.61				

Sample Name and Session	Spot Name	Model Ages (Ma)													
		$^{207}\text{Pb}/^{206}\text{Pb}$		$^{207}\text{Pb}/^{235}\text{U}$		$^{206}\text{Pb}/^{238}\text{U}$		ρ value	$^{207}\text{Pb}/^{206}\text{Pb}$		$^{207}\text{Pb}/^{235}\text{U}$		$^{206}\text{Pb}/^{238}\text{U}$		disc %
		$\pm 2\sigma$	$\pm 2\sigma$	$\pm 2\sigma$	$\pm 2\sigma$	$\pm 2\sigma$	$\pm 2\sigma$		$\pm 2\sigma$	$\pm 2\sigma$	$\pm 2\sigma$	$\pm 2\sigma$	$\pm 2\sigma$		
Session 2 (17SRB-A25A5, 17SRB-L53)															
GJ1 (608.5 \pm 0.4 Ma)															
GJ1 - 1	0.0597	0.0007	0.7895	0.0180	0.0960	0.0018	0.4127	587	26	591	10	591	11	-0.69	
GJ1 - 2	0.0608	0.0007	0.7981	0.0180	0.0955	0.0018	0.4368	627	26	596	10	588	10	6.69	
GJ1 - 3	0.0604	0.0008	0.7992	0.0180	0.0960	0.0019	0.3015	613	30	596	10	591	11	3.78	
GJ1 - 4	0.0597	0.0007	0.7906	0.0170	0.0957	0.0017	0.3572	590	26	591	10	589	10	0.12	
GJ1 - 5	0.0603	0.0007	0.7958	0.0180	0.0956	0.0018	0.7231	610	24	594	10	589	10	3.64	
GJ1 - 6	0.0601	0.0009	0.7960	0.0190	0.0963	0.0019	0.2533	600	30	594	11	593	11	1.25	
GJ1 - 7	0.0602	0.0007	0.7992	0.0180	0.0965	0.0018	0.3997	607	24	596	10	594	10	2.17	
GJ1 - 8	0.0601	0.0008	0.8030	0.0180	0.0970	0.0017	0.2358	603	27	598	10	597	10	1.09	
GJ1 - 9	0.0610	0.0008	0.8089	0.0180	0.0968	0.0018	0.5124	634	28	602	10	596	11	6.41	
GJ1 - 10	0.0606	0.0007	0.8118	0.0190	0.0972	0.0018	0.6931	620	24	603	10	598	11	3.70	
GJ1 - 11	0.0602	0.0007	0.7974	0.0170	0.0963	0.0017	0.2764	609	24	595	10	593	10	2.75	
GJ1 - 12	0.0599	0.0007	0.8015	0.0180	0.0973	0.0018	0.2630	596	26	597	10	599	11	-0.42	
GJ1 - 13	0.0600	0.0008	0.7971	0.0190	0.0964	0.0018	0.4887	597	30	596	10	593	11	0.66	
GJ1 - 14	0.0600	0.0007	0.7889	0.0170	0.0952	0.0018	0.4913	602	25	590	10	586	10	2.66	
GJ1 - 15	0.0601	0.0008	0.7927	0.0180	0.0956	0.0018	0.3299	602	28	593	10	589	10	2.26	
GJ1 - 16	0.0601	0.0007	0.7924	0.0180	0.0953	0.0017	0.6510	605	23	592	10	587	10	3.07	
Plesovice (337.1 \pm 0.4 Ma)															
Plesovice - 1	0.0539	0.0005	0.3959	0.0086	0.0533	0.0010	0.6606	366	22	339	6	335	6	1.17	
Plesovice - 2	0.0535	0.0008	0.3878	0.0088	0.0527	0.0010	0.2526	346	33	333	6	331	6	0.54	
Plesovice - 3	0.0541	0.0008	0.3937	0.0089	0.0526	0.0010	0.3209	377	31	337	7	331	6	1.91	
Plesovice - 4	0.0538	0.0005	0.3950	0.0086	0.0531	0.0009	0.4180	358	22	338	6	334	6	1.26	
Plesovice - 5	0.0536	0.0006	0.3965	0.0086	0.0534	0.0009	0.2647	350	25	339	6	336	6	1.07	
Plesovice - 6	0.0531	0.0005	0.3922	0.0083	0.0534	0.0009	0.4836	329	21	336	6	336	6	0.09	
Plesovice - 7	0.0536	0.0006	0.3956	0.0085	0.0535	0.0010	0.3636	350	23	338	6	336	6	0.74	
Plesovice - 8	0.0532	0.0005	0.3889	0.0083	0.0530	0.0009	0.4906	334	23	334	6	333	6	0.09	
Plesovice - 9	0.0538	0.0006	0.3916	0.0086	0.0529	0.0009	0.4834	358	23	336	6	333	6	0.90	
Plesovice - 10	0.0536	0.0006	0.3911	0.0083	0.0529	0.0009	0.3084	353	24	335	6	332	6	0.84	
Plesovice - 11	0.0539	0.0006	0.3944	0.0085	0.0531	0.0009	0.0361	365	26	338	6	333	6	1.26	
Plesovice - 12	0.0538	0.0006	0.3923	0.0083	0.0530	0.0009	0.3404	358	23	336	6	333	6	0.99	
Plesovice - 13	0.0534	0.0006	0.3958	0.0084	0.0538	0.0010	0.2989	343	24	339	6	338	6	0.27	
Plesovice - 14	0.0536	0.0005	0.3978	0.0084	0.0538	0.0009	0.5263	351	21	340	6	338	6	0.56	
Plesovice - 15	0.0533	0.0005	0.3908	0.0083	0.0533	0.0010	0.6810	337	22	335	6	335	6	0.06	
Plesovice - 16	0.0537	0.0006	0.3942	0.0086	0.0536	0.0010	0.5277	354	24	337	6	336	6	0.30	
Plesovice - 17	0.0533	0.0006	0.3963	0.0088	0.0541	0.0011	0.3230	337	27	339	6	339	7	-0.12	
Plesovice - 18	0.0542	0.0006	0.3911	0.0087	0.0525	0.0010	0.3211	374	26	335	6	330	6	1.58	
Plesovice - 19	0.0538	0.0007	0.3959	0.0090	0.0534	0.0010	0.4675	360	28	339	7	335	6	1.04	
Plesovice - 20	0.0533	0.0007	0.3924	0.0087	0.0535	0.0010	0.4061	340	28	336	6	336	6	0.03	
Plesovice - 21	0.0533	0.0007	0.3919	0.0086	0.0533	0.0010	0.2826	335	28	336	6	335	6	0.30	
Plesovice - 22	0.0530	0.0006	0.3891	0.0084	0.0531	0.0009	0.3025	326	23	334	6	333	6	0.09	
Plesovice - 23	0.0532	0.0006	0.3911	0.0085	0.0531	0.0009	0.4045	335	25	335	6	334	6	0.39	
Plesovice - 24	0.0530	0.0006	0.3895	0.0085	0.0532	0.0010	0.5552	324	24	334	6	334	6	-0.06	

Sample Name and Session	Spot Name	Model Ages (Ma)																						
		$^{207}\text{Pb}/^{206}\text{Pb}$		$^{207}\text{Pb}/^{235}\text{U}$		$^{206}\text{Pb}/^{238}\text{U}$		p value	$^{207}\text{Pb}/^{206}\text{Pb}$		$^{207}\text{Pb}/^{235}\text{U}$		$^{206}\text{Pb}/^{238}\text{U}$		disc %									
Session 3 (17SRB-A15A4)																								
GJ1 (608.5 ± 0.4 Ma)																								
GJ1 - 1	0.0595	0.0010	0.7903	0.0250	0.0962	0.0023	0.4114	579	35	592	14	592	14	-2.16										
GJ1 - 2	0.0591	0.0009	0.7777	0.0240	0.0952	0.0022	0.1155	566	35	584	14	586	13	-3.46										
GJ1 - 3	0.0598	0.0009	0.7899	0.0240	0.0954	0.0023	0.4010	596	35	591	14	587	13	1.50										
GJ1 - 4	0.0601	0.0009	0.7903	0.0240	0.0952	0.0022	0.4634	603	33	591	14	586	13	2.88										
GJ1 - 5	0.0599	0.0009	0.7877	0.0250	0.0953	0.0022	0.3806	596	33	591	13	587	13	1.57										
GJ1 - 6	0.0602	0.0009	0.7997	0.0250	0.0960	0.0023	0.1560	606	34	597	14	591	13	2.54										
GJ1 - 7	0.0602	0.0009	0.7972	0.0240	0.0958	0.0022	0.3070	611	34	595	14	590	13	3.63										
GJ1 - 8	0.0598	0.0009	0.7875	0.0250	0.0954	0.0023	0.5446	590	34	590	14	587	13	0.44										
GJ1 - 9	0.0600	0.0009	0.7955	0.0250	0.0961	0.0023	0.4414	599	33	594	14	592	13	1.25										
GJ1 - 10	0.0602	0.0009	0.8003	0.0250	0.0963	0.0022	0.4813	606	32	597	14	592	13	2.30										
GJ1 - 11	0.0608	0.0010	0.8031	0.0250	0.0954	0.0024	0.4119	627	36	598	14	587	14	6.74										
GJ1 - 12	0.0602	0.0009	0.7920	0.0240	0.0953	0.0023	0.3183	606	33	592	14	587	13	3.27										
Plesovice (337.1 ± 0.4 Ma)																								
Plesovice - 1	0.0533	0.0008	0.3854	0.0120	0.0523	0.0012	0.5279	338	33	331	9	329	7	0.67										
Plesovice - 2	0.0531	0.0008	0.3888	0.0120	0.0531	0.0012	0.4258	330	35	333	9	333	8	0.03										
Plesovice - 3	0.0528	0.0008	0.3916	0.0120	0.0536	0.0012	0.3087	315	35	336	9	337	8	-0.39										
Plesovice - 4	0.0534	0.0010	0.3901	0.0130	0.0529	0.0012	0.4131	340	40	334	9	332	8	0.63										
Plesovice - 5	0.0531	0.0008	0.3875	0.0120	0.0528	0.0012	0.2625	327	36	333	9	332	7	0.27										
Plesovice - 6	0.0527	0.0008	0.3853	0.0120	0.0529	0.0012	0.3554	311	36	331	9	332	8	-0.45										
Plesovice - 7	0.0552	0.0010	0.4048	0.0130	0.0530	0.0013	0.3018	414	42	345	10	333	8	3.63										
Plesovice - 8	0.0555	0.0009	0.3998	0.0120	0.0521	0.0012	0.0215	428	35	341	9	327	7	4.37										
Plesovice - 9	0.0537	0.0008	0.3947	0.0120	0.0532	0.0012	0.3906	353	34	338	9	334	8	1.05										
Plesovice - 10	0.0549	0.0010	0.4057	0.0130	0.0535	0.0012	0.4427	402	40	346	9	336	8	2.86										
Plesovice - 11	0.0538	0.0009	0.4009	0.0130	0.0539	0.0013	0.5331	359	39	342	10	338	8	1.12										
Plesovice - 12	0.0537	0.0008	0.3930	0.0120	0.0529	0.0012	0.2052	355	34	337	9	332	7	1.26										
Plesovice - 13	0.0545	0.0009	0.4011	0.0130	0.0533	0.0012	0.2253	386	37	342	9	334	7	2.36										
Plesovice - 14	0.0535	0.0008	0.3927	0.0120	0.0532	0.0012	0.1927	347	34	336	9	334	7	0.63										
Plesovice - 15	0.0530	0.0008	0.3886	0.0120	0.0532	0.0012	0.1879	324	34	333	9	334	7	-0.18										
Plesovice - 16	0.0556	0.0008	0.4055	0.0120	0.0528	0.0012	0.4449	434	32	346	9	332	7	4.28										
Plesovice - 17	0.0532	0.0008	0.3877	0.0120	0.0528	0.0012	0.3517	335	33	333	9	332	7	0.30										
Plesovice - 18	0.0532	0.0008	0.3900	0.0120	0.0531	0.0012	0.1473	332	33	334	9	334	7	0.15										

Sample Name and Session	Spot Name	Model Ages (Ma)																					
		$^{207}\text{Pb}/^{206}\text{Pb}$			$^{207}\text{Pb}/^{235}\text{U}$			$^{206}\text{Pb}/^{238}\text{U}$			p value	$^{207}\text{Pb}/^{206}\text{Pb}$	$^{207}\text{Pb}/^{235}\text{U}$	$^{206}\text{Pb}/^{238}\text{U}$	$\pm 2\sigma$	disc %							
Session 4 (17SRB-J53, 17SRB-D46, 17SRB-R75, 17SRB-M95)																							
<i>GJ1 (608.5 ± 0.4 Ma)</i>																							
GJ-1 - 1	0.0602	0.0005	0.8135	0.0170	0.0977	0.0015	0.3548	609	20	604	10	601	9	1.38									
GJ-1 - 2	0.0602	0.0005	0.8245	0.0170	0.0993	0.0015	0.4558	609	17	610	10	610	9	-0.23									
GJ-1 - 3	0.0605	0.0006	0.8218	0.0180	0.0984	0.0015	0.2987	621	21	609	10	605	9	2.64									
GJ-1 - 4	0.0604	0.0005	0.8068	0.0170	0.0969	0.0015	0.4947	613	19	601	10	596	9	2.87									
GJ-1 - 5	0.0605	0.0005	0.8253	0.0170	0.0989	0.0015	0.5676	619	17	611	10	608	9	1.83									
GJ-1 - 6	0.0606	0.0006	0.8201	0.0170	0.0981	0.0015	0.3755	623	20	608	10	603	9	3.30									
GJ-1 - 7	0.0604	0.0005	0.8183	0.0170	0.0977	0.0015	0.2898	615	18	607	9	601	9	2.35									
GJ-1 - 8	0.0600	0.0006	0.8173	0.0170	0.0984	0.0015	0.5408	600	20	606	10	605	9	-0.79									
GJ-1 - 9	0.0606	0.0006	0.8253	0.0180	0.0985	0.0016	0.3869	626	20	611	10	606	9	3.37									
GJ-1 - 10	0.0600	0.0006	0.8280	0.0190	0.0992	0.0017	0.4178	600	23	612	11	610	10	-1.57									
GJ-1 - 11	0.0603	0.0004	0.8151	0.0170	0.0979	0.0015	0.4067	616	15	606	9	602	9	2.27									
GJ-1 - 12	0.0603	0.0006	0.8151	0.0170	0.0978	0.0015	0.4034	612	21	605	10	601	9	1.76									
GJ-1 - 13	0.0597	0.0006	0.8120	0.0190	0.0985	0.0017	0.6251	587	23	604	10	606	10	-3.07									
GJ-1 - 14	0.0596	0.0007	0.8171	0.0180	0.0993	0.0016	0.2319	589	26	606	10	610	10	-3.51									
GJ-1 - 15	0.0607	0.0006	0.8186	0.0180	0.0973	0.0016	0.5621	625	21	607	10	599	10	4.39									
GJ-1 - 16	0.0604	0.0007	0.8357	0.0190	0.0999	0.0018	0.4769	614	24	617	10	614	11	0.05									
<i>Plesovice (337.1 ± 0.4 Ma)</i>																							
Plesovice - 1	0.0533	0.0004	0.3978	0.0082	0.0540	0.0008	0.3391	340	18	340	6	339	5	0.00									
Plesovice - 2	0.0534	0.0004	0.4007	0.0084	0.0544	0.0008	0.5764	341	18	342	6	341	5	-0.32									
Plesovice - 3	0.0538	0.0005	0.3955	0.0084	0.0533	0.0008	0.3971	364	21	338	6	335	5	7.60									
Plesovice - 4	0.0537	0.0005	0.4011	0.0083	0.0544	0.0009	0.4196	353	20	342	6	342	5	3.10									
Plesovice - 5	0.0541	0.0006	0.4028	0.0087	0.0540	0.0008	0.3110	372	23	344	6	339	5	8.27									
Plesovice - 6	0.0540	0.0006	0.4019	0.0087	0.0543	0.0009	0.4781	365	23	343	6	341	5	6.45									
Plesovice - 7	0.0538	0.0007	0.4029	0.0091	0.0543	0.0010	0.3616	358	28	344	7	341	6	4.19									
Plesovice - 8	0.0536	0.0006	0.3975	0.0085	0.0538	0.0009	0.2711	349	24	340	6	338	5	2.71									
Plesovice - 9	0.0538	0.0005	0.4029	0.0088	0.0540	0.0009	0.5279	359	21	344	6	339	6	4.45									
Plesovice - 10	0.0534	0.0005	0.4000	0.0083	0.0542	0.0009	0.4074	340	20	342	6	340	5	-0.47									
Plesovice - 11	0.0539	0.0006	0.4002	0.0088	0.0536	0.0009	0.5274	360	24	342	6	337	6	5.36									
Plesovice - 12	0.0534	0.0004	0.3988	0.0084	0.0540	0.0008	0.5868	343	17	341	6	339	5	0.68									
Plesovice - 13	0.0535	0.0006	0.4065	0.0088	0.0550	0.0009	0.3642	349	24	346	6	345	6	0.81									
Plesovice - 14	0.0534	0.0005	0.3992	0.0086	0.0540	0.0009	0.7186	343	19	341	6	339	5	0.59									
Plesovice - 15	0.0531	0.0005	0.3992	0.0084	0.0544	0.0009	0.4683	330	22	341	6	342	6	-3.23									
Plesovice - 16	0.0534	0.0005	0.3978	0.0083	0.0543	0.0009	0.6785	346	22	340	6	341	5	1.76									
Plesovice - 17	0.0541	0.0009	0.4073	0.0100	0.0548	0.0012	0.5674	370	38	347	7	344	7	6.69									
Plesovice - 18	0.0533	0.0005	0.3958	0.0086	0.0538	0.0009	0.5409	340	19	339	6	338	5	0.44									
Plesovice - 19	0.0538	0.0006	0.3991	0.0090	0.0538	0.0009	0.2798	356	26	341	7	338	6	4.43									
Plesovice - 20	0.0537	0.0005	0.4023	0.0087	0.0543	0.0009	0.4924	359	20	343	6	341	5	4.60									
Plesovice - 21	0.0535	0.0006	0.3986	0.0089	0.0539	0.0010	0.5064	350	27	341	6	338	6	2.79									
Plesovice - 22	0.0537	0.0005	0.4028	0.0086	0.0542	0.0009	0.4531	353	20	344	6	341	5	2.74									
Plesovice - 23	0.0527	0.0006	0.3989	0.0090	0.0545	0.0010	0.6116	312	26	341	7	342	6	-8.45									

Sample Name and Session	Spot Name	Model Ages (Ma)																
		$^{207}\text{Pb}/^{206}\text{Pb}$			$^{207}\text{Pb}/^{235}\text{U}$			$^{206}\text{Pb}/^{238}\text{U}$			p value	$^{207}\text{Pb}/^{206}\text{Pb}$			$^{207}\text{Pb}/^{235}\text{U}$			disc %
		$\pm 2\sigma$	$\pm 2\sigma$	$\pm 2\sigma$	$\pm 2\sigma$	$\pm 2\sigma$	$\pm 2\sigma$	$\pm 2\sigma$	$\pm 2\sigma$	$\pm 2\sigma$		$\pm 2\sigma$	$\pm 2\sigma$	$\pm 2\sigma$	$\pm 2\sigma$	$\pm 2\sigma$		
<i>Session 5 (17SRB-054, 17SRB-D48, 17SRB-C47, 17SRB-J29)</i>																		
<i>GJ1 (608.5 ± 0.4 Ma)</i>																		
GJ-1 - 1	0.0009	0.4030	0.8159	0.0220	0.0985	0.0021	0.4164	616	33	606	13	606	12	1.68				
GJ-1 - 2	0.0009	0.3931	0.8062	0.0220	0.0977	0.0021	0.4439	602	32	600	13	602	12	0.00				
GJ-1 - 3	0.0009	0.3126	0.8233	0.0230	0.0992	0.0022	0.6012	609	31	610	13	610	13	-0.13				
GJ-1 - 4	0.0009	0.4718	0.8186	0.0220	0.0987	0.0021	0.3241	610	34	608	13	607	12	0.53				
GJ-1 - 5	0.0009	0.2763	0.8280	0.0240	0.0996	0.0022	0.5515	604	34	612	13	612	13	-1.32				
GJ-1 - 6	0.0009	0.4609	0.8186	0.0220	0.0992	0.0021	0.4450	591	33	607	13	610	13	-3.07				
GJ-1 - 8	0.0009	0.4802	0.8276	0.0230	0.0997	0.0021	0.3955	608	33	613	12	612	13	-0.72				
GJ-1 - 9	0.0012	0.5859	0.8140	0.0240	0.0981	0.0024	0.2725	596	45	604	14	603	14	-1.23				
GJ-1 - 10	0.0008	0.4339	0.8229	0.0220	0.0988	0.0021	0.4282	607	30	609	12	607	12	0.00				
GJ-1 - 11	0.0009	0.3603	0.8248	0.0230	0.0984	0.0021	0.5393	615	32	611	13	605	13	1.69				
GJ-1 - 12	0.0008	0.1916	0.8265	0.0230	0.0987	0.0021	0.4365	615	30	611	13	607	12	1.35				
GJ-1 - 13	0.0015	0.7226	0.8320	0.0270	0.1009	0.0030	0.3312	587	56	614	15	620	18	-5.32				
GJ-1 - 14	0.0012	0.3246	0.8270	0.0250	0.0992	0.0024	0.5295	630	42	612	14	610	14	3.35				
GJ-1 - 15	0.0008	0.2791	0.8265	0.0220	0.0985	0.0021	0.5266	637	29	612	12	606	12	5.17				
GJ-1 - 16	0.0009	0.5930	0.8240	0.0220	0.0992	0.0021	0.2825	613	33	610	12	610	13	0.56				
<i>Plesovice (337.1 ± 0.4 Ma)</i>																		
Plesovice - 1	0.0543	0.0010	0.4081	0.0130	0.0549	0.0014	0.6783	373	42	347	9	345	9	8.21				
Plesovice - 2	0.0541	0.0007	0.3951	0.0110	0.0532	0.0011	0.7300	372	30	338	8	334	7	11.28				
Plesovice - 3	0.0534	0.0008	0.3935	0.0110	0.0536	0.0012	0.5357	343	33	337	8	337	7	1.90				
Plesovice - 4	0.0537	0.0008	0.3984	0.0110	0.0539	0.0012	0.2294	357	39	340	8	338	7	5.50				
Plesovice - 5	0.0534	0.0008	0.4013	0.0110	0.0546	0.0012	0.5203	339	35	343	8	342	7	-0.99				
Plesovice - 6	0.0533	0.0008	0.3983	0.0110	0.0542	0.0011	0.4570	337	32	340	8	340	7	-0.91				
Plesovice - 7	0.0532	0.0008	0.4046	0.0120	0.0550	0.0013	0.5481	333	36	345	8	345	8	-3.53				
Plesovice - 8	0.0533	0.0009	0.4022	0.0110	0.0546	0.0012	0.3451	342	35	343	8	342	8	-0.12				
Plesovice - 9	0.0534	0.0008	0.4003	0.0110	0.0543	0.0012	0.5015	346	31	342	8	341	7	1.50				
Plesovice - 10	0.0528	0.0009	0.3921	0.0110	0.0540	0.0012	0.4480	316	41	337	9	339	7	-6.70				
Plesovice - 11	0.0539	0.0008	0.4013	0.0110	0.0539	0.0012	0.6828	360	33	343	8	338	7	6.48				
Plesovice - 12	0.0539	0.0008	0.4058	0.0120	0.0546	0.0012	0.3118	365	34	346	8	343	7	6.51				
Plesovice - 13	0.0534	0.0009	0.3970	0.0110	0.0539	0.0012	0.4904	341	36	339	8	338	8	0.80				
Plesovice - 14	0.0535	0.0008	0.3992	0.0110	0.0541	0.0012	0.6343	345	33	341	8	339	8	1.65				
Plesovice - 15	0.0540	0.0008	0.4044	0.0110	0.0543	0.0013	0.3539	366	34	345	8	341	8	7.39				
Plesovice - 16	0.0534	0.0008	0.4022	0.0110	0.0544	0.0012	0.4528	341	35	343	8	341	7	-0.06				
Plesovice - 17	0.0534	0.0008	0.3969	0.0110	0.0537	0.0012	0.5730	341	35	339	8	337	7	1.13				
Plesovice - 18	0.0533	0.0010	0.4064	0.0110	0.0552	0.0013	0.4574	331	41	346	8	346	8	-4.39				
Plesovice - 19	0.0541	0.0008	0.4108	0.0120	0.0551	0.0012	0.5779	368	35	349	8	346	8	6.45				
Plesovice - 20	0.0542	0.0009	0.4077	0.0120	0.0545	0.0012	0.5119	375	36	347	8	342	7	9.62				
Plesovice - 21	0.0537	0.0008	0.4058	0.0110	0.0549	0.0012	0.5497	354	34	346	8	345	7	2.76				
Plesovice - 22	0.0535	0.0009	0.4007	0.0110	0.0543	0.0012	0.5018	343	36	342	8	341	7	0.65				

disc % = Percent discordance = [$(^{207}\text{Pb}/^{206}\text{Pb} \text{ Age} / ^{206}\text{Pb}/^{235}\text{U} \text{ Age}) - 1$] * 100

APPENDIX 4: COMPILED LU-HF AND SM-ND ISOTOPIC ANALYSES

Appendix 4, Table 1: Compiled Zircon Lu/Hf Isotopic Results

Sample	Spot Name	Assigned $^{176}\text{Hf}/^{177}\text{Hf}$			$^{176}\text{Lu}/^{177}\text{Hf}$			ϵHf_0	Initial $^{176}\text{Hf}/^{177}\text{Hf} \pm 2\sigma$			$\epsilon\text{Hf}_i^1 \pm 2\sigma$	Minumum T_{DM}^2				
		Age (Ma)	Corrected	$\pm 2\sigma$	Corrected	$\pm 2\sigma$	$\pm 2\sigma$		$\pm 2\sigma$	$\pm 2\sigma$	$\pm 2\sigma$						
<i>Boothia Ferroan Granitoid Complex</i>																	
<i>17SRB-A025A5, Fayalite Granite</i>																	
A25-A5 - 1	1828	0.28139	0.00003	0.00076	0.000002	-49.4	0.28136	0.00011	-8.8	1.1	2715						
A25-A5 - 2	1828	0.28139	0.00004	0.00060	0.000014	-49.2	0.28137	0.00014	-8.4	1.4	2698						
A25-A5 - 3	1828	0.28143	0.00003	0.00071	0.000085	-48.1	0.28140	0.00011	-7.5	1.2	2653						
A25-A5 - 4	1828	0.28138	0.00003	0.00084	0.000002	-49.6	0.28135	0.00012	-9.1	1.2	2730						
A25-A5 - 5	1828	0.28139	0.00003	0.00063	0.000009	-49.4	0.28136	0.00012	-8.7	1.2	2711						
A25-A5 - 6	1828	0.28140	0.00003	0.00064	0.000033	-48.8	0.28138	0.00012	-8.1	1.2	2684						
A25-A5 - 7	1828	0.28137	0.00004	0.00054	0.000069	-50.1	0.28135	0.00014	-9.3	1.4	2737						
A25-A5 - 8	1828	0.28136	0.00004	0.00087	0.000003	-50.4	0.28133	0.00014	-10.0	1.4	2771						
A25-A5 - 9	1828	0.28137	0.00004	0.00066	0.000062	-50.2	0.28134	0.00013	-9.5	1.3	2749						
A25-A5 - 10	1828	0.28137	0.00003	0.00040	0.000001	-50.0	0.28136	0.00012	-9.0	1.2	2726						
A25-A5 - 11	1828	0.28139	0.00003	0.00081	0.000027	-49.5	0.28136	0.00012	-9.0	1.2	2725						
A25-A5 - 12	1828	0.28136	0.00004	0.00076	0.000026	-50.5	0.28133	0.00015	-10.0	1.5	2768						
A25-A5 - 13	1828	0.28136	0.00002	0.00029	0.000010	-50.5	0.28135	0.00007	-9.4	0.8	2741						
A25-A5 - 14	1828	0.28137	0.00003	0.00047	0.000066	-50.2	0.28135	0.00009	-9.3	1.0	2737						
A25-A5 - 15	1828	0.28136	0.00004	0.00037	0.000003	-50.3	0.28135	0.00013	-9.2	1.3	2734						
A25-A5 - 16	1828	0.28136	0.00004	0.00080	0.000004	-50.3	0.28134	0.00012	-9.7	1.3	2759						
A25-A5 - 17	1828	0.28134	0.00004	0.00063	0.000011	-51.1	0.28132	0.00014	-10.4	1.4	2787						
A25-A5 - 21	1828	0.28136	0.00003	0.00046	0.000008	-50.3	0.28135	0.00010	-9.4	1.0	2741						
A25-A5 - 22	1828	0.28137	0.00004	0.00088	0.000004	-50.1	0.28134	0.00013	-9.7	1.3	2759						
A25-A5 - 23	1828	0.28139	0.00003	0.00086	0.000002	-49.2	0.28136	0.00012	-8.8	1.2	2713						
A25-A5 - 24	1828	0.28135	0.00003	0.00042	0.000001	-50.8	0.28133	0.00010	-9.8	1.0	2763						
A25-A5 - 25	1828	0.28137	0.00004	0.00054	0.000024	-50.1	0.28135	0.00014	-9.3	1.4	2737						
A25-A5 - 26	1828	0.28137	0.00003	0.00051	0.000013	-50.0	0.28135	0.00012	-9.1	1.2	2729						
A25-A5 - 27	1828	0.28138	0.00003	0.00025	0.000011	-49.7	0.28137	0.00011	-8.5	1.1	2703						
A25-A5 - 28	1828	0.28139	0.00004	0.00082	0.000001	-49.2	0.28136	0.00015	-8.7	1.5	2712						
A25-A5 - 29	1828	0.28136	0.00004	0.00077	0.000006	-50.6	0.28133	0.00012	-10.0	1.3	2772						
A25-A5 - 32	1828	0.28136	0.00004	0.00059	0.000005	-50.4	0.28134	0.00013	-9.6	1.3	2754						
A25-A5 - 33	1828	0.28137	0.00003	0.00065	0.000003	-50.1	0.28134	0.00010	-9.5	1.1	2746						
A25-A5 - 34	1828	0.28138	0.00004	0.00076	0.000014	-49.6	0.28135	0.00014	-9.1	1.4	2729						
A25-A5 - 35	1828	0.28138	0.00004	0.00073	0.000043	-49.5	0.28136	0.00016	-9.0	1.6	2722						
A25-A5 - 36	1828	0.28136	0.00004	0.00073	0.000014	-50.5	0.28133	0.00013	-9.9	1.3	2768						
A25-A5 - 37	1828	0.28135	0.00003	0.00081	0.000008	-50.6	0.28133	0.00012	-10.1	1.2	2776						
A25-A5 - 38	1828	0.28138	0.00006	0.00072	0.000052	-49.6	0.28136	0.00022	-9.0	2.3	2726						
A25-A5 - 39	1828	0.28138	0.00003	0.00085	0.000003	-49.7	0.28135	0.00012	-9.3	1.2	2737						
A25-A5 - 40	1828	0.28136	0.00002	0.00039	0.000030	-50.4	0.28135	0.00009	-9.4	0.9	2744						
<i>17SRB-L053A, Charnockite</i>																	
L53 - 1	1827	0.28133	0.00004	0.00028	0.000004	-51.6	0.28132	0.00013	-10.8	1.3	2707						
L53 - 2	1827	0.28133	0.00006	0.00044	0.000023	-51.4	0.28132	0.00021	-10.8	2.1	2706						
L53 - 4	1827	0.28134	0.00003	0.00029	0.000025	-51.2	0.28133	0.00011	-10.4	1.1	2690						
L53 - 5	1827	0.28130	0.00003	0.00029	0.000018	-52.4	0.28129	0.00010	-11.6	1.1	2739						
L53 - 6	1827	0.28132	0.00002	0.00030	0.000008	-52.0	0.28130	0.00008	-11.2	0.9	2723						
L53 - 7	1827	0.28129	0.00007	0.00022	0.000002	-52.9	0.28128	0.00023	-12.0	2.3	2758						
L53 - 8	1827	0.28133	0.00007	0.00028	0.000005	-51.6	0.28132	0.00023	-10.8	2.4	2707						
L53 - 9	1827	0.28134	0.00003	0.00035	0.000013	-51.0	0.28133	0.00011	-10.3	1.1	2682						
L53 - 10	1827	0.28132	0.00004	0.00037	0.000005	-51.9	0.28131	0.00014	-11.2	1.4	2722						

Appendix 4, Table 1 cont.

L53 - 12	1827	0.28130	0.00003	0.00051	0.000012	-52.5	0.28128	0.00012	-12.0	1.2	2755
L53 - 13	1827	0.28131	0.00004	0.00042	0.000028	-52.3	0.28129	0.00013	-11.6	1.3	2741
L53 - 14	1827	0.28130	0.00003	0.00034	0.000030	-52.4	0.28129	0.00012	-11.7	1.2	2743
L53 - 15	1827	0.28131	0.00003	0.00023	0.000004	-52.1	0.28130	0.00011	-11.2	1.2	2724
L53 - 16	1827	0.28133	0.00004	0.00038	0.000031	-51.4	0.28132	0.00015	-10.7	1.6	2702
L53 - 17	1827	0.28134	0.00003	0.00028	0.000004	-51.1	0.28133	0.00011	-10.3	1.2	2685
L53 - 18	1827	0.28133	0.00003	0.00028	0.000003	-51.5	0.28132	0.00011	-10.7	1.2	2701
L53 - 19	1827	0.28130	0.00003	0.00025	0.000007	-52.7	0.28129	0.00012	-11.8	1.2	2749
L53 - 20	1827	0.28135	0.00004	0.00033	0.000015	-50.9	0.28134	0.00015	-10.1	1.5	2676
L53 - 21	1827	0.28131	0.00004	0.00034	0.000008	-52.3	0.28129	0.00014	-11.6	1.4	2738
L53 - 22	1827	0.28132	0.00002	0.00023	0.000007	-51.8	0.28131	0.00007	-11.0	0.8	2714
L53 - 23	1827	0.28133	0.00004	0.00028	0.000021	-51.6	0.28132	0.00015	-10.8	1.5	2707
L53 - 24	1827	0.28133	0.00004	0.00029	0.000011	-51.3	0.28132	0.00012	-10.5	1.3	2694
L53 - 25	1827	0.28128	0.00004	0.00026	0.000020	-53.1	0.28128	0.00014	-12.3	1.4	2767
L53 - 26	1827	0.28132	0.00003	0.00034	0.000015	-51.7	0.28131	0.00012	-11.0	1.2	2714
L53 - 28	1827	0.28135	0.00003	0.00026	0.000007	-50.8	0.28134	0.00010	-10.0	1.0	2671
L53 - 29	1827	0.28132	0.00003	0.00027	0.000012	-52.0	0.28131	0.00010	-11.2	1.0	2721
L53 - 30	1827	0.28132	0.00003	0.00029	0.000004	-51.9	0.28131	0.00011	-11.2	1.1	2721
L53 - 31	1827	0.28135	0.00003	0.00047	0.000023	-50.7	0.28133	0.00012	-10.2	1.2	2679
L53 - 32	1827	0.28134	0.00004	0.00025	0.000008	-51.2	0.28133	0.00015	-10.4	1.5	2689
L53 - 33	1827	0.28135	0.00004	0.00036	0.000009	-50.7	0.28134	0.00013	-10.0	1.3	2671
<i>17SRB-A015A3, Hornblende-Biotite Granite</i>											
A15-A4 - 1	1828	0.28139	0.00003	0.00047	0.000057	-49.4	0.28137	0.00012	-8.8	1.2	2624
A15-A4 - 2	1828	0.28139	0.00004	0.00054	0.000043	-49.3	0.28137	0.00014	-8.8	1.4	2621
A15-A4 - 3	1828	0.28141	0.00003	0.00116	0.000082	-48.6	0.28137	0.00012	-8.8	1.2	2625
A15-A4 - 4	1828	0.28142	0.00004	0.00090	0.000096	-48.2	0.28139	0.00013	-8.1	1.3	2593
A15-A4 - 5	1828	0.28142	0.00003	0.00039	0.000120	-48.2	0.28141	0.00012	-7.5	1.2	2567
A15-A4 - 6	1828	0.28143	0.00004	0.00104	0.000110	-47.9	0.28139	0.00013	-8.0	1.3	2590
A15-A4 - 7	1828	0.28142	0.00004	0.00064	0.000098	-48.3	0.28140	0.00012	-7.9	1.3	2584
A15-A4 - 8	1828	0.28143	0.00006	0.00038	0.000009	-48.0	0.28141	0.00022	-7.3	2.2	2560
A15-A4 - 10	1828	0.28145	0.00003	0.00102	0.000130	-47.4	0.28141	0.00012	-7.5	1.3	2567
A15-A4 - 11	1828	0.28142	0.00004	0.00040	0.000047	-48.4	0.28140	0.00014	-7.7	1.4	2576
A15-A4 - 12	1828	0.28140	0.00003	0.00055	0.000057	-48.8	0.28138	0.00011	-8.3	1.1	2604
A15-A4 - 13	1828	0.28144	0.00004	0.00093	0.000087	-47.6	0.28141	0.00012	-7.6	1.3	2571
A15-A4 - 14	1828	0.28143	0.00004	0.00084	0.000160	-47.9	0.28140	0.00015	-7.7	1.1	2578
A15-A4 - 15	1828	0.28143	0.00003	0.00107	0.000074	-48.0	0.28139	0.00011	-8.1	1.5	2595
A15-A4 - 16	1828	0.28143	0.00004	0.00136	0.000080	-48.1	0.28138	0.00015	-8.6	1.5	2613
A15-A4 - 17	1828	0.28141	0.00004	0.00099	0.000120	-48.8	0.28137	0.00014	-8.8	1.4	2625
A15-A4 - 18	1828	0.28141	0.00005	0.00085	0.000054	-48.5	0.28138	0.00016	-8.4	1.6	2606
A15-A4 - 19	1828	0.28140	0.00003	0.00035	0.000024	-49.0	0.28139	0.00012	-8.3	1.2	2603
A15-A4 - 20	1828	0.28138	0.00003	0.00046	0.000023	-49.8	0.28136	0.00012	-9.2	1.2	2639
A15-A4 - 21	1828	0.28139	0.00003	0.00093	0.000120	-49.3	0.28136	0.00011	-9.3	1.1	2643
A15-A4 - 22	1828	0.28141	0.00005	0.00147	0.000098	-48.6	0.28136	0.00017	-9.3	1.7	2643
A15-A4 - 23	1828	0.28140	0.00003	0.00053	0.000045	-49.0	0.28138	0.00010	-8.5	1.0	2612
A15-A4 - 24	1828	0.28141	0.00004	0.00088	0.000110	-48.6	0.28138	0.00013	-8.5	1.3	2610
A15-A4 - 25	1828	0.28139	0.00004	0.00036	0.000018	-49.2	0.28138	0.00013	-8.5	1.3	2609
A15-A4 - 26	1828	0.28141	0.00004	0.00109	0.000077	-48.6	0.28137	0.00014	-8.7	1.4	2620
A15-A4 - 27	1828	0.28143	0.00004	0.00080	0.000130	-47.9	0.28140	0.00016	-7.7	1.6	2576
A15-A4 - 28	1828	0.28142	0.00002	0.00056	0.000017	-48.4	0.28140	0.00007	-7.9	0.7	2585
A15-A4 - 29	1828	0.28142	0.00003	0.00110	0.000084	-48.3	0.28138	0.00010	-8.5	1.0	2612
A15-A4 - 30	1828	0.28142	0.00004	0.00078	0.000072	-48.3	0.28139	0.00013	-8.1	1.3	2592
A15-A4 - 31	1828	0.28141	0.00004	0.00100	0.000100	-48.5	0.28138	0.00015	-8.5	1.6	2612
A15-A4 - 32	1828	0.28140	0.00003	0.00042	0.000120	-49.1	0.28138	0.00010	-8.5	1.0	2609

Appendix 4, Table 1 cont.

A15-A4 - 34	1828	0.28137	0.00004	0.00053	0.000032	-50.1	0.28135	0.00015	-9.6	1.5	2657
A15-A4 - 35	1828	0.28137	0.00004	0.00060	0.000021	-50.1	0.28135	0.00015	-9.7	1.5	2660
A15-A4 - 36	1828	0.28140	0.00004	0.00045	0.000048	-48.8	0.28139	0.00015	-8.2	1.5	2599
A15-A4 - 38	1828	0.28141	0.00006	0.00035	0.000011	-48.7	0.28140	0.00020	-8.0	2.0	2587
A15-A4 - 40	1828	0.28139	0.00004	0.00097	0.000140	-49.2	0.28136	0.00013	-9.2	1.4	2641
A15-A4 - 41	1828	0.28138	0.00003	0.00078	0.000028	-49.6	0.28135	0.00009	-9.4	0.9	2650
A15-A4 - 42	1828	0.28139	0.00004	0.00079	0.000073	-49.4	0.28136	0.00012	-9.2	1.3	2642
A15-A4 - 43	1828	0.28141	0.00004	0.00129	0.000120	-48.7	0.28136	0.00014	-9.1	1.4	2636
A15-A4 - 44	1828	0.28141	0.00005	0.00241	0.000140	-48.6	0.28133	0.00018	-10.4	1.8	2690
A15-A4 - 45	1828	0.28141	0.00003	0.00067	0.000019	-48.6	0.28139	0.00011	-8.2	1.2	2598
A15-A4 - 46	1828	0.28145	0.00005	0.00168	0.000190	-47.1	0.28139	0.00017	-8.0	1.7	2590
A15-A4 - 47	1828	0.28142	0.00004	0.00134	0.000032	-48.2	0.28138	0.00013	-8.6	1.3	2616
A15-A4 - 48	1828	0.28145	0.00004	0.00067	0.000052	-47.1	0.28143	0.00015	-6.7	1.6	2535
A15-A4 - 49	1828	0.28144	0.00004	0.00104	0.000068	-47.7	0.28140	0.00016	-7.8	1.6	2583
A15-A4 - 50	1828	0.28141	0.00004	0.00127	0.000007	-48.5	0.28137	0.00013	-8.9	1.3	2626
A15-A4 - 51	1828	0.28141	0.00004	0.00178	0.000083	-48.6	0.28135	0.00015	-9.6	1.5	2657
A15-A4 - 52	1828	0.28139	0.00006	0.00110	0.000083	-49.4	0.28135	0.00021	-9.6	2.2	2655
A15-A4 - 53	1828	0.28138	0.00005	0.00101	0.000030	-49.6	0.28135	0.00016	-9.6	1.7	2659
A15-A4 - 54	1828	0.28138	0.00005	0.00036	0.000027	-49.8	0.28137	0.00018	-9.0	1.8	2633
A15-A4 - 55	1828	0.28141	0.00004	0.00058	0.000018	-48.5	0.28139	0.00014	-8.0	1.4	2590
17SRB-C047A, Hornblende Biotite Granite											
C47 - 1	1830	0.28137	0.00005	0.00024	0.000003	-50.1	0.28136	0.00016	-9.1	1.7	2641
C47 - 2	1830	0.28143	0.00003	0.00056	0.000012	-48.0	0.28141	0.00012	-7.4	1.3	2568
C47 - 3	1830	0.28137	0.00002	0.00026	0.000011	-50.0	0.28136	0.00007	-9.0	0.9	2636
C47 - 4	1830	0.28139	0.00003	0.00031	0.000019	-49.3	0.28138	0.00010	-8.4	1.2	2610
C47 - 5	1830	0.28140	0.00004	0.00052	0.000016	-49.1	0.28138	0.00016	-8.5	1.7	2614
C47 - 6	1830	0.28140	0.00005	0.00062	0.000028	-48.9	0.28138	0.00017	-8.4	1.8	2610
C47 - 7	1830	0.28138	0.00004	0.00036	0.000010	-49.6	0.28137	0.00013	-8.8	1.4	2627
C47 - 9	1830	0.28139	0.00005	0.00037	0.000005	-49.4	0.28137	0.00016	-8.6	1.7	2619
C47 - 10	1830	0.28139	0.00003	0.00029	0.000008	-49.3	0.28138	0.00011	-8.4	1.3	2610
C47 - 11	1830	0.28138	0.00004	0.00034	0.000011	-49.8	0.28137	0.00013	-9.0	1.4	2633
C47 - 12	1830	0.28143	0.00004	0.00046	0.000010	-48.0	0.28141	0.00015	-7.2	1.6	2561
C47 - 13	1830	0.28142	0.00003	0.00026	0.000010	-48.3	0.28141	0.00010	-7.4	1.2	2565
C47 - 14	1830	0.28138	0.00004	0.00049	0.000001	-49.7	0.28136	0.00015	-9.1	1.6	2638
C47 - 16	1830	0.28145	0.00005	0.00035	0.000018	-47.1	0.28144	0.00018	-6.3	1.9	2519
17SRB-D048A, Charnockite											
D48 - 1	1826	0.28134	0.00004	0.00032	0.000017	-51.0	0.28133	0.00013	-10.3	1.4	2682
D48 - 2	1826	0.28133	0.00004	0.00036	0.000002	-51.6	0.28131	0.00013	-11.0	1.4	2711
D48 - 3	1826	0.28131	0.00004	0.00034	0.000016	-52.2	0.28130	0.00015	-11.5	1.6	2732
D48 - 4	1826	0.28131	0.00004	0.00038	0.000008	-52.1	0.28130	0.00013	-11.4	1.4	2732
D48 - 5	1826	0.28125	0.00008	0.00036	0.000007	-54.4	0.28124	0.00027	-13.7	2.7	2826
D48 - 6	1826	0.28137	0.00003	0.00052	0.000057	-50.1	0.28135	0.00011	-9.7	1.3	2657
D48 - 7	1826	0.28132	0.00003	0.00040	0.000010	-51.9	0.28130	0.00012	-11.3	1.3	2727
D48 - 8	1826	0.28136	0.00004	0.00036	0.000003	-50.3	0.28135	0.00012	-9.6	1.4	2652
D48 - 9	1826	0.28133	0.00003	0.00035	0.000022	-51.4	0.28132	0.00012	-10.7	1.3	2700
D48 - 10	1826	0.28135	0.00003	0.00040	0.000018	-50.6	0.28134	0.00012	-10.0	1.3	2671
D48 - 11	1826	0.28131	0.00004	0.00031	0.000020	-52.1	0.28130	0.00015	-11.4	1.6	2730
D48 - 12	1826	0.28134	0.00004	0.00030	0.000003	-51.2	0.28133	0.00014	-10.5	1.5	2692
D48 - 13	1826	0.28135	0.00003	0.00050	0.000005	-50.9	0.28133	0.00012	-10.4	1.3	2687
D48 - 14	1826	0.28132	0.00003	0.00046	0.000005	-51.9	0.28130	0.00011	-11.4	1.3	2728
D48 - 15	1826	0.28133	0.00003	0.00033	0.000005	-51.4	0.28132	0.00011	-10.7	1.3	2700

Appendix 4, Table 1 cont.

D48 - 17	1826	0.28135	0.00005	0.00037	0.000025	-50.6	0.28134	0.00019	-10.0	2.0	2670
D48 - 18	1826	0.28137	0.00003	0.00038	0.000024	-49.9	0.28136	0.00010	-9.2	1.2	2639
D48 - 19	1826	0.28134	0.00004	0.00037	0.000010	-51.3	0.28132	0.00014	-10.6	1.5	2697
D48 - 20	1826	0.28134	0.00004	0.00029	0.000010	-51.1	0.28133	0.00016	-10.3	1.7	2683
D48 - 21	1826	0.28131	0.00004	0.00067	0.000028	-52.3	0.28128	0.00013	-12.0	1.4	2756
D48 - 22	1826	0.28138	0.00005	0.00051	0.000011	-49.8	0.28136	0.00017	-9.3	1.8	2641
D48 - 23	1826	0.28136	0.00005	0.00044	0.000020	-50.5	0.28134	0.00018	-10.0	1.9	2669
D48 - 24	1826	0.28134	0.00004	0.00050	0.000008	-51.2	0.28132	0.00016	-10.7	1.7	2699
D48 - 25	1826	0.28130	0.00003	0.00041	0.000004	-52.6	0.28128	0.00009	-12.0	1.1	2755
D48 - 26	1826	0.28135	0.00004	0.00032	0.000006	-50.8	0.28134	0.00013	-10.1	1.4	2675
D48 - 28	1826	0.28132	0.00007	0.00034	0.000001	-51.7	0.28131	0.00023	-11.0	2.4	2714
<i>17SRB-J029A3</i>											
J29 - 1	1841	0.28138	0.00005	0.00059	0.000019	-49.8	0.28136	0.00018	-9.0	1.9	2725
J29 - 4	1841	0.28137	0.00004	0.00031	0.000004	-50.1	0.28136	0.00015	-9.0	1.6	2726
J29 - 5	1841	0.28137	0.00004	0.00027	0.000014	-50.1	0.28136	0.00014	-8.9	1.5	2720
J29 - 6	1841	0.28138	0.00004	0.00046	0.000024	-49.6	0.28137	0.00016	-8.7	1.7	2709
J29 - 7	1841	0.28135	0.00004	0.00036	0.000003	-50.7	0.28134	0.00014	-9.6	1.5	2754
<i>17SRB-O054A</i>											
O54 - 1	1840	0.28134	0.00004	0.00035	0.000006	-51.1	0.28133	0.00015	-10.1	1.6	2632
O54 - 2	1840	0.28135	0.00003	0.00037	0.000005	-50.9	0.28133	0.00010	-10.0	1.2	2628
O54 - 8	1840	0.28140	0.00005	0.00038	0.000018	-49.0	0.28139	0.00019	-8.0	2.0	2551
O54 - 9	1840	0.28138	0.00003	0.00026	0.000008	-49.8	0.28137	0.00012	-8.7	1.3	2577
O54 - 11	1840	0.28135	0.00004	0.00040	0.000003	-50.7	0.28134	0.00013	-9.8	1.4	2621
O54 - 12	1840	0.28132	0.00004	0.00033	0.000003	-51.9	0.28131	0.00012	-10.9	1.4	2665
O54 - 13	1840	0.28134	0.00005	0.00030	0.000007	-51.3	0.28132	0.00018	-10.3	1.9	2638
O54 - 14	1840	0.28136	0.00005	0.00045	0.000071	-50.3	0.28135	0.00019	-9.4	2.0	2605

Appendix 4, Table 1 cont.

Boothia Neoarchean Porphyroclastic Basement

17SRB-0009A3												
09 - 3	2514	0.28121	0.00003	0.00151	0.000098	-55.6	0.28114	0.00012	-1.1	1.3	2944	
09 - 5	2514	0.28123	0.00007	0.00128	0.000100	-55.0	0.28117	0.00025	0.0	2.5	2892	
09 - 30	2514	0.28122	0.00005	0.00131	0.000100	-55.3	0.28116	0.00017	-0.4	1.7	2912	
09 - 20	2514	0.28122	0.00004	0.00098	0.000025	-55.2	0.28118	0.00012	0.2	1.3	2880	
09 - 25	2514	0.28119	0.00004	0.00004	0.000013	-56.4	0.28119	0.00013	0.7	1.3	2858	
09 - 19	2514	0.28123	0.00004	0.00117	0.000050	-55.0	0.28117	0.00015	0.1	1.6	2886	
09 - 21	2514	0.28120	0.00003	0.00031	0.000130	-56.0	0.28119	0.00011	0.6	1.1	2861	
09 - 24	2514	0.28124	0.00003	0.00108	0.000069	-54.7	0.28119	0.00012	0.6	1.2	2861	
09 - 6	2514	0.28128	0.00005	0.00113	0.000095	-53.4	0.28122	0.00019	1.8	1.9	2800	
09 - 27	2514	0.28121	0.00005	0.00095	0.000091	-55.7	0.28116	0.00017	-0.2	1.7	2901	
09 - 28	2514	0.28119	0.00004	0.00126	0.000100	-56.4	0.28113	0.00015	-1.5	1.5	2962	
09 - 17	2514	0.28127	0.00004	0.00117	0.000140	-53.8	0.28121	0.00014	1.4	1.5	2823	
09 - 39	2514	0.28122	0.00003	0.00111	0.000040	-55.4	0.28117	0.00010	-0.2	1.0	2899	
09 - 22	2514	0.28131	0.00006	0.00230	0.000300	-52.2	0.28120	0.00022	1.0	2.3	2843	
09 - 11	2514	0.28122	0.00004	0.00127	0.000076	-55.3	0.28116	0.00015	-0.3	1.5	2906	
09 - 37	2514	0.28120	0.00004	0.00118	0.000099	-55.9	0.28115	0.00013	-0.8	1.4	2930	
09 - 33	2514	0.28122	0.00004	0.00075	0.000200	-55.2	0.28119	0.00015	0.6	1.6	2860	
09 - 23	2514	0.28123	0.00004	0.00127	0.000063	-55.1	0.28116	0.00014	-0.2	1.5	2900	
09 - 13	2514	0.28121	0.00003	0.00095	0.000029	-55.6	0.28117	0.00012	-0.1	1.2	2895	
09 - 8	2514	0.28121	0.00006	0.00155	0.000220	-55.9	0.28113	0.00020	-1.4	2.0	2960	
09 - 10	2514	0.28122	0.00004	0.00102	0.000090	-55.3	0.28117	0.00012	0.1	1.3	2886	
09 - 4	2514	0.28119	0.00005	0.00146	0.000051	-56.3	0.28112	0.00019	-1.7	1.9	2975	
09 - 35	2514	0.28124	0.00004	0.00117	0.000068	-54.7	0.28118	0.00015	0.4	1.6	2870	
09 - 26	2514	0.28126	0.00004	0.00174	0.000190	-53.8	0.28118	0.00016	0.3	1.6	2875	
09 - 31	2514	0.28119	0.00005	0.00105	0.000014	-56.3	0.28114	0.00018	-1.0	1.9	2941	
09 - 9	2514	0.28122	0.00005	0.00137	0.000096	-55.4	0.28115	0.00016	-0.6	1.6	2922	
18SRB-00118A												
O112 - 26	2510	0.28123	0.00006	0.00139	0.000066	-55.0	0.28116	0.00023	-0.3	2.3	2933	
O112 - 10	2510	0.28123	0.00006	0.00155	0.000067	-55.0	0.28116	0.00022	-0.6	2.2	2945	
O112 - 15	2510	0.28124	0.00006	0.00144	0.000070	-54.8	0.28117	0.00020	-0.2	2.0	2926	
O112 - 21	2510	0.28121	0.00003	0.00098	0.000100	-55.7	0.28116	0.00012	-0.3	1.2	2931	
O112 - 7	2510	0.28124	0.00004	0.00139	0.000060	-54.7	0.28117	0.00015	-0.1	1.6	2919	
O112 - 12	2510	0.28120	0.00007	0.00132	0.000110	-56.0	0.28114	0.00024	-1.2	2.4	2979	
O112 - 9	2510	0.28119	0.00005	0.00079	0.000064	-56.4	0.28115	0.00016	-0.7	1.6	2954	
O112 - 5	2510	0.28122	0.00004	0.00199	0.000300	-55.3	0.28112	0.00013	-1.7	1.4	3005	
O112 - 3	2510	0.28127	0.00005	0.00112	0.000060	-53.5	0.28122	0.00018	1.6	1.8	2829	
O112 - 6	2510	0.28122	0.00005	0.00119	0.000120	-55.3	0.28116	0.00017	-0.3	1.8	2932	
O112 - 4	2510	0.28123	0.00004	0.00105	0.000120	-55.1	0.28118	0.00012	0.1	1.3	2910	
O112 - 8	2510	0.28120	0.00006	0.00101	0.000043	-56.1	0.28115	0.00020	-0.8	2.0	2959	
O112 - 23	2510	0.28124	0.00006	0.00123	0.000079	-54.7	0.28118	0.00020	0.2	2.0	2903	
O112 - 14	2510	0.28122	0.00006	0.00081	0.000100	-55.5	0.28118	0.00020	0.1	2.1	2907	
O112 - 18	2510	0.28123	0.00004	0.00128	0.000061	-55.1	0.28117	0.00015	-0.2	1.6	2926	
O112 - 19	2510	0.28116	0.00006	0.00084	0.000062	-57.5	0.28112	0.00022	-2.0	2.2	3018	

Isotopic ratios are corrected for ^{176}Yb isobaric interference

Depelted Mantle values from Belousov et al., (2010); CHUR values from Bouvier et al., (2008)

$$^1 \varepsilon\text{Hf} = 10^4 * ((^{176}\text{Hf}/^{177}\text{Hf}_{\text{sample}} - ^{176}\text{Hf}/^{177}\text{Hf}_{\text{CHUR}}) / ^{176}\text{Hf}/^{177}\text{Hf}_{\text{CHUR}})$$

² Minimum T_{DM} calculated from whole rock Lu/Hf values

$$^2 T_{\text{DM}} = \lambda^{-1} * \ln [1 + (^{176}\text{Hf}/^{177}\text{Hf}_{(\text{sample})} - ^{176}\text{Hf}/^{177}\text{Hf}_{(\text{DM})}) / (^{176}\text{Lu}/^{177}\text{Lu}_{(\text{sample})} - ^{176}\text{Lu}/^{177}\text{Lu}_{(\text{DM})})]$$

Appendix 4, Table 2: Whole Rock Sm/Nd Isotopic Results

Sample	Sm (ppm)	Nd (ppm)	$^{147}\text{Sm}/^{144}\text{Nd}$	Present $^{143}\text{Nd}/^{144}\text{Nd}$	Initial $^{143}\text{Nd}/^{144}\text{Nd}$	$\pm 2\sigma$	Age (Ma)	ϵNd^1	$\pm 2\sigma$	T_{DM}^2
Boothia Ferroan Granitiod Complex										
17SRB-A015A3	18.6	142.7	0.0789	0.51086	0.50991	0.00001	1826	-7.14	0.16	2572
17SRB-R077B2	59.6	480.4	0.0750	0.51082	0.50991	0.00001	1826	-7.06	0.15	2546
17SRB-A025A4	10.3	55.3	0.1125	0.51125	0.50989	0.00002	1827	-7.47	0.16	2844
17SRB-J029A3	13.0	73.6	0.1071	0.51118	0.50988	0.00002	1840	-7.32	0.19	2792
17SRB-L054A	18.5	113.0	0.0990	0.51104	0.50986	0.00002	1823	-8.31	0.18	2775
Boothia Neoarchean Porphyroclastic Granitoids										
17SRB-O009A3	6.8	34.9	0.1028	0.51107	0.50937	0.00002	2550	-0.21	0.28	2833
17SRB-M026A2	6.2	34.0	0.1094	0.51117	0.50935	0.00002	2550	-0.47	0.30	2872
Boothia 2.48 Ga Quartz Diorite										
17SRB-M096A4	10.0	72.4	0.0838	0.51088	0.50951	0.00001	2480	1.71	0.18	2644
17SRB-M054A3	8.6	45.8	0.1131	0.51165	0.50930	0.00002	2480	-2.31	0.22	2823
17SRB-R007A2	8.2	40.3	0.1232	0.51127	0.50942	0.00002	2480	-0.02	0.24	2822

¹ $\epsilon\text{Nd} (\text{T}) = 10^4 * (\frac{^{143}\text{Nd}}{^{144}\text{Nd}_{\text{sample}}} / (\frac{^{143}\text{Nd}}{^{144}\text{Nd}_{\text{CHUR}}} - 1))$

² $T_{\text{DM}} = \lambda^{-1} * \ln [1 + (\frac{^{143}\text{Nd}}{^{144}\text{Nd}_{\text{sample}}} - \frac{^{143}\text{Nd}}{^{144}\text{Nd}_{\text{DM}}}) / (\frac{^{147}\text{Sm}}{^{144}\text{Nd}_{\text{sample}}} - \frac{^{147}\text{Sm}}{^{144}\text{Nd}_{\text{DM}}})]$

Depleted Mantle values after Goldstein *et al.*, (1984); CHUR values after Bouvier *et al.*, 2008)

APPENDIX 5: ZIRCON TRACE-ELEMENT ANALYSES AND STANDARDS

APPENDIX 5, Table 1: COMPILED ZIRCON TRACE ELEMENT COMPOSITIONS ANALYSES

Sample								
Name	17SRB-J29A1							
Rock Type	Fayalite Granite							
Spot Name	J29-2	J29-7	J29-10	J29-11	J29-13	J29-14	J29-15	J29-17
<i>ppm</i>								
P	232	156	228	197	185	182	292	203
Sc	323	260	272	294	255	258	304	275
Ti	18.6	5.8	7.8	20.5	11.2	11.2	16.7	15.2
Y	1137	629	637	443	493	404	1068	752
Nb	2.20	2.83	2.38	2.38	3.06	2.76	2.17	2.56
La	0.21	0.27	3.67	0.04	0.42	0.01	4.24	0.46
Ce	8.1	8.1	15.6	4.8	9.4	6.5	17.1	8.0
Pr	0.763	0.262	1.515	0.062	0.220	0.083	1.920	0.336
Nd	10.1	2.9	10.8	1.4	1.9	1.3	14.6	4.0
Sm	12.6	3.8	6.3	2.6	2.6	2.3	12.3	5.4
Eu	0.42	0.13	0.49	0.08	0.08	0.06	0.46	0.22
Gd	44.0	16.4	21.8	12.1	12.2	10.3	41.2	24.2
Tb	11.9	5.2	6.1	3.6	4.1	3.3	11.2	7.1
Dy	120.9	58.2	63.5	39.5	46.1	38.2	113.6	74.8
Ho	40.2	21.6	22.2	14.5	16.9	13.7	37.8	26.2
Er	160.4	94.8	91.2	64.7	75.0	60.6	151.0	108.3
Tm	30.3	19.3	17.8	13.6	15.3	12.4	28.7	21.4
Yb	256.5	171.6	154.9	120.6	141.6	111.5	243.6	182.2
Lu	48.7	33.8	30.3	24.2	27.9	22.2	46.5	35.4
Ta	0.99	1.31	1.02	1.06	1.63	1.19	0.91	1.13
Th	122.7	95.1	99.6	52.1	83.6	67.3	126.9	102.6
U	168.2	214.1	144.2	108.4	200.4	141.9	168.8	169.5
(wt%) Hf	1.025	1.173	1.014	1.102	1.193	1.086	0.993	1.016
Th/U	0.729	0.444	0.691	0.481	0.417	0.474	0.752	0.605
¹ Eu/Eu*	0.055	0.050	0.126	0.046	0.046	0.035	0.062	0.058
² Ce/Ce*	4.862	7.323	1.599	23.080	7.513	45.228	1.447	4.945
³ (Gd/Lu) _N	0.112	0.060	0.089	0.062	0.054	0.057	0.109	0.084

¹Eu/Eu* = Eu_N/ √(La_N * Gd_N)

²Ce/Ce* = Ce_N/ √(La_N * Pr_N)

³Normalized to chondritic values from McDonough and Sun (1995)

Analyzed in Session 1

APPENDIX 5, Table 1 cont.

Sample															
Name	17SRB-J53A1							17SRB-J53A1							
Rock Type	Grt-Bt Suite (Core)							Grt-Bt Suite (Rim)							
Spot Name	J53-2	J53-3	J53-4	J53-5	J53-7	J53-8	J53-9	J53-10	J53-12	J53-15	J53-1	J53-6	J53-11	J53-13	J53-14
ppm															
P	338	368	306	389	404	344	337	273	323	302	242	241	235	278	228
Sc	284	287	273	284	299	282	284	260	288	277	266	256	253	262	286
Ti	30.7	22.2	30.2	48.0	38.9	35.3	38.0	33.5	31.9	32.6	4.0	8.2	6.5	15.2	14.2
Y	531	642	416	409	697	567	551	459	550	489	348	422	408	428	504
Nb	0.88	1.01	0.88	0.95	0.89	0.96	0.92	1.46	0.90	3.19	1.15	1.62	1.26	1.39	4.19
La	1.27	0.55	0.15	0.06	0.11	0.06	1.58	1.42	0.19	0.60	0.02	1.03	1.88	0.29	5.66
Ce	19.9	14.7	8.3	8.1	10.6	9.7	23.7	20.4	10.6	16.3	5.1	13.2	26.0	13.5	62.7
Pr	3.800	1.708	0.521	0.349	1.161	0.562	4.820	3.120	0.915	1.310	0.110	1.900	3.850	0.920	12.900
Nd	33.2	19.4	6.8	5.1	18.5	8.9	42.3	29.6	11.4	12.5	1.9	15.1	28.5	8.3	95.3
Sm	20.5	17.9	7.8	7.0	21.0	10.7	23.9	19.8	11.8	10.9	3.5	9.4	16.5	7.6	57.3
Eu	4.15	3.31	1.54	1.22	2.56	1.65	6.02	4.99	1.83	2.37	0.31	2.05	4.94	1.32	14.00
Gd	37.4	42.0	23.9	20.7	52.2	32.7	39.7	29.8	31.9	27.3	12.0	14.5	24.7	19.7	42.2
Tb	7.7	9.3	5.5	5.3	11.4	7.9	8.2	6.1	7.5	6.6	3.5	3.6	5.2	4.8	7.1
Dy	65.5	81.3	50.4	49.0	94.4	70.7	67.7	54.6	67.6	59.2	34.9	38.1	46.3	46.7	54.7
Ho	19.1	23.2	14.9	14.5	26.2	20.7	19.9	16.1	19.8	17.6	11.9	14.0	13.8	14.8	16.4
Er	68.6	82.4	53.6	53.4	88.7	74.2	70.5	59.7	71.8	66.2	49.5	66.2	55.1	59.9	70.8
Tm	12.1	14.7	9.6	9.8	15.1	13.3	12.6	11.1	13.3	11.8	10.7	15.7	11.0	12.0	16.2
Yb	99.1	115.4	78.6	80.4	118.4	109.0	100.4	92.7	109.5	101.0	98.3	162.5	97.5	104.8	164.1
Lu	18.1	21.0	14.5	14.9	20.8	19.8	18.3	17.2	20.1	18.9	19.9	34.0	18.8	20.4	33.8
Ta	0.32	0.35	0.31	0.32	0.33	0.33	0.32	0.34	0.36	1.03	0.52	0.94	0.47	0.49	1.95
Th	95.7	131.2	64.7	74.0	139.2	110.3	91.5	86.2	107.7	100.4	84.0	115.9	111.3	112.7	115.2
U	53.3	62.0	35.6	41.1	72.7	51.4	48.7	58.6	91.7	62.3	232.1	452.8	176.9	122.9	577.0
(wt%) Hf	0.985	0.985	0.974	0.949	0.965	0.968	0.985	0.999	0.973	1.014	0.966	1.128	1.015	1.024	1.248
Th/U	1.795	2.117	1.817	1.801	1.915	2.146	1.878	1.471	1.174	1.612	0.362	0.256	0.629	0.917	0.200
¹ Eu/Eu*	0.457	0.368	0.344	0.310	0.236	0.270	0.596	0.626	0.287	0.419	0.147	0.535	0.747	0.328	0.868
² Ce/Ce*	2.192	3.676	7.140	13.281	7.069	12.927	2.078	2.346	6.160	4.450	24.467	2.283	2.338	6.351	1.775
³ (Gd/Lu)*	0.255	0.247	0.204	0.171	0.311	0.204	0.268	0.214	0.197	0.179	0.074	0.053	0.162	0.119	0.155

¹Eu/Eu* = Eu_N / √(La_N * Gd_N)²Ce/Ce* = Ce_N / √(La_N * Pr_N)³Normalized to chondritic values from McDonough and Sun (1995)

Analyzed in Session 1

APPENDIX 5, Table 1 cont.

Sample											
Name	17SRB-L52A										
Rock Type	Charnockite										
Spot Name	L52-2	L52-4	L52-5	L52-6	L52-7	L52-8	L52-9	L52-13	L52-14	L52-16	L52-18
ppm											
P	231	205	198	287	236	187	244	239	176	191	284
Sc	283	250	240	324	285	239	274	254	235	252	241
Ti	29.8	8.4	10.1	29.1	21.3	16.3	28.2	23.6	10.1	18.8	16.5
Y	693	358	337	950	626	303	340	405	383	617	282
Nb	2.15	1.91	2.21	1.72	1.70	2.21	1.67	1.83	2.26	1.68	1.50
La	0.05	0.05	0.04	0.21	0.07	0.13	0.05	0.01	0.03	0.01	0.07
Ce	13.0	14.0	16.5	16.5	12.6	13.7	9.3	11.5	12.8	13.4	11.1
Pr	0.440	0.130	0.157	1.314	0.424	0.101	0.139	0.118	0.112	0.162	0.094
Nd	6.6	2.0	1.9	17.6	6.6	1.4	2.2	2.1	1.8	2.8	1.6
Sm	8.9	2.9	2.6	18.1	8.6	2.3	2.9	3.4	2.9	5.0	2.4
Eu	1.33	0.45	0.34	3.81	1.70	0.27	0.65	0.48	0.41	0.71	0.42
Gd	31.7	11.2	10.2	54.4	28.4	8.5	11.6	13.2	12.5	21.2	9.1
Tb	8.0	3.3	3.1	12.3	7.3	2.7	3.3	3.8	3.6	6.2	2.7
Dy	77.8	35.7	34.2	114.6	70.7	30.1	35.1	40.4	39.1	63.6	27.6
Ho	25.7	12.7	12.0	35.8	22.9	10.9	12.3	14.5	14.2	22.6	10.0
Er	100.9	55.1	53.4	134.4	90.9	48.4	52.2	63.4	58.7	94.1	43.7
Tm	18.8	11.4	11.1	24.3	17.0	10.0	10.5	13.0	11.8	18.6	9.0
Yb	156.8	102.9	101.2	200.1	142.8	93.0	95.1	119.1	108.4	169.0	82.5
Lu	30.9	21.1	20.5	38.1	28.2	18.9	19.6	24.3	21.7	33.3	16.5
Ta	0.69	0.69	0.88	0.56	0.56	0.83	0.54	0.66	0.85	0.59	0.55
Th	51.8	71.7	83.6	62.1	43.8	71.7	41.6	66.3	58.2	95.2	50.5
U	34.5	57.0	76.3	30.0	27.3	72.3	32.2	54.6	55.0	73.3	41.7
(wt%) Hf	1.006	1.074	1.096	0.944	0.965	1.110	1.010	1.044	1.065	1.056	1.014
Th/U	1.501	1.257	1.096	2.072	1.606	0.992	1.291	1.214	1.058	1.299	1.213
¹ Eu/Eu*	0.241	0.243	0.202	0.370	0.332	0.190	0.344	0.219	0.205	0.211	0.272
² Ce/Ce*	22.141	42.816	49.158	7.663	18.028	28.663	27.515	88.293	56.269	66.659	34.002
³ (Gd/Lu)*	0.127	0.065	0.061	0.177	0.125	0.056	0.073	0.067	0.071	0.079	0.068

¹Eu/Eu* = Eu_N / √(La_N * Gd_N)

²Ce/Ce* = Ce_N / √(La_N * Pr_N)

³Normalized to chondritic values from McDonough and Sun (1995)

Analyzed in Session 2

APPENDIX 5, Table 1 cont.

Sample					
Name 17SRB-R75B					
Rock Type Hbl-Bt Granite					
Spot Name	R75-6	R75-12	R75-15	R75-16	R75-17
ppm					
P	247	173	143	136	204
Sc	201	225	210	197	206
Ti	7.0	7.8	5.1	6.0	6.2
Y	2223	1307	824	282	620
Nb	7.56	7.06	5.73	6.48	7.00
La	1.26	2.88	0.23	0.28	1.13
Ce	31.6	40.9	11.7	8.2	23.3
Pr	1.480	4.880	0.246	0.307	0.550
Nd	15.1	31.6	2.9	2.0	3.9
Sm	20.4	23.9	5.0	1.8	4.7
Eu	1.25	1.63	0.30	0.10	0.26
Gd	74.2	52.6	21.4	6.2	17.2
Tb	21.2	15.6	6.7	2.1	5.4
Dy	222.2	163.0	77.5	26.0	59.3
Ho	75.4	52.2	28.7	9.8	21.3
Er	322.8	224.2	135.1	48.4	96.3
Tm	66.0	48.2	30.1	11.8	20.9
Yb	595.0	435.0	293.2	118.8	195.9
Lu	114.0	78.9	60.1	25.5	39.1
Ta	3.20	4.04	3.50	3.95	3.25
Th	1198.0	548.0	275.4	103.5	416.9
U	1089.0	830.0	816.5	533.5	622.5
(wt%) Hf	1.021	1.167	1.218	1.168	1.110
Th/U	1.100	0.660	0.337	0.194	0.670
¹ Eu/Eu*	0.098	0.140	0.087	0.086	0.089
² Ce/Ce*	5.598	2.639	12.011	6.761	7.144
³ (Gd/Lu)*	0.080	0.082	0.044	0.030	0.055

¹Eu/Eu* = Eu_N/ √(La_N * Gd_N)²Ce/Ce* = Ce_N/ √(La_N * Pr_N)³Normalized to chondritic values from McDonough and Sun (1995)

Analyzed in Session 2

APPENDIX 5, Table 1 cont.

Sample					
Name 18SRB-O112A					
Rock Type Boothia Neoeatchean porphyroclastic granitoid					
Spot Name	O112-3	O112-8	O112-9	O112-10	O112-11
ppm					
P	181	639	346	567	378
Sc	333	374	338	339	236
Ti	12.3	5.5	15.3	5.9	12.1
Y	301	1262	769	1217	1840
Nb	2.38	1.07	2.49	1.13	2.78
La	9.40	0.80	4.30	0.55	10.84
Ce	46.7	6.9	28.0	3.4	44.7
Pr	7.940	1.250	5.480	0.208	4.410
Nd	54.9	11.5	44.1	2.6	38.6
Sm	21.8	12.2	24.3	5.4	15.7
Eu	5.41	1.46	4.39	0.13	12.63
Gd	38.2	52.4	36.8	28.5	45.1
Tb	7.8	15.2	8.7	9.5	13.5
Dy	53.3	144.5	84.0	111.1	159.0
Ho	10.3	42.4	25.2	41.1	61.8
Er	24.6	149.7	90.6	182.1	279.0
Tm	3.1	25.6	15.8	36.2	57.6
Yb	21.3	202.0	129.7	324.6	523.0
Lu	3.4	36.8	24.9	64.4	104.5
Ta	2.09	0.60	1.95	0.74	< LOD
Th	230.5	89.0	188.0	105.2	439.0
U	784.7	323.4	693.4	312.3	860.0
(wt%) Hf	1.360	1.192	1.264	1.117	0.946
Th/U	0.294	0.275	0.271	0.337	0.510
¹ Eu/Eu*	0.283	0.075	0.223	0.013	0.675
² Ce/Ce*	0.608	0.669	0.592	1.198	0.782
³ (Gd/Lu)*	1.410	0.176	0.183	0.055	0.053

¹Eu/Eu* = Eu_N/ √(La_N * Gd_N)²Ce/Ce* = Ce_N/ √(La_N * Pr_N)³Normalized to chondritic values from McDonough and Sun (1995)

Analyzed in Session 3

APPENDIX 5, Table 1 cont.

Sample													
Name	17SRB-O9A3												
Rock Type	Boothia Neoarchean porphyroclastic granitoid												
Spot Name	09-3	09-5	09-6	09-7	09-8	09-9	09-10	09-11	09-13	09-14	09-15	09-16	09-17
<i>ppm</i>													
P	669	748	688	634	791	351	778	368	640	676	697	747	918
Sc	326	394	369	307	384	299	418	305	400	376	333	380	417
Ti	8.8	9.0	8.0	7.4	9.7	8.9	8.2	10.6	10.0	12.2	8.6	10.6	7.8
Y	1579	1641	1457	1333	1663	666	1651	790	1388	1644	1438	1730	1953
Nb	1.30	1.50	0.99	1.19	1.43	1.36	1.13	1.01	0.88	< LOD	1.07	1.34	1.11
La	3.96	7.86	0.94	2.40	1.48	< LOD	4.99	1.70	0.17	9.99	0.16	5.24	0.33
Ce	40.5	49.9	8.9	26.7	10.8	4.0	22.6	13.0	2.8	63.2	2.1	53.7	2.4
Pr	6.990	7.800	1.597	4.550	1.330	0.131	2.920	2.290	0.388	12.300	0.292	10.190	0.323
Nd	62.6	49.3	14.9	44.1	7.9	2.2	18.1	18.9	4.5	95.3	3.1	92.6	2.9
Sm	31.2	15.9	10.0	22.5	4.9	5.1	9.0	8.8	7.3	31.1	4.3	44.5	3.8
Eu	28.20	12.50	2.60	13.47	1.72	0.25	4.13	3.02	0.26	13.50	0.22	22.00	0.34
Gd	55.4	31.2	34.7	43.6	22.4	24.7	31.5	18.3	38.1	43.2	24.4	59.6	25.0
Tb	12.9	10.5	11.1	10.1	9.3	7.1	10.9	5.5	11.8	11.3	9.6	13.0	10.9
Dy	139.5	133.3	128.8	112.5	130.0	70.1	138.4	65.7	131.6	135.2	121.5	147.5	150.8
Ho	51.9	53.9	49.3	44.1	54.8	22.5	55.3	25.6	47.9	54.0	48.3	57.2	64.6
Er	233.8	261.1	216.7	203.3	268.5	87.6	257.4	122.3	202.7	253.4	219.6	266.7	317.5
Tm	47.9	56.7	43.8	42.8	59.1	16.7	55.4	27.0	40.2	55.3	45.3	57.5	69.3
Yb	423.2	525.0	385.0	384.7	550.9	141.0	499.4	255.1	349.4	498.0	399.7	524.0	642.5
Lu	85.1	106.7	75.6	78.1	112.3	27.0	101.5	51.9	70.6	101.4	79.6	105.9	130.3
Ta	0.75	1.28	0.68	0.78	1.32	0.64	0.89	0.96	0.55	< LOD	0.73	1.08	0.97
Th	67.7	91.7	83.2	81.2	75.0	221.1	89.0	51.3	78.0	83.4	50.6	96.3	61.4
U	310.0	623.0	352.9	326.6	726.5	269.0	514.0	463.3	167.7	694.0	279.2	633.0	563.5
(wt%) Hf	1.235	1.220	1.198	1.229	1.246	1.204	1.185	1.242	1.186	1.158	1.186	1.212	1.267
Th/U	0.218	0.147	0.236	0.249	0.103	0.822	0.173	0.111	0.465	0.120	0.181	0.152	0.109
¹ Eu/Eu*	2.068	1.711	0.426	1.311	0.503	0.067	0.746	0.723	0.048	1.123	0.067	1.302	0.105
² Ce/Ce*	1.862	1.542	1.762	1.955	1.864	-	1.432	1.598	2.622	1.379	2.350	1.778	1.776
³ (Gd/Lu)*	0.080	0.036	0.057	0.069	0.025	0.113	0.038	0.044	0.067	0.053	0.038	0.070	0.024

¹Eu/Eu* = Eu_N/√(La_N * Gd_N)

²Ce/Ce* = Ce_N/√(La_N * Pr_N)

³Normalized to chondritic values from McDonough and Sun (1995)

Analyzed in Session 3

APPENDIX 5, Table 2: ZIRCON TRACE ELEMENT SECONDARY STANDARD ANALYSES

Secondary Standard: 91500 (Wiedenbeck et al., 1995; 2004)

Published Values (% RSD)			Session one				Session two				Session three			
Spot Name	91500-1	91500-2	91500-3	91500-4	91500-1	91500-2	91500-3	91500-4	91500-1	91500-2	91500-3	91500-4	91500-1	91500-2
ppm														
P	NP	-	59	39	70	45	48	55	51	45	41	67	44	53
Sc	NP	-	223	209	207	219	224	217	203	214	218	213	211	206
Ti	**4.2	-	4.2	4.9	4.4	4.1	5.0	4.4	4.8	5.9	3.5	3.2	4.2	4.9
Y	140	10	143	150	148	144	131	132	134	130	118	119	117	115
Nb	0.79	8	1.47	1.33	1.30	2.83	1.44	1.28	1.13	1.22	1.05	1.08	1.01	0.97
La	0.006	54	<LOD	<LOD	<LOD	<LOD	<LOD	<LOD	<LOD	<LOD	<LOD	<LOD	<LOD	<LOD
Ce	2.6	10	2.6	2.6	2.6	2.8	2.6	2.6	2.5	2.6	2.2	2.3	2.3	2.3
Pr	0.024	63	0.002	0.016	0.002	0.010	0.014	0.010	<LOD	<LOD	<LOD	<LOD	<LOD	<LOD
Nd	0.2	16	0.2	0.2	0.2	0.2	0.2	0.2	<LOD	<LOD	0.2	0.2	<LOD	0.1
Sm	0.5	15	0.4	0.4	0.4	0.4	0.5	0.4	0.4	0.4	0.3	0.4	<LOD	0.4
Eu	0.24	12	0.24	0.22	0.25	0.24	0.24	0.26	0.21	0.22	0.16	0.17	<LOD	0.19
Gd	2.2	11	2.5	2.4	2.6	2.4	2.2	2.3	2.3	2.4	1.9	1.7	2.0	1.8
Tb	0.9	8	0.9	0.9	0.9	0.9	0.8	0.8	0.8	0.9	0.6	0.7	0.7	0.7
Dy	11.8	7	12.1	11.7	12.0	12.0	11.2	11.1	10.7	11.4	9.5	9.4	9.2	9.3
Ho	4.8	7	4.8	5.0	5.1	5.0	4.8	4.8	4.5	4.7	4.1	4.1	4.0	3.8
Er	24.6	10	25.2	26.1	26.4	26.1	23.7	24.9	23.2	24.4	21.5	20.8	20.9	20.4
Tm	6.9	5	6.7	6.8	6.8	6.8	6.4	6.5	6.1	6.6	5.5	5.4	5.4	5.3
Yb	73.9	5	70.1	70.5	71.6	72.9	67.2	69.8	64.2	68.1	59.0	57.3	56.3	54.0
Lu	13.1	8	12.2	13.7	13.6	12.9	11.7	12.4	11.8	12.3	10.8	10.9	10.7	10.5
Ta	0.57	7	0.64	0.62	0.56	0.89	0.57	0.59	0.52	0.55	0.53	0.53	0.50	0.51
Th	29.9	7	27.5	29.0	29.2	28.8	27.6	29.7	27.9	29.3	23.2	23.2	21.9	21.9
U	80.0	10	83.3	85.9	85.6	86.7	82.5	86.6	80.4	85.0	67.6	66.7	66.1	65.0
(wt%) Hf	*0.586	-	0.491	0.535	0.532	0.515	0.514	0.547	0.507	0.538	0.598	0.576	0.582	0.567

% RSD = Relative Standard Deviation for ICP-MS ; LOD = Limit of Detection; NP = not published

* Mean from Wiedenbeck et al. (1995), uncertainty of $\pm 5\%$

**Fu et al. (2008), ± 1.2 (2SD)

APPENDIX 6: SAMPLE LOCATIONS

APPENDIX 6, Table 1: Sample Locations

<i>Sample Name (Prefix: 17SRB-)</i>	<i>Suite</i>	<i>Easting</i>	<i>Northing</i>
A014	Charnockite	509159	7754662
A018	Charnockite	509953	7759775
D046	Charnockite	446052	7730724
D048	Charnockite	443698	7732809
L052	Charnockite	441025	7727316
L053	Charnockite	441788	7726218
L054	Charnockite	441821	7724937
L055	Charnockite	442672	7723739
A025	Fayalite Granite	501834	7788783
A055	Fayalite Granite	507184	7809460
A057	Fayalite Granite	509229	7808027
J029	Fayalite Granite	521604	7798380
M095	Fayalite Granite	516715	7813938
A015	Hornblende-Biotite Granite	510002	7755473
A016	Hornblende-Biotite Granite	510956	7756479
C047	Hornblende-Biotite Granite	506934	7733718
L042	Hornblende-Biotite Granite	523221	7754707
L040	Hornblende-Biotite Granite	521713	7757163
L055	Hornblende-Biotite Granite	442672	7723739
O026	Hornblende-Biotite Granite	521018	7768373
O027	Hornblende-Biotite Granite	520626	7767198
O058	Hornblende-Biotite Granite	518972	7748319
O060	Hornblende-Biotite Granite	520204	7746594
R074B	Hornblende-Biotite Granite	533441	7768804
R075	Hornblende-Biotite Granite	533050	7767872
R077B	Hornblende-Biotite Granite	531832	7767469
T023	Hornblende-Biotite Granite	527837	7768793
C040	Garnet-Biotite Suite	506913	7742663
C041	Garnet-Biotite Suite	507271	7741064
C043	Garnet-Biotite Suite	507391	7737825
J050	Garnet-Biotite Suite	500103	7735312
J053	Garnet-Biotite Suite	506750	7749027
L057	Garnet-Biotite Suite	443529	7721383
O054	Garnet-Biotite Suite	515488	7752770
O056	Garnet-Biotite Suite	517012	7750670
T022	Garnet-Biotite Suite	526140	7767503
J051	Migmatite Xenolith	518543	7733940
R077A	Migmatite Xenolith	531832	7767469
	Boothia Neoarchean		
O009A	Porphyroclasic Granitoid	468888	7798242
	Boothia Neoarchean		
18SRB-O112	Porphyroclasic Granitoid	465478	7838249

APPENDIX 7: EXTENDED COMPARISON TO CHURCHILL LATE- TO POST-TECTONIC MAGMATISM

Hudson Granites and Coeval Minettes

The Hudson granites (Peterson et al., 2002), whose emplacement temporally overlaps the BFGC (~1.85-1.81 Ga), are the most prevalent late- to post-collisional felsic magmatic rocks in the hinterland of the Trans-Hudson orogen, with occurrences across the central Rae and central Hearne cratons (Fig. 1). These are high silica (>70 wt. %), peraluminous granitoids whose compositions plot dominantly in the alkali-calcic and magnesian fields on the Frost et al. (2001) discrimination diagrams (Fig. 4) and which have initial ϵ_{Nd} values between -7 and -13. On the basis of their field relationships, their minimum-melt CIPW normative compositions and ~ 5 kbar metamorphic pressure estimates derived from the surrounding rocks, Peterson et al. (2002) proposed that the Hudson granites were near-solidus granite magmas (600-700°C) that were both generated and emplaced in the mid-crust. Although a low-temperature origin is consistent with the observation of significant zircon inheritance in these granitoids, application of the zircon saturation thermometer (Watson and Harrison, 1984) to Hudson granite geochemical data indicates somewhat hotter conditions than deduced by Peterson et al. (2002), with temperatures ranging from 760-850 °C (avg. = 809 °C). Even assuming 50 % of the zircon in these rocks is inherited, T_{ZircSat} remains well above minimum melt conditions (avg. = 749 °C). Peterson et al. (2002) and Peterson and Pehrsson (2010) suggested that the Hudson granites are intra-crustal melts generated as a result of collision-related crustal thickening associated with the Snowbird and Trans-Hudson orogens, with subsequent extension at ca. 1.83 Ga.

While the role of mantle-derived magmas is not immediately apparent in previous studies of the Hudson granite petrogenesis, outcrop evidence of magma mingling textures between granitoid and minette-related magmas have locally been documented in both the Rae and Hearne cratons (Sandeman et al., 2000; Peterson and Pehrsson, 2010; Sandeman and Hadlari, 2010). As noted previously, these alkali-rich mafic magmas have Nd isotope compositions that overlap those of the Hudson granites (Cousens et al. 2001; Peterson et al., 2002; Peterson and Pehrsson, 2010; Sandeman and Hadlari, 2010)). Different models have been proposed for the genesis of these minette magmas. Cousens et al. (2001) proposed they were derived from Churchill Province lithospheric mantle that had been metasomatically enriched over broad areas during Neoarchean flat subduction. The long time interval between metasomatism and minette-magma generation allowed the ϵ_{Nd} of the enriched mantle to evolve to strongly negative values. In contrast,

Peterson et al. (2002) and Peterson and Pehrsson (2010) proposed the minettes were derived from a mixed crust-mantle sources that formed as a result of tectonic imbrication of Churchill Province lower crust and underlying upper mantle during Snowbird and Trans-Hudson orogenesis. In this model, Nd isotope composition of the minettes reflects that of the Neoarchean crustal rocks in the mixed source. Whichever model is correct, the intrusion of these mantle-derived mafic magmas would have contributed to heating the Churchill Province lower and middle crust.

There are a number of similarities between the Hudson and BFGC granitoids including: 1) crystallization ages, 2) mid-crustal emplacement levels, 3) occurrence as plutons with a general NE-SW sense of elongation, possibly related to pluton emplacement along zones of structural weakness, and 4) strongly negative ϵ_{Nd} initial values. There are also significant mineralogical and geochemical differences between the two sets of granitoids. Unlike the Hudson granites, many of the BFGC plutons are characterized by the presence of anhydrous mafic minerals (fayalite, orthopyroxene, clinopyroxene, pigeonite). These mineralogical differences are a manifestation of the higher temperature of the BFGC magmas, which enabled the formation of more H₂O-poor melts that could crystallize and preserve these anhydrous minerals. Additionally, the BFGC has a broader range of SiO₂ contents, a ferroan rather than magnesian character and, unlike the exclusively peraluminous Hudson granites, include both metaluminous and peraluminous varieties. These geochemical differences likely relate different magma source rocks and to differences in the conditions of magma generation.

The Hudson granites are spatially associated with 1.9 – 1.83 Ga dextral shear zones (Theriault *et al.*, 2018; Sanborn-Barrie *et al.*, 2014, Henderson and Roddick, 1990), which give many of the Hudson granite plutons a NE-SW sense of elongation (Peterson *et al.*, 2002). The BFGC plutons are generally elongate in a similar NE-SW orientation and are also proximal to but not coincident with the Sanagak Lake shear zone (Fig. 2). However, the SLsz has a sinistral rather than a dextral sense of motion (Drayson *et al.*, in prep). In addition, the SLsz shearing was initiated prior to BFGC emplacement, as opposed to emplaced magmatism exploiting or emplaced coeval to the shear zones (Wodikca *et al.*, 2016; Theriault *et al.*, 2018, Berman *et al.*, 2010). These shear zones are all attributed to far-field stresses associated with crustal shortening in the Trans-Hudson orogeny.

Kivalliq Igneous Suite / Nueltin granites

The Kivalliq igneous suite, of which the Nueltin granites are a part, occur over wide areas of the central Rae and Hearne cratons (Peterson et al., 2002, 2015). These magmas, which were mostly emplaced at shallow crustal levels, were generated between 1770-1730 Ma, ~ 40 – 120 Myr after the Hudson granites and the BFGC. The Kivalliq suite represents a broad range of magma compositions from gabbros and anorthosites to rapakivi granites as well as the extrusive equivalents of some of these plutonic rock types. The Nueltin granites are generally high silica (>70 wt. %), ferroan, alkalic to alkali-calcic granitoids, many of which are weakly peraluminous but also including some metaluminous varieties (Fig. 8). Zircon saturation temperatures calculated using data reported for these granitoids (Peterson et al., 2002; 2015) average 835 °C, higher than the Hudson granites. On average, the Nueltin granitoids have higher REE contents and more pronounced negative Eu anomalies than the Hudson granites. Notably, a subset of Nueltin granites within the northern Hearne craton (Peterson et al., 2015b) show enrichment in Y, Th, LREE, F, much like the hornblende-biotite granite suite of the BFGC. The $\epsilon_{\text{Nd}_{1.83\text{Ga}}}$ values of the felsic components of the Kivalliq/Nueltin suites encompass a similar range as the Hudson granites and the BFGC (-7 to -11) (Peterson et al., 2002). The mafic rocks of this suite show a broader range of $\epsilon_{\text{Nd}_{1.83\text{Ga}}}$ values (~ -1 to -10) than the felsic rocks, which has been interpreted to reflect derivation of these magmas from both normal and enriched mantle sources and also some degree of crustal contamination (Peterson et al., 2015). The Kivalliq suite is interpreted to be an example of bimodal anorogenic magmatism in which lithospheric delamination triggered a broad-scale mantle upwelling and intrusion of alkalic and sub-alkalic basaltic magma into the lower crust, which in turn caused crustal melting and the generation of the Nueltin suite granitoids (Peterson et al., 2015b; Scott et al., 2015).

Despite being regarded as younger anorogenic magmatism, the Nueltin suite granitoids share more similarities to the BFGC than the Hudson granites. The similarities include: 1) high emplacement temperatures (> 800°C), 2) ferroan and mixed peraluminous/metaluminous compositions, 3) higher average LREE and other incompatible element concentrations, 4) compositions that plot inside or near the within-plate-granite (WPG) field on the Nb versus Y trace-element discrimination diagram, in contrast to data from the Hudson granites, which plot largely in the syn-collisional and volcanic arc granite fields (Fig __), and 4) similar negative $\epsilon_{\text{Nd}_{1.83\text{Ga}}}$ values. These similarities in chemical and isotopic compositions could signify the respective source rocks for the Nueltin and BFGC granitoids shared many geochemical

characteristics. However, there are still notable differences between the Kivalliq/Nueltin suites and BFGC. The encompassing Kivalliq suite was likely emplaced at shallow crustal levels, evidenced by the presence of extrusive equivalents. Most notably, unlike the BFGC and Hudson granites where relationship with mantle-material is more cryptic, the Kivalliq/Nueltin suites have a clear association with mafic material. It is possible that mafic magma underplating was more prevalent in the so-called Nueltin corridor (Peterson et al., 2002) where Kivalliq/Nueltin suite rocks are widespread.

Cumberland batholith

The Cumberland batholith (CB) is a colossal ($221,000 \text{ km}^2$) plutonic complex situated on Baffin Island, Nunavut, with emplacement ages between 1.87 to 1.84 Ga (Whalen et al., 2010). Two different terrane boundaries subdivide the batholith into northern, central, and southern domains. Notably, a significant portion of the CB samples are orthopyroxene-bearing. The batholith spans a wide range of $\text{FeO}^\text{T}/(\text{FeO}^\text{T} + \text{MgO})$ but the majority of samples plot near the ferroan-magnesian boundary on the Frost et al. (2001) discrimination diagram. The batholith also has a broad range of values of the MALI index but most samples plot in the calc-alkalic or alkali-calcic fields. Finally, like the BFGC, the CB includes both moderately peraluminous to moderately metaluminous compositions. In terms of trace elements, the CB on average has similar to lower LREE than the Hudson granites and lower total REE than the BFGC. The CB is interpreted to have been emplaced at mid-crustal depths, however zircon saturation temperatures average $755 \text{ }^\circ\text{C}$ (Whalen et al., 2010), which is similar to the Hudson granites but markedly lower than the Nueltin granites or the BFGC. These lower zircon saturation temperatures are surprising given the common occurrence of the high-temperature mineral, orthopyroxene, in the CB granitoids. It may be that the CB magmas were distinctly zircon undersaturated at emplacement and only crystallized zircon after extensive cooling and differentiation at the emplacement site. Alternatively, the whole-rock compositions may be far removed from liquid compositions in which case T_{ZircSat} would not be a good indicator of magma temperature.

Much like the BFGC and Hudson granites, the Cumberland batholith is interpreted to be derived from dominantly crustal sources with rare instances of mafic magma mingling. The initial εNd values of the CB as a whole range from ~ -16 to -2 but the great majority of samples, including samples from all three domains of the batholith, have εNd between -7 and -2 , which suggests that in addition to a dominant older crustal contribution, there was also a mantle contribution, likely derived from an enriched mantle source. Initially, the favoured tectonic model for the CB was

lithospheric delamination triggered by an over-thickened and partially eclogitized lower crust (Whalen *et al.*, 2010), but, on the basis of its trace-element composition, the CB has recently been proposed as an example of slab failure magmatism (Whalen and Hildebrand, 2019).

Although there are some similarities between the CB and the BFGC (the presence of orthopyroxene, mid-crustal emplacement depths), there are also many differences including the somewhat less ferroan and more calcic nature of the CB as well as its lower incompatible element concentrations and less negative initial ϵ_{Nd} values. The geological setting of the CB also differs significantly than the BFGC and other 1.9-1.7 Ga granitoid suites of the Churchill Province discussed above. Specifically, the CB occurs near and across major terrane boundaries whereas the BFGC, Hudson and Nueltin granitoid suites largely occur in the interior of large crustal blocks. Thus, there is no reason to presume that tectonic models proposed for the CB would also apply to the BFGC.